Summer 2005

Investigation of the Superconducting Properties of Niobium Radio-Frequency Cavities

Gianluigi Ciovati
Old Dominion University

INVESTIGATION OF THE SUPERCONDUCTING PROPERTIES OF NIOBIUM RADIO-FREQUENCY CAVITIES

by

Gianluigi Ciovati
B.S. March 2000, University of Milan
M.S. August 2003, Old Dominion University

A Dissertation Submitted to the Faculty of
Old Dominion University in Partial Fulfillment of the
Requirement for the Degree of

DOCTOR OF PHILOSOPHY

PHYSICS

OLD DOMINION UNIVERSITY
August 2005

Approved by:

_____
Colm T. Whelan (Co-Director)

_____
Peter Kneisel (Co-Director)

_____
Gail E. Dodge (Member)

_____
Richard V. Gregory (Member)

_____
Leposava Vuskovic (Member)

ABSTRACT

INVESTIGATION OF THE SUPERCONDUCTING PROPERTIES OF NIOBIUM RADIO-FREQUENCY CAVITIES

Gianluigi Ciovati
Old Dominion University, 2005
Co-Directors of Advisory Committee: Dr. Colm T. Whelan
Dr. Peter Kneisel

Radio-frequency (rf) superconducting cavities are widely used to increase the energy of a charged particle beam in particle accelerators. The maximum gradients of cavities made of bulk niobium have constantly improved over the last ten years and they are approaching the theoretical limit of the material. Nevertheless, rf tests of niobium cavities are still showing some "anomalous" losses (so-called "Q-drop"), characterized by a marked increase of the surface resistance at high rf fields, in absence of field emission. A low temperature "in-situ" baking under ultra-high vacuum has been successfully applied by several laboratories to reduce those losses and improve the cavity's quality factor. Several models have been proposed to explain the cause of the Q-drop and the baking effect. We investigated the effect of baking on niobium material parameters by measuring the temperature dependence of a cavity's surface impedance and comparing it with the Bardeen-Cooper-Schrieffer's theory of superconductivity. It was found that baking allows interstitial oxygen to diffuse from the surface deeper into the bulk. This produces a significant reduction of the normal electrons' mean free path, which causes an increase of the quality factor. The optimum baking parameters are 120 °C for 24-48 h. We were also able to identify the origin of the Q-drop as due to a high magnetic field, rather then electric field, by measuring the quality factor of a cavity as function of the rf field in a resonant mode with only magnetic field present on the surface. With the aid of a thermometry system, we were able to localize the losses in the high magnetic field region. We measured the Q-drop in cavities which had undergone different treatments, such as anodization, electropolishing and post-purification, and with different metallurgical properties and we study the effectiveness of baking in each case. As a

result, none of the models proposed so far can explain all the experimental observations. We elaborated a model proposing a reduction of the lower critical field due to oxygen contamination as the cause for the Q-drop, and the dilution of oxygen into the bulk during bake-out as the cause for its recovery.

ACKNOWLEDGMENTS

I would like to thank Dr. Peter Kneisel for his help and support since the first day I arrived at Jefferson Lab. His knowledge, energy and enthusiasm have been a great example for me. I would like to thank my advisor at Old Dominion University, Dr. Colm Whelan, for his interest and advice on my research, and the members of the advisory committee: Dr. Dodge, Dr. Gregory and Dr. Vuskovic.

I would like to thank Dr. Juergen Halbritter for his constant guidance and suggestions in interpreting the data. I am also thankful to Dr. Ganapati Rao Myneni and Dr. Jacek Sekutowicz for their support and willingness to share their knowledge and ideas. I also greatly appreciated many interesting discussions with Dr. Alex Gurevich and Dr. Jean Delayen. Being at Jefferson Lab I experienced the wonderful technical abilities of many people, in particular Larry Turlington for preparing drawings, John Brawley and Steve Manning for their abilities in cavity welding, and the greatest machinists, Bob Manus and Gary Slack, for their help in fabricating the cavities and all those "last-minute" fixes. I would like also to thank John Mammosser, Isaiah Daniels, Byron Golden and Ralph Afanador who helped me in many occasions with the chemical treatment and cleaning of the cavities, Pete Kushnick for cryo-support and Danny Forehand for operating the high-temperature furnace. A great thank goes to Michael Morrone for doing such a wonderful job in making all the thermometers of the temperature mapping system. Thanks also to Dr. Bill Lanford for the hydrogen measurements on samples.

I would like to thank Dr. Warren Funk and Dr. Swapan Chattopadhyay from the Management of the Accelerator Division for their financial support of my research activities during very busy times for the Lab.

On a more personal level, I would like to thank my Mom, Dad and Sister for always encouraging me and for their confidence in my abilities.

TABLE OF CONTENTS

Chapter Page

Chapter Page

LIST OF TABLES

Table Page

LIST OF FIGURES

Figure Page

Figure Page

Figure Page

Figure Page

Figure Page

CHAPTER 1

INTRODUCTION

Radio-frequency (rf) superconductivity is a widely used technology in the field of particle accelerators. In the last few years, numerous projects have been initiated for many different purposes: material science, such as the Spallation Neutron Source [1] project in construction in USA and the X-ray Free Electron Laser (XFEL) [2] under construction at the Deutsches Elektronen-Synchrotron laboratory (DESY) in Germany; nuclear physics, such as the Rare Isotope Accelerator [3] planned to be built in the USA; transmutation of nuclear waste, such as the eXperimental Accelerator Driven System (XADS) project in Europe [4] and the Japan Proton Accelerator Research Complex (J-PARC) in Japan [5]. The most important project in the field of high energy physics, after the Large Hadron Collider (LHC) will become operational at CERN (Counseil Européenne pour la Recherche Nucléaire), is the International Linear Collider (ILC) [6], which consists of colliding beams of electrons and positrons, accelerated up to 0.5-1 TeV center-of-mass with a luminosity greater than 10^{34} $cm^{-2}s^{-1}$. In August 2004 the International Technology Recommendation Panel (ITRP) recommended that the technology of choice for the construction of the ~ 30 km long linear accelerators will be rf superconductivity.

Superconducting cavities are used to accelerate a large variety of charged particles (electrons, positrons, proton, antiprotons, and heavy ions) and their main advantage is that they have about five orders of magnitude lower losses than normal-conducting (copper) cavities. Even though superconducting cavities need to be refrigerated at cryogenic temperatures (2-4 K), their efficiency in converting ac power into beam power is about 70%, compared to about 15% of the normal-conducting ones, with obvious reduction in the operation cost of an accelerator.

This dissertation follows the form of *The Physical Review A*.

The beam aperture of superconducting cavities is also larger than in normal-conducting ones, which allows preservation of a better beam quality.

The material of choice to fabricate rf superconducting cavities is predominantly bulk niobium, which is the elemental superconductor with the highest critical temperature (T_c = 9.25 K) and thermodynamic critical field (B_c ~ 200 mT). These are the most important properties for application to particle accelerators since superconductivity will vanish above T_c or B_c.

Niobium has also good metallurgical properties which allow the use of standard fabrication methods to build rf cavities.

Since their first use in the field of particle accelerators in 1974 in Stanford, the performance of rf superconducting niobium cavities have improved over the last thirty years, reaching lower surface resistance and higher accelerating gradients. More accelerators employed the benefits of superconducting cavities and the largest installation is now the Continuous Electron Beam Accelerator Facility (CEBAF) at Jefferson Lab [7], in the USA, with 338 cavities operating since 1993. During this three-decade long development, several loss mechanisms which were limiting the performances of niobium cavities well below the theoretical limits were discovered and overcome. Nowadays, the state of the art of the technology is represented by DESY's nine-cell cavities resonating at 1.3 GHz and operating at peak surface magnetic field (B_p) of about 150 mT and quality factor of about 10^{10} in a complete cryomodule [8].

The major limitation towards achieving the ultimate limit of niobium is represented by anomalous losses (the so-called "Q-drop") which dramatically increase the power dissipated on the cavity walls starting at about B_p ~ 100 mT, which were first observed in 1997 [9, 10]. In the next two years it was found that a low-temperature (100-140 °C) "in-situ" baking of the cavity would significantly reduce those high-field losses [11, 12].

While many experiments were performed and models were proposed over the last few years, there is still no clear understanding about the origins of the high-field losses and an explanation of the baking effect. Furthermore, non-linearities in the dependence of the surface resistance with the rf field appear at low (B_p ~ 10 mT) and medium fields (B_p up to about 80 mT) and their origin is not yet clear.

Understanding the behavior of the surface resistance of niobium in rf field and the influence of surface treatments is important both from an application standpoint, especially in view of a large project as ILC where about 20,000 cavities operating at 35 MV/m are required, and from a physics standpoint, to improve the knowledge of rf superconductivity.

The aim of this thesis is to systematically investigate the material properties of superconducting niobium cavities with different surface treatments, with particular emphasis on the low-temperature "in-situ" baking, and to study non-linearities of the surface resistance as function of the rf field, with particular focus on the high-field Q-drop. Niobium material parameters such as the mean free path of the normal electrons, the energy gap, the critical temperature and the penetration depth had been obtained by comparing low-field surface impedance measurements, sampling up to 300 nm deep in the niobium, with the Bardeen-Cooper-Schrieffer (BCS) theory of superconductivity in order to understand the changes produced by the "in-situ" baking and correlate them with cavity performances at high fields.

Measurements of the field dependence of the surface resistance at low, medium and high field have been compared with different models to verify their validity. In particular, the origin of the high field Q-drop has been attributed to electric field [13], magnetic field [14] or grain boundary effects [15] by different models and the experiments reported in this thesis clarify that issue by measuring a cavity in a resonant mode with only surface magnetic field, a cavity in two modes with different ratios of magnetic to electric fields and a cavity made of a single grain.

This thesis is organized as follows: chapter 2 gives a brief description of the electrodynamics of rf cavities while chapter 3 gives a review of the theory of superconductivity with particular emphasis on the surface impedance and the critical fields. Chapter 4 gives a brief outline of the loss mechanisms characterizing superconducting cavities and of the models which try to explain them. Chapter 5 presents a description of experimental techniques related to the cavity preparation and tests, such as surface treatments and test equipment and procedures. Chapter 6 is dedicated to the systematic study of the material properties of niobium cavities with different baking parameters and their influence on the non-linearities of the surface resistance at low,

medium and high rf field. Chapter 7 presents the results of a series of rf tests on a single-cell cavity excited in two different resonant modes in order to clarify the nature of the high-field losses. Chapter 8 reports about rf tests on particular cavity-shapes, materials and surface treatments to achieve the theoretical critical rf field in superconducting niobium cavities. Chapter 9 presents a discussion of the baking effect and the possible causes of the high-field Q-drop. Finally, the conclusions are given in chapter 10.

CHAPTER 2

BASICS OF RADIO-FREQUENCY CAVITIES

2.1 Radio-frequency fields in cavities

A resonant rf cavity is a device which is able to store a stationary electromagnetic field in a limited volume of space. A good approximation of an ideal cavity is given by a perfect dielectric surrounded by a metal with infinite electrical conductivity.

Combining Maxwell's equations, the rf fields in the cavity are obtained from the eigenvalue equation

$$\left(\nabla^2 - \frac{1}{c^2}\frac{\partial^2}{\partial t^2}\right)\begin{Bmatrix}\mathbf{E}\\ \mathbf{H}\end{Bmatrix} = 0 \tag{1}$$

with the boundary conditions

$$\hat{n}\times\mathbf{E} = 0, \quad \hat{n}\cdot\mathbf{H} = 0 \tag{2}$$

at the cavity walls. Here $\hat{n}$ is the unit vector normal to the surface of the conductor, $\mathbf{E}$ is the electric field and $\mathbf{H}$ is the magnetic field.

In cylindrically symmetric cavities, the symmetry axis coincides with the beam line and the simplest example of a cavity is a cylindrical waveguide shorted by metal plates placed at a certain distance d ("pill-box" cavity) for which the eigenvalue equation can be solved analytically.

In cylindrically symmetric cavities, the discrete mode spectrum resulting from Eq. (1) splits into two groups, transverse magnetic (TM) modes, where the magnetic field is transverse to the cavity symmetry axis, and transverse electric (TE) modes, where it is the electric field that is transverse. Modes are classified as TM_{mnp}, where the integers m, n and p count the number of sign changes of E_z in the ϕ, r and z directions respectively.[1] Only TM_{0np} (n = 1, 2, 3..., p = 0, 1, 2...) modes have a nonvanishing longitudinal electric field on axis and the TM_{010} is used for particle acceleration in most cavities. It can be

[1] TE modes are classified in the same manner.

shown that the cavity's mode spectrum is inversely proportional to the cavity size and detailed expression of the fields in the various modes can be found in [16].

For practical applications for particle accelerators, the cavity shape is more complicated than a "pill-box" and is optimized using numerical simulations with computer codes to obtain the field distributions. One of the most commonly used 2-D codes is SUPERFISH [17], while HFSS [18] and MAFIA [19] are popular 3-D codes. Figure 1 shows a sketch of the cavity used for our tests. The geometry is the same as for the cavities used in the CEBAF accelerator [7].

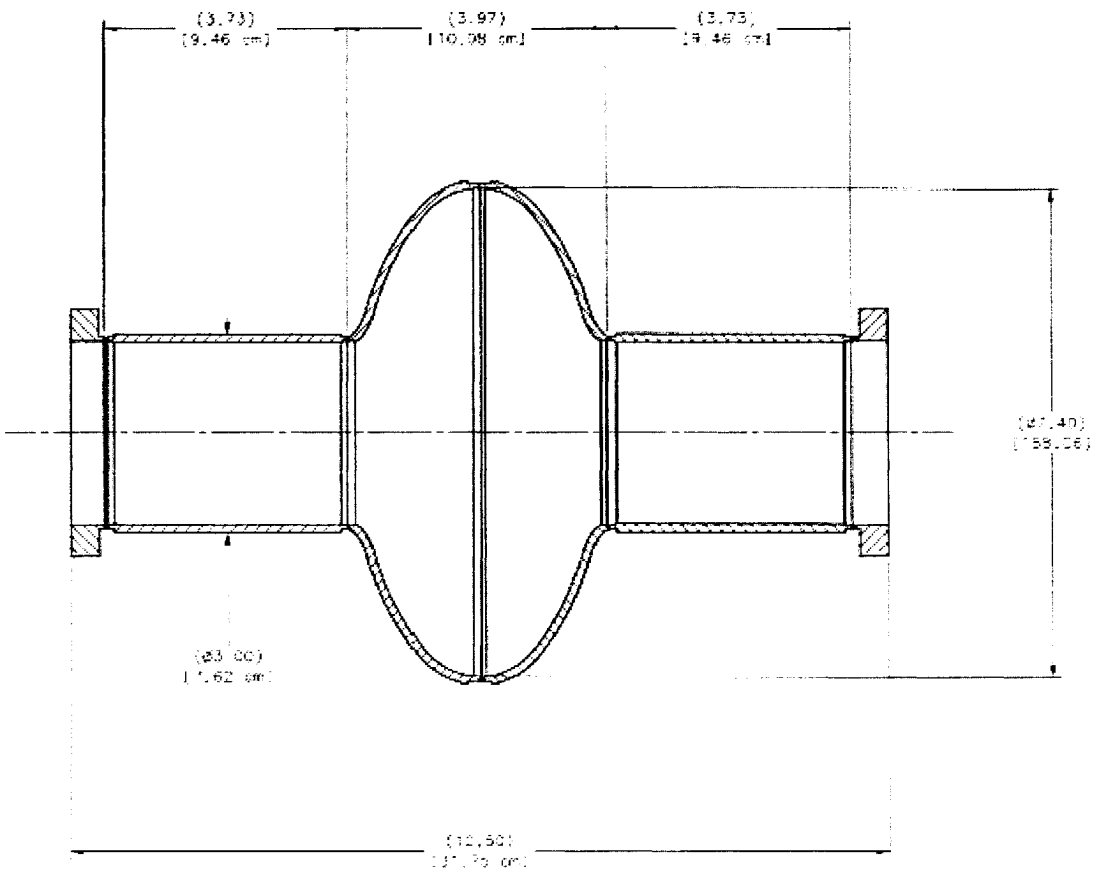

FIG 1. Geometry of the single cell cavity used for the measurements reported in this thesis.

2.2 Figures of merit

2.2.1 Accelerating voltage

Consider a charged particle traveling at speed v entering the cavity on axis at time $t = 0$ and leaves at a time $T = d/v$, where d is the cavity length. During the transit, it sees a time-varying electric field and in order to see a field pointing in the same direction to receive the maximum acceleration from the cavity, the charge must leave the cavity when the electric field changes sign. Therefore, the time it takes the charge to traverse the cavity needs to equal one-half an rf period:[2]

$$T = \frac{\pi}{\omega_0} = \frac{d}{v}, \tag{3}$$

where ω_0 is the angular frequency of the accelerating mode. Equation (3) is used to determine the cavity length, d.

We can define the accelerating voltage (V_{acc}) of a cavity as the ratio between the maximum energy gain possible during transit and the particle's charge q,

$$V_{acc} = \left| \int_0^d E_z(r=0,z) e^{i\omega_0 z/c} dz \right|. \tag{4}$$

The average accelerating field (E_{acc}) is also defined as:

$$E_{acc} = \frac{V_{acc}}{d}. \tag{5}$$

2.2.2 Peak surface fields

The highest accelerating field that a cavity can have is limited by the maximum surface fields it can maintain. The peak surface electric field (E_p) must be kept low in order to reduce the risk of having field emission (see section 4.4) while the peak surface magnetic field (B_p) must be kept below the rf critical magnetic field in order to avoid a quench to the normal state in superconducting cavities. In the TM_{010} mode, the magnetic field is concentrated in the equator region, while the electric field is strongest at the

---

[2] In first approximation, we neglect the change of speed of the particle traversing the cavity, as it is usually close to the speed of light.

cavity irises (Fig. 2). The ratios E_p/E_{acc} and B_p/E_{acc} can be optimized by modifying the cavity shape.

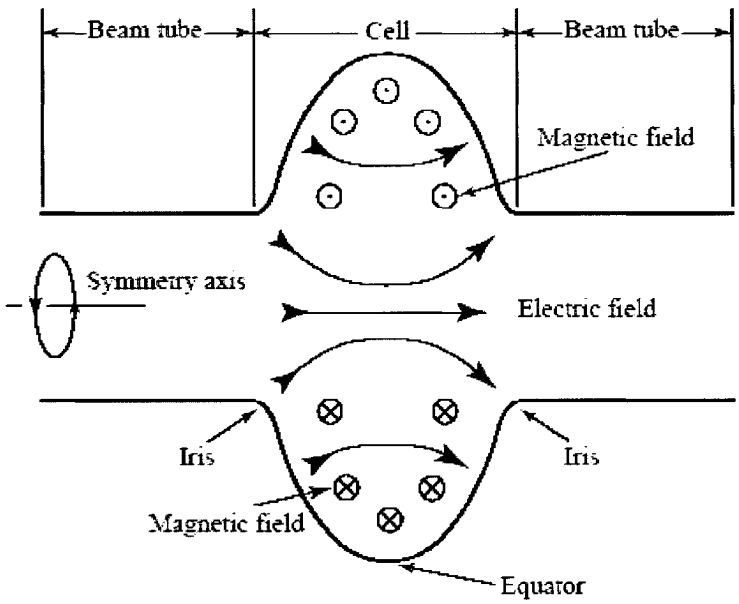

FIG. 2. Schematic of a single-cell cavity excited in the TM_{010} mode [20].

2.2.3 Geometry factor and shunt impedance

An important figure of merit for accelerating cavities is the quality factor (Q_0), defined as the ratio between the cavity stored energy (U) and the power dissipated in the cavity walls (P_c) in one rf radian,

$$Q_0 = \frac{\omega_0 U}{P_c}. \tag{6}$$

The cavity stored energy is given by

$$U = \frac{1}{2}\mu_0 \int_V |\mathbf{H}|^2 \, dv = \frac{1}{2}\varepsilon_0 \int_V |\mathbf{E}|^2 \, dv, \tag{7}$$

and the dissipated power due to Joule heating is[3]

[3] We assume that the surface resistance does not change over the cavity surface.

$$P_c = \frac{1}{2} R_s \int_S |\mathbf{H}|^2 \, ds \,. \tag{8}$$

It is possible to define the geometry factor (G) as

$$G = Q_0 R_s = \frac{\omega_0 \mu_0 \int_V |\mathbf{H}|^2 \, dv}{R_s \int_S |\mathbf{H}|^2 \, ds}, \tag{9}$$

which depends only on the cavity shape and not on its size for a given field configuration.

Another quantity that characterizes the losses in a cavity is the shunt impedance (R), defined as

$$R = \frac{V_{acc}^2}{P_c} \tag{10}$$

and expresses how much acceleration is obtained for a certain power dissipation. The ratio R/Q_0 is given by

$$\frac{R}{Q_0} = \frac{V_{acc}^2}{\omega_0 U} \tag{11}$$

and this quantity is independent on the cavity size and material.

Ideally, it is desirable to design an accelerating cavity with the highest possible values of the geometry factor and R/Q_0 and the lowest possible values of E_p/E_{acc} and B_p/E_{acc}, but in reality there is a trade-off between all these parameters. The figures of merit, computed with SUPERFISH [17], for the single-cell cavity used for our experiments are shown in Table I.

TABLE I. Figures of merit for the CEBAF single-cell cavity used for our tests.

E_p/E_{acc}	1.78
B_p/E_{acc}	4.43 mT/(MV/m)
G	273 Ω
R/Q_0	96.5 Ω

CHAPTER 3

SUPERCONDUCTIVITY

3.1 Introduction

Superconductivity, discovered in 1911 by Kammerlingh-Onnes [21], is characterized in simple terms by two basics effects: absence of electrical resistance and perfect diamagnetism.

Below a certain temperature, called critical temperature (T_c), some materials exhibit an abrupt drop of the dc electrical resistance to an immeasurably low value. This means, for example, that a wire made of superconducting material can carry current without any power dissipation. Several pure elements, compounds and alloys exhibit superconducting behavior below a wide range of critical temperatures, as can be seen in Table II.

The second signature of superconductivity is its ability to completely expel an applied magnetic field from the interior of the material when cooled down below the critical temperature and therefore to behave as a perfect diamagnet. This effect was discovered by Meissner and Ochsenfeld in 1933 [22]. The exclusion of the magnetic field is due to electrical "screening currents" that flow at the surface of the superconducting metal and which generate a magnetic field that exactly cancels the externally applied field inside the superconductor. These screening currents are generated whenever a superconducting metal is brought inside a magnetic field. This may be understood from the fact that a superconductor has zero electrical resistance and therefore the induced "eddy currents" will never decay. However, the screening currents also appear in a situation where the magnetic field is applied after the metal has gone through the superconducting transition, so that the Meissner effect cannot be explained merely by zero resistance; i.e. the magnetic field is a thermodynamic entity. If magnetic field applied to a superconductor exceeds a certain value, called critical magnetic field B_c, the superconducting state is destroyed. This implies that there exists also a maximum value of the current that a superconductor may carry.

TABLE II. Critical temperatures of some elements, alloys and metallic compounds.

	T_c [K]
Al	1.2
In	3.4
Sn	3.7
Hg	4.2
Ta	4.5
Pb	7.2
Nb	9.3
Ta-Nb	6.3
NbN	16
Nb_3Sn	18
MgB_2	39
$Y_1Ba_2Cu_3O_{7-\delta}$	~ 90[4]

In 1950 it was discovered [23] that the critical temperature is inversely proportional to the square root of the mass of the isotope, for isotopes of the same element. This is the so-called "isotope effect".

Measurements of the optical properties of superconductors in 1956 [24] showed that absorption of electromagnetic waves in the superconducting state begins abruptly at a frequency (ν_0) whose value approaches zero as the temperature increases towards the critical temperature. Well below the critical temperature ν_0 is substantially constant and has a value of about 500 GHz.

In the same year, measurements of the specific heat of superconductors [25] showed a significant jump occurring at the critical temperature without the appearance of any latent heat and, at lower temperatures, an exponential dependence of the electronic specific heat (C_{es}) on temperature of the form

$$C_{es} \approx \gamma T_c a e^{-bT_c/T}, \tag{12}$$

[4] This compound with $T_c > \sim 30$ K is called a "high-temperature superconductor" and the exact value of the critical temperature depends on the precise stoichiometry.

where a and b are numerical constants and γ is the Sommerfeld constant. In the normal state, the electronic specific heat is $C_{en} = \gamma T$.

3.2 Phenomenological models

In 1934 Gorter and Casimir [26] interpreted the thermodynamics of superconductors in terms of coexisting fluids of normal and "super" electrons which can move through the metal without resistance. Based on this so-called "two-fluid model", London was able to derive in 1935 [27] two equations that describe the resistance-less and perfect diamagnetism of superconductivity. The superelectrons accelerate steadily in the presence of a constant electric field ($d\mathbf{v}_s/dt = e\mathbf{E}/m$) so that the supercurrent density is governed by

$$\frac{d\mathbf{J}_s}{dt} = n_s e \frac{d\mathbf{v}_s}{dt} = \frac{n_s e^2}{m}\mathbf{E} \tag{13}$$

where n_s is the density of superelectrons. Equation (13) is the first London equation and, using Maxwell's equations with Eq. (13), the following is obtained

$$\nabla^2 \dot{\mathbf{B}} = \frac{\mu_0 n_s e^2}{m}\dot{\mathbf{B}}. \tag{14}$$

Calling $\lambda_L = \sqrt{m/\mu_0 n_s e^2}$, the solution of Eq. (14) in a simple one-dimensional case is

$$\dot{B}(x) = \dot{B}_a e^{-x/\lambda_L} \tag{15}$$

where B_a is the applied field. London, in order to describe the Meissner effect, assumed that Eq. (14) is valid not only for the time-derivative of **B** but also for **B** itself, since the magnetic field inside a superconductor is not only constant but zero.

The second London equation is

$$\mathbf{B} = -\frac{m}{n_s e^2}\nabla \times \mathbf{J}_s \tag{16}$$

and Eq. (14) becomes

$$\nabla^2 \mathbf{B} = \frac{1}{\lambda_L^2}\mathbf{B}, \tag{17}$$

showing that the magnetic field decreases exponentially inside the superconductor. The distance to which the magnetic field decays to *1/e* of its value at the surface is called "London penetration depth" λ_L.

London was able to derive Eqs. (13) and (16) using a quantum mechanical description of a superelectrons wavefunction having the property that <**p**> = 0 [28]. The average velocity of the superelectrons would then be $\langle \mathbf{v}_s \rangle = -e\mathbf{A}/m$ and the supercurrent density could be express in term of the vector potential **A**

$$\mathbf{J}_s = n_s e \langle \mathbf{v}_s \rangle = -\frac{n_s e^2}{m}\mathbf{A}. \tag{18}$$

London's equations (13) and (16) could therefore be derived directly using Eq. (18).

The London penetration depth depends on the material and increases with temperature, diverging rapidly close to T_c. The two-fluid model gives the following expression for the superelectron density n_s (normalized to the total electron density n) as a function of temperature

$$\frac{n_s}{n} = 1 - \left(\frac{T}{T_c}\right)^4 \tag{19}$$

yielding the following temperature dependence of the London penetration depth

$$\lambda_L(T) = \frac{\lambda_L(0)}{\sqrt{1-\left(\frac{T}{T_c}\right)^4}} \tag{20}$$

which was found to agree well with experimental data between 0.6 and 0.95 T_c.

The value of $\lambda_L(0)$ of niobium calculated using the definition given by London is about 20 nm and is about a factor two lower than the experimental data. In order to explain this discrepancy, Pippard proposed in 1950 [29] a nonlocal generalization of Eq. (18), in analogy with Chamber's nonlocal generalization of Ohm's law. He introduced a characteristic dimension of the superconducting wavefunction, called "coherence length" ξ_0 which plays a role analogous to the mean free path l in the nonlocal electrodynamics of normal metals. The value of ξ_0 could be estimated by using an uncertainty-principle argument to be

$$\xi_0 = a\frac{\hbar v_F}{kT_c}, \tag{21}$$

where a = 0.15 is a constant obtained from a fit of experimental data, v_F is the Fermi velocity and k is Boltzmann's constant. The value of the coherence length is of the order of a few tens of nanometers in elemental superconductors.

The nonlocal expression of Eq. (18) suggested by Pippard is

$$\mathbf{J}_s(\mathbf{r}) = -\frac{3}{4\pi\xi_0}\frac{n_s e^2}{m}\int\frac{\mathbf{R}\left[\mathbf{R}\cdot\mathbf{A}(\mathbf{r}')\right]}{R^4}e^{-R/\xi}d\mathbf{r}' \tag{22}$$

where $\mathbf{R} = \mathbf{r} - \mathbf{r}'$ and the coherence length in the presence of scattering was assumed related to that of pure material, ξ_0, by

$$\frac{1}{\xi} = \frac{1}{\xi_0} + \frac{1}{l}. \tag{23}$$

A complete theory of superconductivity (called the BCS theory) was presented by Bardeen, Cooper and Schrieffer in 1957 [30] and is described in the next section.

3.3 The Bardeen-Cooper-Schrieffer theory

A successful theory of superconductivity must be able to explain the following:

1. in the superconducting state there is a change in the behavior of the conduction electrons which is marked by the appearance of a gap in the energy spectrum, as suggested by its electrical and optical properties.
2. The crystal lattice does not change, but must play an important role since the critical temperature depends on the atomic mass (isotope effect)
3. The superconducting-to-normal transition is a phase change of second order, as seen from the specific heat.

The probability of an energy level being occupied by an electron in a normal metal is given by the Fermi-Dirac distribution

$$f(E) = \frac{1}{e^{(E-E_F)/kT}+1} \tag{24}$$

where E_F is the Fermi energy. At absolute zero, the Fermi-Dirac function is a step-function and the points which represent the momenta of the electrons in three-

dimensional momentum space occupy a sphere of radius p_F, known as the "Fermi sea", where $p_F = \sqrt{2mE_F}$.

Bardeen, Cooper and Schrieffer considered a model of two electrons added to a Fermi sea at absolute zero, with the stipulation that the electrons interact with each other but not with those in the sea, except via Pauli's exclusion principle. Electron-electron interaction may occur through exchange of a lattice phonon. A schematic of the interaction is shown in Fig. 3. From momentum conservation, we can see that if an electron is scattered from $\hbar\mathbf{k}$ to $\hbar\mathbf{k}'$, the phonon must carry the momentum $\mathbf{q} = \mathbf{k} - \mathbf{k}'$ and it can be shown that if the electron energy before and after scattering differs less than $\hbar\omega_\mathbf{q}$ (where $\omega_\mathbf{q}$ is the phonon angular frequency), the overall result of the process is that there is an attraction between the two electrons.

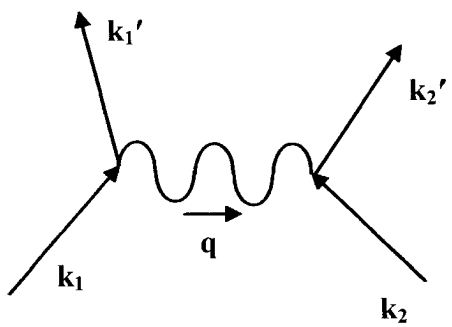

FIG. 3. Feynmann diagram of electron-electron interaction transmitted by a phonon.

The physical idea behind this process is that the first electron polarizes the medium by attracting positive ions and these excess positive ions attract the second electron. The electrons are forming a so-called Cooper pair. The distance between the emission of the phonon and absorption by another electron is the BCS coherence length ξ_0.

Considering the problem of adding electron pairs to the Fermi sea at 0 K, their momenta before and after scattering must lie within a range $\Delta k = m\omega_L/p_F$ of the Fermi momentum p_F (ω_L is an "average" phonon frequency typical of the lattice). Since all the

pairs of values of k_i and k_j must satisfy the condition $\mathbf{k}_i + \mathbf{k}_j = \text{constant}^5 = \mathbf{K}$, it can be shown (Fig. 4) that the largest number of allowed scattering processes, yielding the maximum lowering of the energy, is obtained by pairing electrons with equal and opposite momenta. Furthermore, from the requirement of antisymmetry of the pair wavefunction with respect to exchange of the two electrons, the state which gives the lower energy is the singlet one, so that the spin of the electrons forming a pair must be opposite. A Copper pair wavefunction can therefore be written as

$$\psi_0(\mathbf{r}) = \left[\sum_{k>k_F} g_{\mathbf{k}} \cos(\mathbf{k}\cdot\mathbf{r})\right]\left(\uparrow_1\downarrow_2 - \downarrow_1\uparrow_2\right), \tag{25}$$

where $\mathbf{r} = \mathbf{r}_1 - \mathbf{r}_2$, $g_{\mathbf{k}}$ are weighting coefficients, $\uparrow_1$ refers to "up" spin state of electron 1, whereas $\downarrow_1$ refers to its "down" state.

Solving the Schroedinger equation for the pair wavefunction (assuming an approximated attractive potential equal to a constant $-V$ for momentum states out to a cutoff energy $\hbar\omega_c$ away from E_F and equal to zero beyond $\hbar\omega_c$) one obtains a bound state with energy lower than $2E_F$. Therefore, in forming a pair with equal and opposite momenta and opposite spin, the lowering of the potential energy due to the interaction exceeds the amount by which the kinetic energy is in excess of $2E_F$.

The results obtained when two additional electrons are added to the metal at 0 K apply equally well to the situation in which two electrons already belonging to the metal, with momenta infinitesimally below p_F, are transformed into a Cooper pair. The number of electrons that can form Cooper pairs is limited by the availability of empty states to which the pair of electrons may scatter so that an equilibrium condition is reached. Only a small fraction of electrons, with energies within $kT_c \approx \hbar\omega_c$, form Cooper pairs.

---

[5] In each scattering event the total momentum of the two electrons is conserved.

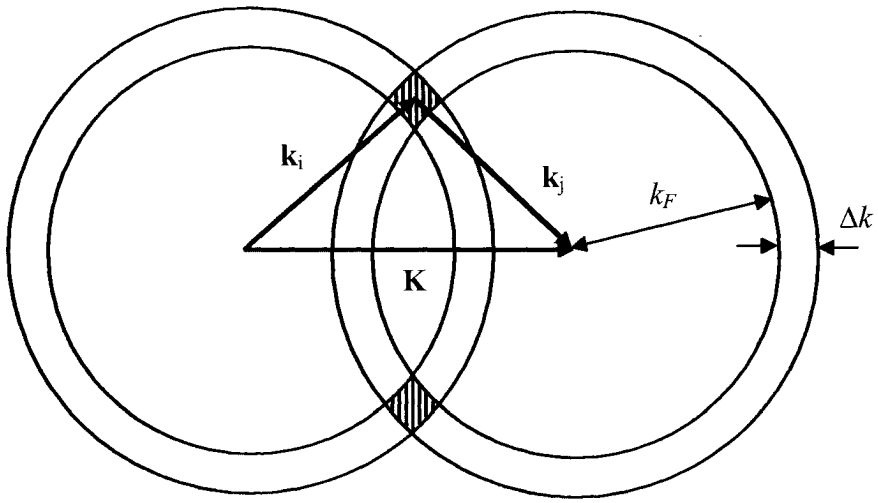

FIG. 4. The figure shows two shells of radius k_F and thickness Δk whose centers are separated by the vector **K**. The number of pairs for which $\mathbf{k}_i - \mathbf{k}_j = \mathbf{K}$ is proportional to the shaded areas. This number is maximum when $\mathbf{K} = 0$.

The BCS theory gives the following expression for the wavefunction describing the ground state of $N/2$ Cooper pairs

$$|\psi_G\rangle = \prod_{\mathbf{k}=\mathbf{k}_1,\ldots,\mathbf{k}_M} \left(u_{\mathbf{k}} + v_{\mathbf{k}} c^*_{\mathbf{k}\uparrow} c^*_{-\mathbf{k}\downarrow}\right)|\phi_0\rangle, \tag{26}$$

where M denotes the highest occupied level, $|v_{\mathbf{k}}|^2$ indicates the probability that the pair ($\mathbf{k}\uparrow$, $-\mathbf{k}\downarrow$) is occupied, whereas the probability that is unoccupied is $|u_{\mathbf{k}}|^2 = 1 - |v_{\mathbf{k}}|^2$. $|\phi_0\rangle$ is the vacuum state with no particles present and $c^*_{\mathbf{k}\uparrow}$ is a "creation operator" which creates an electron of momentum $\hbar\mathbf{k}$ and spin up. The paired electrons belong all to the same quantum state and have the same energy, because they are all continuously being scattered between single-electron states having momenta within the range $\hbar\Delta k$, so that their modes of motion cannot be distinguished in any way.

The fractional occupation number $v_{\mathbf{k}}^2$ is given by

$$v_{\mathbf{k}}^2 = \frac{1}{2}\left[1 - \frac{E_{\mathbf{k}} - E_F}{\sqrt{(E_{\mathbf{k}} - E_F)^2 + \Delta^2}}\right]. \tag{27}$$

Δ is the so-called energy gap and is given by

$$\Delta = \frac{\hbar\omega_c}{\sinh\left[1/N(E_F)V\right]} \approx 2\hbar\omega_c e^{-1/N(E_F)V}, \tag{28}$$

where the approximation is justified in the weak-coupling limit $N(E_F)V<<1$. $N(E_F)$ is the density of states of electrons for electrons at the Fermi energy of the normal metal and V is the amplitude of the interaction potential. The fractional occupation number as a function of the momentum is shown in Fig. 5 and it shows that, in the superconducting ground state, even at absolute zero there are vacancies with $p_i < p_F$ and occupied states with $p_i > p_F$.

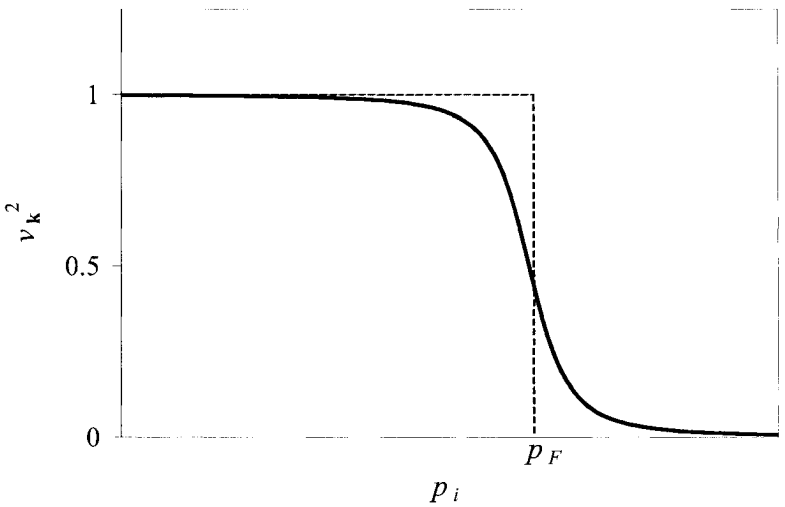

FIG. 5. Probability that the two-electron state ($\mathbf{k}_i\uparrow$, $-\mathbf{k}_i\downarrow$) is occupied in the BCS ground state wavefunction (solid line) and probability that a single-electron state with momentum $\hbar k_i$ is occupied in a normal metal at absolute zero (dashed line).

The theory establishes that the ratio between the energy gap at 0 K and the critical temperature is a constant $\Delta(0)/kT_c = 1.764$ but in reality this ratio is different from one material to another due to differences in the electron-phonon interaction strength. The energy gap is also related to the coherence length ξ_0 which represents the spatial

extension of a Cooper pair wavefunction. The BCS theory provides the following expression for ξ_0

$$\xi_0 = 0.18\frac{\hbar v_F}{kT_c}, \tag{29}$$

in good agreement with Eq. (21) determined by Pippard. The fact that the coherence length is about two orders of magnitude larger than the inter-atomic distance shows that the superconducting state is characterized by a long-range correlation. Figure 6 shows a schematic representation of the energy spectrum of a superconductor, compared with one of a normal conductor.

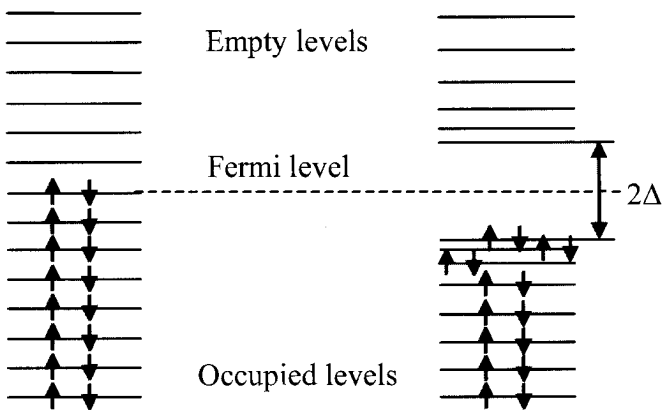

FIG. 6. Schematic of the energy spectrum of a superconductor (right), showing a gap in the energy levels, compared to a normal conductor one (left).

At temperatures greater than the absolute zero, the excited state of a superconductor can be constructed in a one-to-one correspondence with the normal state. In the first excited state, one electron would have a momentum $\hbar\mathbf{k}$ and spin up while the complementary state is empty. The unpaired electron behaves almost like a free electron and is called "quasi-particle". The electronic density of states of a superconductor [$N_s(E)$] relative to the density of states of a normal electron at the Fermi energy is given by

$$\frac{N_s(E)}{N(E_F)} = \begin{cases} \dfrac{E - E_F}{\sqrt{(E - E_F)^2 - \Delta^2}} & E > E_F + \Delta \\ 0 & E < E_F + \Delta \end{cases} . \tag{30}$$

Figure 7 shows this normalized density of states.

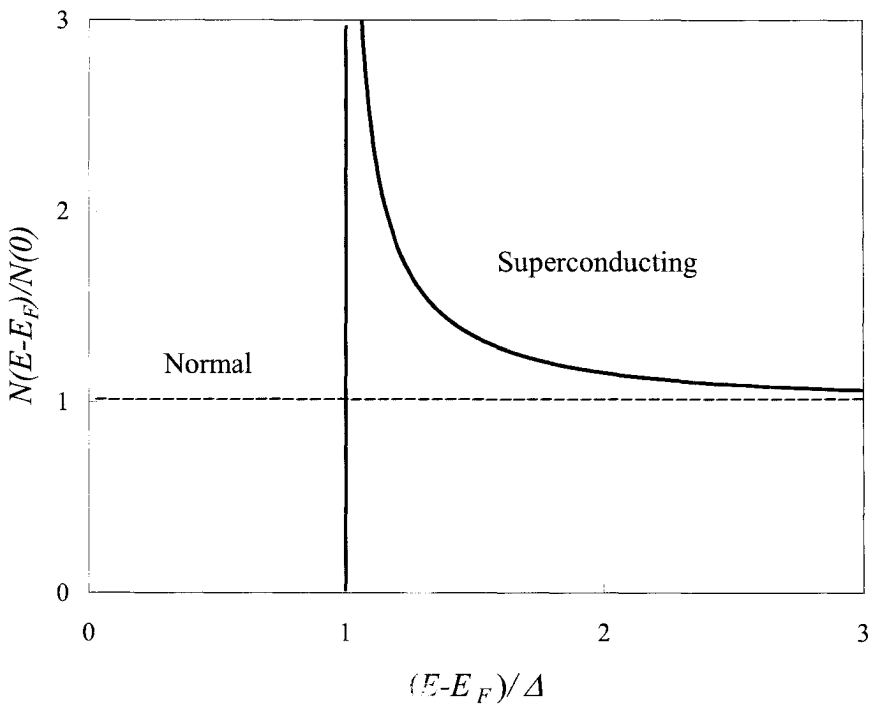

FIG. 7. Density of states of superconducting compared to normal state.

The energy gap decreases at $T > 0$ K, since more quasi-particles are thermally excited, until becomes zero at T_c. An approximation of the temperature dependence of the energy gap, shown in Fig. 8, is given by [29]

$$\Delta(T) = \Delta(0)\sqrt{\cos\left(\frac{\pi t^2}{2}\right)} \tag{31}$$

where t is the reduced temperature T/T_c.

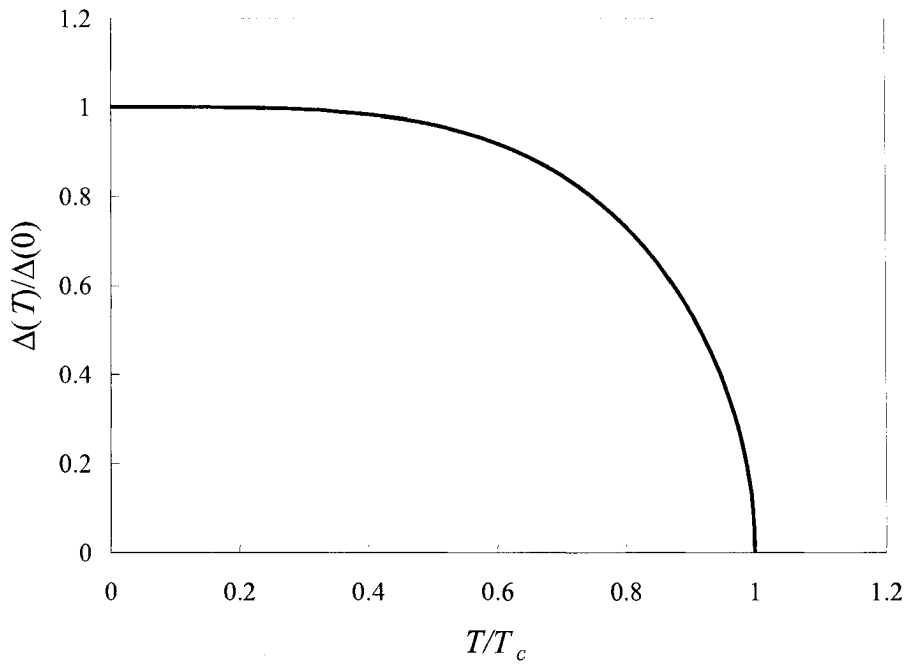

FIG. 8. Temperature dependence of the energy gap.

The absence of resistance in a superconductor is due to the fact that, when carrying a current, each Cooper pair acquires a momentum $\hbar\mathbf{K}$ which is the same for all pairs. The entire momentum distribution is shifted bodily in momentum space by an amount $\hbar\mathbf{K}/2$ and the states which make up the pair wavefunction have momenta of the form $[(\mathbf{k}_i+ \mathbf{K}/2)\uparrow, (-\mathbf{k}_i+ \mathbf{K}/2)\downarrow]$. In a normal metal, resistance is inevitably present because the electrons can be scattered (due to impurity atoms, lattice defects or thermal vibrations) with a change in momentum so that their free acceleration is hindered. In a superconductor, the electrons which make up a Cooper pair are constantly scattering each other, but since the *total* momentum remains constant in such a process there is no change in the current flowing. The total momentum of a pair can be changed only if the pair is broken up but this requires a minimum energy of 2Δ which has to be supplied from somewhere.

3.4 The Ginzburg-Landau theory

In 1950 Ginzburg[6] and Landau [32] proposed a theory of superconductivity alternative to the London theory. A pseudowavefunction $\psi(\mathbf{r}) = |\psi(\mathbf{r})|e^{i\phi(\mathbf{r})}$ was introduced as a complex order parameter with $|\psi(\mathbf{r})|^2$ representing the local density of superconducting electrons, $n_s(\mathbf{r})$. According to the phase transition of second order, the Helmholtz free energy density (f) of the superconducting state differs from that of the normal state by an amount which can be written as a power series in $|\psi(\mathbf{r})|^2$ of the form

$$f_s = f_n + \alpha|\psi|^2 + \frac{\beta}{2}|\psi|^4 + \frac{1}{2m^*}\left|\left(-i\hbar\nabla - e^*\mathbf{A}\right)\psi\right|^2 + \frac{\mu_0 H^2}{2}, \tag{32}$$

where m^* and e^* are respectively twice the mass and the charge of the electron. The first two terms of Eq. (32) are adequate near the second order phase transition at T_c. The last term is the energy due to the presence of a magnetic field. The third term can be re-written as

$$\frac{1}{2m^*}\left[\hbar^2\left(\nabla|\psi|\right)^2 + \left(\hbar\nabla\phi - e^*\mathbf{A}\right)^2|\psi|^2\right]. \tag{33}$$

The first term gives the extra energy associated with gradients in the magnitude of the order parameter. The second term gives the kinetic energy associated with supercurrents in a gauge-invariant form $\left[\mathbf{v}_s = \left(\mathbf{p}_s - e^*\mathbf{A}\right)/m^*\right]$. In the London gauge, ϕ is constant and equating this term to the corresponding one obtained by London, the following definition of the Ginzburg-Landau penetration depth is obtained

$$\lambda_{GL} = \sqrt{\frac{m^*}{\mu_0|\psi|^2 e^{*2}}}. \tag{34}$$

The central problem of the Ginzburg-Landau approach is now to find functions ψ and $\mathbf{A}$ which make the free energy density a minimum subject to appropriate boundary conditions. This leads to the Ginzburg-Landau differential equations

$$\alpha\psi + \beta|\psi|^2\psi + \frac{1}{2m^*}\left(-i\hbar\nabla - e^*\mathbf{A}\right)^2\psi = 0 \tag{35}$$

---

[6] Ginzburg and Abrikosov received the Nobel prize in 2003 for their contribution to the theory of superconductors.

$$\mathbf{J} = \frac{e^*}{m^*}\psi^*\left(-i\hbar\nabla - e^*\mathbf{A}\right)\psi\,. \tag{36}$$

A characteristic length (ξ_{GL}) for variation of the order parameter was defined as

$$\xi_{GL}(T) = \frac{\hbar}{\sqrt{2m^*|\alpha(T)|}} \propto \frac{1}{\sqrt{1-t}} \tag{37}$$

and is different from the coherence length introduced by Pippard, $\xi_{GL}(T) \approx \xi_0$ for pure metals well below T_c. It is useful to introduce the so-called Ginzburg Landau parameter (κ_{GL}) defined as the ratio of the two characteristic lengths

$$\kappa_{GL} = \frac{\lambda_{GL}(T)}{\xi_{GL}(T)}\,. \tag{38}$$

It varies slowly with temperature as $\kappa_{GL}(0)/(1 + t^2)$.

The Ginzburg-Landau theory (GL theory) is useful in describing the behavior of thin films in the presence of a magnetic field and in identifying two types of superconductors described in section 3.7.2. In 1959 Gor'kov [33] showed that the GL theory is a limiting case of the BCS theory for temperatures close to T_c.

3.5 The penetration depth

A general definition of the magnetic field penetration depth into a bulk sample with plane geometry is given by

$$\lambda = \frac{1}{H(0)}\int_0^\infty H(z)\,dz = \frac{A(0)}{\mu_0 H(0)}, \tag{39}$$

and is obtained by solving the following equations

- Maxwell's equation

$$-\frac{d^2A(z)}{dz^2} = \mu_0 J(z) \tag{40}$$

- material equation

$$J(z) = -\frac{3}{4\mu_0\xi_0\lambda_L^2(T)}\int\frac{A(z')}{(z-z')^2}K(z-z',T)\,dz' \tag{41}$$

where the BCS range function $K(z\text{-}z',T)$ is very similar to the exponential form $e^{-(z-z')/\xi}$ proposed by Pippard.

The boundary conditions for the vector potential are

$$-\left.\frac{dA(z)}{dz}\right|_{z=0} = \mu_0 H(0), \qquad A(\infty) = 0 \tag{42}$$

plus boundary conditions for electrons hitting the surface: specular or diffuse reflection. This problem can be solved exactly applying Fourier analysis [34]. If $A(z')$ is constant over the range of $K(z-z',T)$, (41) reduces to the London equation $J(z) = -\frac{1}{\mu_0 \lambda_L^2} A(z)$. However, if $A(z)$ varies significantly on the scale of ξ_0 the nonlocality of the electrodynamics must be taken into account. It is possible to give an estimate of the penetration depth at 0 K in two limits, the "local" ($\lambda_L > \xi_0$) and the "anomalous" or nonlocal one ($\lambda_L < \xi_0$)

$$\lambda \approx \lambda_L \qquad \text{local limit, } \lambda_L > \xi_0 \tag{43}$$

$$\lambda \approx \left(\lambda_L^2 \xi_0\right)^{1/3} \qquad \text{nonlocal limit, } \lambda_L < \xi_0 \tag{44}$$

The previous results apply to a pure metal, for which the mean free path of the normal electrons l is much larger than the coherence length. In the presence of impurities, this approximation is not valid and the effect of a finite mean free path has to be taken into account in Eq. (41). An approximate expression for the penetration depth at 0 K in the "dirty" limit ($l < \xi_0$) is given by

$$\lambda = \lambda_L \sqrt{1 + \frac{\xi_0}{l}}\,. \tag{45}$$

The temperature dependence of the penetration depth $\lambda_L(T)$ is not universal in all superconductors. This is due to the fact that close to T_c, all superconductors become local since $\lambda_L(T) > \xi_0$, so that $\lambda(T) \approx \lambda_L(T) \sim (T_c - T)^{-1/2}$. At lower temperatures $\lambda(T) \approx (\lambda_L^2 \xi_0)^{1/3} \sim (T_c - T)^{-1/3}$. This implies a crossover between the two expressions near the temperature at which $\lambda_L(T) \sim \xi_0$, but this occurs at different values of T/T_c for different superconductors. In particular, the two-fluid dependence given by Eq. (20) does not apply equally well to all materials. The GL theory gives the following expressions for the penetration depth, coherence length and Ginzburg-Landau parameter close to T_c in the pure and dirty limit

$$\lambda_{GL}(t) = \frac{\lambda_L(0)}{\sqrt{2(1-t)}} \qquad \text{pure} \qquad (46)$$

$$\lambda_{GL}(t) = \frac{\lambda_L(0)}{\sqrt{2(1-t)}}\sqrt{\frac{\xi_0}{1.33l}} \qquad \text{dirty} \qquad (47)$$

$$\xi_{GL}(t) = 0.74\frac{\xi_0}{\sqrt{1-t}} \qquad \text{pure} \qquad (48)$$

$$\xi_{GL}(t) = 0.855\sqrt{\frac{\xi_0 l}{1-t}} \qquad \text{dirty} \qquad (49)$$

$$\kappa_{GL} = 0.96\frac{\lambda_L(0)}{\xi_0} \qquad \text{pure} \qquad (50)$$

$$\kappa_{GL} = 0.715\frac{\lambda_L(0)}{l} \qquad \text{dirty} \qquad (51)$$

A detailed description of the dependence of the penetration depth on material parameters and temperature was given by Halbritter [35].

Figure 9 shows the ratio of the penetration depth to the London penetration depth as a function of the ratio $\lambda_L(0)/\xi_0$ for $T = 0.2T_c$, pure and dirty limits and diffuse reflection as predicted by the BCS theory. Figure 10 shows $\lambda(T)/\lambda_L(0)$ as a function of the so-called reduced parameter $y = 1/\sqrt{1-t^4}$ in the clean and dirty limits and diffuse reflection as given by the BCS theory.

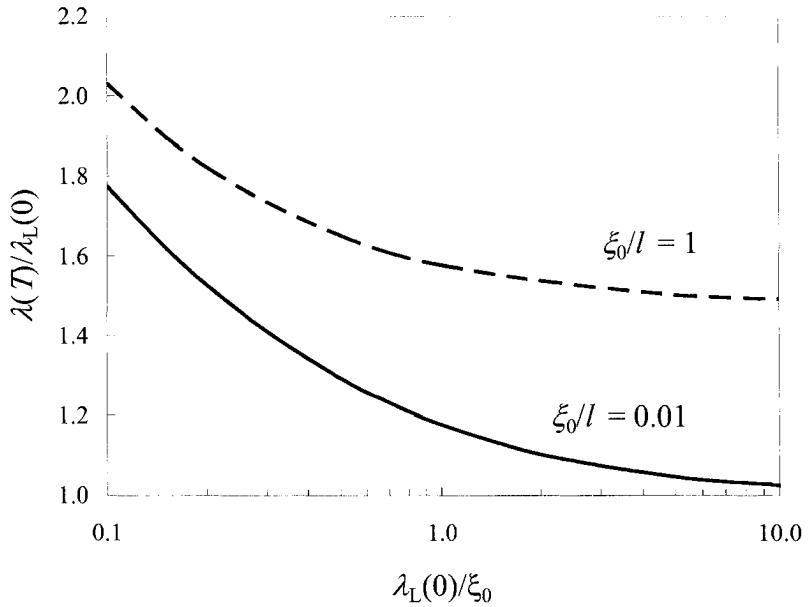

FIG. 9. Increase of penetration depth due to nonlocal effects as a function of $\lambda_L(0)/\xi_0$ for $T = 0.2T_c$, diffuse reflection, clean ($\xi_0/l = 0.01$) and dirty ($\xi_0/l = 1$) limit.

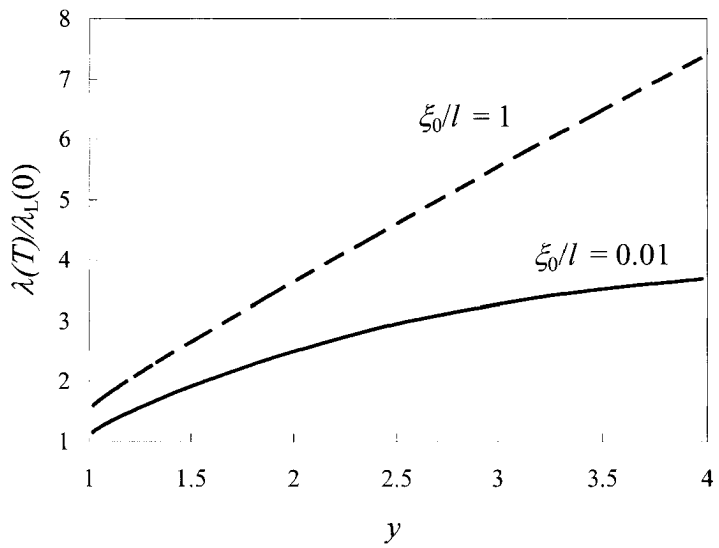

FIG. 10. Temperature dependence of the penetration depth as a function of the reduced parameter y in the clean ($\xi_0/l = 0.01$) and dirty ($\xi_0/l = 1$) limit for $\lambda_L(0)/\xi_0 = 2$.

3.6 The surface resistance

The fact that a superconductor has no resistance is only strictly true for a direct current of constant value. If the current is changing, an electric field is developed and some power is dissipated. This can be explained using the simple "two-fluid" model: in the case of a constant direct current, there must be no electric field in the metal, otherwise superelectrons would be accelerated continuously in this field and the current would increase indefinitely. If there is no field there is nothing to drive the normal electrons.

If we apply an alternating field, the supercurrent will lag behind because of the inertial mass of the superelectrons. Hence the superelectrons present inductive impedance and, since there is now an electric field present [the equation describing the alternating electric field in the superconductor is identical to Eq. (17)], some of the current will be carried by the normal electrons.

At lower temperatures the fraction of normal electrons decrease and the surface resistance becomes smaller. If the frequency of the alternating current (ac) is higher than about 100 GHz, the photons of the electromagnetic field have enough energy to excite superelectrons above the energy gap, causing a transition to the normal state due to pair breaking.

3.6.1 Surface impedance of a normal conductor

The surface impedance is defined as $Z_s = R_s + iX_s$ where R_s is the ac surface resistance and X_s is the surface reactance. For a normal metal, the applied electric field is decreasing exponentially into the metal over a characteristic length called "skin depth" (δ) given by

$$\delta = \frac{1}{\sqrt{\pi f \mu_0 \sigma}}, \tag{52}$$

where f is the frequency of the ac field and σ is the electrical conductivity.
The components of the surface impedance in a normal metal are given by

$$R_s = X_s = \sqrt{\frac{\pi f \mu_0}{\sigma}} = \frac{1}{\sigma\delta}. \tag{53}$$

At very low temperature and/or high frequency, the skin depth may become shorter than the electrons' mean free path. In this case the relation between current and field become

nonlocal and Ohm's law is not valid. This effect is called "anomalous skin effect" and results in a more complicated expression of the surface resistance [36] which depends on mean free path, frequency and the product ρl ($\rho = 1/\sigma$ is the resistivity). In the limit of very large l the following expression of the surface resistance is obtained

$$R_s(l \to \infty) = \left[\frac{\sqrt{3}\pi}{4} \rho l (\mu_0 f)^2 \right]^{1/3}, \tag{54}$$

which is independent of the mean free path and resisitivity (the product ρl is a material constant) and is proportional to $f^{2/3}$.

3.6.2 Surface impedance of a superconductor

The "two-fluid" model gives the following expressions for the real and imaginary parts of the surface impedance of a superconductor

$$R_s = \frac{1}{2} \mu_0^2 \omega^2 \sigma_n \lambda_L^3 \tag{55}$$

$$X_s = \omega \mu_0 \lambda_L \tag{56}$$

where σ_n is the electrical conductivity of the normal electrons. A derivation of the surface impedance on the basis of the BCS theory was implemented by Halbritter [37]. For frequencies smaller than the gap frequency ($\hbar\omega < 2\Delta$) energy from the electromagnetic field can be absorbed only by thermally excited quasiparticles. The dissipated power due to the rf field $H(r)e^{i\omega t}$ is given by the net number of absorbed photons multiplied by the photon energy $\hbar\omega$ and by a matrix element $|\mathbf{M}(\mathbf{p}_i, \mathbf{p}_f, \hbar\mathbf{k}, \hbar\omega)|$, which describes the absorption process and then integrated over available states and photons

$$P = 4\pi^2 \omega \int_\Delta^\infty 2 \left| f(E) - f(E + \hbar\omega) \right| N(E) N(E + \hbar\omega) dE \int |\mathbf{M}|^2 \, d\mathbf{k} d\mathbf{p}_i d\mathbf{p}_f, \tag{57}$$

where $f(E)$ is the Fermi distribution function, $N(E)$ is the density of state, $\mathbf{p}_i$ and $\mathbf{p}_f$ are respectively the initial and final momenta of the quasiparticles between which a photon ($\hbar\mathbf{k}$, $\hbar\omega$) has been exchanged. For $T < T_c/2$, $\hbar\omega << kT$, $\hbar\omega << \Delta$, the matrix element can be considered constant and the following expression for the surface resistance is obtained

$$R_s \propto P \propto \frac{(\hbar\omega)^2}{kT} \ln\left(\frac{4kT}{\hbar\omega} \right) e^{-\Delta/kT}. \tag{58}$$

There can be noticed a deviation from the ω^2 dependence predicted by the "two-fluid" model and an exponential decrease with temperature due to the smaller number of thermally excited quasiparticles.

The reduced matrix element $|\mathbf{M}(k, \omega)|^2$ depends on the material parameters such as coherence length, penetration depth and mean free path and Fig. 11 shows it as a function of the photon wave number k.

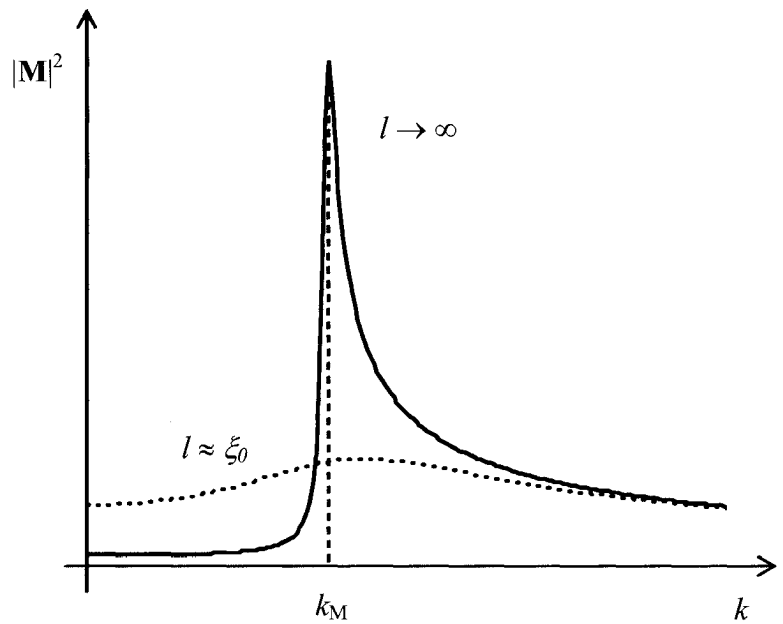

FIG. 11. Dependence of the reduced transition matrix element on photon wave number.

$|\mathbf{M}|^2$ has a sharp maximum at $k_M = \sqrt{\hbar\omega/2\Delta}/\xi_0$, which is decreasing at higher ξ_0/l ratios. In the clean limit, the photon absorption is dominated by the peak of momentum transfer but as l decreases and gets closer to ξ_0 this peak broadens significantly and the penetration depth increases slowly, the net result being a decrease of the surface resistance. When l decreases below ξ_0 the penetration depth starts increasing faster and overtakes the resonance broadening effect, causing the increase of the surface resistance.

The minimum at about $l \approx \xi_0$ is more pronounced the larger λ_L/ξ_0 is and the lower the frequency is. A calculation of the surface impedance according to the BCS theory can be done by numerical methods, using a computer code written by Halbritter [38]. Figure 12 shows the surface resistance normalized to the reactance $\omega\mu_0\lambda_L$ as a function of the ratio λ_L/ξ_0 for two values of the ratio ξ_0/l at $T = 0.2T_c$, $\hbar\omega/\Delta = 0.01$ and diffuse electron scattering at the surface.

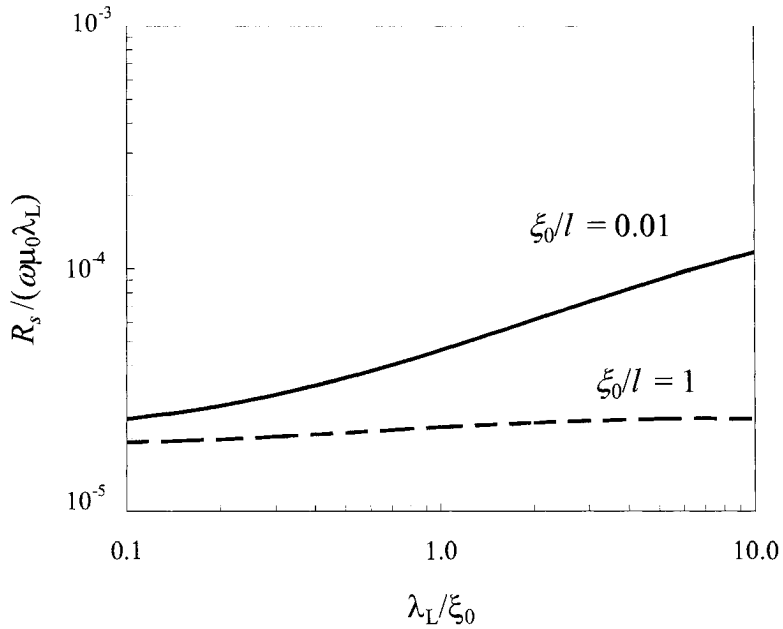

FIG. 12. Normalized surface resistance as a function of λ_L/ξ_0 at $T = 0.2T_c$ and $\hbar\omega/\Delta = 0.01$ for $\xi_0/l = 0.01$ and 1.

The temperature dependence of the surface resistance of superconducting niobium at 1.5 GHz is given as an example in Fig. 13. The surface resistance of a normal conductor such as copper at the same frequency is approximately constant between 9 K and 1 K and is about 1.5 mΩ which is five order of magnitudes higher than niobium at 2 K.

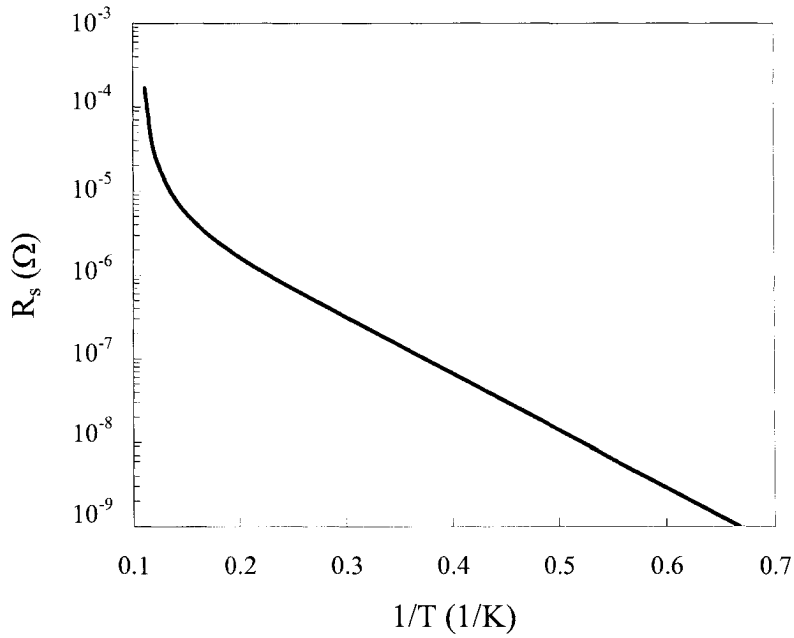

FIG. 13. Temperature dependence of the surface resistance of superconducting niobium at 1.5 GHz.

3.7 Critical magnetic field

3.7.1 Thermodynamic critical field

As mentioned in section 3.1, there is a limit to the strength of magnetic field which can be applied to a superconductor if it is to remain superconducting. The transition to the normal state can be analyzed using thermodynamic arguments. In considering the critical magnetic field of a superconductor, we are interested in the Gibbs free energy, because we want to compare the difference in the magnetic contribution to the free energy of the two phases when they are in the same applied magnetic field. In general, the change in free energy per unit volume due to an applied field H_a is given by

$$\Delta g(H_a) = -\mu_0 \int_0^{H_a} m dH, \tag{59}$$

where m is the magnetization per unit volume. Since a superconductor is an ideal diamagnet, the magnetization is $M = -H_a$ while in the normal state it is negligible. So the magnetic field raises the free energy density in the superconducting state g_s to

$$g_s(T,H) = g_s(T,0) + \frac{1}{2}\mu_0 H_a^2 . \tag{60}$$

At the critical field the free energy density in the superconducting and normal state are equal so that the thermodynamic critical field H_c is given by

$$H_c = \sqrt{\frac{2}{\mu_0}\left[g_n(T,0) - g_s(T,0)\right]} . \tag{61}$$

The BCS theory gives the following expression for the critical field at 0 K

$$H_c = \sqrt{\frac{0.472\gamma}{\mu_0}}T_c \tag{62}$$

where γ is the Sommerfeld constant [$\gamma = 2\pi^2 N(E_F)k^2/3$]. The direct proportionality between critical field and T_c suggests that for applications to rf cavities for particle accelerators, where high fields are required, the superconductor should have a high critical temperature. The critical magnetic field depends on temperature and a parabolic dependence well describes the experimental data

$$H_c(T) = H_c(0)\left[1 - \left(\frac{T}{T_c}\right)^2\right]. \tag{63}$$

The difference in entropy [$s = -(\partial g/\partial T)_{P,H}$] per unit volume between normal and superconducting state is given by

$$s_n - s_s = -\mu_0 H_c \frac{dH_c}{dT} \tag{64}$$

and since dH_c/dT is negative Eq. (64) shows that $s_n > s_s$ therefore the superconducting state is more ordered than the normal state. Since H_c falls to zero as the temperature is raised towards T_c the entropy is continuous through the phase transition which is therefore of second-order. But in the presence of an applied magnetic field the transition temperature is reduced to a lower value $T_0 < T_c$ and since $H_c(T_0) \neq 0$ the entropy is discontinuous at the phase transition, indicating a first-order transition with the existence of a latent heat. This latent heat arises because at temperatures between T_c and 0 K the entropy of the normal state is greater than that of the superconducting state, so heat must be supplied if the transition is to take place at constant temperature. If the superconductor is thermally isolated, the latent heat comes from the thermal energy of the crystal lattice.

3.7.2 Type-I and type-II superconductors

Ginzburg and Landau discussed the surface energy associated with a normal/superconducting phase boundary. Qualitatively, the Gibbs free energy per unit volume is increased by $\mu_0 H_a^2 \lambda_L/2$ over the penetration depth due to the diamagnetism and is lowered by $\mu_0 H_c^2 \xi_0/2$ over the coherence length due to the increase of the superelectrons density. The net boundary energy per unit area is $\mu_0(H_c^2 \xi_0 - H_a^2 \lambda_L)/2$. If $\xi_0 > \lambda_L$, then there is a positive surface energy and the formation of normal/superconducting regions is not favorable but if the coherence length is smaller than the penetration depth, there is a negative surface energy and is energetically favorable to have normal/superconducting boundaries. Figure 14 shows a representation of the contributions to the Gibbs free energy leading to a negative surface energy. Ginzburg and Landau determined that the exact crossover between positive and negative surface energies happens for $\kappa_{GL}\left(\approx \xi_0/\lambda_L\right) = 1/\sqrt{2}$. Materials with $\kappa_{GL} < 1/\sqrt{2}$ are called type-I superconductors and are characterized by a net transition to the normal state at H_c. Abrikosov [37] recognized that for materials with $\kappa_{GL} > 1/\sqrt{2}$ (type-II superconductors), there exists a critical field, called lower critical field (H_{c1}), above which the magnetic flux penetrates the superconductors in the form of a regular array of flux tubes ("fluxoids"), each carrying a quantum of flux $\Phi_0 = hc/2e$. This is called "mixed state" and the order parameter $\psi(\mathbf{r})$ goes to zero at the axis of each flux tube over a distance of the order of the coherence length. These normal conducting "cores" are surrounded by shielding currents which rotate in the opposite sense than that of the diamagnetic surface current. Figure 15 shows a schematic representation of the mixed state.

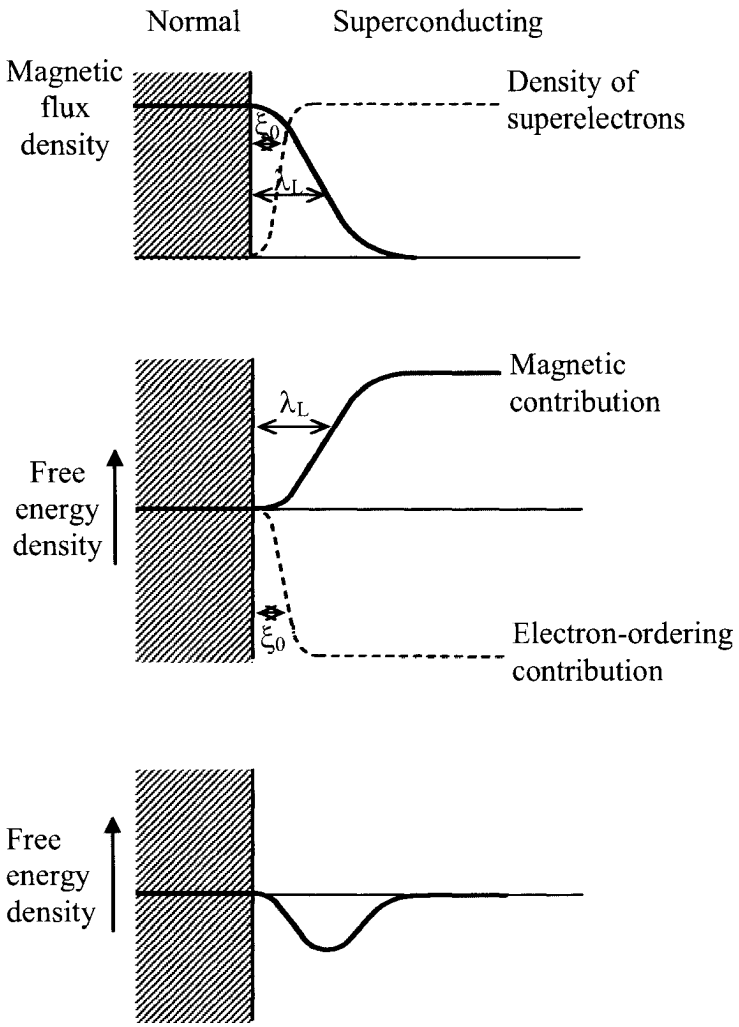

FIG. 14. Negative surface energy for a type-II superconductor. Penetration depth and coherence length (top), contributions to free energy (middle) and total free energy (bottom).

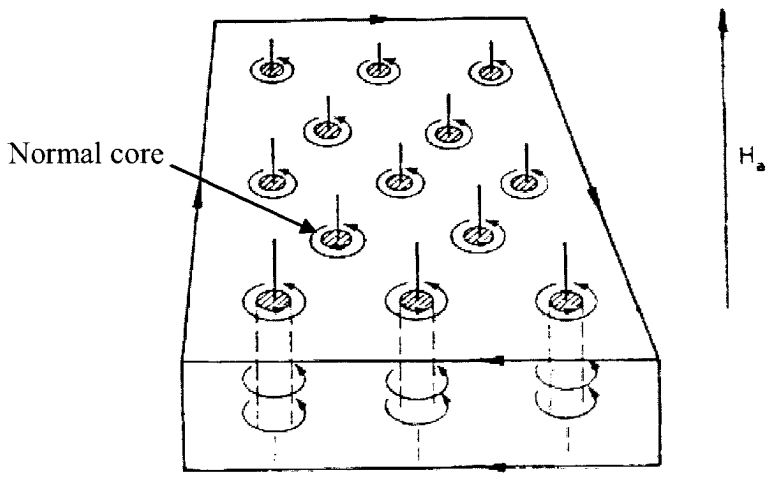

FIG. 15. Schematic representation of the mixed state in a type-II superconductor showing normal cores and encircling supercurrent vortices. The surface current is able to maintain the bulk diamagnetism [40].

If the strength of the applied magnetic field is increased above H_{c1} in a type-II superconductor, the fluxoids pack closer together and the average flux density in the superconductor increases. At a sufficiently high value of applied magnetic field, called upper critical field (H_{c2}) the order parameter $\psi(\mathbf{r})$ goes to zero by a second order phase transition. Figure 16 shows the phase diagram of type-I and type-II superconductors.

The GL theory allows one to express H_{c1} and H_{c2} in terms of the thermodynamic critical field H_c and of the Ginzburg-Landau parameter κ_{GL}. The following expression for the lower critical field at 0 K is valid only for $\kappa_{GL} >> 1$,

$$H_{c1} = \frac{H_c}{\sqrt{2}} \frac{\ln \kappa_{GL}}{\kappa_{GL}}. \tag{65}$$

The exact solution for arbitrary κ_{GL} requires a numerical solution [41] of the Ginzburg-Landau equations. The temperature dependence of the lower critical field is about the same as for the thermodynamic critical field. The upper critical field at 0 K is given by

$$H_{c2} = \frac{\Phi_0}{2\pi\mu_0 \xi_{GL}^2} = \sqrt{2}\kappa_{GL} H_c \tag{66}$$

and its temperature dependence is given by

$$H_{c2}(t) = H_{c2}(0)\left(\frac{1-t^2}{1+t^2}\right). \tag{67}$$

H_c is approximately the geometric mean of H_{c1} and H_{c2}. The relation between H_{c2} and ξ_{GL} given by Eq. (66) indicates the following temperature dependence of the Ginzburg-Landau coherence length, which is valid at temperatures lower than T_c[7]

$$\xi_{GL}(t) = \xi_{GL}(0)\sqrt{\frac{1+t^2}{1-t^2}}. \tag{68}$$

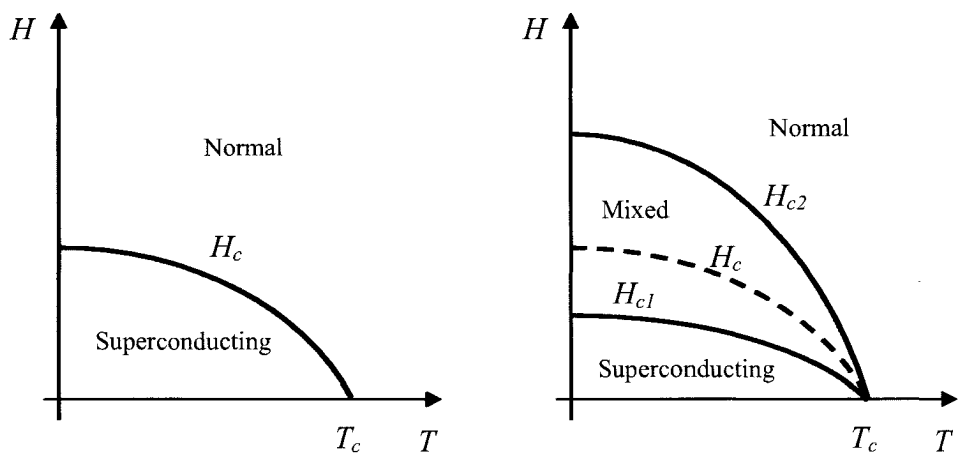

FIG. 16. Phase diagram of type-I (left) and type-II (right) superconductors.

In 1963 Saint-James and de Gennes [42] showed that superconductivity can persist in a surface layer of thickness ~ξ_{GL} of a superconductor in contact with an insulator, even in a magnetic field whose strength is sufficient to drive the bulk material normal. This happens up to a field called H_{c3}. The value of H_{c3} depends on the angle the applied field makes to the surface and is maximum when the applied field is parallel to the surface. In this case $H_{c3} = 1.695H_{c2}$ while it is equal to H_{c2} when the field is perpendicular to the

[7] As a remainder, the dependencies given by Eqs. (48) and (49) are valid only close to T_c.

surface. Measurements of H_{c3} can be useful in investigating the surface properties of a superconductor, which is particularly useful for rf applications.

The temperature dependence of the thermodynamic critical field (H_c), of the upper critical field (H_{c2}) and their values at 0 K can be obtained by measuring the magnetization of the sample as a function of the applied magnetic field and temperature [40]. The knowledge of $H_{c2}(0)$ and $H_c(0)$ allows to calculate $\xi_{GL}(0)$ and $\kappa_{GL}(0)$ using Eq. (66). The London penetration depth can be finally obtained by $\lambda_L(0) = \kappa_{GL}(0)\xi_{GL}(0)$.

3.7.3 The superheating field

Since in the presence of a magnetic field the first order phase transition superconducting-to-normal at $T_c(H)$ takes place at nucleation centers, there is a possibility for a "superheated" superconducting state to persist metastably at $H > H_c$, as well as for a "subcooled" normal conducting state to persist at $H < H_c$. Matricon and Saint-James [43] solved GL equations numerically for the one-dimensional case where half of the space was occupied by a superconductor and the magnetic field was applied parallel to the surface. They calculated the dependence of the superheating field on κ_{GL} and in the various limits it is given by

$$\begin{aligned} H_{sh} &\approx \frac{0.89}{\sqrt{\kappa_{GL}}} H_c \qquad && \text{for } \kappa_{GL} \ll 1 \\ H_{sh} &\approx 1.2 H_c && \text{for } \kappa_{GL} \approx 1 \\ H_{sh} &\approx 0.75 H_c && \text{for } \kappa_{GL} \gg 1. \end{aligned} \tag{69}$$

Alternatively, one way of estimating the superheating field is using the surface energy balance given by the GL theory. In the one-dimensional formulation of the GL theory, the superheating field defines the field at which the order parameter is driven to zero at the surface of a superconductor filling a half-space. This can be pictured as a nucleation of the normal phase in the form of a plane at the surface (Plane Nucleation). In a type-I superconductor the superheating field (H_{sh}) is obtained by balancing the diamagnetic energy $\mu_0 H_a^2 \lambda_{GL}/2$ and the loss in condensation energy $\mu_0 H_a^2 \xi_{GL}/2$ so that

$$H_{sh} = \sqrt{\frac{\xi_{GL}}{\lambda_{GL}}} H_c = \frac{1}{\sqrt{\kappa_{GL}}} H_c. \tag{70}$$

This energy balance can be extended to other dimensional forms of nucleation such as a line and a point. The line nucleation can be pictured as a vortex-like nucleation (Vortex Line Nucleation) where the normal phase is created in the form of a line lying at the surface. In this case the magnetic field distribution and the order parameter variation are centered about the nucleus and are semi-cylindrical with their characteristic lengths. The diamagnetic energy is given by $-\mu_0 \pi H^2 \lambda_{GL}^2/4$ and the loss in condensation energy is $-\mu_0 \pi H^2 \xi_{GL}^2/4$. Balancing the two contributions, the superheating field is obtained

$$H_{sh} = \frac{\xi_{GL}}{\lambda_{GL}} H_c = \frac{1}{\kappa_{GL}} H_c. \tag{71}$$

A similar argument applies to the case of the nucleation at a point (Point Nucleation) where the magnetic field and order parameter distributions are hemispherical and centered about the point of nucleation so that

$$H_{sh} = \frac{1}{\kappa_{GL}^{3/2}} H_c. \tag{72}$$

The time it takes to nucleate fluxoids was measured [44] to be of the order of microseconds and is very long compared to the rf period of superconducting cavities in the gigahertz range. Therefore, there is a stronger tendency for the metastable superconducting state to persist up to H_{sh}. Measurements of the rf critical field on Sn, In and Pb (type-I superconductors) [45] are in good agreement with the VLN superheating field, and Saito was able to show [46] that the same model describes well rf critical field measurements done on cavities made of Pb, Nb and Nb_3Sn (the last two being type-II superconductors) [47]. Saito gives the following formula for the rf critical field and its temperature dependence

$$H_{c,rf}(t) = \sqrt{2} \frac{1}{\kappa_{GL}(0)} H_c(0)\left(1 - t^4\right), \tag{73}$$

where the factor $\sqrt{2}$ converts the formula for the dc superheating field to a formula for ac fields.

Table III gives a list of the main material parameters for Pb (type-I), Nb (type-II) and Nb_3Sn (strong type-II) which are used to fabricate superconducting rf cavities for particle accelerators. It can be seen that niobium is the elemental superconductor with the highest critical temperature and rf critical field and is the material most commonly used for rf

cavities, both as a bulk or thin film. While high-temperature superconductors have much higher upper critical field than niobium, the fact that their Ginzburg-Landau parameter is also high (>10) limits the value of the superheating field[8] therefore reducing their possibility for use in rf cavities for particle accelerators. In addition, defects like "weak-links" allow flux penetration already at much lower fields.

3.8 Oxidation of niobium

Any niobium surface exposed to pressures greater than about 10^{-10} mbar and temperatures lower than 1000 K will oxidize instantaneously due to the high bonding energy between Nb and O (5 - 7 eV, due to localized, directional *d*-bonds between O and Nb). The oxidation process is well described by the Cabrera-Mott theory [55]: oxygen from O_2 or H_2O adsorbed on a niobium surface is ionized by conduction electrons tunneling through the oxide layer. The oxygen ions O^{2-} are driven towards the metal by a negative electrical contact potential (Mott potential, $V_M \approx$ -0.5 V), increasing the oxide thickness. In the early phase of growth, the oxide growth rate is limited by the diffusion of ions aided by the Mott potential. In the later phase of growth the rate is limited by the tunneling of electrons through the oxide aided by a positive ionic diffusion potential ($V_D \approx 0.17$ V) and the nucleation of $\{NbO_6\}$ octahedra. The oxidation of niobium by dry O_2 is much slower (~ 5×10^{-6} nm/s) than "wet" oxidation by H_2O or H_2O_2 (~ 0.1 nm/s) [56].

The surface oxide layer is nanocrystalline niobium pentoxide Nb_2O_5 about 1 - 3 nm thick. Nb_2O_5 is a dielectric with a relative dielectric constant $\varepsilon_r = 10 - 20$ [57] and is made of $\{NbO_6\}$ octahedral joined by sharing a corner or a side, as shown in Fig. 17. The main deviations to the crystalline structure are due to extended defects such as crystallographic shear planes and localized defects such as oxygen vacancies.

The metallic interface oxide NbO_x ($x \approx 1$) is only about 0.5 nm thick. The oxidation of NbO_x leading to Nb_2O_5 is accompanied by a volume expansion by a factor of about three and therefore the niobium is strained and cracked and NbO_x clusters are injected into the niobium (Fig. 18).

---

[8] If Eq. (73) will be verified for such materials.

TABLE III. Material parameters for Pb, Nb and Nb_3Sn at 0 K ($B = \mu_0 H$).

	Pb	*Nb*	*Nb_3Sn*
λ_L (nm)	28 [48]	32 [48, 49] 36 [50] 42 [46] 46 [51]	50 [48]
ξ_0 (nm)	110 [48]	27 [46] 28 [51] 39 [49, 50]	6 [48]
Δ/kT_c	2.05 [48, 40] 1.95 [45]	1.75-1.95 [48]	2.2 [48]
B_c (mT)	80 [40]	200 [46, 52, 54]	540 [46]
B_{c1} (mT)	-	174 [52] 190 [46]	35 [53]
B_{c2} (mT)	-	390 [54] 400 [52] 410 [51] 450 [46]	23000 [53]
$B_{c,rf}$ (mT)	71 [46]	178 [46]	103 [46]

Studies on the effects of interstitial oxygen in niobium [58] showed that the critical temperature decreases by 0.93 K per atomic percent of oxygen, the upper critical field and the Ginzburg-Landau parameter at 0 K increase with increasing oxygen concentrations, while the thermodynamic critical field and the residual resistivity ratio (*RRR*) decrease. The *RRR* is defined as the ratio between the electrical resistvity at 300 K over the value at 4.2 K in the normal conducting state and is an indication of the purity of the material. In a region of the material where oxygen is the main impurity, the *RRR* is given by 3.5/(at. % of oxygen).

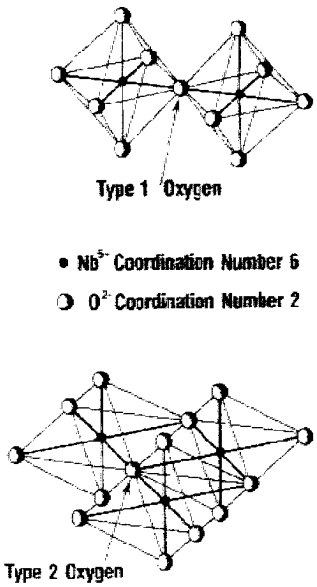

FIG. 17. Nb_2O_5 is obtained by joining $\{NbO_6\}$ octahedral by sharing a corner with common oxygen or a side with two common oxygens [56].

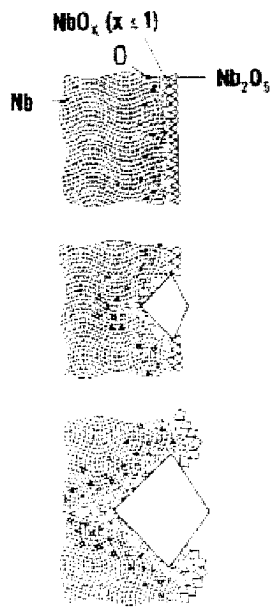

FIG. 18. Sketch of initial oxidation stages showing O solution, NbO surface layer, Nb_2O_5 nucleation yielding straining of Nb [56].

CHAPTER 4

LOSSES IN SUPERCONDUCTING NIOBIUM CAVITIES

4.1 Introduction

The behavior of an ideal superconducting rf cavity is characterized by a value of the surface resistance equal to the theoretical BCS value at the operating temperature and by a slight decrease of the surface resistance with increasing rf field, due to overheating of the rf surface, up to the rf critical field where the cavity is no more thermally stable and the transition to the normal conducting state will occur (quench). Several effects contribute to deviations from this ideal behavior: the surface resistance is higher than the theoretical value due to the so-called residual resistance and it is often seen to decrease with increasing rf fields up to about 15 mT peak surface magnetic field. The surface resistance then starts to increase moderately with rf field up to a point where the decrease is more rapid, due to field emission or the so-called high-field "Q-drop". The cavity might also quench at fields lower than the rf critical field due to defects or show a very sharp drop of the quality factor due to multipacting. Figure 19 shows an ideal quality factor vs. rf field behavior and a real one with the additional losses. The next sections will summarize the present knowledge about these loss mechanisms.

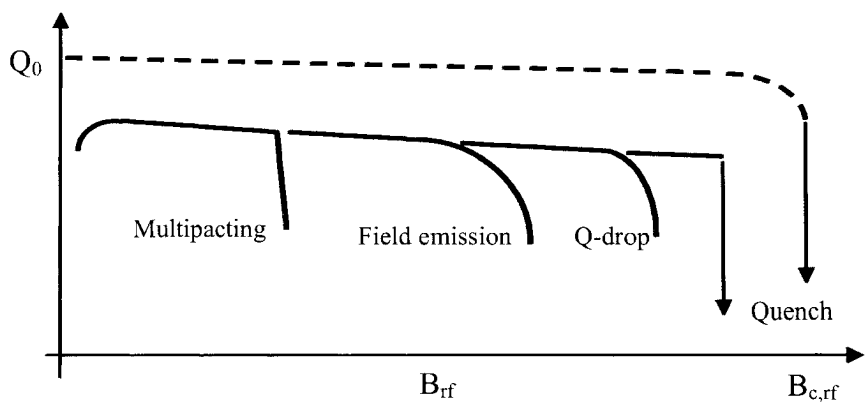

FIG. 19. Sketch of ideal Q_0 vs. field behavior (dashed line) and with losses.

4.2 Residual resistance

Measurements of the surface resistance of a superconducting rf cavity as a function of temperature show a clear deviation from the BCS theory predictions that can be well described introducing an additive constant called residual resistance (R_{res}). Sources of residual resistance can be residues from chemical etching, foreign material inclusions, condensed gases, residual dc magnetic fields, hydrides and oxides. Typically, the measured values of residual resistance are between two and fifteen nanoohms.

4.2.1 Residual losses from trapped magnetic flux

A well controllable source of residual losses is trapped dc magnetic flux due to insufficient shielding of an external dc field close to the cavity. Even if the external field is below the lower critical field, magnetic flux is trapped at "pinning" sites such as lattice defects or other inhomogeneities in the material and since the core of the trapped fluxoids is normalconducting, it introduces additional losses. Experimentally, this contribution for bulk niobium cavities is given by [59]

$$R_{mag} = 0.03(\mathrm{n\Omega})\,H_{ext}\,(\mathrm{A/m})\sqrt{f\,(\mathrm{GHz})}. \tag{74}$$

4.2.2 Residual losses from hydrides

A significant source of residual losses comes from the formation of a metallic hydride phase during cool-down of a niobium cavity from room temperature to 2 K [60] and causing the so-called "Q-disease". According to the phase diagram of the Nb-H system, there is a transition to an ordered phase at about 140 K for low hydrogen concentrations (about 100 ppm). The amount of hydrogen present in niobium cavities can be increased to high enough values for the hydride phase to form by the acid treatments. Although hydrogen is very mobile in niobium even at low temperatures, it can be easily trapped near the surface where the density of defects is greatest or removed by NbO_x precipitates straining the lattice. If the cool-down is slower than about 1 K/min when the temperature is in the range 80 – 150 K there is time for the hydride phase to nucleate near the surface and introducing residual losses of the order of hundreds of nanoohms. A common way to

avoid these losses is to degas the hydrogen by heating the niobium cavity in vacuum at 600 – 900 °C for several hours.

4.2.3 Residual losses from oxides

The natural oxide layer of niobium is a dielectric and is therefore a possible source of residual losses due to both electric and magnetic fields according to the following formulas [61]:

$$R^E_{diel} = \omega\mu_0 d\varepsilon_r \tan\delta_E, \qquad R^B_{diel} = \omega\mu_0 d\mu_r \tan\delta_B \tag{75}$$

where d is the oxide layer thickness, $\tan\delta$ is the loss tangent (defined as the ratio of the imaginary to the real component of the dielectric constant or of the permeability), ε_r and μ_r are the relative dielectric and permeability constants respectively. For the niobium pentoxide, $d \cong 3$ nm, $\varepsilon_r \cong 30$, $\tan\delta_E \cong 10^{-5}$, yielding surface resistances lower than 10^{-3} nΩ at 1.5 GHz. Condensed gases such as oxygen have $\tan\delta_B \cong 10^{-3}$ and can result in residual losses of the order of a nanoohm ($\mu_r \cong 1$).

While bulk dielectric losses are negligible, interface losses can yield measurable residual resistance. These losses arise from the high defect density at the oxide-metal interface resulting in a high density of localized electron states $n_L \approx 10^{20}/\text{cm}^3$ which hybridize with the high density of conduction electrons $n_c \approx 10^{22}/\text{cm}^3$ forming interface states n_{IS}. These interface states inside the niobium energy gap mediate the interaction of the rf field with phonons in different ways:

- resonant absorption of photons from the rf field and energy transfer to phonons yielding $R^E_{res} \approx 10^{-8}/\varepsilon_r^2\ \Omega$ and $R^B_{res} \approx 5\cdot10^{-10}(f/\text{GHz})^2\ \Omega$
- surface plasmon type excitation yielding $R^E_{res} \approx \omega\mu_0 d_n$ where d_n is the equivalent thickness for the oxide-metal interface

Oxide channels and islands caused by crack corrosion create "weak links" in the niobium in a mean distance a_J, especially at grain boundaries, resulting in the following residual losses [62]

$$R^{WL}_{res} = \frac{2\left(\omega\mu_0\lambda(T)\right)^2}{1+\left(\omega\tau_J(T)\right)^2}\frac{\lambda_J(T)^3}{a_J G_b}, \tag{76}$$

which are temperature independent for $T < T_c/2$. λ_J is the Josephson penetration depth defined as $\lambda_J(T) = \sqrt{\Phi_0 / \left[2\pi\mu_0 d_J J_{cJ}(T)\right]} \cong 0.18$ μm, J_{cJ} is the weak link critical current density ($\cong 10^{11}$ A/m^2) and d_J is twice the BCS penetration depth plus the oxide thickness. G_b is the grain boundary specific resistance of the order of 2×10^{-13} Ωm^2 [63] and $\tau_J(T) = \Phi_0 / \left[2\pi J_{cJ}(T) G_b\right]$. At gigahertz frequencies $\omega\tau_J << 1$ and $R^{WL}{}_{res} \propto \omega^2$.

A possible way to reduce these residual losses is to eliminate the original oxide layer by heating the niobium cavity in vacuum at temperatures greater than 1000 °C and allow a controlled dry oxidation by introducing oxygen in the furnace [64].

4.3 Multipacting

Multipacting is a phenomenon where an electron emitted from the cavity surface is accelerated by the rf field and eventually impacts a wall again, producing secondary electrons. The number of the secondary electrons depends on surface conditions and on the impact energy of the primary. The secondaries are accelerated and, upon impact, produce more electrons. The electron current increases exponentially if the number of emitted electrons exceeds the number of impacting ones and if the trajectories satisfy certain resonance conditions. Multipacting therefore occurs at certain field levels and cause a sharp reduction of the cavity Q_0 due to the energy gained by the electrons and by heating of the surface due to the impacting electrons.

During one-point multipacting the charges impact the cavity wall at, or very near, the emission site itself. Emitted electrons are accelerated by the electric field perpendicular to the surface while, simultaneously, the magnetic field forces them along quasi-cyclotron orbits, so that they return to their point of origin. This resonant phenomenon occurs if the rf period is an integer multiple of the cyclotron period. The number of rf periods n required by an electron to return to the point of origin is called the multipacting order.

Two-point multipacting occurs when the electron trajectories include two impact sites and the resonance condition typically requires that the time between impacts is a half-integer multiple of the rf period.

The following experimental formulas allow calculating the field levels at which multipacting defined by the magnetic field can occur as one-point or two-point respectively [65]:

$$B_{p,n}(mT) = \frac{0.03}{n} f(MHz) \qquad \text{one-point} \tag{77}$$

$$B_{p,n}(mT) = \frac{0.06}{2n-1} f(MHz) \qquad \text{two-point.} \tag{78}$$

Another possible cause of two-point multipacting, produced in narrow-gap parallel plate geometries, is due solely to the electric field accelerating the electrons between the gap. The resonant condition for multipacting requires that the charge traverses the gap in half-integer rf period.

Multipacting can be overcome by rf conditioning of the cavity surface, where the electrons bombardment can burn the emission site but it can be avoided by a proper design of the cavity shape (elliptical cavities are less prone to multipacting than pill-box like cavities) and a proper cleaning of the surface to lower the secondary emission coefficient.

4.4 Field emission

Field emission is characterized by the generation of an electron current due to electrons emitted from a spot ("emitter") on the cavity surface and is accompanied by bremsstrahlung x-rays and heating. Both these effects progressively lower the cavity Q_0 at higher accelerating gradients. Emitters on the cavity surface are contaminants deposited during various stages of cavity preparation and they can be metals, semiconductors or insulators [20].

The theory of field emission proposed by Fowler and Nordheim (FN) [66] shows that the work function barrier at the metal surface is lowered by an applied electric field so that electrons can tunnel out into the vacuum. The original expression for the electron current density as a function of the applied field according to the FN theory is modified by introducing a field enhancement factor β_{FN} to well describe field emission data from superconducting cavities:

$$j(E) = \frac{A_{FN}(\beta_{FN}E)^2}{\phi} \exp\left(-\frac{B_{FN}\phi^{3/2}}{\beta_{FN}E}\right), \tag{79}$$

where A_{FN} and B_{FN} are constants and ϕ is the work function of the metal. The field enhancement factor depends on the nature and geometry of the emitter.

Field emission is the main technological limitation of superconducting niobium cavities and in order to avoid it, it is imperative to maintain the cleanest conditions during the cavity preparation and assembly. A successful technique which is routinely used to reduce the number of particles on the cavity surface is high pressure water rinsing (HPR) with a jet of ultra-pure water at the pressure of about 80 bar [67]. The final assembly of a cavity is done in a class 10 clean room.

If field emission is encountered during the rf test of a cavity, it is sometimes possible to overcome it by rf processing with or without the presence of few millitorr of helium gas introduced into the cavity. During the processing phenomenon, the current density can reach values high enough to raise the local temperature up to the melting point of the emitter.

4.5 Thermal breakdown

Thermal breakdown or "quench" consists in a transition of the cavity to the normal conducting state due to the presence of "defects" in the niobium. Defects are typical normal conducting inclusions heated by the rf field. When the temperature of the defect exceeds T_c, the superconducting region surrounding it becomes normal conducting, resulting in greatly increased power dissipation. The quench field can be estimated considering a simple model where a hemispherical defect of radius a and surface resistance R_n is embedded in niobium with thermal conductivity κ cooled by liquid helium at temperature T_b. By equating the power dissipated at the defect with the power dissipated in the helium bath, the magnetic field at which a quench will occur is given by [68]:

$$H_{quench} = \sqrt{\frac{4\kappa(T_c - T_b)}{aR_n}}. \tag{80}$$

This formula suggests that a way to increase the quench field is reducing the defect size and improving the thermal conductivity of niobium. These tasks can be achieved by scanning the niobium sheets used for cavity fabrication with an eddy-current system [69] to detect major defects and by purifying the niobium by heating the cavity in ultra-high vacuum at $T > 1200$ °C for several hours [70]. During the heat treatment, the cavity should be surrounded by titanium foils which act as solid state getter for interstitial impurities such as oxygen, hydrogen, etc.

4.6 Low field Q-increase

The low field Q-increase is an increase (about 40%) of the quality factor Q_0 between 2 and 15-20 mT peak surface magnetic field. It has been observed in many tests in several laboratories but mainly on cavities with a resonant frequency of the fundamental mode (TM_{010}) above 1 GHz and low residual resistance.

Halbritter's model [71] for this effect involves non-equilibrium superconductivity. In particular, at low temperature and low rf fields thermal equilibrium between quasi-particles and phonon bath is not achieved. To allow this phenomenon to take place two conditions are necessary: a mismatch between the quasi-particle absorption and relaxation rate and the presence of localized states inside the superconducting niobium energy gap.

At a temperature of 2 K, a resonant frequency of 1.5 GHz and rf magnetic field of 2 mT, quasi-particles absorb photons from the rf field at a rate $1/\tau_{ab} \approx 2$ GHz. Under the same conditions, the quasi-particles relaxation rate $1/\tau_r$, which is the sum of the quasi-particle-phonon scattering rate plus the recombination rate, is only about 0.03 GHz.

NbO_x clusters formed during the oxidation of niobium have a locally reduced energy gap Δ_L, as shown in Fig. 20. At low rf field, quasi-particles are confined in these localized states by $\Delta_L < \Delta^*$ with the average gap Δ^* smaller than the energy gap of pure niobium. This results in a higher surface resistance. At higher rf field, quasi-particles are driven out of the localized states and occupy states above the niobium energy gap, causing a decrease of the surface resistance to the mean BCS value. Once quasi-particles have energies greater than the niobium gap they are no longer localized and they reach

thermal equilibrium with the phonons, because those can easily transfer their energy to the helium bath (at 2 K the phonon mean free path is greater than the cavity wall thickness).

Halbritter gives the following formula for the absorbed rf power per unit area P:

$$P = \frac{R_s}{2} H^2 = \int n_c \lambda I_r(\varepsilon) \hbar\omega \, d\varepsilon, \tag{81}$$

where n_c is the density of conduction electrons, λ is the rf penetration depth and I_r is the quasi-particle relaxation rate. Quasi-particles out of thermal equilibrium yield constant absorption, making the integral in Eq. (81) independent of the rf field amplitude. As a result the surface resistance is inversely proportional to the square of the rf field.

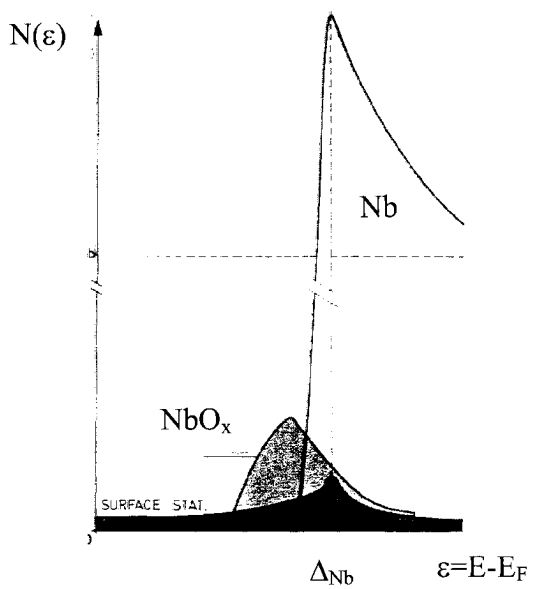

FIG. 20. Density of states $N(\varepsilon)$ as a function of the energy of Nb (white area), NbO_x (grey area) and surface states (black area) from [72].

4.7 Medium field Q-slope

Beyond the field at which the low field Q-increase saturates, the cavity quality factor begins a gradual decrease. This continues up to a field where the degradation becomes stronger due to either field emission or Q-drop (typically 90 mT peak surface magnetic

field at 1.5 GHz). This region of gradual reduction is called "medium field Q-slope" and is a more or less pronounced common feature of all niobium superconducting cavities.

A model of the medium field Q-slope by Halbritter [62] involves heating of the rf surface to a temperature above the helium bath temperature due to the niobium-helium thermal resistance. The surface resistance is expressed as a Taylor series with even exponents of the peak surface magnetic field:

$$R_s\left(T,B_p\right)=R_{s0}\left(T\right)\left[1+\gamma^*\left(T\right)\left(\frac{B_p}{B_c}\right)^2+O\left(B_p^4\right)\right], \tag{82}$$

where R_{s0} is the surface resistance at about 15 mT [$= R_{BCS0}(T) + R_{res}$], $B_c = 200$ mT is the niobium critical field and T is the He bath temperature. The medium field Q-slope is represented by the variable $\gamma^*(T)$. $\gamma^* = 1$ implies a 25% increase in surface resistance between 15 and 100 mT peak surface magnetic field. From Ginzburg-Landau theory, the value of gamma should be lower than 0.1 by pair-breaking but it is enhanced by the niobium thermal resistance. Halbritter gives the following formula for $\gamma^*(T)$:

$$\gamma^*\left(T\right)=\frac{\partial R_{s0}}{\partial T}\frac{B_c^2}{2}\left(\frac{d}{\kappa}+R_K\right)\approx R_{BCS}\left(T\right)\frac{B_c^2\Delta}{2kT^2}\left(\frac{d}{\kappa}+R_K\right), \tag{83}$$

where κ and R_K are the niobium thermal conductivity and Kapitza resistance respectively, d is the wall thickness.

A similar model to explain the medium field Q-slope based on the global heating of the cavity surface was proposed by Visentin [73]. The model is based on a Taylor series of the surface resistance up to first order in temperature, resulting in the following dependence from the peak magnetic field:

$$R_s=\frac{R_{s0}}{1-CB_p^2}, \tag{84}$$

where the parameter C is related to γ^* defined in the previous model by $C = \gamma^*/B_c^2$.

Recently, Gurevich solved the kinetic equation for the distribution function of quasi-particles in a type II superconductor in the clean limit and in a strong rf field [74]. This led to an intrinsic nonlinear dependence of the BCS surface resistance due to the pairbreaking effect. For rf fields much smaller then the critical field, the following expression of the surface resistance was obtained:

$$R_s(T,B_p)=R_{s0}(T)\left[1+\gamma(T)\left(\frac{B_p}{B_c}\right)^2\right], \tag{85}$$

where the factor γ is the sum of BCS pairbreaking and thermal contributions:

$$\gamma(T)=\frac{R_{BCS0}(T)}{R_{s0}(T)}C\left(\frac{\Delta}{kT}\right)^2+\gamma^*(T). \tag{86}$$

C is a dimensionless parameter, weakly dependent on frequency and equal to 0.028 at 1.5 GHz.

4.8 High field Q-drop

Field emission is the usual obstacle to achieving high accelerating gradients in superconducting cavities but sometimes the Q_0 versus field curve is characterized by a sharp decrease of the quality factor at high field in the absence of x-rays: the so-called "Q-drop". Several models have been proposed over the last few years to explain the presence of this severe degradation. The following sections will present a brief review of the most significant models.

4.8.1 Interface tunnel exchange (ITE) model

Halbritter considers the electric surface impedance of niobium covered by its natural oxide layer. The amorphous, non-stoichiometric Nb_2O_{5-y} ($y<1$) introduces a high density of localized states n_L in the band structure of the niobium-oxide interface (Fig. 21) that allow interface tunnel exchange (ITE) with the high density of states of the metal (n_m) at the Fermi energy. This process defines a distance $z^*(\omega)$ up to which n_L are in equilibrium with n_m for a sinusoidal rf field. This equilibrium is disturbed by a time dependent trap energy $\Delta\varepsilon(z, t) = ezE_\perp e^{i\omega t}$. In superconducting niobium, the presence of an energy gap prevents ITE up to a field E_0 such that electrons in localized states gain enough energy to overcome the gap. ITE enhances the electric surface resistance R_s^E by several orders of magnitude and the model predicts the following dependence of R_s^E from the peak surface electric field [13]:

$$R_s^E \propto \frac{\omega\mu_0 n_L d}{\kappa^2}\left(e^{-c/E_p}-e^{-c/E_0}\right), \tag{87}$$

where d is the oxide thickness, $1/\kappa$ is the characteristic tunnel distance ($\approx$ 0.2 nm) and c is given by the following expression

$$c = \frac{2\kappa\Delta\varepsilon_r}{e\beta^*}. \tag{88}$$

β^* is a static field enhancement factor.

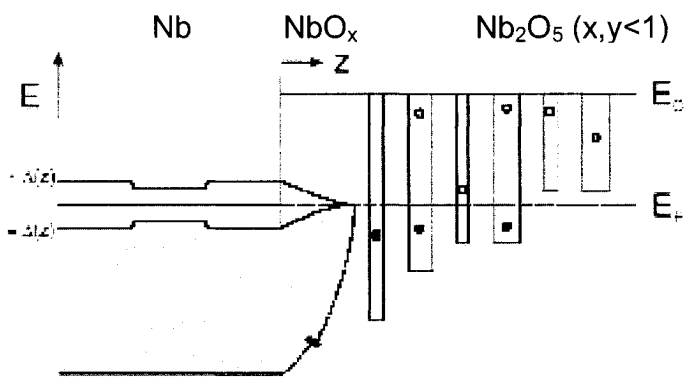

FIG. 21. Band structure at Nb-NbO_x-Nb_2O_{5-y} interfaces [62] showing a reduction of the energy gap in metallic NbO_x and localized states in the dielectric Nb_2O_{5-y}.

4.8.2 Magnetic field enhancement (MFE) model

Knobloch *et al.* [14] consider the effect of the roughness of the cavity inner surface on the local quench field. Niobium cavities are chemically etched to remove damaged layers of material but this process produces a more or less rough surface, depending on the treatment used. Steps up to 10 μm high have been measured particularly at grain boundaries. A geometric magnetic field enhancement factor, β_m, is introduced to account for the deformation of the field lines pattern. When the local field $\beta_m B_p$ at sharp ridges parallel to the current density, exceeds the critical field, a region of width w_{nc} becomes normal conducting, lowering the quality factor of the resonator (Fig. 22). At higher fields, a larger fraction of the cavity quenches causing a progressive decrease of Q_0 up to a point where the cooling provided by the liquid helium is not sufficient to maintain the cavity in the superconducting state.

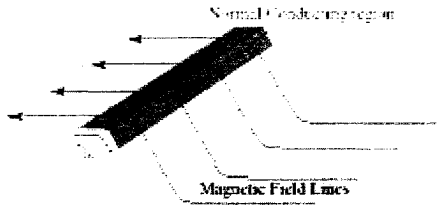

FIG. 22. Schematic of a grain boundary that has quenched due to magnetic field enhancement [14] for current parallel to ridges.

Electromagnetic and thermal analysis of a typical grain boundary step yield an estimate of the width (w_{nc}) and of the power dissipated per unit length by the quenched grain boundary (P') as $w_{nc} \cong 1$ μm, $P' \cong 17$ W/m. The model assumes the following distribution of field enhancement factors β_m:

$$n(\beta_m) = \frac{1}{N} e^{-\sqrt{|\beta_m - \beta_0|}/\sigma}, \tag{89}$$

where β_0 and σ are the respectively the "center" and the "width" of the distribution and are used as fit parameters and N is a normalization constant. An estimate of the total number of grain boundaries, N_{gb}, is given by:

$$N_{gb} \approx \frac{A_{eff}}{l_{gb}^2}, \tag{90}$$

where l_{gb} is an estimate of the average length of a grain boundary and A_{eff} is the cavity "effective area" which is the area where most of the power is dissipated and is defined as:

$$A_{eff} = \frac{\oint_{A_{cavity}} B^2(x)\,dx}{B_p^2} = \frac{2\omega U}{G H_p^2}. \tag{91}$$

The total power dissipated by all grain boundaries is given by:

$$P_{gb}(B_p) = \frac{2P' l_{gb} N_{gb}}{\pi} \int_{\beta_1}^{\infty} \int_{\gamma_1}^{\frac{\pi}{2}} \left[\beta_{eff}(\beta_m, \gamma) \frac{B_p}{B_c} \right]^2 n(\beta_m)\, d\gamma\, d\beta_m. \tag{92}$$

B_c is the critical field, β_1 is defined as B_c/B_p, β_{eff} is an "effective" field enhancement factor which takes into account the angle γ between the magnetic field and the grain step:

$$\beta_{eff} = \sqrt{\beta_m^2 \sin(\gamma)^2 + \cos(\gamma)^2}. \tag{93}$$

Finally, γ_1 is defined by the condition $\beta_{eff}(\gamma_1) = B_c/B_p$. The cavity quality factor as a function of the peak magnetic surface field predicted by the model is given by:

$$Q_0(B_p) = \frac{\omega U(B_p)}{P_{gb}(B_p) + P_{sc}(B_p)}, \tag{94}$$

where P_{sc} are the superconducting losses which are adjusted to match the experimental Q_0 at low field.

4.8.3 Grain boundaries decoupling

Bonin and Safa [15] consider grain boundaries as superconductor-insulator-superconductor (SIS) Josephson junctions. These "weak links" are characterized by their critical current density $J_{c,gb}$ and their specific resistance $G_b = R_{gb}a^2$ where R_{gb} is the normal state resistance and a is the grain size. At high enough fields, the surface current density might exceed $J_{c,gb}$ causing a transition of the grains to the normal state and increased power dissipation. The field H_{gb} corresponding to the grain boundaries decoupling can be estimated as:

$$H_{gb} = \frac{\Delta\lambda_J}{G_b e}. \tag{95}$$

Since not all the grain boundaries have the same $J_{c,gb}$, in order to estimate their contribution to the surface resistance, an adequate distribution function $\rho(J_{c,gb})dJ_{c,gb}$ is needed.

4.8.4 Thermal instability (TI) model

As the power dissipated in the cavity increases at higher fields, a point might be reached where the efficiency of the power transfer from the inner surface to the liquid helium is not sufficient to keep the temperature of the rf surface stable. In that case, the temperature would quickly runaway, due to the exponential increase of the surface resistance and the cavity would quench. The easiest way to describe this thermal instability is by using Eq. (84), although close to the breakdown field the difference between the temperature of the rf surface T_m and the bath temperature T_0 diverges, making the first order expansion of the surface resistance incorrect.

A more adequate approach is given by solving the conservation law for the heat flux flowing through the niobium and at the niobium-helium interface [74]:

$$\frac{H_p^2}{2} R_s\left(T_m, B_p\right) = \frac{\left(T_m - T_0\right)}{R_K + \frac{d}{\kappa}}, \tag{96}$$

where $R_s(T_m, B_p)$ is given by

$$R_s\left(T_m, B_p\right) = R_{BCS0}\left(T_m\right)\left[1 + C\left(\frac{\Delta}{kT_m}\right)^2\left(\frac{B_p}{B_c}\right)^2\right] + R_{res} \tag{97}$$

and $R_{BCS0}(T_m)$ is an approximate expression for the temperature dependence of the BCS surface resistance [68]

$$R_{BCS0}\left(T_m\right) = \frac{A f^2}{T_m} e^{-\frac{\Delta}{kT_m}}, \tag{98}$$

where A is a fitting constant which depends on material parameters. Substituting Eq. (97) in Eq. (96) one obtains a quadratic or bi-quadratic equation for B_p as a function of T_m, depending whether the non-linear contribution in Eq. (97) is considered or not. Since the model predicts that a small overheating ($T_m - T_0 \cong 0.3$ K) is sufficient to induce a thermal breakdown, the thermal properties of niobium at the helium bath temperature can be used as fitting parameters to compare the model with the experimental data of R_s as a function of B_p.

CHAPTER 5

EXPERIMENTAL PROCEDURES

5.1 Introduction

This chapter will describe the typical procedures adopted to prepare a cavity for an rf test in liquid helium, followed by a detailed description of the experimental setup and techniques used to measure the quality factor as a function of the peak fields and the surface impedance as a function of temperature. The last section of this chapter is devoted to a description of the thermometry system used to map the temperature of the cavity surface during the high-power test. This tool is particularly useful to localize and quantify the losses in different regions of the cavity.

5.2 Cavity preparation procedures

5.2.1 Ultrasonic cleaning

The first step to clean a bulk niobium cavity is a degreasing by immersion in an ultrasonically agitated solution of ultra-pure water and soapy detergent for about 30 min. After this process the cavity is rinsed thoroughly with ultra-pure water. This treatment is applied also to all the ancillary components to be assembled on the cavity, such as flanges, antennas, nuts, bolts and washers.

5.2.2 Chemical etching

The performance of a superconducting cavity relies on the properties of a thin layer (about 100 nm) of niobium. In order to remove damaged layers of material, due for example to the deep-drawing of the cell, the cavity is chemically etched to obtain a smooth, polished surface. Two techniques are currently used: buffered chemical polishing (BCP) and electropolishing (EP).

Buffered chemical polishing consists in filling the cavity with a mixture of acid nitric, fluoric and phosphoric in ratio 1:1:1 or 1:1:2. The nitric acid oxidizes the niobium, while the fluoric acid removes the oxide, according to the following equations:

$$6\ Nb + 10\ HNO_3 \rightarrow 3\ Nb_2O_5 + 10\ NO\uparrow + 5\ H_2O \quad (99)$$

$$Nb_2O_5 + 10\ HF \rightarrow 2\ NbF_5 + 5\ H_2O. \quad (100)$$

These reactions are highly exothermic and the phosphoric acid is used as a buffer to slow down the kinetic of the process. Typical etching rates are 1 – 2 μm/min and 5 – 7 μm/min for 1:1:2 and 1:1:1 solutions respectively. The etching rate depends on several factors such as temperature, the amount of niobium already dissolved in the acid, and agitation. At Jefferson Lab, BCP is done either in a closed cabinet where acid is constantly flowing in the cavity at approximately 15 °C and a flow rate of 16 l/min or under a fume hood where the cavity is filled with the acid mixture at about 25 °C and manually stirred. With the last method, it is necessary to repeat the process a few times, cooling off the acid before each step. Once the etching is complete and the cavity has been emptied, an acid film is still present on the surface due to the high viscosity of the mixture and it is important to rinse the cavity many times to avoid undesired reactions such as hydrogen diffusing in the niobium.

Electropolishing is done by applying a constant voltage between a cylindrical aluminum cathode and the niobium cavity (anode) partially filled with a mixture of acid sulfuric and fluoric in ratio 9:1. The following reactions produce the dissolution of niobium:

$$2\ Nb + 5\ SO_4^{--} + 5\ H_2O \rightarrow Nb_2O_5 + 10\ H^{+} + 5\ SO_4^{--} + 10\ e^{-} \quad (101)$$

$$Nb_2O_5 + 10\ HF \rightarrow 2\ NbF_5 + 5\ H_2O. \quad (102)$$

The cavity is rotated at about 1 rpm and the acid is flowed at a rate of about 4 l/min and the temperature is kept between 25 and 30 °C. The etching rate is about 0.3 μm/min. After EP the acid is quickly drained and the cavity is rinsed several times with ultra-pure water. The best surface finish is obtained when the voltage is set so that the average current density is between 30 and 100 mA/cm^2 and, typically, 50 mA/cm^2 is chosen [75]. Figure 23 shows a schematic representation of the electropolishing process. Analysis of the roughness on chemically etched niobium samples generally shows that EP provides smoother surfaces than BCP [76].

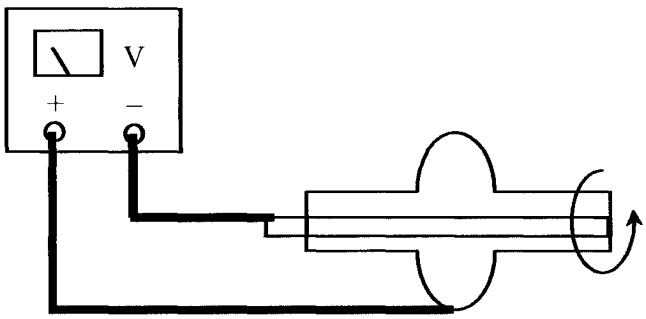

FIG. 23. Schematic of the EP process. The pure aluminum cathode is covered by a porous Teflon bag to trap the hydrogen gas produced during the polishing which is then blown away by nitrogen gas flowing on the upper half-cell. The positive voltage is applied to the cavity by a copper strap tightened at the equator. The cavity is continuously rotated during the process.

5.2.3 High pressure rinsing

After the chemical etching, the interior of the cavity is cleaned by a jet of ultra-pure water pressurized at 80 bar. Water is sprayed by a nozzle on the top of a wand moving up and down inside the cavity, which is set vertically on a rotating table. The typical speed of the wand is 0.5 cm/min, the typical cavity rotation is 1 rpm and the flow rate is 15 l/min. The process runs for about 1 h.

High pressure rinsing (HPR) is a very important step to achieve the ultimate cavity performance: the process is used to remove dust particles and contaminants from the surface which are responsible for field emission.

All the components of the HPR system (pump, pipes, filter...) must be kept exceptionally clean and also the quality of the water must meet very tight specifications (TOC < 5 ppb, resistivity > 18 MΩ cm, less than 500 cts/l for particles > 0.05 μm).

5.2.4 Assembly

After the HPR, the cavity dries overnight in a class 10 clean room. Prior to assembly all the parts are cleaned by a jet of pure nitrogen in front of a particle counter for about

15 min. Two flanges are bolted to the cavity: the top one has a pick-up antenna, the bottom one has an antenna used to input power in the cavity and a pump-out port. Typically, niobium flanges with indium wire as gasket or stainless steel flanges with $AlMg_3$ [77] gaskets are used. Finally the cavity is mounted on a vertical stand and connected to the stand's vacuum line. Ultra-high vacuum is provided by a turbomolecular pump backed by a rotary scroll pump. The typical pressure prior to cool-down is 10^{-8} mbar.

5.2.5 Low temperature baking

"In-situ" low temperature (100-140 °C) baking is often applied as final treatment of a bulk niobium cavity. The effect of baking will be largely discussed in the next chapters. For our experiments, baking was done in two ways: the first way is to insert the cavity under vacuum in an oven where heaters blow hot nitrogen on the outer cavity surface. The temperature is controlled by thermocouples attached on top and bottom of the cavity. Another way is to keep the cavity in the dewar used for the rf test at 2 K and heat the helium gas with a resistive heater. The temperature is controlled by diodes placed inside the dewar.

5.3 Measurements of the surface impedance

5.3.1 Q_0 vs. field measurements

A resonant mode of the cavity is excited by an rf signal provided by an external source through an input coupler inside the cavity. A pick-up coupler is used to sample the energy stored in the cavity. A coupler is typically an antenna coupling with the electric field or a loop coupling with the magnetic field of the cavity. For our experiments, we use both types of couplers. The system rf generator-couplers-cavity can be represented by an equivalent circuit sketched in Fig. 24. In the equivalent circuit, the couplers are represented by transformers and the cavity by a resonant R-L-C circuit. Given the rf generator waveform, it is possible to calculate the response of the cavity by solving the circuit's equations [68].

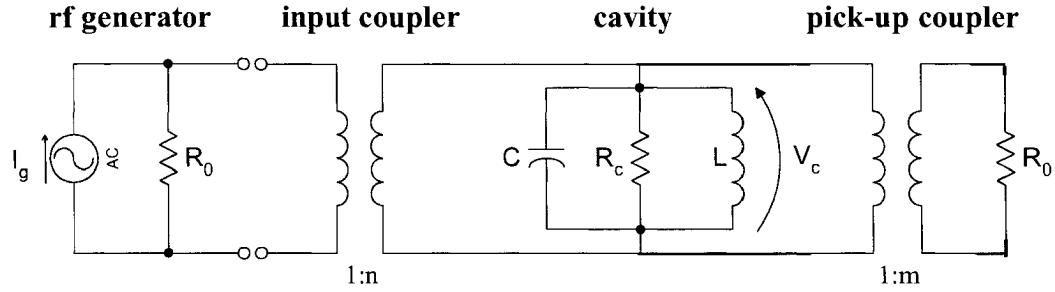

FIG. 24. Equivalent circuit for a cavity with input and pick-up couplers.

The total dissipated power (P_{tot}) is the sum of the power dissipated in the cavity plus the power coupled by the input (P_{ext1}) and pick-up coupler (P_{ext2}). This allows defining a "loaded" quality factor, Q_L:

$$\frac{1}{Q_L} = \frac{P_{tot}}{\omega U} = \frac{1}{Q_0} + \frac{1}{Q_{ext1}} + \frac{1}{Q_{ext2}}, \tag{103}$$

where the Q_{ext} is defined as the ratio between the energy stored in the cavity and the power coupled by the coupler in one rf radian. The power coupled by an external coupler (P_{ext}) relative to the power dissipated in the cavity walls (P_c) defines the so-called coupling coefficient β:

$$\beta = \frac{P_{ext}}{P_c} = \frac{Q_0}{Q_{ext}}. \tag{104}$$

For the pick-up coupler, $P_{ext} << P_c$ so that $\beta << 1$. The value of the coupling coefficient depends only on the geometry of the coupler.

In order to determine the quality factor of the cavity it is necessary to measure Q_L and the couplers' Q_{ext} or coupling coefficient β. This can be done by pulsing the input power (P_i) from the rf generator and looking at the power transmitted through the pick-up coupler (P_t) and the power reflected through the input coupler (P_r) on an oscilloscope. When the system has reached equilibrium, after the rf has been switched on, the power dissipated in the cavity is the difference between the incident and the sum of the reflected and transmitted power:

$$P_c = P_i - P_r - P_t. \tag{105}$$

The shape of the reflected power during the rf pulse determines the coupling conditions: if P_r goes through zero before reaching a non-zero steady state value, the cavity is said to be "overcoupled"; it is called "undercoupled" otherwise. If the reflected power remains zero in steady state, the cavity is "critically coupled" which means that the system input coupler-cavity perfectly matches the impedance of the rf generator so that all the incident power is transferred to the cavity. The shape of P_i, P_r, and P_t during a pulse is given as an example in Fig. 25 for different coupling conditions.

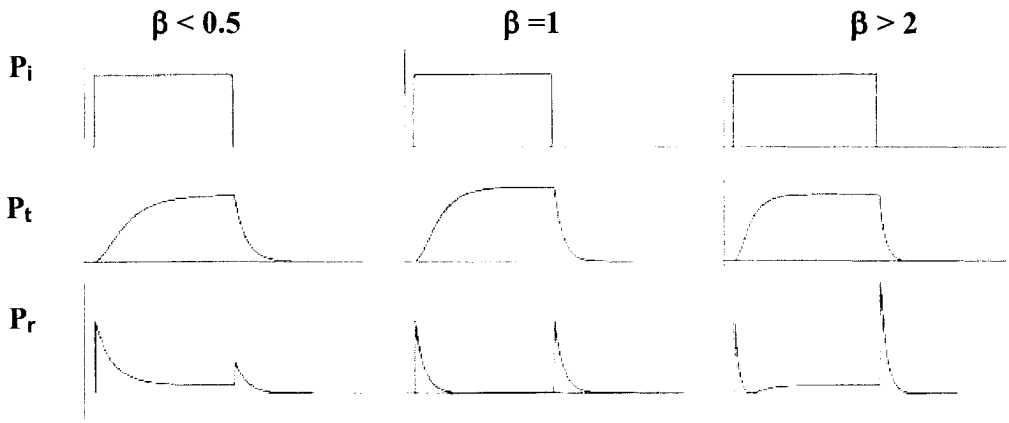

FIG. 25. Envelope of the incident, transmitted and reflected powers for different coupling conditions.

The coefficient Γ is obtained measuring P_i and P_r in steady state:

$$\Gamma = \frac{1 \pm \sqrt{\frac{P_r}{P_i}}}{1 \mp \sqrt{\frac{P_r}{P_i}}}, \tag{106}$$

where the upper signs are for overcoupling and the lower ones are for undercoupling. The coupling coefficients of the pick-up and input coupler are given respectively by:

$$\beta_2 = \frac{P_t}{P_c} \tag{107}$$

$$\beta_1 = \Gamma(1+\beta_2). \tag{108}$$

When the rf power is switched off, the transmitted power, proportional to the cavity stored energy, decays exponentially to $1/e$ in the time τ_L:

$$\frac{dP_t}{dt} = -\frac{P_t}{\tau_L} \tag{109}$$

and by measuring the time constant τ_L and the cavity resonant frequency f_0, the loaded Q is given by:

$$Q_L = 2\pi f_0 \tau_L. \tag{110}$$

Finally, the quality factor of the cavity is given by:

$$Q_0 = (1+\beta_1+\beta_2)Q_L. \tag{111}$$

The accelerating field E_{acc} is given by:

$$E_{acc} = \frac{1}{L}\sqrt{\frac{R}{Q_0}Q_{ext2}P_t}, \tag{112}$$

where R/Q_0 was defined in Sec. 2.2.3 and L is the cell length. The peak fields are simply obtained by multiplying (112) by the ratio E_p/E_{acc} and B_p/E_{acc} calculated by a computer code for a certain cavity shape and field configuration. The measurement of the coupling coefficients is done following the outlined procedure at low fields, in absence of anomalous losses. Once the Q_{ext} of the pick-up probe has been determined, a measurement of Q_0 as a function of the peak fields is obtained by raising the incident power in continuous wave operation and measuring P_i, P_r, and P_t:

$$Q_0 = \frac{Q_{ext2}P_t}{P_i - P_r - P_t} \tag{113}$$

and E_{acc} is calculated with (112). The quality factor is also measured at low field ($B_p \approx$ 10 mT) during lowering the helium bath pressure from 840 torr to 2 torr. The surface resistance as a function of temperature between 4.3 and 1.4 K can be calculated using Eq. (9). The temperature is obtained from the helium bath pressure measured with a Baratron gauge.

The powers measured by the power meters need to be multiplied by the attenuations introduced by the cables and couplers from the cavity to the meter. The relative error for power is given by

$$\frac{\Delta P}{P}=\sqrt{\left(\frac{\Delta C}{C}\right)^2+\left(\frac{\Delta P_m}{P_m}\right)^2}, \tag{114}$$

where C is the attenuation factor and P_m is the power measured by the meter. $\Delta C/C$ is about 4% while $\Delta P_m/P_m$ is about 3%. This error is approximately the same for incident, reflected and transmitted power.

The relative error for Q_0 measured during the calibration procedure at low field is given by

$$\frac{\Delta Q_0}{Q_0}=\sqrt{\frac{\beta_1^2\left\{4\left(\frac{\beta_2}{1+\beta_2}\right)^2+\frac{\rho}{2}\left[\frac{1}{(1+\rho)^2}+\frac{1}{(1-\rho)^2}\right]\right\}+4\beta_2^2}{(1+\beta_1+\beta_2)^2}\left(\frac{\Delta P}{P}\right)^2+\left(\frac{\Delta f_0}{f_0}\right)^2+\left(\frac{\Delta \tau_L}{\tau_L}\right)^2} \tag{115}$$

where ρ is the square root of the ratio P_r/P_i. The relative error for the time constant measurement is about 3%, while the frequency error is negligible. The error on the measurement of Q_0 is minimal for $\rho = 0$ which corresponds to critical coupling. β_1 is typically between 0.5 and 2 while β_2 is about 0.1 or smaller, corresponding to an error on Q_0 of about 4%. The relative error of Q_{ext2} used for the high field measurements is given by

$$\frac{\Delta Q_{ext2}}{Q_{ext2}}=\sqrt{\left(\frac{\Delta Q_0}{Q_0}\right)^2+4\left(\frac{\Delta P}{P}\right)^2} \tag{116}$$

and is typically about 10%. The relative errors of Q_0 and E_{acc} for the high power tests are given by:

$$\frac{\Delta Q_0}{Q_0}=\sqrt{\left(\frac{\Delta Q_{ext2}}{Q_{ext2}}\right)^2+4\left(\frac{\Delta P}{P}\right)^2}, \tag{117}$$

$$\frac{\Delta E_{acc}}{E_{acc}}=\frac{1}{2}\sqrt{\left(\frac{\Delta Q_{ext2}}{Q_{ext2}}\right)^2+\left(\frac{\Delta P}{P}\right)^2} \tag{118}$$

and is typically about 14% and 6% respectively. All the errors in the Q_0 vs. field plots are systematic.

5.3.2 rf system for Q_0 vs. field measurements

The quality factor of a superconducting niobium cavity at 2 K is typically of the order of 10^{10}. This means that the bandwidth $\Delta f = f_0/Q_L$ of the TM_{010} mode ($f_0 \approx 1.5$ GHz) is less than 1 Hz. Mechanical vibrations can easily shift the resonant frequency by more than the bandwith and a feedback system is needed to "lock" the rf source to the cavity mode. This is typically achieved with a Phase Locked Loop (P.L.L.). The feedback signal is provided by the transmitted power from the cavity: samples of P_t and of the power from the rf source are routed to the inputs "rf" and "lo" of a microwave mixer. The mixer's output is filtered so that only the dc voltage proportional to the phase difference of the two inputs is transmitted to the frequency control of the oscillator. This error signal provides the correction to the rf source frequency to follow oscillations in the resonant frequency of the cavity.

A schematic of the rf system used for Q_0 vs. field measurements is given in Fig. 26. The square-wave generator is used to pulse the rf signal through a PIN diode while the bidirectional coupler allows to sample the incident and reflected power from the cavity. The limiting amplifier outputs the same power (5 dBm), for input powers between -30 dBm and 15 dBm, so that the power at the "rf" port of the mixer is always at the optimum level. A trombone style phase shifter and an additional phase shifter for fine tuning in line with the oscillator permits one to adjust the relative phase of the mixer's two inputs. A variable attenuator is used to raise the input power to a 200 W amplifier, which provides the rf input to the cavity.

The cryostat is about three meters deep into the ground and a lead shield covers the top-plate during the rf test, to prevent x-rays (produced by field emission) from spreading into the working area. The rf system is also interlocked to prevent high power rf to reach the cavity under unsafe conditions.

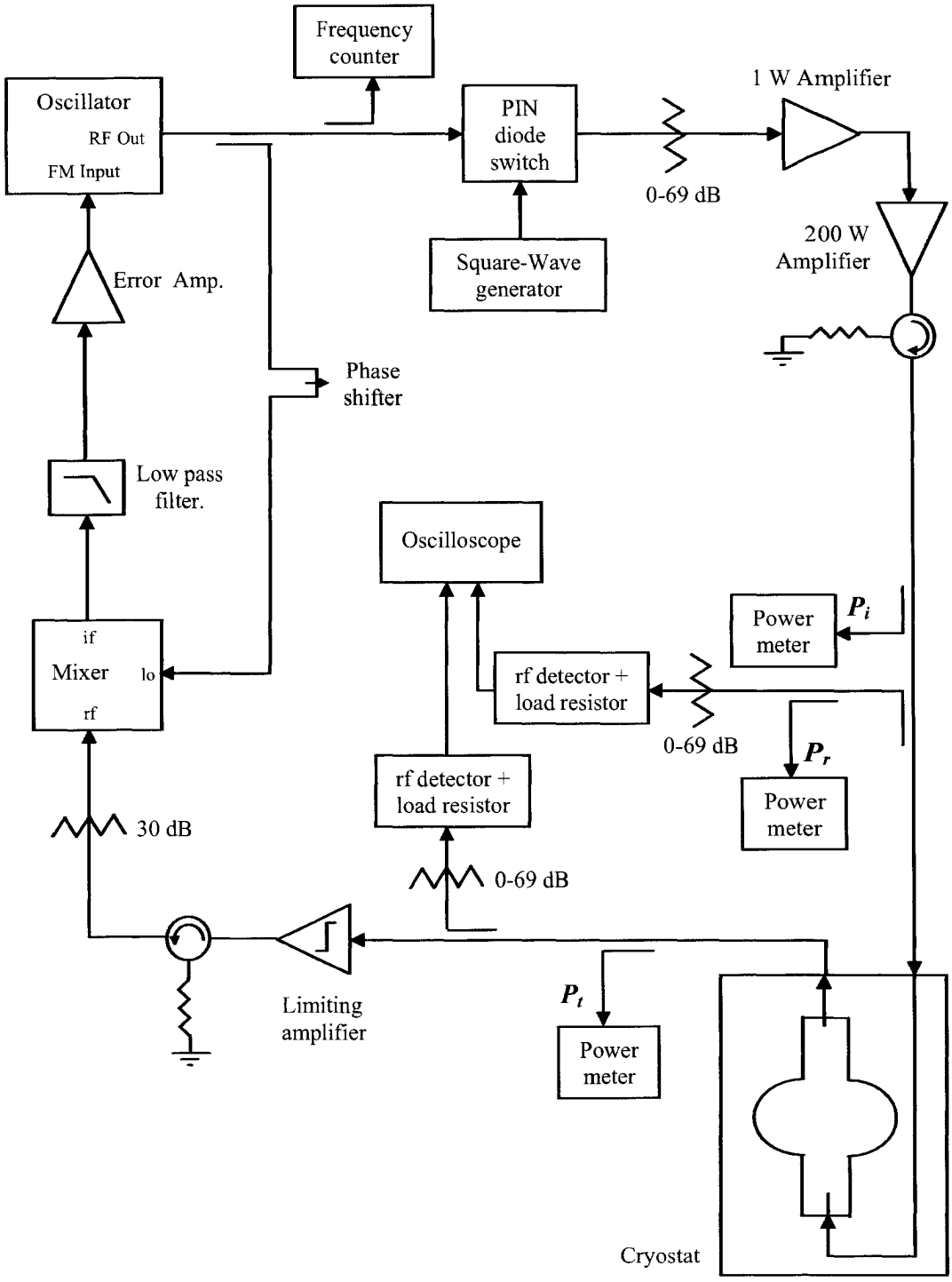

FIG. 26. Schematic of the rf system used for the Q_0 vs. field measurements.

5.3.3 Penetration depth measurements

After the high power rf test, the liquid helium is boiled off using a resistive heater. Once the temperature reaches about 4.5 K, the heater is turned off and the dewar is slowly warmed up by its static heat leak (≈ 1 W). Also, the cryostat is opened to atmospheric pressure to equalize pressure fluctuations from the He recovery system. Typically, it takes about 8 h for the temperature to rise from 4.5 K to 10 K. During the warm-up a network analyzer is connected to the cavity to track the mode's resonant frequency and quality factor (by the 3 dB method). The network analyzer excites the cavity at very low field levels ($B_p \approx 2$ mT). Fig. 27 shows the TM_{010} resonance curve at 4.3 K.

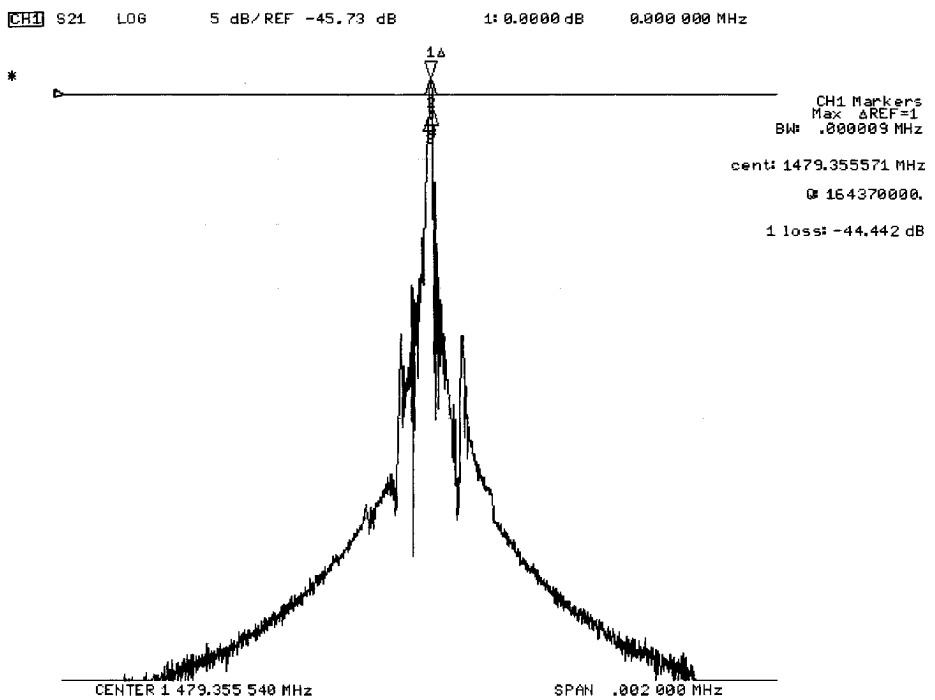

FIG. 27. Resonant curve of the TM_{010} mode measured with a network analyzer at 4.3 K.

The temperature is measured by four calibrated Cernox® thermometers in contact with the upper and lower cavity irises, as shown in Fig. 28. The thermometers are pressed

on the cavity by spring loaded set-screws and Apiezon® N grease is used to assure a good thermal contact. A computer code written in LabView™ automatically acquires frequency, quality factor and temperature every 30 s.

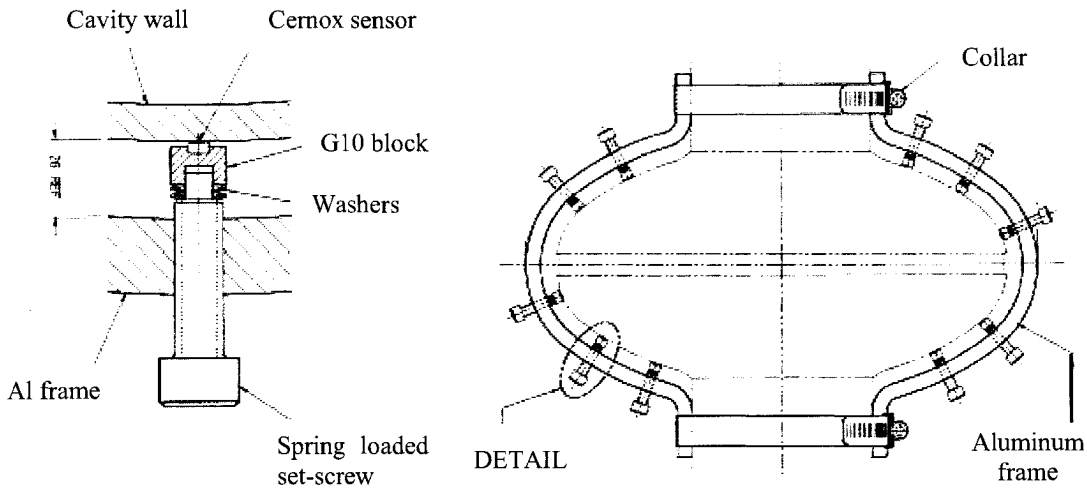

FIG. 28. Temperature sensors assembly on the single cell cavity.

The change of penetration depth is obtained from the frequency shift during warm-up through the following formula [78]:

$$\lambda(T)-\lambda(T_0)=\frac{G}{\mu_0\pi f_0^2(T_0)}\left[f_0(T)-f_0(T_0)\right], \tag{119}$$

where T_0 is typically 7-8 K. Since df_0/dT is maximum close to T_c and f_0 is very sensitive to the external pressure acting on the cavity walls, a high precision measurement is achieved by the slow warm-up and the dewar opened to atmosphere. The surface resistance is obtained from the measurement of Q_L with the network analyzer using Eqs. (111) and (9).

Above 10 K, the cryostat is warmed up to 300 K by a combination of resistive heater and warm helium gas, while still measuring the cavity surface impedance. At 2 K, the rf field penetration in the niobium is only about 40 nm, while it increases to about 300 nm

at 10 K and 3 μm at 300 K. The ratio of the resistivity at 300 K and 10 K gives the *RRR* of the niobium surface.

Since the cavity quality factor changes by several orders of magnitude between 4.5 K ($Q_0 \approx 2 \cdot 10^8$) and 300 K ($Q_0 \approx 9 \cdot 10^3$), it is useful to have a variable input coupler to better match the cavity impedance to the network analyzer, improving the measurement accuracy. A picture of the variable coupler used for our experiments is shown in Fig. 29.

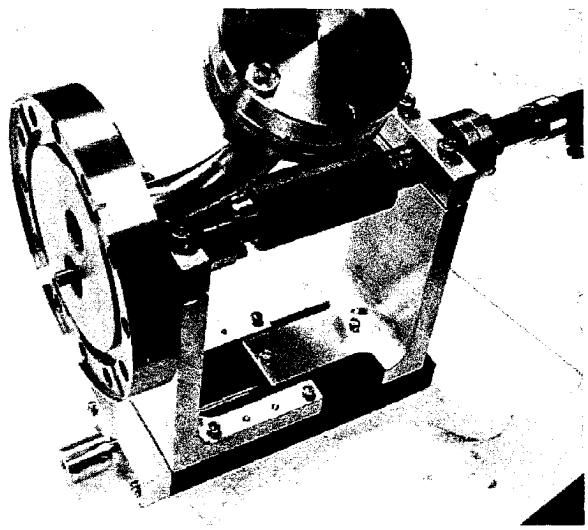

FIG. 29. Variable input coupler used for the penetration depth measurements attached to a stainless steel flange.

A long copper antenna connected to an rf feedthrough moves inside a bellows, changing the penetration, and therefore the coupling, in the cavity's beam pipe. A stepper motor actuates a rotary feedthrough, on the top of the dewar insert, which is connected to the finely threaded rod of the coupler's base and allows to stretch or compress the bellows. The Q_{ext} of the coupler increases exponentially with the antenna's penetration length which can be changed by as much as 2.5 cm, corresponding to about three order of magnitude change of Q_{ext}. During the pump-down between 4.3 and 1.4 K, the coupling is constantly adjusted to the increasing quality factor for more precise measurements, while above 4.5 K, the Q_{ext} is fixed to about $4 \cdot 10^7$. One disadvantage of the variable coupler is

that it can be a source of contamination, as any moving part inside the cavity, potentially lowering the maximum achievable field due to FE.

The network analyzer used for our experiments is the model Agilent 8753E. The frequency span is adjusted to the bandwidth of the resonance curve during warm-up and the instrument's IF filter bandwidth is set to 1000 Hz. The highest quality factor that can be measured accurately with the network analyzer is about 3×10^7 at 1.5 GHz, which is the Q_0 of the cavity at 7 K.

The error of the change of penetration depth is given by:

$$\Delta\left(\lambda(T)-\lambda(T_0)\right)=\left[\lambda(T)-\lambda(T_0)\right]\sqrt{\left[\frac{\Delta f_0(T)}{f_0(T)-f_0(T_0)}\right]^2+\left[\frac{2\Delta f_0(T_0)}{f_0(T_0)}\right]^2}. \qquad (120)$$

The error of the frequency measurement $\Delta f_0(T)$ is about 25 Hz, while the error of the reference frequency $\Delta f_0(T_0)$ is about 100 Hz, due to pressure oscillations. The resulting error of the change of penetration depth is about 1.6 nm. The error of the surface resistance measurements depends on the error of the bandwidth measurement and is estimated to be about 2 μΩ up between 8 and 9 K, while it is about 10 μΩ up to 20 K. The error of the absolute temperature measurement is about 1 mK up to 8 K, while it is about 5 mK up to 12 K.

5.4 Temperature mapping system

One of the most powerful tools designed to study cavity losses has been a thermometry system used to map the local temperature on the cavity surface. Its effectiveness lies in the fact that any loss mechanism ultimately produces heat in the cavity wall.

The setup we developed is largely based on a state-of-the-art system built at Cornell [20] and it consists of an array of 576 carbon resistors distributed over the exterior cavity surface.

5.4.1 Thermometers

The temperature sensing element is a 100 Ω carbon Allen-Bradley resistor (5%, 1/8 W) whose resistance increases exponentially with decreasing temperature. At 2 K, the

resistance is typically 7 kΩ, the sensitivity is about 10 Ω/mK and very small temperature variations can be detected. However, the resistance of these thermometers changes when they are cycled at room temperature, so that each thermometer needs to be recalibrated for every cavity test.

Low thermal conductivity manganin wires, 0.254 mm in diameter, are soldered to the resistor leads. The resistors are encapsulated in a G-10 housing filled with epoxy (Stycast 2850 FT) to thermally isolate them from the helium bath. The top surface of the resistor (bakelite) is ground away until the carbon elements are exposed and a thin layer of GE-Varnish (7031), 50% diluted with a mixture of toluene and ethyl alcohol, is applied to electrically isolate the resistor from the cavity. Spring loaded pins ("pogo sticks") are mounted with stycast in recessed holes in the bottom of the G-10 housing. Figure 30 shows a schematic of the thermometer and a detailed fabrication procedure can be found in [20].

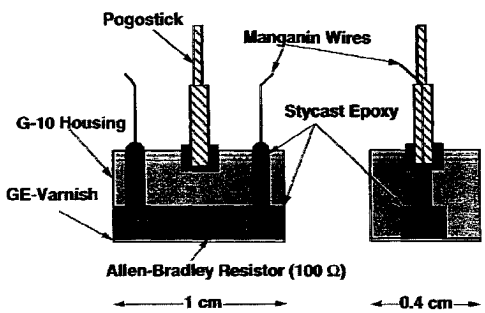

FIG. 30. Schematic of the thermometer used for the temperature mapping system [20].

To place the thermometers in contact with the cavity, 36 printed circuit boards (PCB) of G-10 material (3.175 mm thick) are machined to match the contour of the CEBAF cavity shape, leaving a 1 cm gap. 16 holes (1.38 mm drill bit, 1 cm deep) are drilled perpendicular to the cavity and the pogo sticks are inserted into them. Copper traces on the board link the thermometers to a 3M-3431-5003 34 pin right angle insulation displacement connector (IDC). Figure 31 shows a picture of a complete thermometer board.

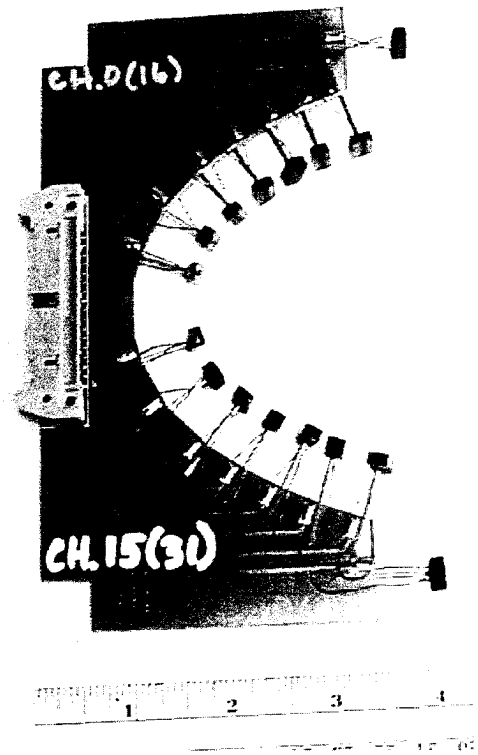

FIG. 31. Thermometer board designed to match the contour of a CEBAF cavity shape, holding 16 thermometers.

Four semicircular aluminum plates are attached to the top and bottom beam tubes of the cavity to form two rings. Each ring has 36 radial grooves (4 mm wide) into which the thermometer boards slide. Two split locking rings each with 36 threaded holes (2.84 mm diameter) are bolted on the aluminum plates. Set screws are inserted in the threaded holes and are used to push the boards against the cavity. Apiezon N grease is applied to the varnished side of the thermometers to assure good contact with the cavity.

The 36 boards are spaced azimuthally 10° apart, the spacing between thermometers on neighboring boards varies from about 0.65 cm at the iris, to 1.7 cm at the equator. The spacing along a board is about 1 cm and the largest gap is across the equator (1.7 cm) due to a recess on the cavity surface because of the equatorial weld. Figure 32 shows a picture of the thermometer boards mounted on the cavity. The main constraint on the design of the assembly was to keep the overall size smaller than the radius (20 cm) of the cryostat used to cool the cavity to 2 K.

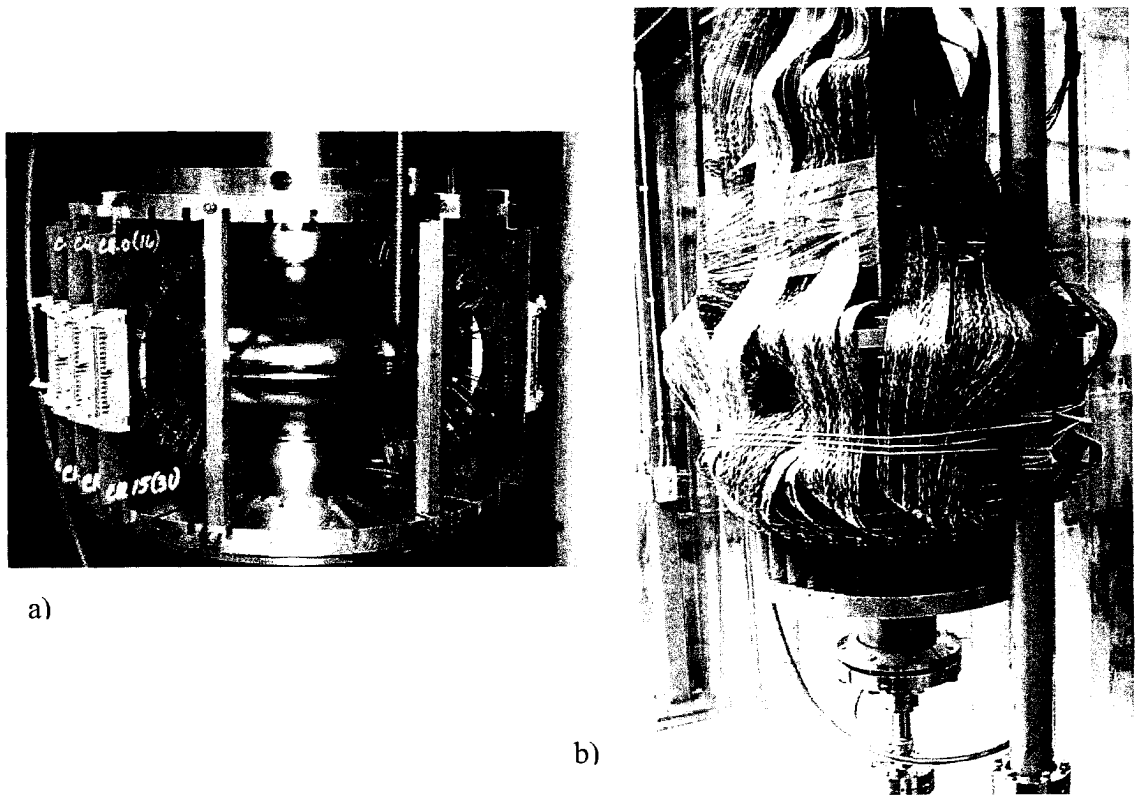

a)

b)

FIG. 32. Assembly of thermometer boards on the cavity (a) and completed setup (b).

5.4.2 Electrical connections

A stainless steel feed-through box is mounted on the test stand top plate and provides the interface between the wiring inside the cryostat and to the data acquisition system. A G-10 PCB board (3.175 mm thick) has 36 DB-37 connectors on the air side and thirty-six 34-pin IDC connectors on the helium side. It is very important to have perfect soldering of the connectors pins to the pads on the PCB board since it has to be vacuum tight to the point where less than 8 ppm of air can leak into the dewar. A larger leak will contaminate the helium recovery system to which the cryostat is connected. The PCB board is mounted on a stainless steel support plate, which acts as reinforcement, and is screwed on the front side of the feed-through box with twenty-two 4.83 mm diameter screws. A ribbon O-ring makes the plate leak tight. A picture of the feed-through box is shown in Fig. 33.

The thermometer boards are connected to the IDC connectors on the top of the test stand top plate by thirty-six 34-conductors (0.32 mm diameter) twisted pair flat ribbon cables. The additional heat leak in the 2 K bath due to the cables was less than 1 W.

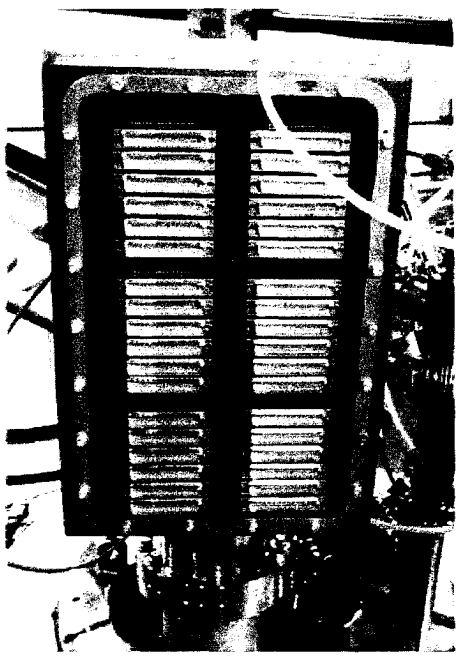

FIG. 33. Feed-through box which interfaces the dewar inside with the air side and is able of maintaining a contamination smaller than 8 ppm.

Thirty-six 34-conductors (0.32 mm diameter) 6 meter long shielded jacketed ribbon cables bring the signal from the air side of the feed-through box to 18 PCB boards (two cables/board). Each board has sixty-four 1 MΩ chip resistors soldered in series to the Allen-Bradley resistors (two for each thermometer) which, in conjunction with the driving voltage act as a current source for the thermometer. The thermometers are connected in parallel and they are driven by a Keithley 2400 voltage source, remotely controlled by a computer via general purpose interface bus (GPIB). The PCB board provides also an easy interface between the shielded ribbon cables and the 96-pin connector of the data acquisition card. Figure 34 shows a picture of the interface PCB board and a schematic of the thermometers excitation.

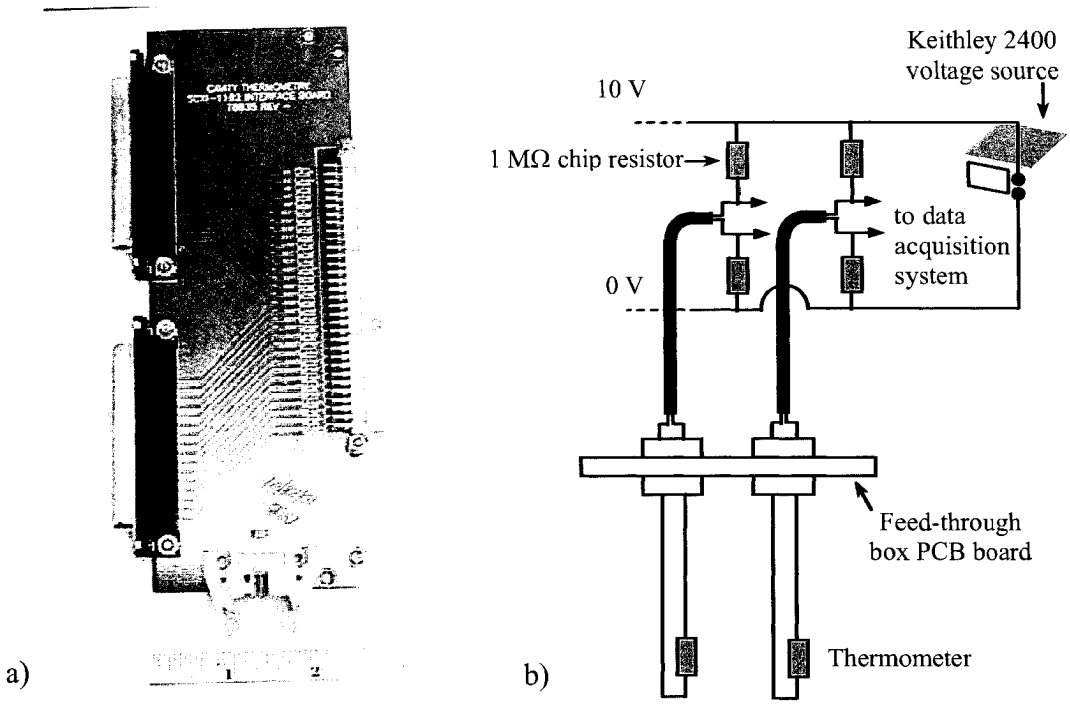

FIG. 34. Picture of the interface PCB board (a) and schematic of the thermometers excitation (b).

5.4.3 Data acquisition

The data acquisition system for the voltage across the 576 thermometers is based on the SCXI™ system from National Instruments: two SCXI-1001 chassis are placed outside the radiation shielding around the dewar and contain eighteen SCXI-1102 modules, each of which is capable of multiplexing 32 differential inputs. These modules are designed for high accuracy thermocouple measurements, they include an instrumentation amplifier with programmable gain of 1 or 100 and they have 333 kS/s maximum sampling rate. The typical thermometers excitation voltage is 10 V at 2 K, so that the voltage drop across the 7 kΩ resistor is about 35 mV. The analog signal from the SCXI-1102 modules are routed to a personal computer (PC) via a 2 m long SH68-68 shielded cable and they are digitized by a National Instrument PCI-6052E 16 bit analog

to digital converter (ADC). The maximum rate of conversion is 333 kHz. A LabVIEW™ program controls the SCXI modules, the voltage source and a Lakeshore 218 temperature monitor. This last instrument makes a four-wire measurement of the resistance of four calibrated Lakeshore germanium thermometers (GR-200A-250), excited by a 10 μA current, used to monitor the helium bath temperature (T_b). The resistance is converted into temperature using calibration curves in the LabVIEW™ program and the average value is calculated. A LabVIEW™ program on a laptop computer in the control room, about 7 m away from the dewar, runs the program on the remote PC using a virtual instrument (VI) server connection through the laboratory network. It also retrieves the data from the remote computer and reads the incident, reflected and transmitted power from the power meters via GPIB to calculate the quality factor and accelerating field of the cavity.

5.4.4 Thermometer calibration and map acquisition

The voltage across each thermometer (ΔV) is obtained as the average between the absolute voltage measured with one polarity of the voltage source and with opposite polarity. By doing this, any contact voltages or amplifier offsets are canceled out. The thermometer resistance is then calculated as the ratio between ΔV and the excitation current, which is given by the ratio between the voltage source and the 2 MΩ resistances of the chip resistors. This operation can be repeated multiple times to obtain an average value of the thermometer resistance for better accuracy.

During the pumping on the helium bath to lower the temperature from 4.3 K to 2 K, the resistance (R_i) of each thermometer is measured at about 0.1 K intervals to obtain curves of R_i versus T_b. The data are well described by a third-order polynomial fit of $1/T_b$ as a function of $x_i = \ln R_i$:

$$1/T_b = a_i + b_i x_i + c_i x_i^2 + d_i x_i^3 \quad i=0,1..575 \tag{121}$$

where a_i, b_i, c_i and d_i are fit parameters to be determined for each resistor. For each thermometer the square deviation between the measured data and the fit is computed. Thermometers are deemed faulty if this value exceeds the mean of all thermometers by a

factor of two. Bad thermometers are subsequently ignored during the acquisition of the temperature maps.

Once the calibration is completed, the temperature of each thermometer with zero field in the cavity (T_{0i}) is obtained through the polynomial coefficients and the difference with the helium bath temperature T_{b0} is plotted on a 2D view of the cavity surface. Once the rf field is switched on in the cavity, the temperature of each thermometer (T_i) is continuously acquired and the helium bath temperature (T_b) is subtracted. The difference between $T_i - T_b$ and $T_{0i} - T_{b0}$ is plotted, resulting in a "live" temperature map of the cavity surface. It takes about 0.128 s for a single scan to be plotted, but multiple scans are preferred for better accuracy.

Studies performed on the kind of thermometers used for this system [79] showed that their efficiency (defined as the ratio of the measured temperature rise to the theoretical temperature rise) is about 35% ± 13% and their response is linear for power flux values between 1 $\mu W/cm^2$ and 1 W/cm^2. The temperature error due to self-heating is also linear and is about 1 mK with 5 μA excitation current at 2 K. Figure 35 shows the user interface of the LabVIEW™ programs used for the thermometers calibration and temperature map acquisition.

a)

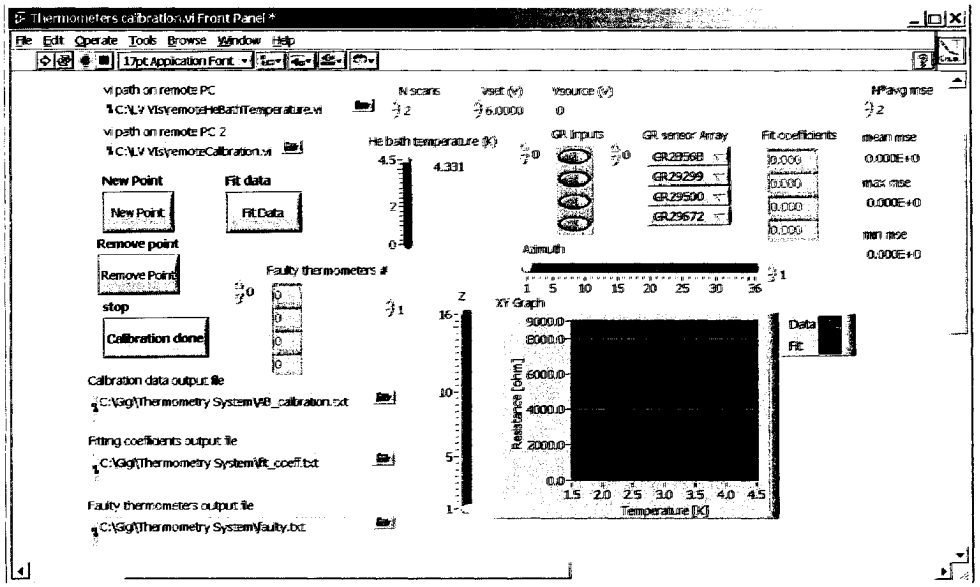

b)

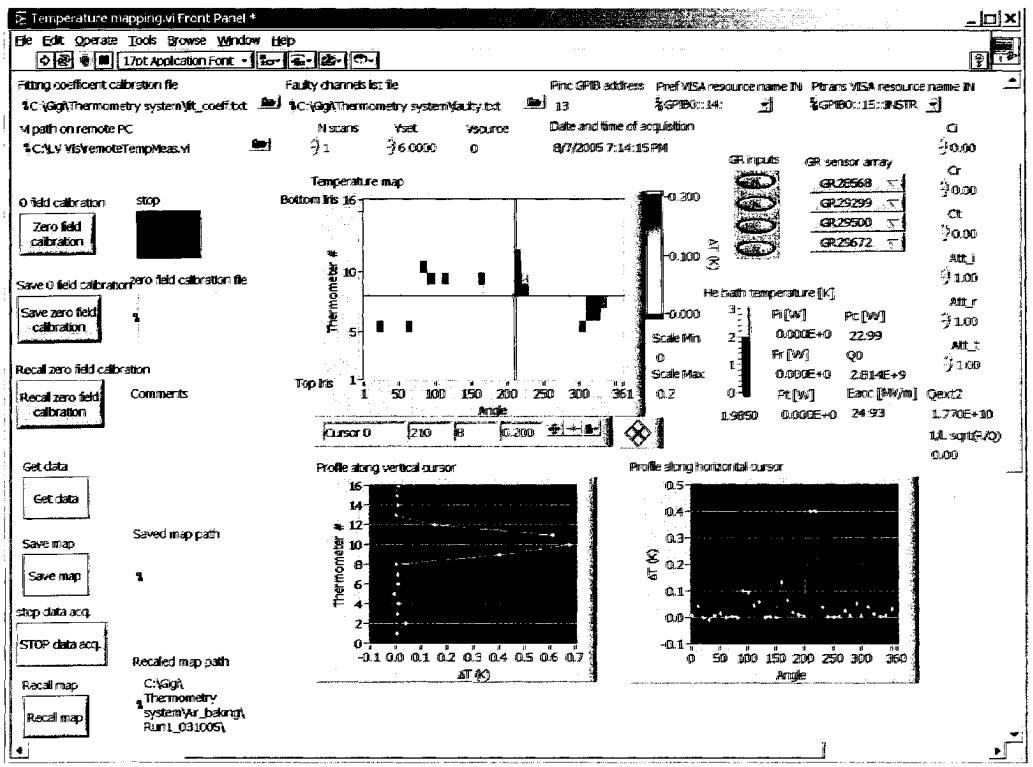

FIG. 35. User interface of the thermometers calibration (a) and temperature mapping (b) LabVIEW™ programs. The graph in (a) plots the resistance as a function of T_b for each thermometer, selected through the slide cursors at the side and on top. The graph in (b) shows a 2D color map of all resistors (darker color indicates higher temperature) and the temperature profiles along vertical and aximuthal coordinates, selected by the cursor, are shown in the graphs at the bottom.

CHAPTER 6

EFFECT OF LOW-TEMPERATURE BAKING ON NIOBIUM CAVITIES

6.1 Introduction

Low-temperature (100-140 °C) baking appears to be an indispensable process to be applied to high *RRR* bulk niobium cavities to recover from the high field *Q*-drop. The effects produced on the superconducting parameters of the niobium cavity surface have been investigated for several baking temperatures. The baking time was fixed to 48 h, plus 2 h for temperature ramp-up and ramp-down, as commonly used in various laboratories.

The cavity used for this series of experiments is a single-cell of the same geometry as used in the CEBAF accelerator made from 1/8" thick *RRR* > 200 niobium. The cavity was built in 1993 and the half-cells were post-purified in a titanium box at 1400 °C for 4 h to increase the thermal conductivity. As a consequence of the heat treatment, the niobium re-crystallized in millimeter-size grains. Prior to this series of tests, about 150 μm were etched from the inner surface and the best performance of the cavity was quench-limited at B_p = 100 mT. Niobium flanges were subsequently replaced with Nb55Ti. All the results presented in this chapter were obtained by measurements on this single cell cavity, except for the "air" baking test of section 6.2.1.

6.2 Experimental results

The cavity preparation is outlined in paragraph 5.2 and after a pre-chemistry which removes about 200 μm from the inner surface, the typical etching, is done with BCP 1:1:1, removing about 7 μm of niobium. The amount of material removal is calculated from the frequency shift after chemistry; the frequency sensitivity has been calculated with SUPERFISH to be 12 kHz/μm.

Two 15×12 mm niobium samples cut from the same sheet are processed with the cavity. One of the samples is placed on a sample-holder connected to the same vacuum line as the cavity, while the other one is kept in the clean room. After baking, both samples are mounted on a fixture which is evacuated to about 10^{-7} torr and shipped to SUNY Albany, where the hydrogen distribution near the surface is measured with the nuclear reaction analysis technique [80]. As discussed in Sec. 4.2.2, hydrogen can be responsible for residual losses in niobium cavities and we wanted to investigate whether it plays any role in the high-field Q-drop and the baking effect. Figure 36 shows a picture of the sample-holder with the niobium sample and Fig. 37 shows the single cell cavity assembled on the vertical test stand ready to be inserted in the cryostat for low-temperature rf tests.

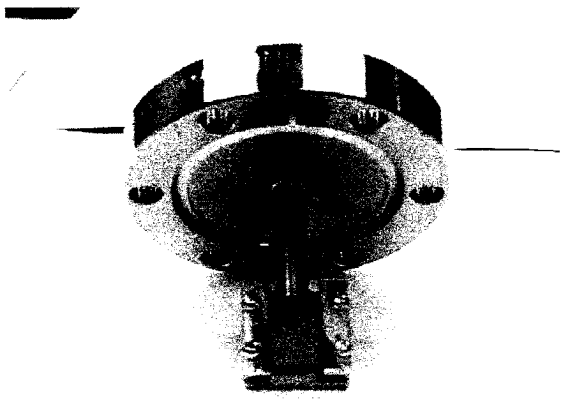

FIG. 36. Sample-holder with niobium sample used for measurements of the hydrogen distribution near the surface before and after baking.

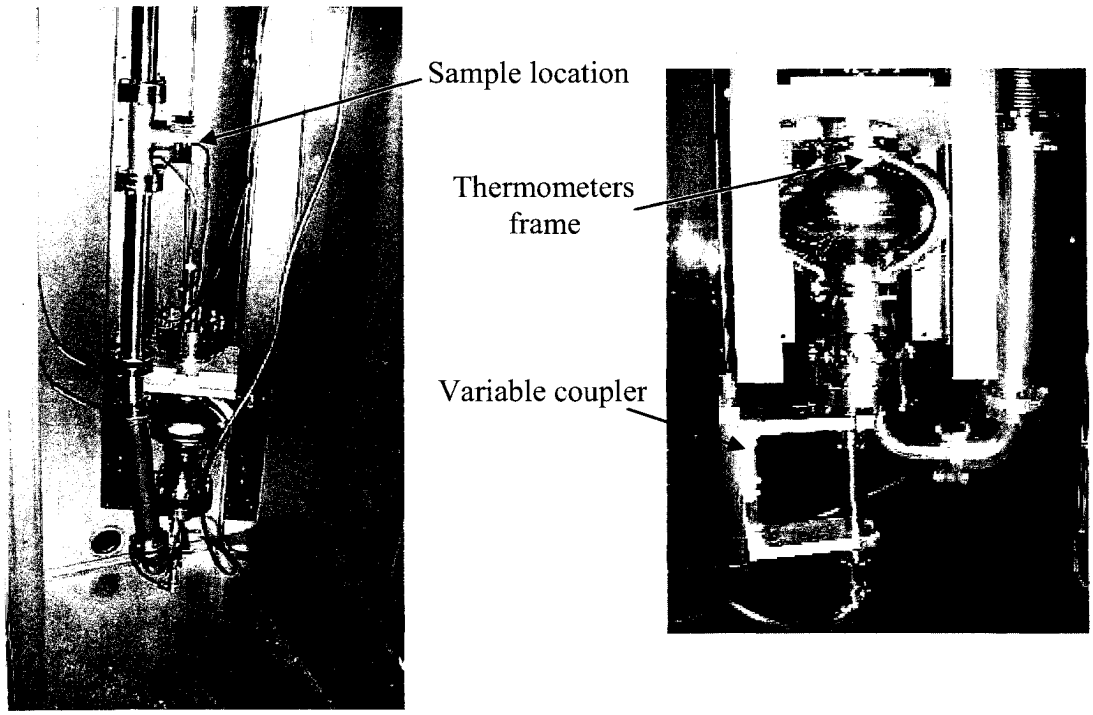

FIG. 37. Cavity assembled on the test stand.

The typical test sequence is:

- Q_0 versus temperature is measured between 4.2 and 1.37 K at a peak surface magnetic field of 4 mT.
- Q_0 versus B_p is measured at 2.2, 2 and 1.37 K.
- Frequency and Q_0 are measured between 5 K and 290 K.
- The Cernox® thermometers are removed from the cavity. The cavity and the sample are "in-situ" baked. The partial pressure of the main gas species are recorded with a residual gas analyzer during bake-out.
- The thermometers are attached back to the cavity and the measurements listed in the first three bullets are repeated on the baked cavity.

The surface resistance and penetration depth data are fitted with a computer code that includes the complete BCS theory calculation for diffuse electrons at the surface, written by Halbritter [38]. Details on the computer code are given in Appendix A. The

parameters obtained from the fits are the critical temperature (T_c), the energy gap at 0 K [$\Delta(0)$], the normal electrons mean free path (l), the residual resistance (R_{res}) and the penetration depth at 0 K [$\lambda(0)$]. It has been shown that these parameters are strongly dependent on the surface condition [48, 81], while the values of the London penetration depth λ_L and the coherence length $\xi_F = \pi\xi_0/2$ are considered material constants equal to 32 nm and 62 nm, respectively [37].

The surface resistance in the normal conducting state has been fitted with a computer code [82] that includes the anomalous skin effect and the values of the surface resistivity [$\rho(T)$] at 10 K and 300 K are obtained. The ratio $\rho(300\ K)/\rho(10\ K)$ defines the *RRR* which is related to the impurity content, in this case, up to 300 μm deep in the material. Figure 38 shows the rf penetration into the surface at three different temperatures.

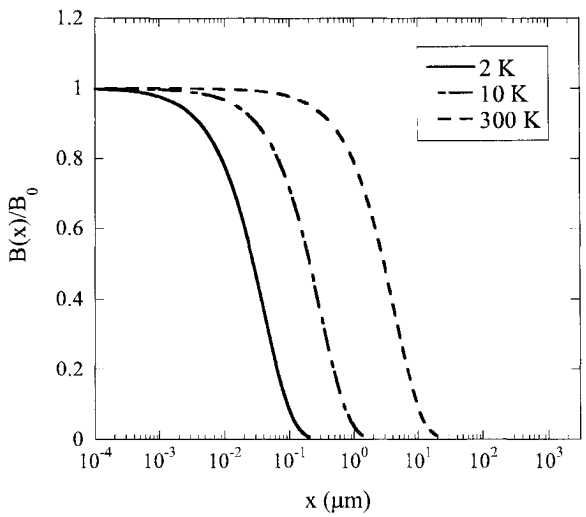

FIG. 38. rf magnetic field amplitude relative to the surface $B(x)/B_0 = e^{-x/\lambda(T)}$ as a function of depth in the niobium at 2 K, 10 K and 300 K. The maximum value of x corresponds to the wall thickness.

Figures 39 and 40 show examples of the typical frequency shift and surface resistance versus temperature above 6 K. Figure 41 shows the typical surface resistance in the normal conducting state.

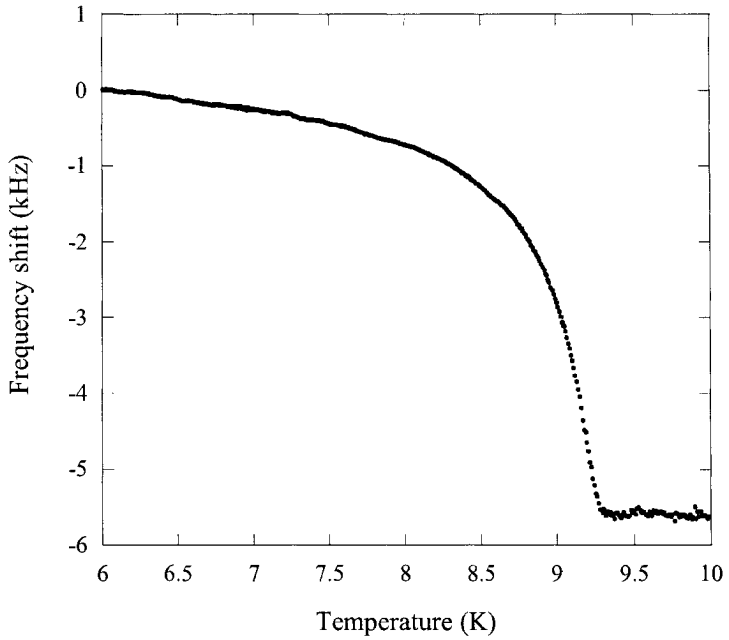

FIG. 39. Typical frequency shift vs. temperature close to T_c at 1.467 GHz. Data are acquired every 30 s.

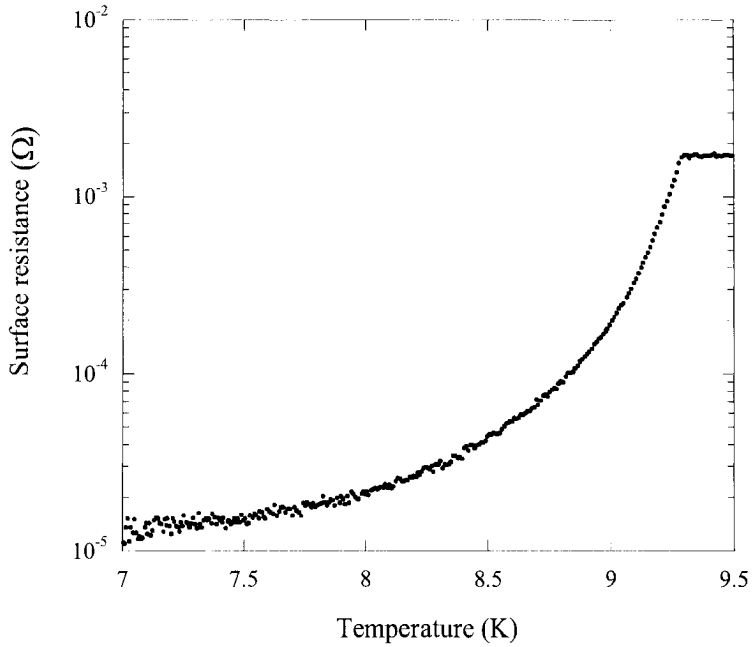

FIG. 40. Typical surface resistance vs. temperature close to T_c at 1.467 GHz.

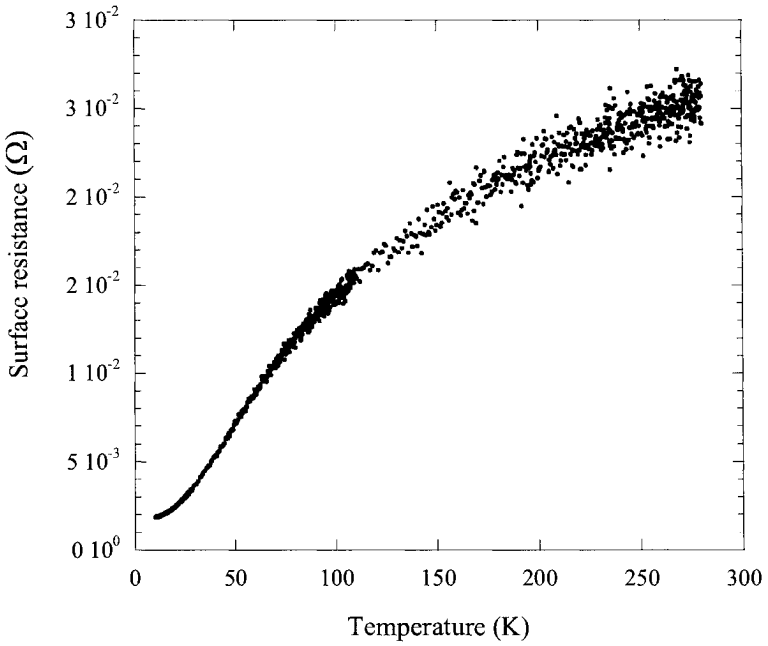

FIG. 41. Typical surface resistance vs. temperature in the normal conducting state.

Figure 42 shows the typical partial pressure profile during baking at 120 °C. The main gas species are hydrogen, water vapor and carbon monoxide. The residual gases are rapidly adsorbed on the surface of the vacuum system upon cool-down to room temperature at the end of baking. The general trend during baking at different temperatures shows that the water vapor signal is already reduced to its minimum after 24 h of baking above 70 °C, while the hydrogen signal increases exponentially for higher baking temperatures up to 160 °C, as shown in Fig. 43.

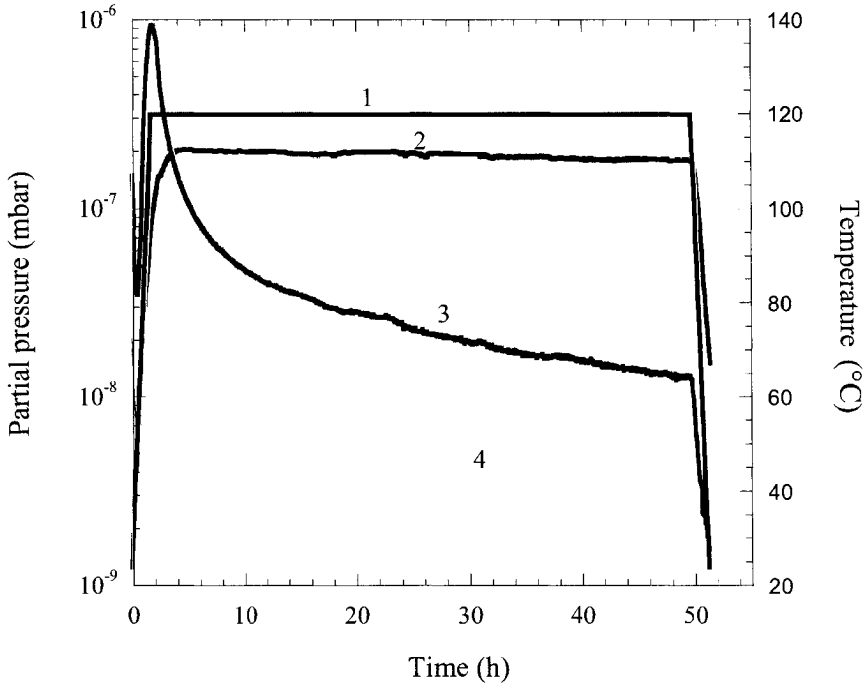

FIG. 42. Partial pressure of H_2 (black-2), H_2O (blue-3) and CO (orange-4) during bake-out at 120 °C. Also shown is the temperature profile (red-1).

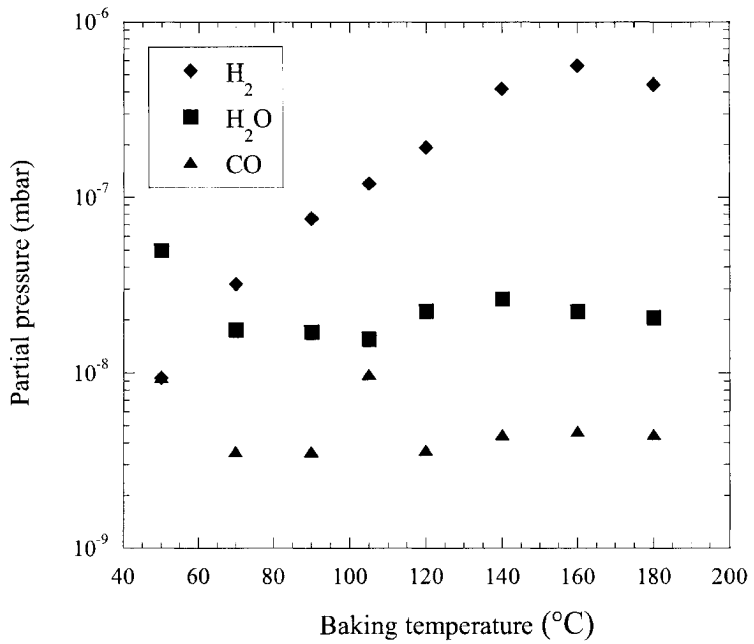

FIG. 43. Partial pressure of the main gases registered after baking for 24 h vs. baking temperature.

Figure 44 shows the surface resistance as a function of $1/T$ between 4.3 and 1.37 K measured before and after baking at 120 °C at $B_p = 4$ mT. The data are compared with the BCS surface resistance plus the residual term and the fitting parameters are the ratio $\Delta(0\ \mathrm{K})/kT_c$, the mean free path l(40 nm), and the residual resistance R_{res}. At 4.3 K, the surface resistance is due mainly to the BCS term and it is reduced by about 50% after baking at 120 °C.

Figure 45 shows the variation of BCS surface resistance at 4.3 K as a function of the baking temperature: the maximum reduction is obtained at 120 °C, as a consequence of a decrease of the mean free path and a slight (< 5%) increase of the energy gap. The average value of $\Delta(0\ \mathrm{K})/kT_c$ in the 40 nm depth before baking is 1.823 ± 0.006 and after baking is 1.853 ± 0.008, consistent with values obtained for oxidized niobium [81]. There is no clear trend of the energy gap, within the experimental error, as a function of the baking temperature.

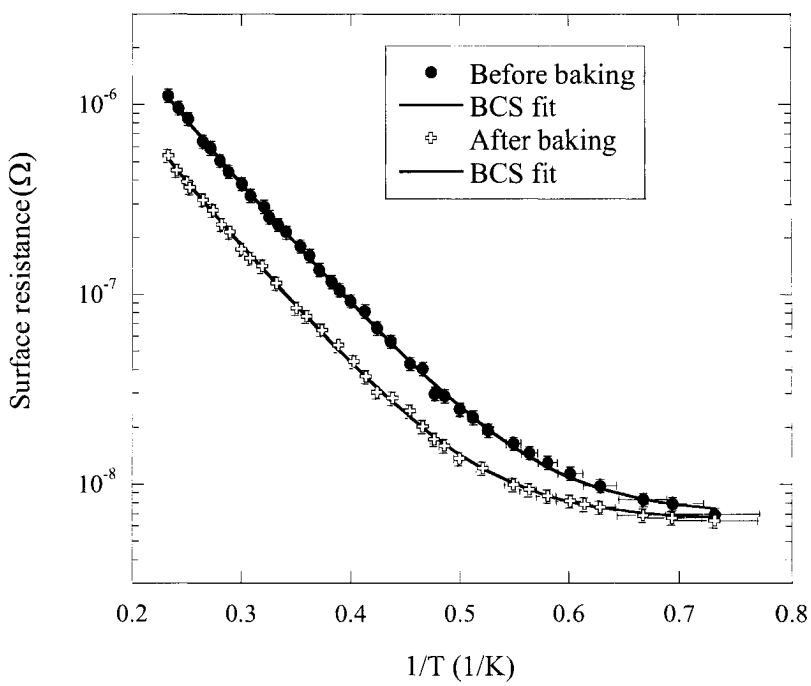

FIG. 44. Surface resistance as a function of $1/T$ before and after 120 °C, 48 h baking.

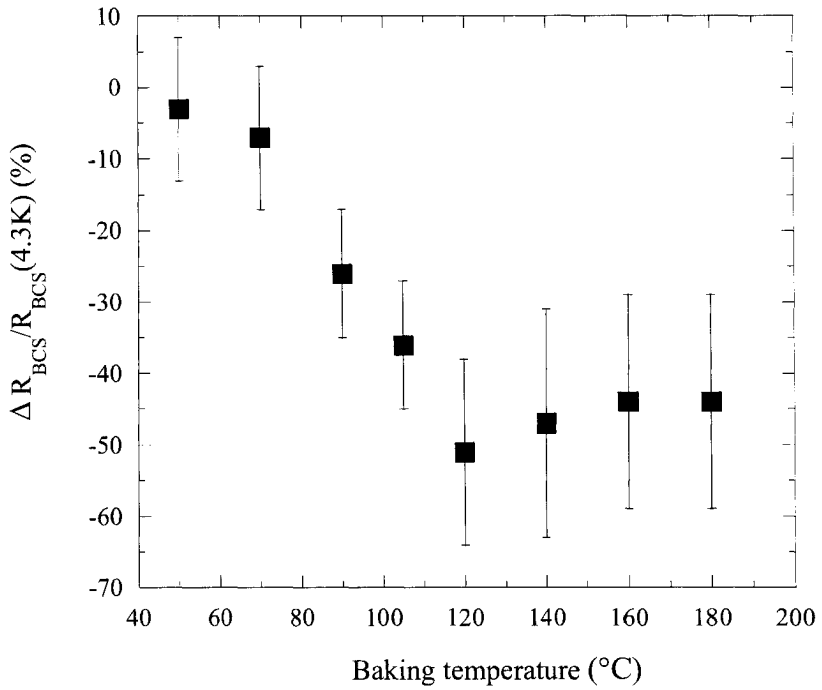

FIG. 45. Variation of BCS surface resistance at 4.3 K as a function of baking temperature.

Table IV lists the values of BCS surface resistance at 4.3 K, the residual resistance and the surface resistance at 2 K along with the limitation occurred in the high power rf test before and after baking at several temperatures. In case of field emission the field enhancement factor β_{FN} can be obtained as the linear coefficient of the plot of $\log[\Delta R_s/E_p^{1.5}]$ vs. $E_p^{1.5}$.

The residual resistance is clearly increasing after baking above 100 °C by about 3.5 nΩ (Table IV). The values of R_{res} in the baseline tests differ by as much as a factor of two, between 4 nΩ and 7.4 nΩ, and the cause for such variations can be assumed to be related to different Nb-Nb_2O_5 morphology and variations in the shielding of the Earth's magnetic field (caused by drifts of the current in the compensation coil). The residual magnetic field is about 3-10 mG, contributing to about 1-4 nΩ to the residual resistance. At 2 K, the residual resistance is almost one third of the surface resistance and due to its increase after baking, the reduction of R_s(2 K) at low field is typically at most 30%.

TABLE IV. BCS surface resistance at 4.3 K, surface resistance at 2 K and B_p = 4 mT, residual resistance and high-field (B_p > 75 mT) limitations.

	R_{BCS}(4.3 K) (nΩ)	R_{res} (nΩ)	R_s(2 K) (nΩ)	Limitation
Baseline	844 ± 59	4.9 ± 0.6	16.3 ± 1.1	FE β_{FN}=230
50 °C bake	816 ± 57	2.4 ± 0.3	15.0 ± 1.1	FE β_{FN}=179
Baseline	1130 ± 79	4.4 ± 0.2	20.5 ± 1.4	Quench
70 °C bake	1048 ± 73	6.4 ± 0.3	21.4 ± 1.5	Quench
Baseline	1148 ± 80	5.2 ± 0.2	22.2 ± 1.6	FE β_{FN}=185
90 °C bake	849 ± 59	5.9 ± 0.2	18.0 ± 1.3	FE β_{FN}=177
Baseline	1112 ± 78	7.4 ± 0.3	24.4 ± 1.7	FE β_{FN}=165
105 °C bake	717 ± 50	10.3 ± 0.3	20.0 ± 1.4	FE β_{FN}=280
Baseline	1110 ± 78	6.9 ± 0.2	24.7 ± 1.7	Q-drop
120 °C bake	542 ± 38	6.4 ± 0.1	13.7 ± 1.0	Quench
Baseline	1059 ± 74	5.4 ± 0.2	22.5 ± 1.6	FE β_{FN}=230
140 °C bake	565 ± 40	8.9 ± 0.2	16.9 ± 1.2	FE β_{FN}=230
Baseline	1110 ± 78	4.0 ± 0.2	21.9 ± 1.6	Q-drop
160 °C bake	618 ± 43	7.5 ± 0.2	16.8 ± 1.2	Quench
Baseline	1090 ± 76	4.2 ± 0.2	20.0 ± 1.4	Q-drop
180 °C bake	610 ± 43	8.0 ± 0.2	18.0 ± 1.3	Quench

Figures 46 and 47 show the surface resistance as a function of temperature between 8 K and T_c and the variation of the penetration depth as a function of the reduced temperature parameter $y = 1/\sqrt{1-(T/T_c)^4}$ before and after baking at 120 °C for 48 h, respectively. The fit of the surface resistance with the BCS theory yields the ratio $\Delta(0\text{ K})/kT_c$, the mean free path in a 300 nm depth and the critical temperature. The value of energy gap is used as fixed parameter in the fit of the penetration depth, which yields the mean free path, the critical temperature and the penetration depth at 0 K.

There is no significant variation in the $\Delta(0\text{ K})/kT_c$ before and after baking at different temperatures: the average value is 1.898 ± 0.013 before baking and 1.887 ± 0.010 after baking. These values are higher than the ones obtained closer to the surface (between 4.3

and 1.37 K) and are closer to 1.97 which was obtained from tunneling experiments on polycrystalline niobium [83].

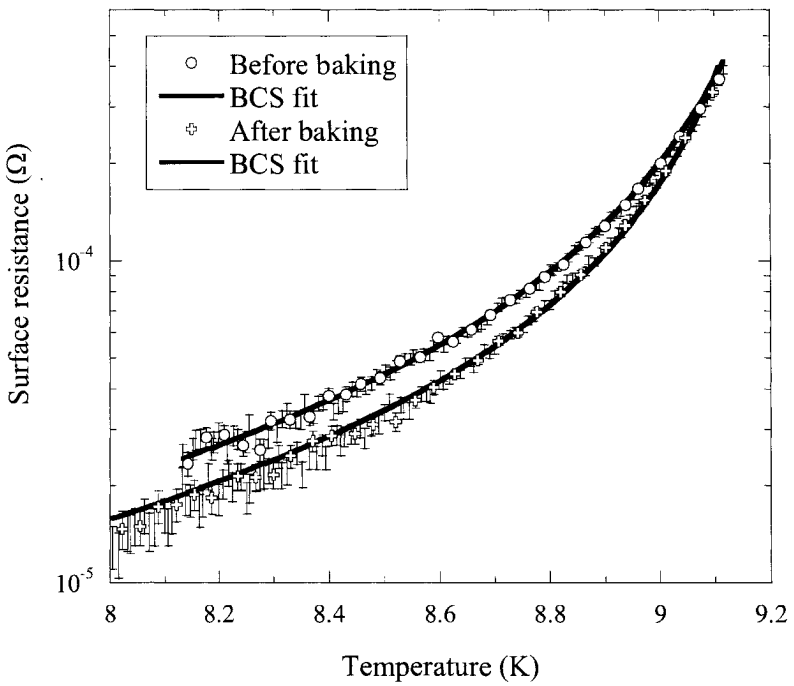

FIG. 46. Surface resistance vs. temperature before and after 120 °C, 48 h baking.

The critical temperature, obtained as a weighted average of the result of the fit of surface resistance and penetration depth, does not show a clear dependence from the baking temperature. The average value before baking is 9.252 ± 0.004 K and it is 9.241 ± 0.005 K after baking.

The surface resistance has a weak dependence on mean free path and the values of l obtained from the fits in the 4.3-1.37 K range have large errors. The penetration depth has a stronger dependence on l and therefore the mean free path is obtained more accurately from measurements between 7 K and 9.1 K. Even though the value of l after a new chemical etching can change by as much as 40% (between 700 nm and 1200 nm), the relative variation before and after baking is well correlated with the baking temperature (Fig. 48).

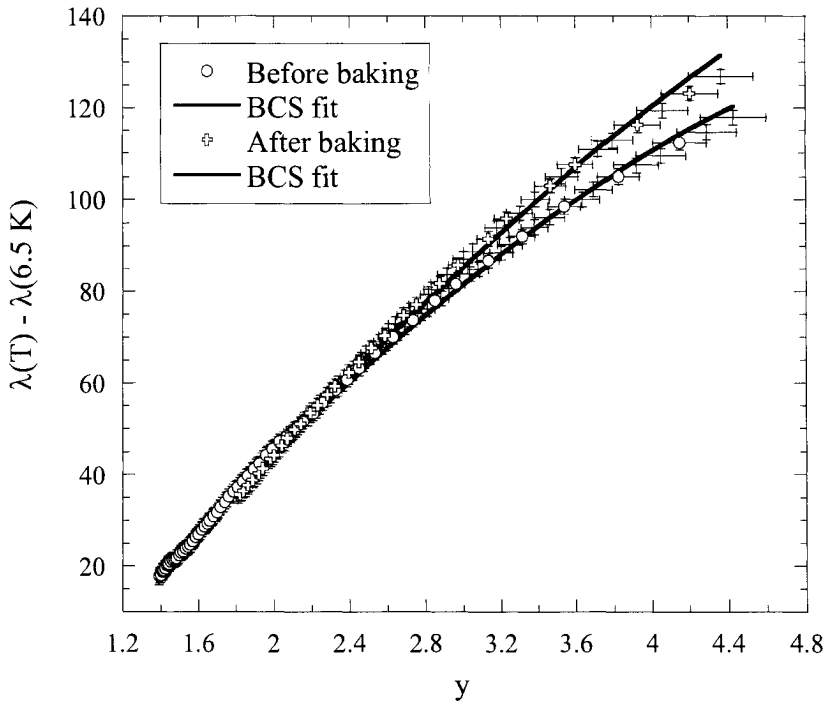

FIG. 47. Variation of penetration depth vs. reduced temperature parameter $y = 1/\sqrt{1-(T/T_c)^4}$ before and after 120 °C, 48 h baking.

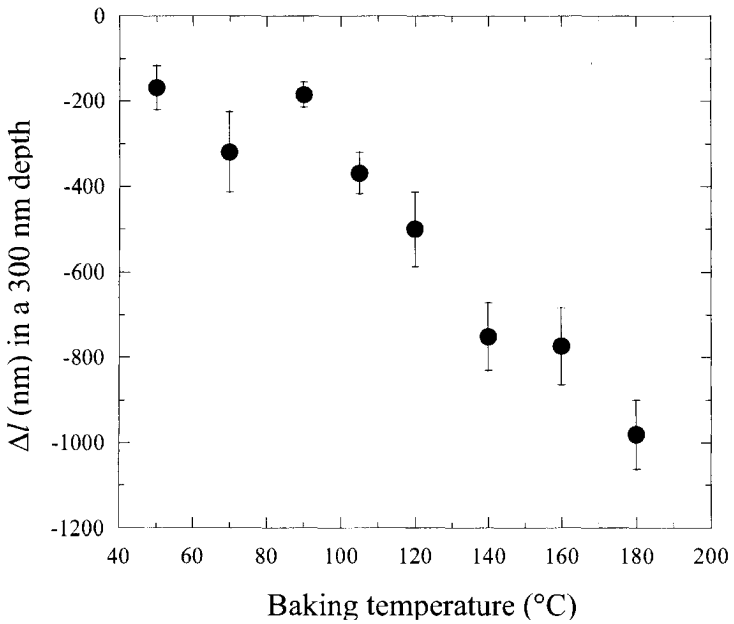

FIG. 48. Variation of mean free path as a function of the baking temperature.

The material parameters before and after baking at different temperatures are listed in Table V. Besides the decrease in the mean free path, a decrease in the surface *RRR* becomes evident after baking at temperatures above 120 °C (Fig. 49). The average value of the *RRR* before baking is 205 ± 3. The average value of the penetration depth at 0 K before baking is 42 ± 4 nm, consistent with measurements on niobium samples [51, 84]. λ(0 K) increases after baking, due to the lower mean free path, consistently with the Eq. (47) for the dirty limit. Table V also indicates that the surface layer of niobium (40 nm) is more "polluted" than the "bulk" (300 nm) up to a baking temperature of 140 °C. Figure 50 is a plot of the variation of penetration depth before and after baking at 160 °C for 48 h and clearly shows the change to the dirty limit after baking.

TABLE V. Material parameters before and after baking at different temperatures which are obtained below 4.3 K at 40 nm depth from the surface and between 7 K and 9.1 K for 300 nm.

	Δ/kT_c (40 nm)	l (40 nm) (nm)	l (300 nm) (nm)	λ (0 K) (nm)	Surf. *RRR* (300 nm)
Baseline	1.89 ± 0.03	364 ± 187	954 ± 38	46 ± 1	255 ± 26
50 °C bake	1.84 ± 0.03	193 ± 76	785 ± 36	46 ± 1	255 ± 26
Baseline	1.81 ± 0.01	695 ± 187	990 ± 61	47 ± 1	195 ± 20
70 °C bake	1.84 ± 0.02	483 ± 130	671 ± 72	43 ± 1	220 ± 22
Baseline	1.85 ± 0.02	1455 ± 611	697 ± 27	45 ± 1	189 ± 19
90 °C bake	1.85 ± 0.02	178 ± 60	514 ± 13	40 ± 1	191 ± 19
Baseline	1.79 ± 0.03	387 ± 190	1077 ± 47	44 ± 1	175 ± 18
105 °C bake	1.82 ± 0.02	64 ± 31	708 ± 14	42 ± 1	209 ± 21
Baseline	1.80 ± 0.02	476 ± 150	854 ± 38	36 ± 1	216 ± 22
120 °C bake	1.89 ± 0.01	26 ± 118	354 ± 78	36 ± 1	211 ± 21
Baseline	1.78 ± 0.02	250 ± 71	1024 ± 42	38 ± 1	218 ± 22
140 °C bake	1.89 ± 0.01	27 ± 102	454 ± 67	32 ± 1	181 ± 18
Baseline	1.81 ± 0.02	508 ± 157	784 ± 90	41 ± 1	196 ± 20
160 °C bake	1.85 ± 0.01	27 ± 74	12 ± 1	78 ± 1	136 ± 14
Baseline	1.85 ± 0.02	841 ± 338	994 ± 81	42 ± 1	196 ± 20
180 °C bake	1.85 ± 0.02	18 ± 16	13 ± 1	92 ± 4	97 ± 10

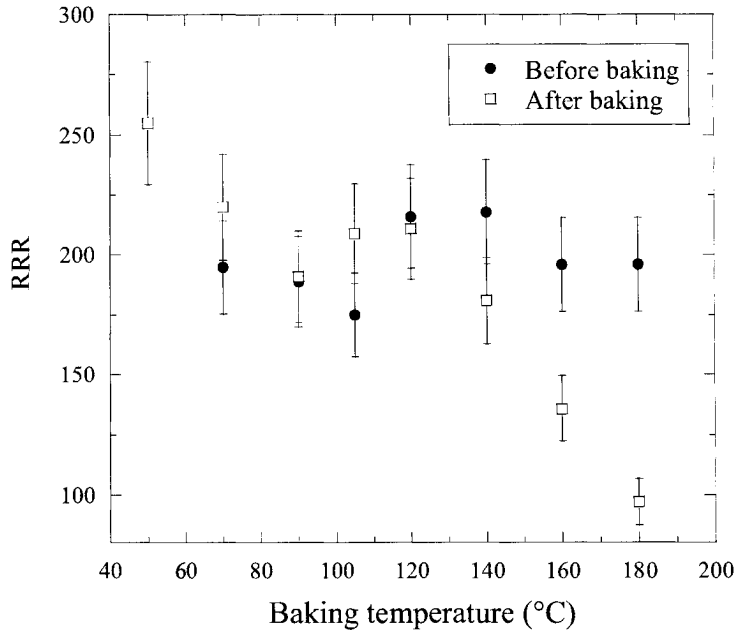

FIG. 49. Surface *RRR* as a function of baking temperature.

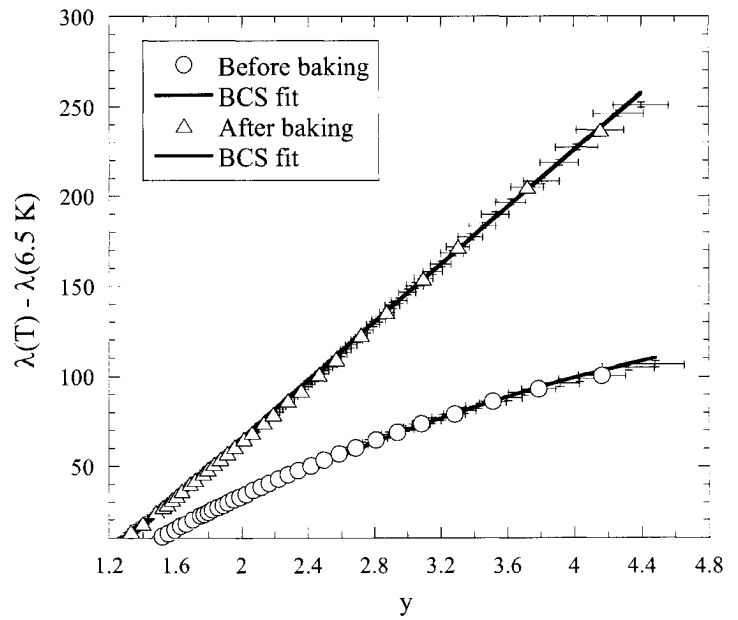

FIG. 50. Variation of penetration depth as a function of the reduced temperature parameter *y* before and after 160 °C, 48 h baking showing the change from clean to dirty limit.

High-power rf tests revealed the high-field Q-drop without field emission on three occasions. The first time the cavity was baked at 120 °C for 48 h, after which the Q-drop became negligible and the cavity quenched at a peak surface magnetic field of 130 mT (Fig. 51). In the second case, after baking at 160 °C for 48 h, the Q-drop became negligible and the cavity quenched at 114 mT peak surface magnetic field (Fig. 52). In the last case, the characteristic behavior of the Q-drop was observed, even though in the presence of little field emission. The cavity was baked at 180 °C for 48 h, after which it quenched at 110 mT peak surface magnetic field (Fig. 53). In all the cases, there is a clear enhancement of the low field Q-slope by baking.

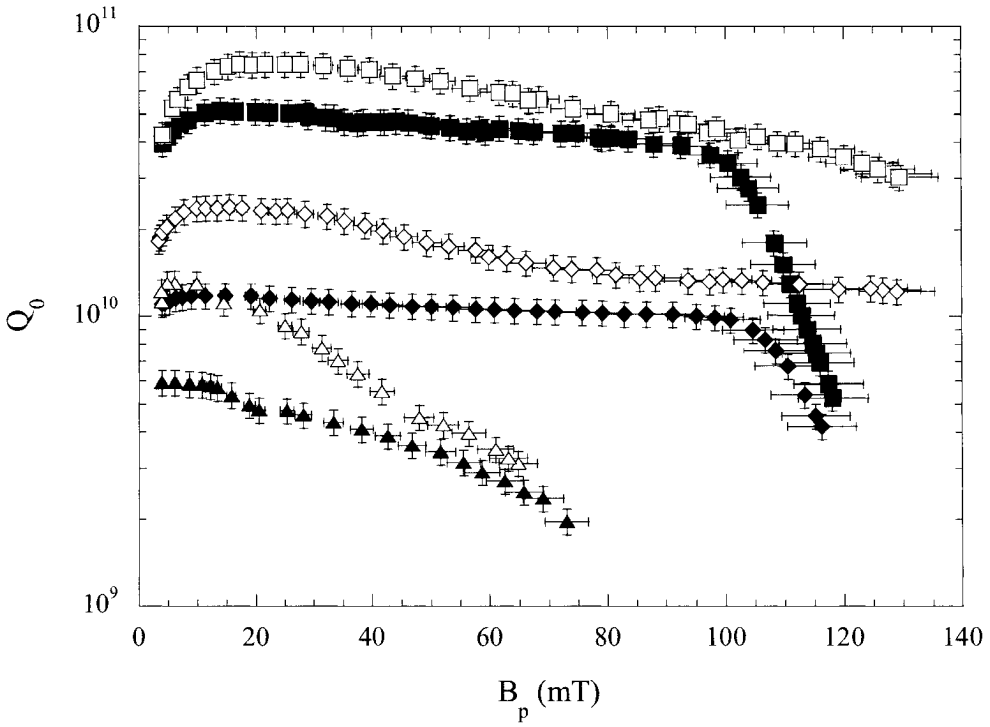

FIG. 51. Q_0 vs. B_p before (solid symbols) and after 120 °C, 48 h baking (open symbols) at three different temperatures: 1.37 K (squares), 2 K (diamonds) and 2.2 K (triangles).

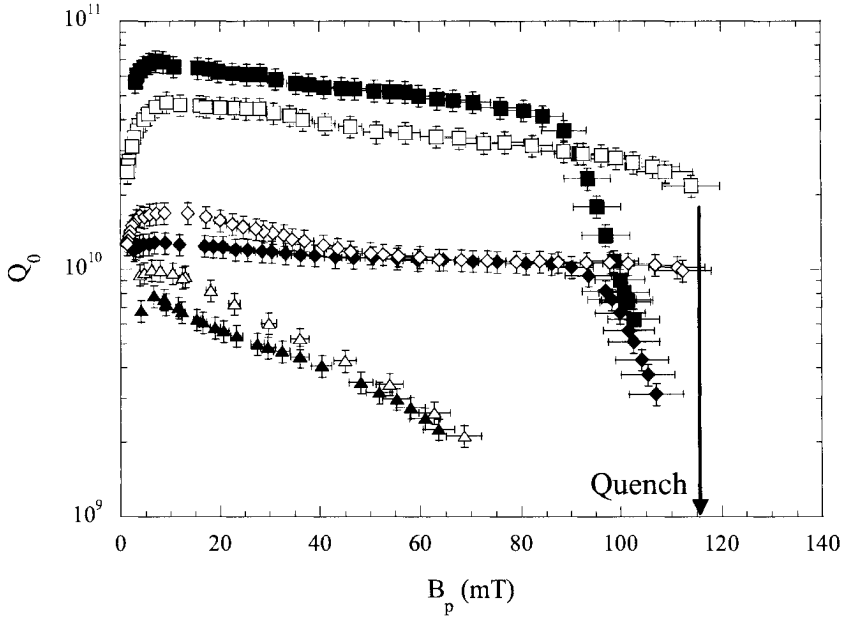

FIG. 52. Q_0 vs. B_p before (solid symbols) and after 160 °C, 48 h baking (open symbols) at three different temperatures: 1.37 K (squares), 2 K (diamonds) and 2.2 K (triangles).

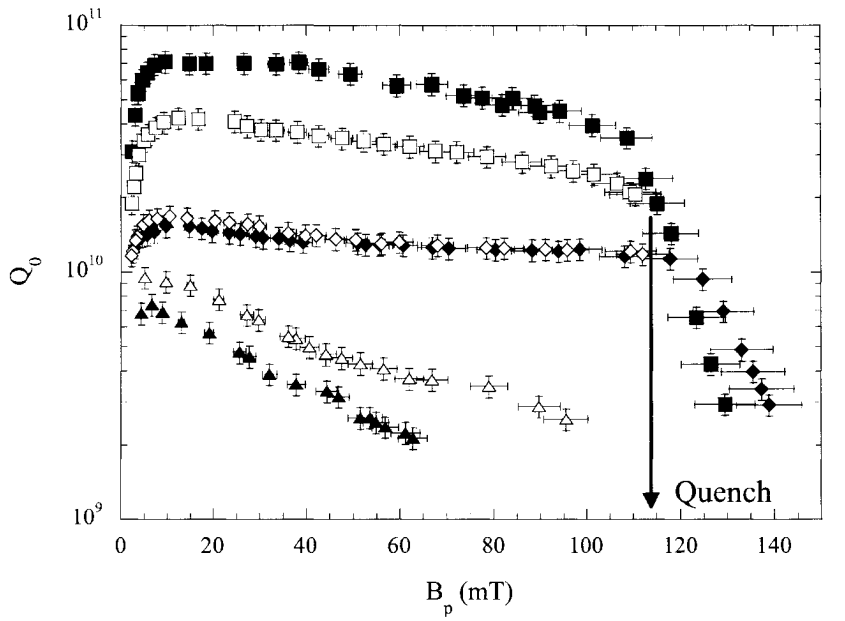

FIG. 53. Q_0 vs. B_p before (solid symbols) and after 180 °C, 48 h baking (open symbols) at three different temperatures: 1.37 K (squares), 2 K (diamonds) and 2.2 K (triangles). Some field emission was present starting at about B_p = 118 mT.

The results from the nuclear reaction analysis of niobium samples baked with the cavity compared with the unbaked samples show that the hydrogen content is significantly reduced in a surface layer of about 0.2 μm by baking (Fig. 54): the hydrogen concentration peak was reduced by as much as a factor of two. Although the results show a clear trend, the depth resolution of the method is about 5 nm and since the hydrogen peak occurs at about that depth, it is questionable whether most of the hydrogen is measured on the surface of the niobium sample rather than inside the sample. Also, the results of these measurements have to be compared with results from thermal desorption spectroscopy [85] where only about 10 ppm ($6.7\times10^{19}/cm^3$) of hydrogen were measured after heating the sample at 145 °C for 60 h.

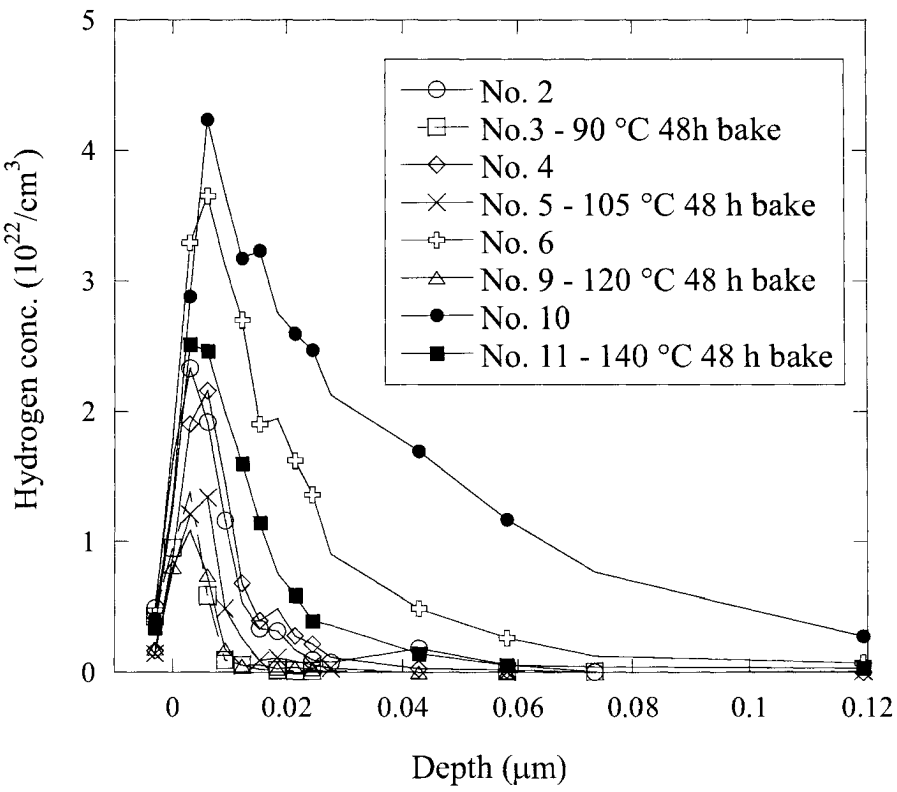

FIG. 54. Hydrogen concentration vs. depth for samples baked and not baked measured with nuclear reaction analysis method.

6.2.1 Baking at atmospheric pressure

A newly fabricated CEBAF shape single cell cavity made of *RRR* ~ 300 niobium has been used to evaluate the effect of low temperature baking at atmospheric pressure rather than under ultra-high vacuum. A layer about 130 μm thick was removed from the internal surface of the cavity by BCP 1:1:1, followed by HPR for about 1 h. A baseline test was measured at 2 K and showed high field Q-drop starting at about B_p = 87 mT. The cavity was vented to atmospheric pressure with pure nitrogen, the beam pipe blank-offs were removed and the bare cavity was placed in the oven and was baked at 120 °C for 48 h by flowing hot nitrogen.

After baking, the cavity was high-pressure rinsed for 1 h, the blank-offs with pump-out port and coupling antennas were assembled on the cavity flanges using indium wire and the cavity was evacuated to about 10^{-8} mbar prior to cool-down at 2 K. The BCS surface resistance at 4.3 K decreased by about 44% while the residual resistance increased from approximately 1 nΩ to about 11 nΩ so that the quality factor at 2 K was the same as before baking. The value of $\Delta(0\ \mathrm{K})/kT_c$ increased from 1.70 to 1.86. At high field, there was no change in the Q-drop after the baking, as can be seen in Fig. 55. The surface impedance was measured during warm-up between 7 K and 10 K and the result from the fit with the BCS theory showed that the mean free path in a 300 nm depth from the surface decreased to about 16 nm: this is the lowest value obtained in this study of the baking effect and indicates a strong impurity diffusion process.

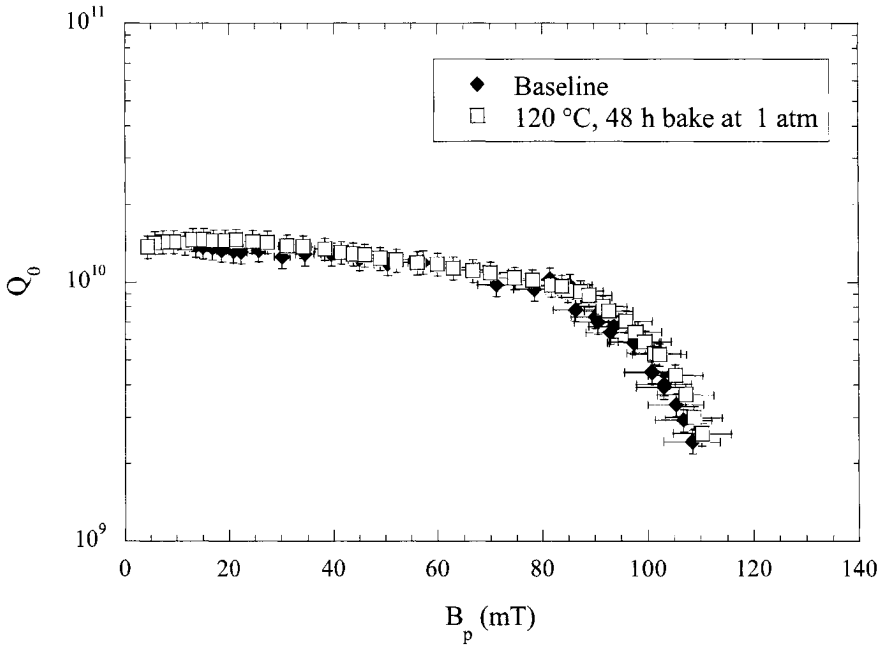

FIG. 55. Q_0 vs. B_p at 2 K before and after baking at 120 °C for 48 h at 1 atm.

Temperature maps of the cavity surface were taken during the test after baking shown in Fig. 55 and revealed few hot spots in the high magnetic field region. Figure 56 shows the temperature difference between the cavity surface and the helium bath at the highest field. The results from these maps are consistent with other measurements [86, 87], showing localized areas of larger heating, rather than uniform losses. The temperature increase as a function of the square of the peak field shows a clear exponential dependence (Fig. 57) which was common to all hot-spots. Such dependence might be explained by the surface resistance being exponentially dependent from temperature. After the cavity was disassembled, the hot spot areas were visually inspected but no surface features were noticeable.

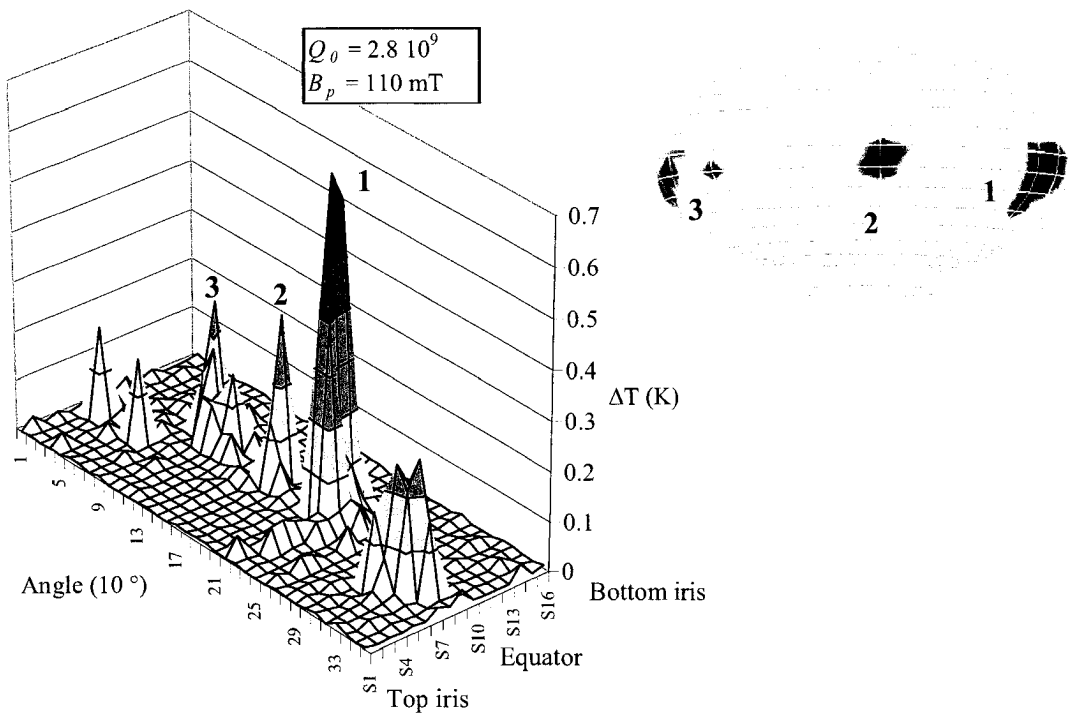

FIG. 56. Temperature map at the highest field achieved after baking (Fig. 55), showing few hot spots on the cavity surface in the high magnetic field region.

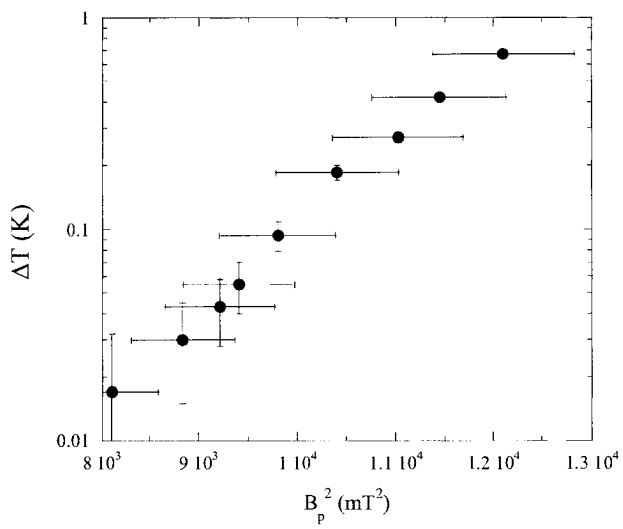

FIG. 57. Temperature rise at the hottest spot (No.1 of Fig. 56) as a function of B_p^2. The temperature of the helium bath was kept constant at 2 K (within 5 mK).

6.3 Models comparison

Surface analysis studies [76, 88, 89, 90] on niobium samples indicate that baking at progressively higher temperatures causes a conversion of the external Nb_2O_5 layer to metallic suboxides (NbO, NbO_2) and an overall reduction of the oxide layer thickness due to oxygen diffusion in the niobium. The rf measurements reported here are consistent with those results and clarify the influence of baking on the niobium material parameters.

The most evident effect of the low-temperature "in-situ" baking is the decrease of the BCS surface resistance mainly due to a reduction of the normal electrons mean free path. As can be seen from Table V, baking at 120 °C for 48 h is sufficient to reduce l(40 nm) to about 24 nm which corresponds to the theoretical minimum of the BCS surface resistance at 1.5 GHz, as explained in section 3.6.2. Increasing the baking temperature does not produce a further substantial reduction of l(40 nm) while still reduces the mean free path l(300 nm) deeper in the niobium. Consistent with these results are the (small) changes in the $\Delta(0\ \mathrm{K})/kT_c$ which shows an overall increase (about 2%) 40 nm deep and a decrease (about 1%) 300 nm deep after baking, indicating oxygen segregation in the near-surface region while up to 300 nm oxygen diffuses deeper in the niobium by baking.

These results suggest that baking at progressively higher temperatures allows oxygen to diffuse deeper in the material causing a progressive reduction of the mean free path. The fact that l(40 nm) does not decrease significantly by baking at temperatures greater than 120 °C could indicated that the oxygen concentration 40 nm from the surface has reached a saturation level.

The residual resistance generally increases by a few nanoohms by baking. The cause for this effect is not well understood but two possibilities are represented by increased oxide-metal interface losses due to oxygen diffusing into the niobium and by a higher sensitivity to the residual dc magnetic field. Measurements done on niobium samples [51] showed an increase of the Curie constant of about 50% by baking suggesting an increase of magnetic impurities.

The results on the measurements of the critical temperature show on average a decrease by 11 mK by baking. Since one atomic percent of interstitial oxygen causes a

decrease of T_c of niobium of 1 K [91, 58], the concentration of interstitial oxygen in the niobium increases by about 0.011 at. % by baking.

The *RRR* decreases for increasing oxygen concentrations by 3.5/at. % [58] and the results presented in Fig. 49 show that the oxygen concentration significantly increases over a 300 nm depth from the surface after baking at temperature greater than 120 °C. The average value of the surface *RRR* before baking indicates an oxygen concentration of 0.017 at. %, increasing up to 0.036 at. % by baking at 180 °C for 48 h, under the reasonable assumption that oxygen is the main impurity.

The results on the measurements of the near-surface hydrogen concentration, show that it is decreased by baking, in contrast with the observed variation of the niobium parameters (for example a decrease of the mean free path) which is consistent with the idea of an impurity diffusing deeper in the material. Therefore, hydrogen is ruled out as a contributor to the high field Q-drop.

The effect of baking on the surface resistance at low, medium and high rf field is discussed in the next sections.

6.3.1 Low field Q-increase

The results of the high-power rf measurements (Figs. 51-53) show that the low field Q-increase is enhanced by baking, it saturates at higher field for lower temperatures and it is reduced by higher residual resistance. The model described in section 4.6 predicts a dependence of the surface resistance inversely proportional to the square of the peak surface magnetic field. Figure 58 shows a plot of R_s as a function of B_p up to 20 mT for some tests along with fits according to the following equation:

$$R_s = \frac{a}{B_p^2} + b. \tag{122}$$

The data both before and after baking are well described by this model and the average correlation factor r^2 over twenty four fits is 0.938.

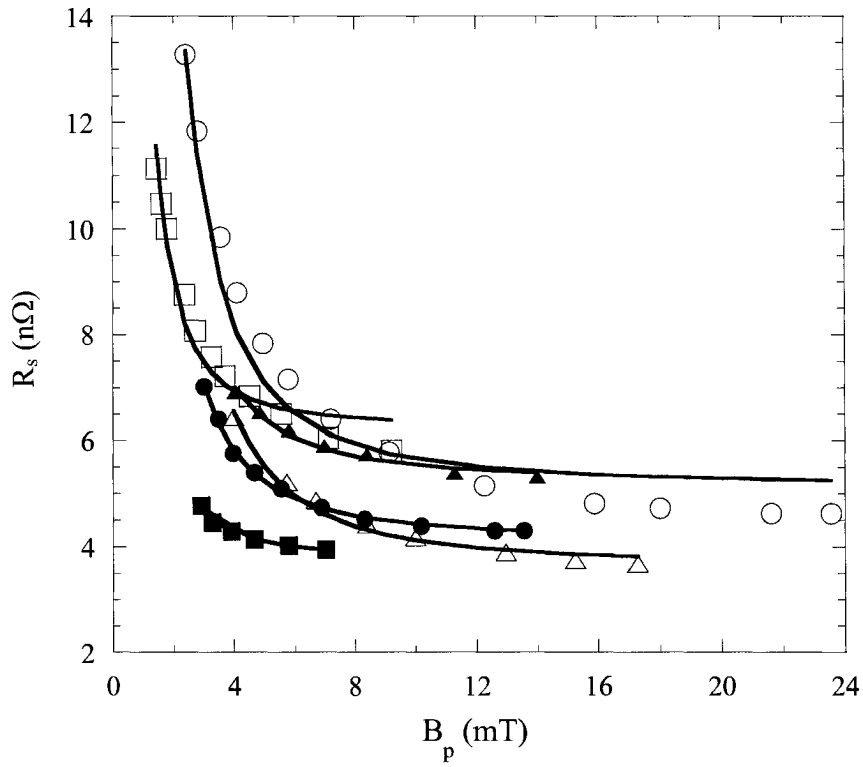

FIG. 58. Surface resistance vs. B_p at low field and 1.37 K; solid lines are fits with Eq. (121) to data before (solid symbols) and after baking (open symbols) at three different temperatures: 120 °C (triangles), 140 °C (circles) and 160 °C (squares).

The values of the fitting parameters a and b before and after baking at different temperatures, from data taken at 2 K and 1.37 K, are listed in Table VI. The parameter a is approximately independent of the baking temperature and increases by about 40% after baking. The parameter b can be identified with the value of the surface resistance at 2 K or 1.37 K, after the Q-increase saturation, it decreases by baking up to 120 °C due to the decrease of the BCS surface resistance while it increases at higher baking temperatures due to the increase of residual resistance. These trends are shown in Fig. 59 for data at 2 K and are verified at 1.37 K also.

TABLE VI. Fitting parameters a and b of the low field Q-increase model before and after baking at different temperatures obtained from data measured at 2 K and 1.37 K.

	T = 1.37 K		T = 2 K	
	a [nΩ/(mT)^2]	b (nΩ)	a [nΩ/(mT)^2]	b (nΩ)
Baseline	26.05	4.44	32.48	20.39
70 °C bake	46.26	5.10	47.01	18.44
Baseline	29.28	5.05	40.15	19.83
90 °C bake	38.51	4.96	28.62	15.89
Baseline	28.39	5.25	29.58	22.89
120 °C bake	46.27	3.66	42.92	11.31
Baseline	26.30	4.17	27.23	20.37
140 °C bake	48.15	5.17	40.22	14.14
Baseline	8.17	3.78	11.35	21.13
160 °C bake	10.98	6.25	8.96	16.33
Baseline	28.40	3.28	26.84	18.26
180 °C bake	42.16	6.27	38.80	16.00

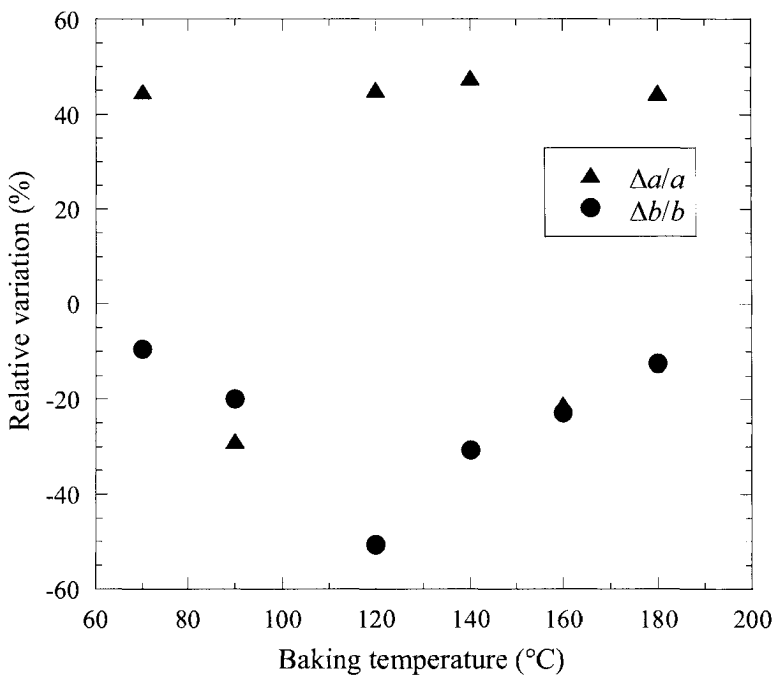

FIG. 59. Relative variation of the fitting parameters a and b by baking at different temperatures, obtained from fits of function (122) to data taken at 2 K.

Although the model is semi-qualitative, it can explain all the experimental observations:

- the quasi-particle relaxation rate is proportional to $T^{3.5}$ so that at lower temperature there is a greater mismatch between absorption and relaxation rates, resulting in an enhancement of the low field Q-increase
- after low-temperature baking oxygen diffusion and segregation forms more niobium oxide clusters, increasing the density of localized states. This effect also increases the term a/B_p^2 in (122)
- high residual resistance means a strong coupling between quasi-particles and phonons which prevents any mismatch and therefore reduces the low field Q-increase effect.

6.3.2 Medium field Q-slope

The results of the high power measurements (Figs. 51-53) show a smooth increase of the surface resistance as a function of the peak surface magnetic field typically between 15 and 80 mT. The data show that the rate of change is temperature dependent, with the minimum being at 2 K.

The plot of Q_0 vs. B_p at 2.2 K, above the superfluid helium transition temperature, typically shows a hysteretic behavior when increasing or decreasing the rf power, (Fig. 60). At the highest field, the transmitted power from the cavity, seen on the oscilloscope, has small and long (the period is about 1.5 s) oscillations. The data in Fig. 60 can be converted in a plot of the heat flux q as a function of the temperature difference between the rf surface and the helium bath (Fig. 61), showing a jump at $q \cong 2$ mW/cm^2. This value is consistent with the heat flux required for the transition from convection cooling to nucleate boiling regime [92]. In the nucleate boiling regime, bubbles start to form near the surface and help to better carry away the heat. Below 2.17 K, the cavity benefits from the excellent cooling properties of superfluid helium, yielding a smaller medium field Q-slope.

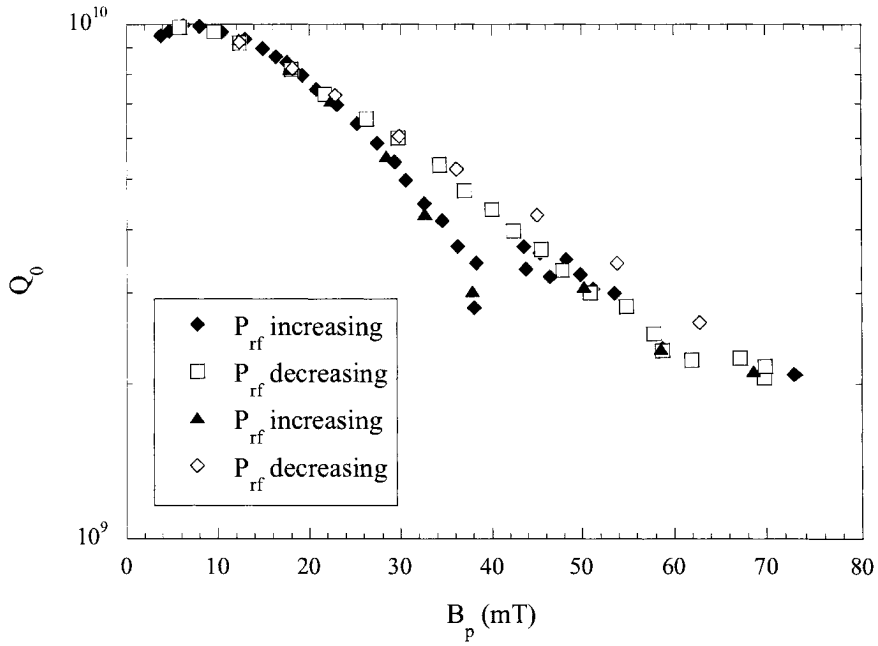

FIG. 60. Q_0 vs. B_p measured at 2.2 K after 160 °C 48 h baking, showing a hysteretic behavior when increasing and reducing the input rf power.

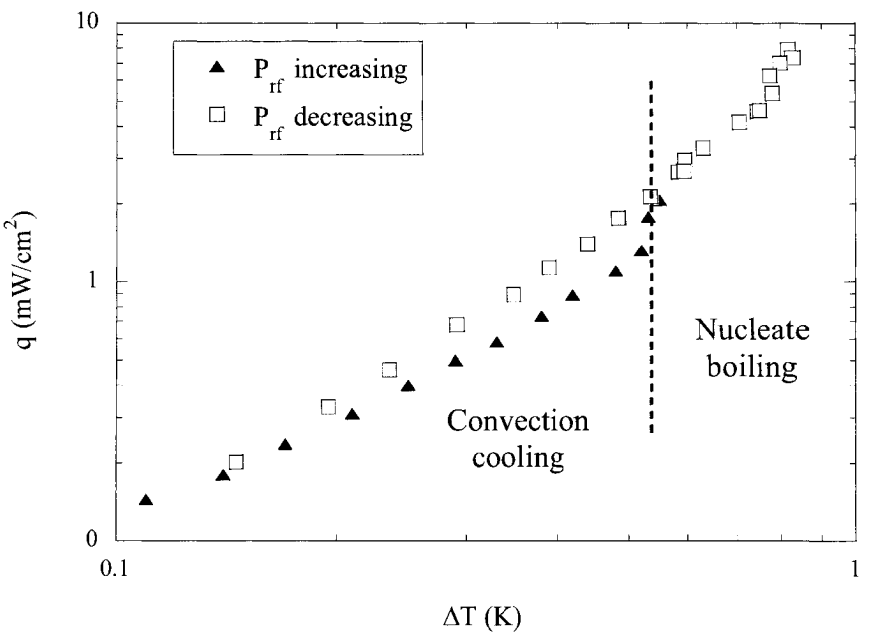

FIG. 61. Heat flux as a function of rf surface-helium ΔT showing the transition from convection cooling to nucleate boiling at $q \cong 2$ mW/cm^2. Data from Fig. 60.

A plot of the surface resistance as a function of B_p in the medium field range often shows a linear or quadratic behavior. The data have been fitted with the quadratic dependencies given by Eq. (82) and (84), and with a linear dependence. The average fit correlation factors are given in Table VII and show that Eq. (82) is best at 1.37 K and 2.2 K while the linear dependence is better at 2 K.

TABLE VII. Average correlation factors for the models describing the medium field Q-slope at three different temperatures before and after baking. The best values for each temperature are highlighted in bold.

		Before baking	
Model	Avg. r^2 (2.2 K)	Avg. r^2 (2 K)	Avg. r^2 (1.37 K)
Quadratic	**0.958**	0.900	**0.973**
Linear	0.931	**0.966**	0.964
Global heating	0.669	0.696	0.887
		After baking	
Model	Avg. r^2 (2.2 K)	Avg. r^2 (2 K)	Avg. r^2 (1.37 K)
Quadratic	**0.974**	0.874	**0.974**
Linear	0.952	**0.952**	0.954
Global heating	0.783	0.631	0.810

The data at 2.2 K show a strong slope consistent with a quadratic dependence of R_s as a function of B_p due to overheating because of the poorer cooling properties of He I. The average value of the slope γ^* before and after baking is 13.7 ± 0.2 and 19.5 ± 0.2 respectively.

A possible explanation for a linear dependence of the surface resistance from the rf field is given by hysteresis losses as proposed by Halbritter for niobium films and high-temperature superconductors [93, 94]. During the oxidation of niobium, crack corrosion forms oxide channels, especially along grain boundaries or surface defects, which create "islands" of size a_J connected by "weak links". Although for bulk niobium it is more

adequate to refer to "strong links", since the junction's critical current density is several orders of magnitude higher ($J_{cJ} \approx 10^{11}$ A/m^2) than for thin films or HTS, Josephson fluxons start to penetrate in the material at a field B_{c1J} given by [95]

$$B_{c1J} = \frac{2\Phi_0}{\pi^2 d_J \lambda_J} \cong 30\,\text{mT}, \tag{123}$$

which is close to the starting field for the medium field Q-slope. d_J and λ_J were defined in Sec. 4.2.3. Josephson fluxons are extended along the islands boundary and, differently from Abrikosov fluxons which penetrate above B_{c1}, they nucleate without any surface barrier, have an insulator as "flux core" and their energy is mostly electromagnetic. According to Halbritter [91], they cause hysteresis losses R_{hys} given by

$$R_{hys}\left(B_p\right) \approx \frac{4}{3\pi} \frac{\omega}{J_{cJ}\left[1+\left(\omega/\omega_0\right)^2\right]^{3/2}} \frac{\lambda}{a_J} B_c \left(\frac{B_p}{B_c}\right) = R^1_{res}\left(\frac{B_p}{B_c}\right), \tag{124}$$

where ω_0 ($\cong$ 5 GHz) is a characteristic nucleation frequency. R_{hys} is temperature independent for $T < T_c/2$. Equation (124) is valid for $a_J >> \lambda$. A schematic representation of "strong links" in niobium is given in Fig. 62 along with all the characteristic lengths.

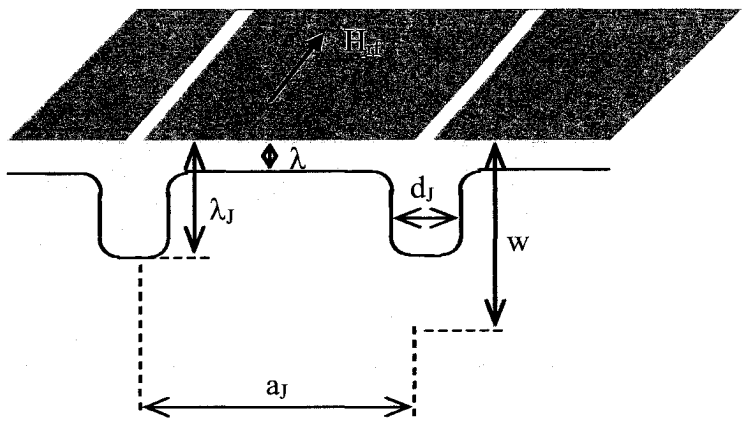

FIG. 62. Characteristic lengths of "strong-links" in niobium. Typically $\lambda_J = 0.18$ μm, $a_J =$ 10-100 μm, $w = 0.01$-0.1 μm and $d_J = 0.082$ μm.

Halbritter also suggested that weak-links caused by niobium-hydride precipitates are a possible cause of hysteresis losses [96] as seen on cavities affected by "Q-disease" discussed in section 4.2.2. The dependence given by Eq. (124) has also been measured on cavities coated with a niobium thin film and values of $R_{res}{}^{1}$ between 100-1000 nΩ [97] were obtained.

The data for the medium field Q-slope have been analyzed using the following expression for the field and temperature dependence of the surface resistance, which includes Eq. (86) and (124):

$$R_s\left(T,B_p\right)=R_{s0}\left(T\right)+R_{res}^{1}\left(\frac{B_p}{B_c}\right)+R_{s0}\left(T\right)\gamma^*\left(T\right)\left(\frac{B_p}{B_c}\right)^2, \tag{125}$$

where $R_{s0}\left(T\right)=R_{BCS}\left(T,15\,\mathrm{mT}\right)+R_{res}$. The fitting parameters are R_{s0}, γ^* and $R_{res}{}^{1}$. The critical field is set to be B_c = 200 mT. Table VIII shows the average values of the low field surface resistance (R_{s0}) and of the linear ($R_{res}{}^{1}$) and quadratic (γ^*) coefficients from a fit of the data at 2 K and 1.37 K, before and after baking at different temperatures.

TABLE VIII. Average values of the fit parameters of Eq. (125) and fit correlation factor r^2 obtained from a comparison with R_s vs. B_p data at 2 K and 1.37 K, before and after baking at different temperatures.

	T = 2 K	
	Before baking	After baking
R_{s0} (nΩ)	21.6 ± 0.1	15.2 ± 0.2
$R_{res}{}^{1}$ (nΩ)	11.6 ± 1.1	20.2 ± 1.9
γ^*	0.04 ± 0.10	0.10 ± 0.24
r^2	0.952	0.950
	T = 1.37 K	
	Before baking	After baking
R_{s0} (nΩ)	4.81 ± 0.03	4.82 ± 0.06
$R_{res}{}^{1}$ (nΩ)	2.27 ± 0.31	4.39 ± 0.47
γ^*	1.36 ± 0.14	1.46 ± 0.17
r^2	0.982	0.988

The linear coefficient R_{res}^{1} is smaller at lower temperatures and is increased by about a factor of two by baking. The quadratic coefficient γ^* is higher at lower temperature, although was not determined accurately at 2 K, and increases slightly by baking. Figure 63 shows the relative variation of the linear and quadratic coefficients at 2 K and 1.37 K respectively due to baking as a function of the baking temperature, showing the highest increase between 120 °C and 140 °C.

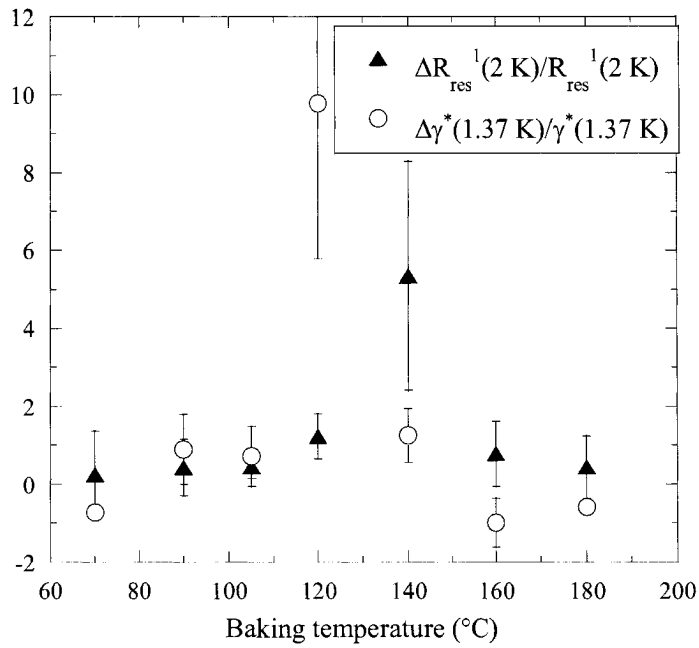

FIG. 63. Relative variation of the linear (R_{res}^{1}) and quadratic (γ^*) fitting coefficients for the medium field Q-slope after baking as a function of baking temperature.

A theoretical estimate of the linear coefficient with Eq. (124) for strong-links due to oxides yields about 20 nΩ (temperature independent) for an island size a_J = 2 mm and J_{cJ} = 7×10^{11} A/m^2, in good agreement with the value obtained from the fit at 2 K. The linear slope due to hydrides was measured to be between 6 and 169 nΩ, depending on the amount of precipitate, and was also characterized by an onset field much smaller ($B_{c1J} \cong 1$ mT) than for oxide strong-links [96]. Hysteresis losses are enforced by baking, most

probably due to oxygen diffusion increasing the length and quantity of the strong-links and reducing J_{cJ}, supporting the hypothesis of oxide strong-links.

A quantitative estimate of the slope γ^* can be done using Eq. (83) with parameters that best represent the cavity we tested such as a wall thickness $d = 2.8$ mm, $\Delta/kT_c = 1.85$, $T_c = 9.25$ K, $l = 300$ nm and values of thermal conductivity and Kapitza resistance of $RRR \sim 700$ niobium [99, 100]. The results are shown in Table IX for γ^* and the slope γ of equation (86) which includes the intrinsic non-linear contribution to the BCS surface resistance. The value of the quadratic coefficient obtained from the fit of the data at 2 K is in good agreement with the theoretical value of γ^*.

A possible explanation for the increase of the quadratic slope γ^* by baking is an increase of the Kapitza resistance by about a factor of two due to oxidation of the outer cavity surface. Halbritter [98] suggested a possible correlation between the medium field Q-slope and the residual resistance but no such correlation emerges from the data.

TABLE IX. Coefficients γ^* and γ of equations (83) and (86) representing the medium field Q-slope with (γ) and without (γ^*) non-linear correction.

Temperature	R_{BCS} (nΩ)	R_K (m^{2}K/W)	κ (W/m K)	γ^*	γ
2 K	14	$1.06 \cdot 10^{-4}$	30	0.16	1.63
1.37 K	0.4	$4.67 \cdot 10^{-4}$	8	0.04	0.26

The cause of the discrepancy between the values of the linear and quadratic coefficients at 1.37 K predicted by the models and obtained from the data fit are not clear. For example, the BCS surface resistance at 1.5 GHz and 1.37 K is about one order of magnitude smaller than the residual resistance and therefore the observed field dependence due to overheating is minimal, as shown by the γ^* values in Table IX. The comparison of Table XI with the measurement results at 1.37 K could therefore be an indication of a quadratic field dependence of the residual losses. Figure 64 shows the

surface resistance as a function of B_p/B_c in the medium field range at 2 K before and after baking at 120 °C along with a fit with Eq. (125).

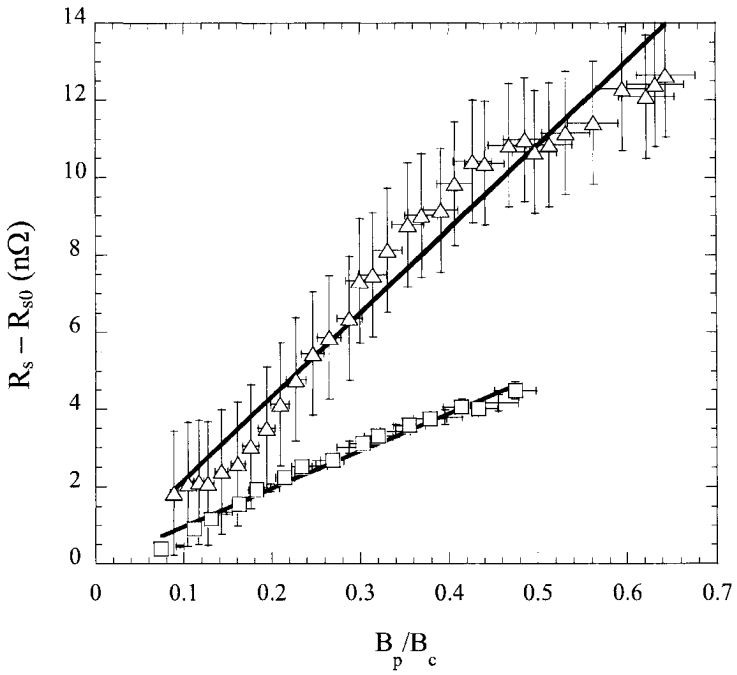

FIG. 64. Increase of the surface resistance at 2 K as a function of B_p/B_c in the medium field range before (squares) and after baking at 120 °C, 48 h (triangles) fitted with Eq. (125) (solid lines).

6.3.3 High field Q-drop

The high field Q-drop discussed in section 4.8 was the limitation of three rf tests, shown in Figs. 51-53. The Q-drop onset is approximately temperature independent. These high field losses are strongly reduced by baking at 120 °C and the maximum field increases by about 12%. Baking at higher temperatures causes a quench at lower field. These results are consistent with published data [11, 73].

The experimental data have been compared with the models described in section 4.8:

- ITE model: the electric surface resistance R_s^E is obtained subtracting the heating term from the measured surface resistance as follows:

$$R_s^E = \frac{R_s}{1+\gamma^*\left(B_p/B_c\right)^2} - R_{s0}. \tag{126}$$

R_{s0} is the surface resistance at low field, where the electric component is negligible. According to the model, the high field Q-drop is due to an electric surface resistance with the following exponential dependence to the peak surface electric field

$$R_s^E = b\left(e^{-c/E_p} - e^{-c/E_0}\right) \tag{127}$$

where b, c and E_0 are fitting parameters.

- MFE model: the data are compared with the model as described in section 4.8.2. The center β_0 and the width σ of the distribution of field enhancement factors are used as fit parameters.
- TI model: the data are compared with the model as described in section 4.8.4. Thermal conductivity and Kapitza resistance are used as fitting parameters.

The results of the fit of the ITE model with the data show an excellent agreement (Fig. 65) both at 2 K and 1.37 K and the average fit correlation factor is 0.999. The ITE model explains the improvements by baking as due to a reduction of the oxide thickness with a consequent decrease of density of localized states n_L and of the electric surface resistance as given by Eq. (87).

The MFE model also gives a good description of the experimental data as can be seen in Fig. 66, where the Q_0 data as a function of B_p in the high field region are plotted with the fits to the model. Nevertheless, two major drawbacks are the fact that it does not explain the improvement by the low-temperature baking (which does not change the surface roughness) and the fact that the Q-drop is present in cavities treated with electropolishing which gives smoother surfaces [76, 86]. The average grain boundary length for the MFE model calculation was set to 1 mm, appropriate for a cavity which had been post-purified.

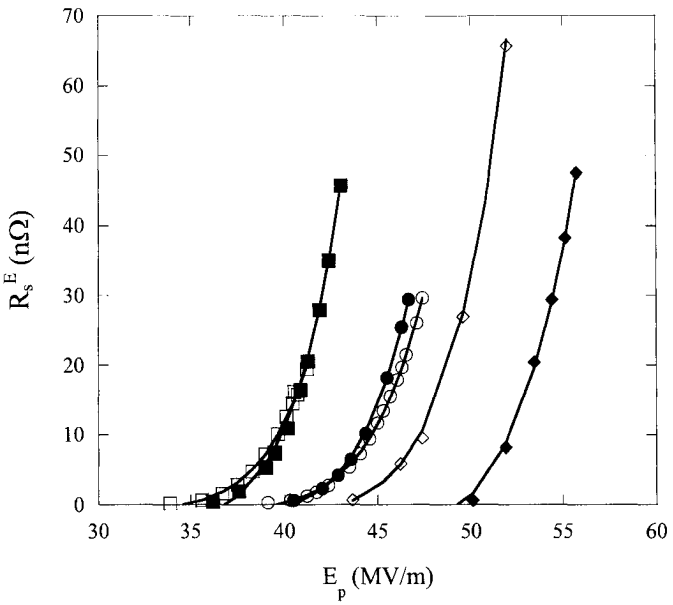

FIG. 65. Electric surface resistance from three different rf tests at 2 K (solid symbols) and 1.37 K (open symbols) fitted with Eq. (127) (solid lines).

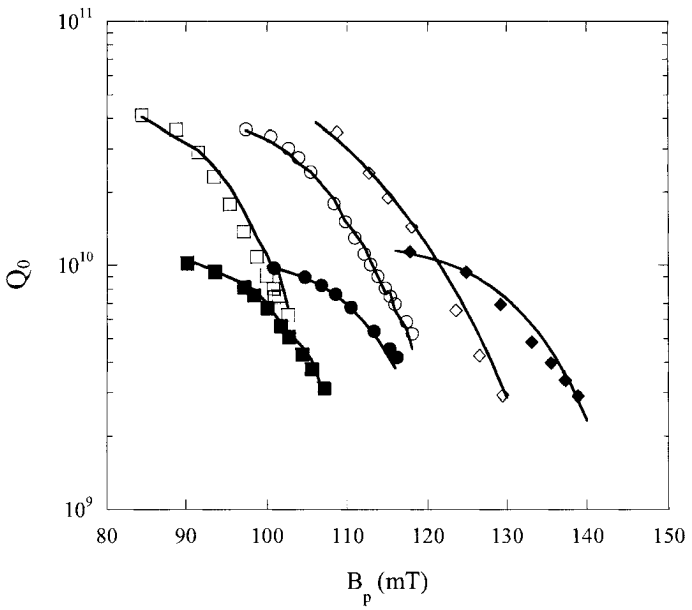

FIG. 66. Quality factor as a function of the peak surface magnetic field in the Q-drop region fitted with the MFE model (solid lines) at 2 K (solid symbols) and 1.37 K (open symbols).

The TI model does not fit the high field Q-drop data: using the same values for the thermal properties of niobium as used for the medium field Q-slope analysis, the thermal instability model does not predict a sharp Q-drop at about 100 mT. Using smaller values of thermal conductivity and Kapitza conductance, the medium field slope increases and only a smooth drop shows at fields higher than the measured onset. The data at 2 K and 1.37 K before baking of Fig. 51 are shown in Fig. 67 with the curves obtained from the TI model with and without the non-linear correction.

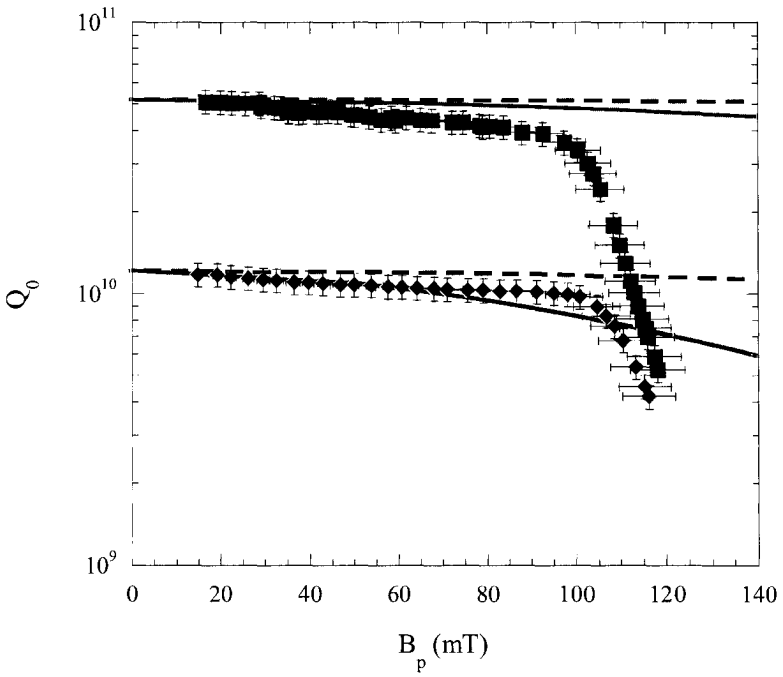

FIG. 67. Q_0 vs. B_p from Fig. 45 at 1.37 K (squares) and 2 K (diamonds) fitted with the TI model with (solid line) and without (dashed line) non-linear correction using the thermal properties in Table IX.

Table X shows the values of the fit parameters b, c and E_0 for equation (126) of the ITE model, and the parameters β_0 and σ for the MFE model. The theoretical value of c from the model is of the order of 450 MV/m, while the average value of β_0 for BCP treated surfaces is about 1.5 [14]. The 6% difference in the value of β_0 and 25% in the

value of σ between 2 K and 1.37 K for the data shown in Fig. 47 could be due to the presence of some field emission.

The shielding of the Earth's magnetic field had been reduced in order to investigate the influence of flux trapping on the high field Q-drop. The cryostat used for cavity testing is wrapped with μ-metal sheets and a compensation coil, reducing the Earth's magnetic field to a few milligauss to have minimal residual resistance due to flux trapping as explained in section 4.2.1. By changing the current in the compensation coil, different values of the residual field are obtained. In the test before 160 °C baking, the cavity was warmed up to 12 K (above T_c) and the current in the compensation coil was reduced. The cavity was then cooled-down and tested at 2 K and 1.37 K. This operation was repeated three times and the results at 1.37 K are shown in Fig. 68. The data suggest that the trapped flux changed neither the Q-drop onset nor its steepness but it only increased the residual resistance.

TABLE X. Fitting parameters for the ITE and MFE models obtained from Q-drop data shown in Figs. 51-53.

	ITE Model			MFE Model	
	b (Ω)	c (MV/m)	E_0 (MV/m)	β_0	σ
Fig. 45, 2 K	1.34	820	40.5	1.64	0.0062
Fig. 45, 1.37 K	0.52	789	39.5	1.62	0.0062
Fig. 46, 2 K	0.57	700	36.9	1.79	0.0069
Fig. 46, 1.37 K	0.30	679	34.7	1.81	0.0070
Fig. 47, 2 K	1.49	956	49.5	1.40	0.0056
Fig. 47, 1.37 K	3.25	919	43.1	1.49	0.0070

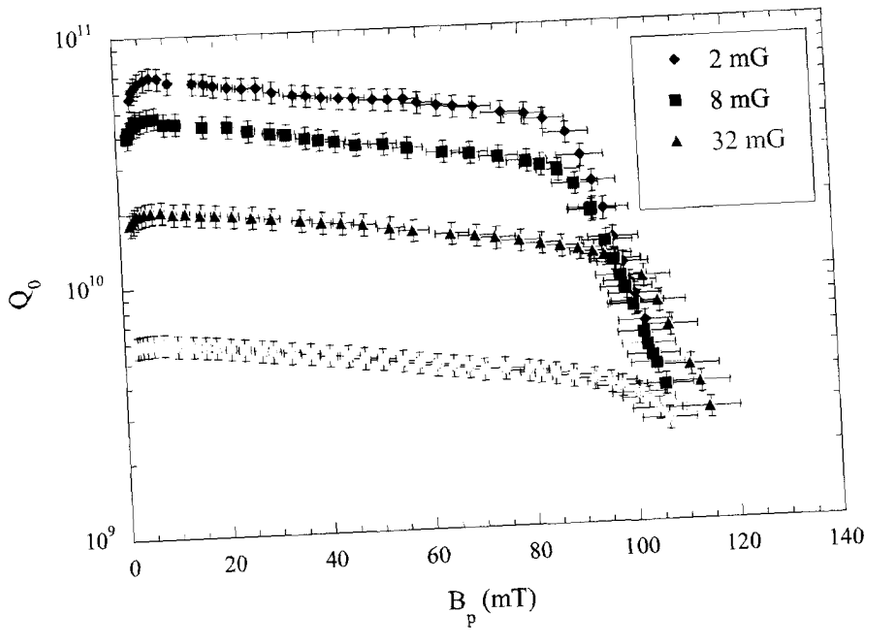

FIG. 68. Q_0 vs. B_p at 1.37 K with different values of residual dc magnetic field.

CHAPTER 7

MEASUREMENTS OF TE_{011} AND TM_{010} MODES

7.1 Introduction

A fundamental question regarding the origin of the high field Q-drop is whether it is caused by an intense electric field, as suggested by the Interface Tunnel Exchange model, or by a magnetic field, as indicated by the Magnetic Field Enhancement model. One possible way to answer this question is to measure the quality factor at high rf fields of a single cell cavity excited in the TE_{011} and TM_{010} modes.

Differently from the TM_{010} mode, which is used for particle acceleration and where the Q-drop had been observed, the TE_{011} mode has only magnetic field on the cavity surface, ruling out any effect of electric field on the surface resistance. Using input and pick-up loop couplers with the proper geometry and orientation it is possible to achieve good coupling to both modes and measure Q_0 vs. B_p without having to open the cavity to atmosphere and therefore maintaining the same surface conditions. The following sections will present a description of the characteristics of the TE_{011} mode compared to the TM_{010} mode, the experimental setup and the measurement results.

7.2 TE_{011}- and TM_{010}-mode characteristics

Figure 69 shows the distribution of the electric and magnetic fields of the TM_{010} mode and of the magnetic field of the TE_{011} mode on the surface of a single cell cavity with the original geometry used in the CEBAF accelerator. The calculations have been done with the 2D code SUPERFISH v.7 and only a quarter section of the cavity is shown due to its symmetry. Figure 70 shows a vector plot of the TE_{011} mode magnetic field in the cavity which is orthogonal to the azimuthally oriented magnetic field in the TM_{010} mode.

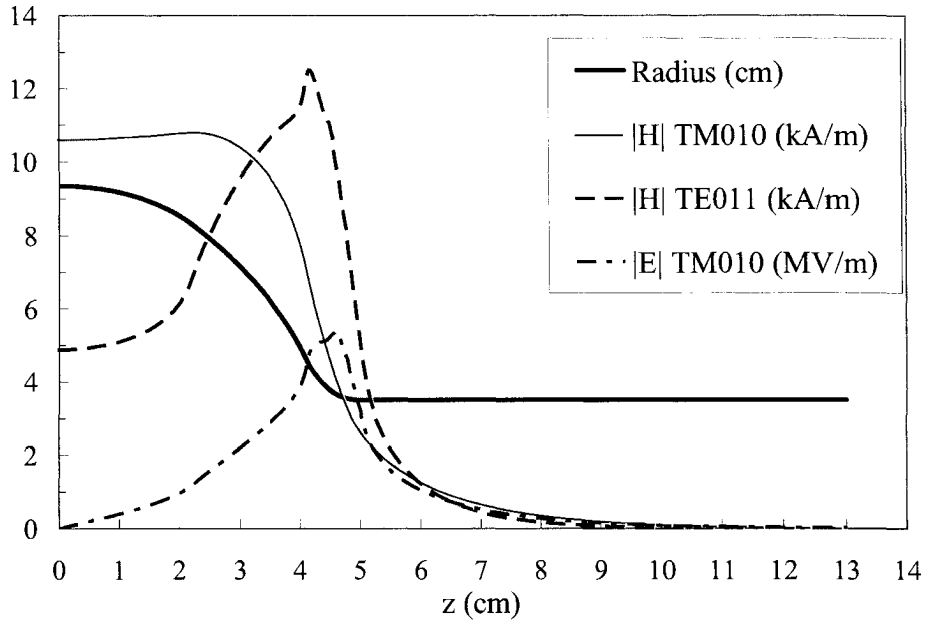

FIG. 69. Surface fields for the TE_{011} and TM_{010} modes for 50 mJ cavity stored energy.

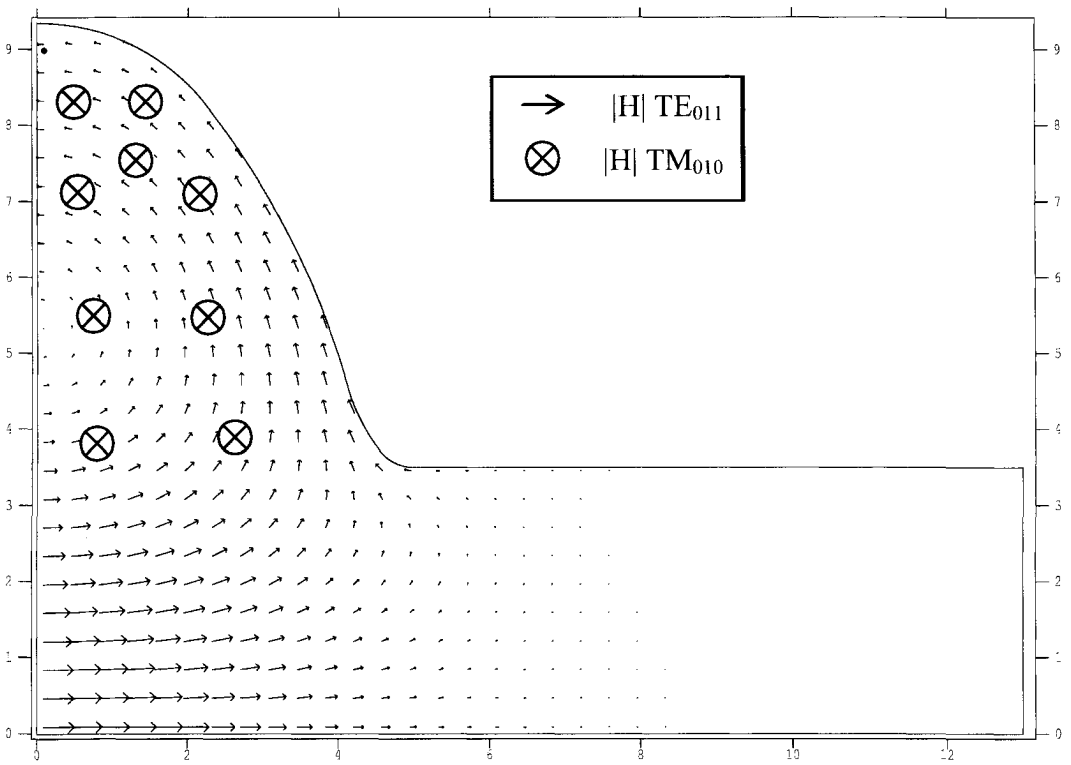

FIG. 70. Vector plot of the magnetic field in the TE_{011} mode compared with the field in the TM_{010} mode.

The peak surface magnetic field in the TM_{010} mode is located approximately 2.5 cm from the equator while the maximum in the TE_{011} mode is about 1 cm from the iris. The distribution of the surface magnetic field can be seen also in Fig. 71, which is a 3D simulation of half-cavity done with the code HFSS v.9 to evaluate the perturbation introduced by the side-ports welded perpendicular to the cavity beam pipes and used to insert the loop couplers.

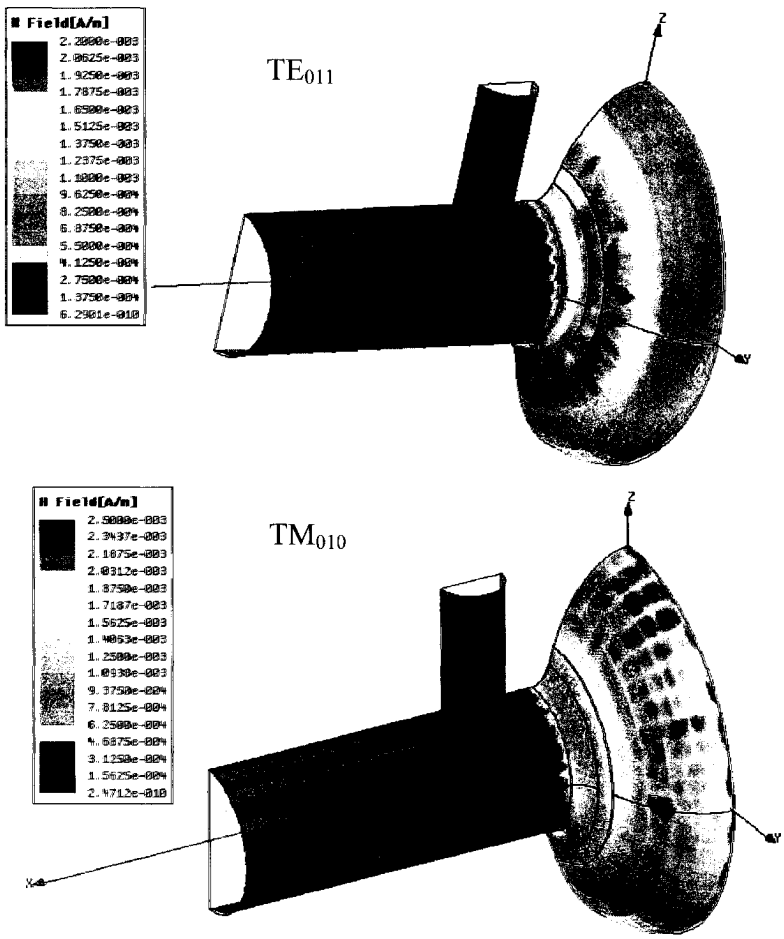

FIG. 71. Surface magnetic field distribution for the TE_{011} and TM_{010} modes in a 3D model of half-cavity with side-ports (see text for explanation).

Table XI shows the main parameters of the two modes. The resonant frequency of the TE_{011} mode is almost a factor of two higher than in the TM_{010}, which results in almost four times higher surface resistance ($R_s \propto f^2$). Nevertheless, the geometry factor is about a factor 2.5 smaller in the TM_{010}, which brings the value of the quality factor at 2 K close to about 10^{10} for both modes. The cavity effective area, defined by Eq. (91), is also smaller in the TE_{011} mode, corresponding to a higher heat flux than in the TM_{010} mode.

TABLE XI. Electromagnetic parameters for the TE_{011} and TM_{010} modes for a CEBAF type single cell cavity calculated with SUPERFISH.

	TM_{010}	TE_{011}
Frequency (MHz)	1467	2824
$G = R_s Q_0$ (Ω)	273	701
$E_p/\sqrt{U}$ (MV/m/$\sqrt{\text{J}}$)	17	0
$B_p/\sqrt{U}$ (mT/$\sqrt{\text{J}}$)	43	50
A_{eff} (m^2)	0.0586	0.0320

7.3 Experimental setup and procedure

The cavity used for these experiments was made by deep drawing half-cell cups from high *RRR* ($\approx$ 300) niobium. Two niobium beam pipes 17 cm long were rolled and electron beam welded (EBW). A nipple was pulled through a hole in each beam pipe and a tube (1.25" ID) with Nb55Ti 2 ¾" Conflat®-style flange welded at one end was joined to the beam pipe. Nb55Ti flanges [77] were welded on the beam pipes which were then welded at the iris of each half-cell. Finally, the equators of the two half-cell assemblies were electron beam welded. Figure 72 shows a sketch of the cavity.

Copper gaskets were used for the Nb55Ti 2 ¾" Conflat®-style flanges while $AlMg_3$ gaskets with stainless steel flanges were initially used to seal the cavity beam pipes. Although Nb55Ti Conflat®-style flanges are not commonly used on niobium cavities, they proved to be very reliable, being leak-tight after about twenty cool-down cycles from room temperature to 2 K.

After the first experiment, the quality factor of the TE_{011} mode at 2 K was significantly lower (1×10^9) than expected. It was discovered that the cause of the low Q was due to excessive rf power dissipated on the stainless steel beam pipe flanges. Although a 2D simulation of the cavity (without side-ports) with SUPERFISH predicted very low field at the flange location (corresponding to $Q_{ext} \cong 10^{12}$), a 3D simulation with HFSS showed that the presence of the side-ports distorts the exponential decay of the rf field in the beam pipe, such that the Q_{ext} of the stainless steel flanges would be about 2.5×10^9, consistent with the measured value. To solve this problem, niobium flanges with a recess to fit the cavity flanges have been used and the surfaces were sealed with 1.5 mm thick indium wire. This configuration uses superconducting flanges with lower dissipated power.

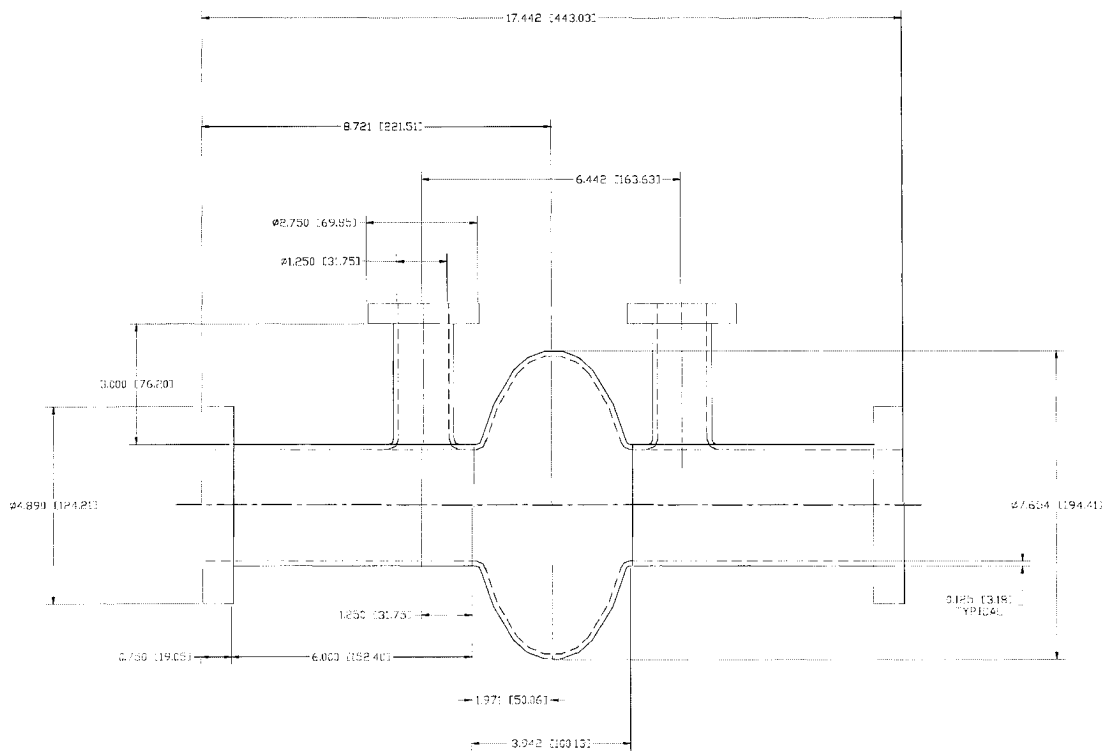

FIG. 72. Sketch of the single cell cavity used for the TE_{011}/TM_{010} measurements. Dimensions are in inches [millimeters].

The TM_{010} and TE_{011} modes are excited with a magnetic loop coupler inserted in the cylindrical side-port close to the cavity iris. The pick-up coupler is also a magnetic loop inserted in the side-port close to the other iris of the cavity. The sizes of the loops and their orientation have been determined experimentally; the best orientation to couple both modes is the one with the plane of the loop parallel to the cavity equatorial plane. Figure 73 shows a drawing and a picture of both couplers. The Q_{ext} of the input coupler is about 2×10^{10} for the TM_{010} mode and 1×10^{10} for the TE_{011} mode while the Q_{ext} of the pick-up coupler is about 7×10^{10} for the TM_{010} mode and 4×10^{10} for the TE_{011} mode.

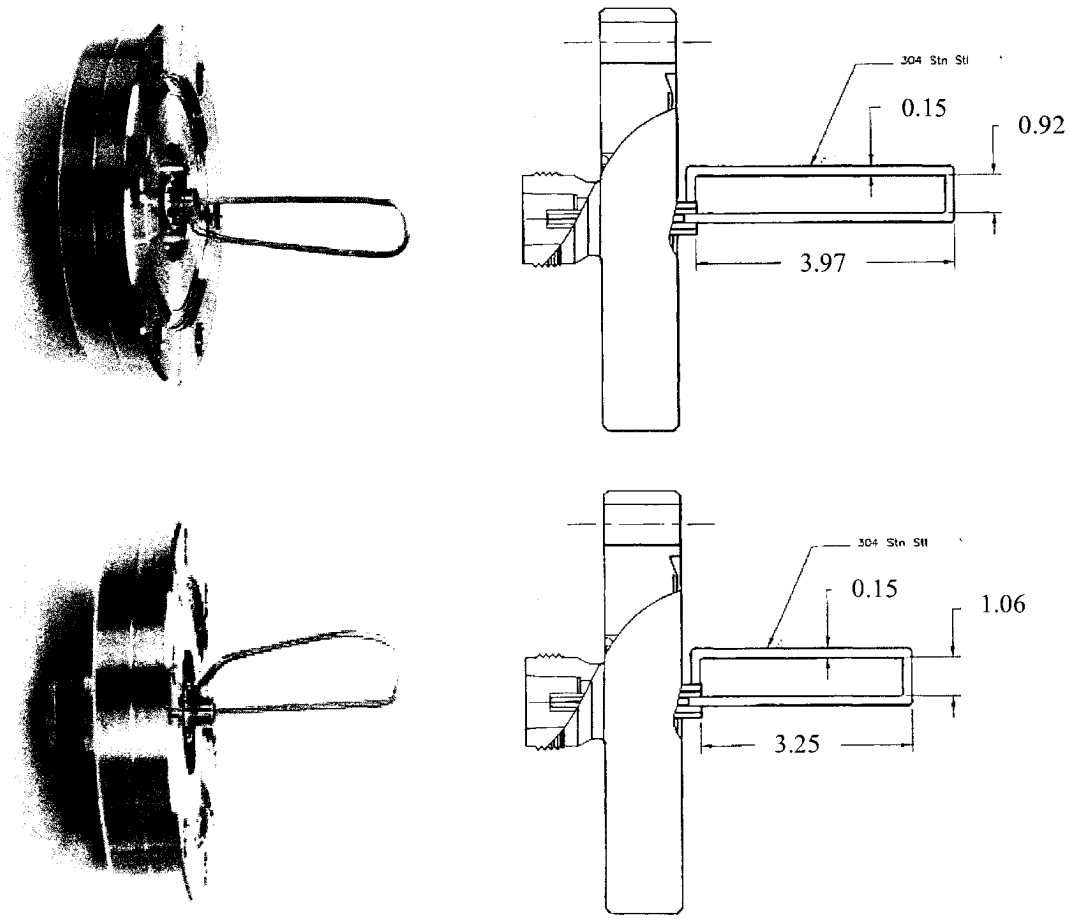

FIG. 73. Pictures (right) and drawings (left) of the input (top) and output (bottom) loop couplers used to excite the TE_{011} and TM_{010} modes. Dimensions are in centimeters.

The standard cavity preparation for rf test at 2 K consists of

- Ultrasonic cleaning for 20 min.
- BCP 1:1:1 at 25 °C or 1:1:2 at 15 °C removing about 20 μm of niobium from the inner cavity surface, after initial removal of about 130 μm.
- HPR with ultra-pure water at a pressure of 80 bar for 1 h.
- Drying overnight in class 10 clean room.
- Assembly of beam pipe niobium flanges and couplers in class 10 clean room
- The cavity is attached to a test stand and evacuated to ~ 10^{-8} mbar prior to cool-down at 2 K.

The temperature dependence of the surface resistance between 4.3 K and 1.9 K and the quality factor as a function of the peak surface magnetic field at 2 K is measured for both modes. Figure 74 shows a picture of the cavity assembled on the test stand.

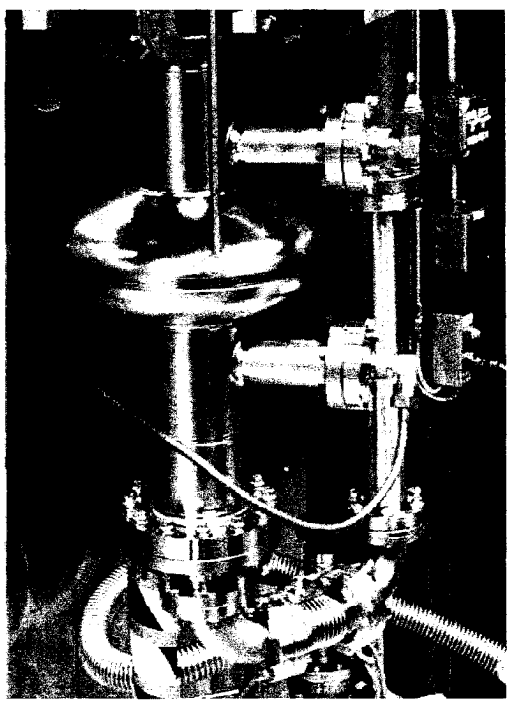

FIG. 74. Single cell cavity used for TE_{011} and TM_{010} measurements attached to the vertical test stand.

7.4 Experimental results

During two high-power rf tests at 2 K, the high field Q-drop was observed in the TE_{011} mode starting at about $B_p \approx 100$ mT, but unfortunately in the TM_{010} mode strong field emission was encountered. After a new surface preparation, a Q-drop at 2 K starting at about $B_p \approx 90$ mT was observed in both modes, in absence of field emission. After the test the cavity was placed in the oven for the 120 °C "in-situ" bake-out, but during that process a leak developed (the melting point for indium is about 150 °C). The cavity was then soaked in nitric acid for about one hour to dissolve any indium droplet that might have ended up in the cavity followed by a new chemical etching with fresh BCP 1:1:1 acid. The results of the high-power rf test at 2 K were very similar to the previous test: the Q dropped in both modes starting at about $B_p \approx 100$ mT.

The cavity was baked in the cryostat up to 100 °C for about 40 h with a resistive heater placed at the bottom of the dewar. Due to the limited power of the heater and the large volume of the dewar, the ramp-up time was about 15 h and the cool-down time was about 17 h. This baking procedure differed from the tests described in chapter 6 that the surrounding gas was helium instead of a nitrogen/air mixture.

Figure 75 shows the result of the test at 2 K in the TM_{010} and TE_{011} mode before and after baking. After bake-out, the TM_{010} mode was measured first and the maximum field increased up to 125 mT but the Q-drop is still present. A brief multipacting activity along with few quenches was found at about $B_p = 100$ mT which lowered the quality factor most probably due to flux trapping [101]. The test on the TE_{011} mode showed a quench at about $B_p = 80$ mT, significantly lower than before baking. We suspect that the breakdown events occurred in the test of the TM_{010} mode might be related to this quench. The BCS surface resistance decreased by about 30% in the TM_{010} mode and 20% in the TE_{010} mode by baking while the residual resistance increased by about 3 nΩ. Figure 76 shows a plot of R_s vs. $1/T$ between 4.3 K and 1.9 K.

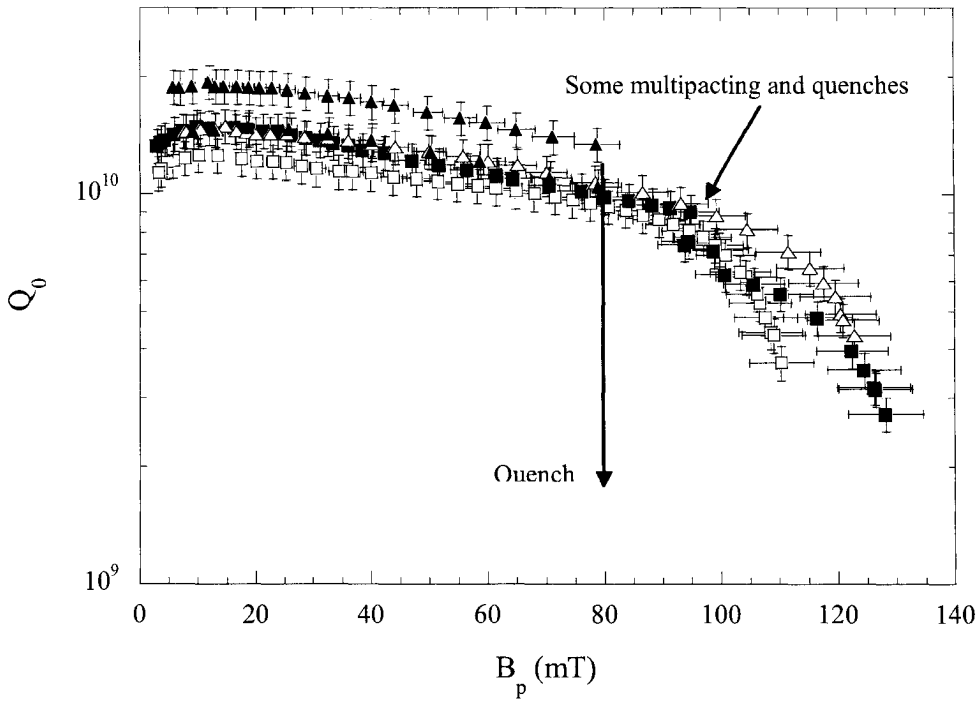

FIG. 75. Q_0 vs. B_p in the TM_{010} mode (squares) and TE_{011} mode (triangles) at 2 K before (open symbols) and after baking at 100 °C for about 40 h (solid symbols).

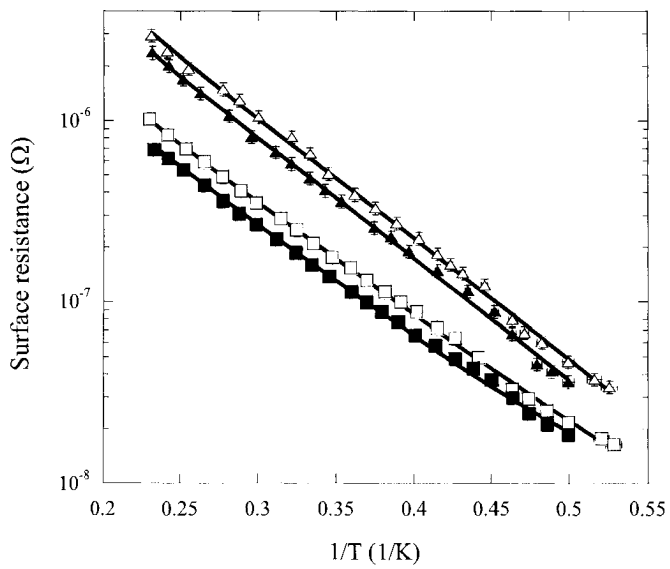

FIG. 76. R_s vs. $1/T$ for the TM_{010} (square) and TE_{011} modes (triangles) before (open symbols) and after (solid symbols) baking at 100 °C for about 40 h. Data points are fitted with the BCS theory plus residual resistance (solid lines).

The cavity had a new surface preparation with BCP 1:1:2 and the results of the rf test at 2 K were very similar to the previous test. The Q-drop was observed in both modes in absence of field emission starting at about B_p = 92 mT in the TM_{010} mode and B_p = 107 mT in the TE_{011} mode. The cavity was baked in the oven with hot nitrogen at 100 °C for 48 h and the following rf test showed an improvement (≈ 12%) in the maximum field in the TM_{010} mode and a slight improvement of the Q_0 at high field in the TE_{011} mode, quenching at B_p = 130 mT. The low-field BCS surface resistance decreased by about 30% in both modes while the residual resistance increased by about 5 nΩ by baking. Figure 77 shows a plot of Q_0 vs. B_p for both modes before and after baking. The cavity was baked again with hot nitrogen at 120 °C for 48 h and the rf test at 2 K showed no improvement in the TM_{010} mode and a quench at lower field (B_p = 95 mT) in the TE_{011} mode.

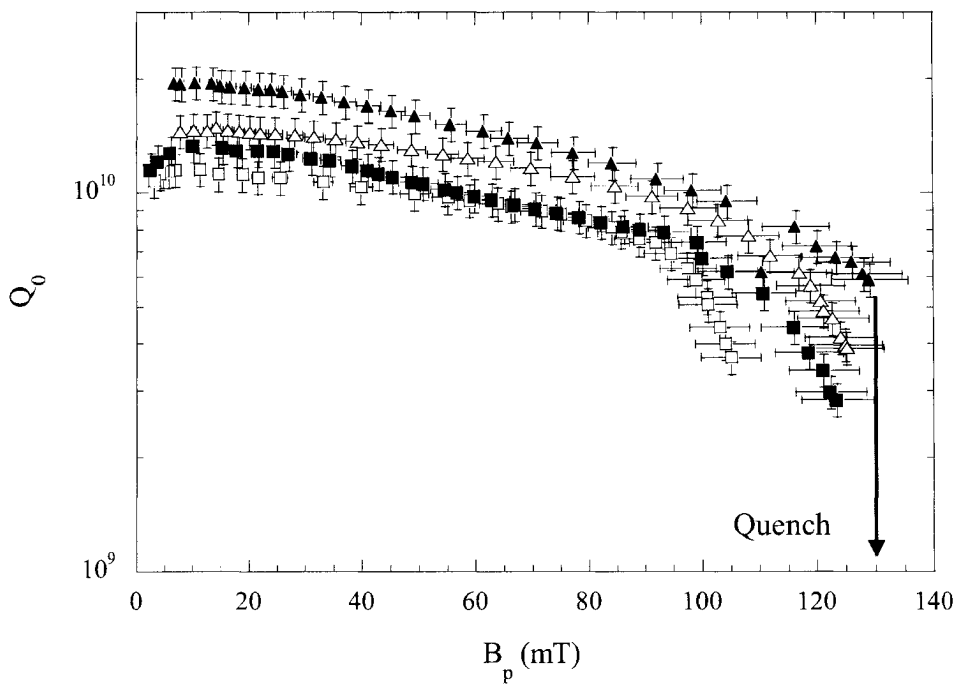

FIG. 77. Q_0 vs. B_p in the TM_{010} mode (squares) and TE_{011} mode (triangles) at 2 K after a new surface preparation (open symbols) and after baking at 100 °C for about 48 h (solid symbols).

After the rf tests, the inner surface of the cavity was visually inspected and two "features" of a millimeter size were seen on the walls, in the area of high magnetic field for the TE_{011} mode. Since they were suspect to be the cause of the premature quenches, they were mechanically ground away with a carbide tool.

7.4.1 Anodization

After a new chemical etching of about 50 μm with BCP 1:1:1, the cavity was anodized by filling it with ammonium hydroxide (NH_3OH) 30% diluted and applying a voltage between the cavity (anode) and a niobium rod (cathode) inserted in the cavity. This process grows a niobium pentoxide layer on the cavity surface at a rate of about 2 nm/V, according to the following equation [102]:

$$2Nb + 5OH^- \rightarrow Nb_2O_5 + 5H^+ + 10e^- . \qquad (128)$$

The current density is about 1 mA/cm^2 and the voltage is applied until the current drops to about 10% of the initial value. The cavity was processed at 45 V, 1 A growing a Nb_2O_5 layer about 90 nm thick (about fifty time thicker than the natural oxide grown without anodization).

The rf test at 2 K did not show a significant difference from the previous ones: the Q-drop starts at about B_p = 95 mT in both modes. The cavity was baked in the cryostat with hot helium up to 115 °C for about 40 h. The ramp-up time was about 20 h and the cool-down time was about 3 h. The maximum field in the TM_{010} mode improved by about 16% with some residual Q-drop while the TE_{011} mode it quenched at the highest field reached before baking (B_p = 102 mT). The BCS surface resistance decreased by about 42% in both modes while the residual resistance increased by about 2 nΩ. Figure 78 shows a plot of Q_0 vs. B_p for both modes before and after baking. The low-field quality factor is lower than usually measured due to higher residual resistance. It was found that the reason for it was a current drift in the power supply of the compensation coil which shields the Earth's magnetic field. The residual field was measured to be about 20 mG, corresponding to about 6 nΩ of additional residual resistance.

The surface impedance of the TM_{010} mode was measured during warm-up between 7 and 9.3 K before and after baking with the same procedure used for the measurements of chapter 6. The data have been compared with the BCS theory and the material parameters

obtained from the fit are shown in Table XII: there is no significant difference with the results from chapter 6.

TABLE XII. Material parameters obtained from a fit of the penetration depth and surface resistance between 7 K and 9.3 K with the BCS theory after anodization and baking.

	Δ/kT_c (300 nm)	l (300 nm) (nm)	T_c (K)	λ (0 K) (nm)
Baseline	1.98 ± 0.1	1011 ± 347	9.250 ± 0.021	37 ± 1
115 °C, 40 h bake	2 ± 0.2	572 ± 191	9.235 ± 0.021	38 ± 4

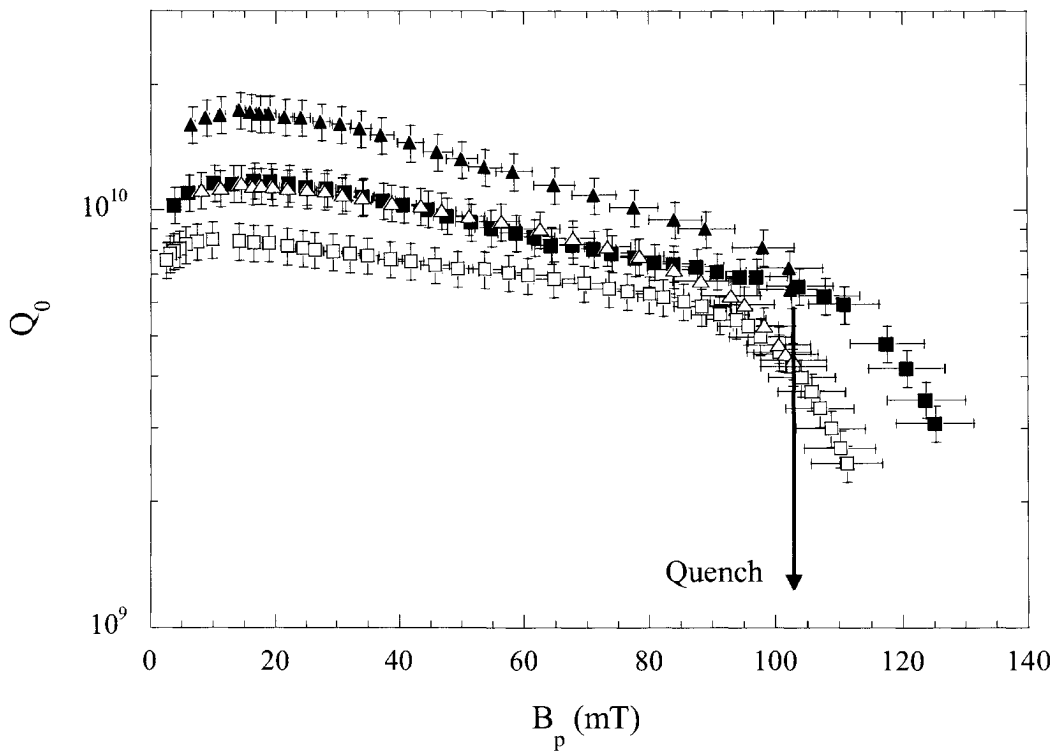

FIG. 78. Q_0 vs. B_p in the TM_{010} mode (squares) and TE_{011} mode (triangles) at 2 K after anodization (open symbols) and after baking at 115 °C for about 40 h (solid symbols).

7.4.2 Post-purification

One way to increase the quench field of a cavity is to improve the thermal conductivity of the niobium. This can be accomplished by heat treating the cavity in a vacuum furnace at 1250 °C in the presence of titanium as a solid state getter material. The treatment followed the recipe developed in Ref. [103]: the temperature is raised to 1250 °C in about 4 h and is held for 12 h, allowing the titanium to sublimate and deposit on the niobium cavity. The temperature is then lowered to 1000 °C at a rate of -0.2 °C/min and the purification of the niobium occurs. The cool-down to room temperature took about 9 h. The maximum pressure was about 10^{-4} mbar at 1250 °C, decreasing to about 10^{-7} mbar before cool-down. The main gas species detected by the RGA were hydrogen, nitrogen and water. As an indication of the effectiveness of the process, the *RRR* of a niobium sample was measured before and after the post-purification: it improved from 390 to 720. During the post-purification process, the niobium homogenizes and re-crystallizes to large (millimeter-size) grains.

About 95 μm were removed from the inner cavity surface by BCP 1:1:1 and the results of the rf test at 2 K showed about 20% increase in the onset of the Q-drop in both modes (110 mT in the TM_{010} mode, 120 mT in the TE_{011} mode). The cavity was in-situ baked with hot helium in the cryostat at 120 °C for about 30 h (ramp-up time was 18 h, cool-down time was 16 h). The test results after baking showed a recovery from the Q-drop in both modes but the TE_{011} quenched at the same field as before baking (B_p = 145 mT) while the maximum field in the TM_{010} increased by 13% (up to 135 mT). The residual resistance increased 7 nΩ in the TM_{010} mode while it did not change in the TE_{011} mode. Figure 79 shows the Q_0 vs. B_p curves at 2 K before and after baking.

The surface impedance of the TM_{010} mode was measured during warm-up between 7 and 9.3 K before and after baking and the material parameters were obtained from a comparison with the BCS theory (Table XIII). The mean free path significantly increased (about a factor of two) as a consequence of the purification process.

TABLE XIII. Material parameters obtained from a fit of the penetration depth and surface resistance between 7 K and 9.3 K with the BCS theory after post-purification and baking.

	Δ/kT_c (300 nm)	l (300 nm) (nm)	T_c (K)	λ (0 K) (nm)
Baseline	1.95 ± 0.1	2349 ± 786	9.242 ± 0.019	40 ± 1
115 °C, 40 h bake	1.99 ± 0.2	834 ± 374	9.200 ± 0.027	37 ± 4

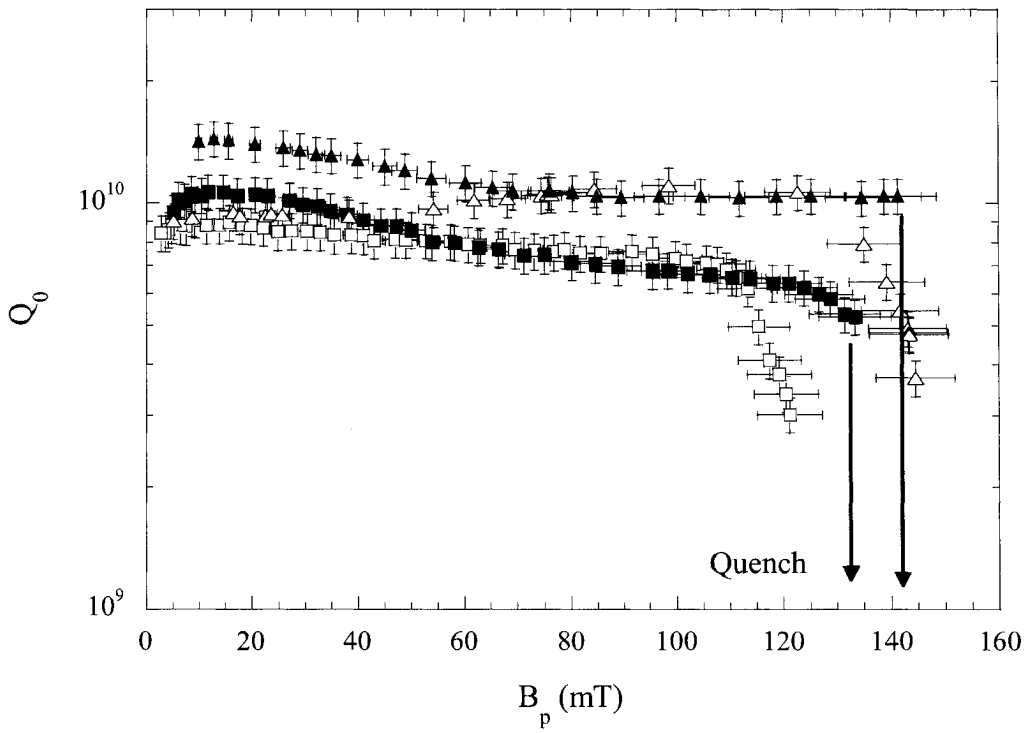

FIG. 79. Q_0 vs. B_p in the TM_{010} mode (squares) and TE_{011} mode (triangles) at 2 K after post-purification (open symbols) and after baking at 120 °C for about 30 h (solid symbols).

The cavity was tested again at 2 K after a new chemical treatment with BCP 1:1:1 removing about 35 μm showing Q-drop starting at about 95 mT and 112 mT in the TM_{010} and TE_{011} mode respectively. The cavity was baked with hot nitrogen at 115 °C for 22 h and the subsequent rf test showed a quench in the TM_{010} at 130 mT (23% higher than

before baking) and the TE_{011} mode also recovered from the Q-drop, quenching at the same field as before baking (B_p = 125 mT).

In a subsequent test about 8 μm were removed from the cavity inner surface with BCP 1:1:2 and the cavity was tested at 2 K, the results being a quench in the TE_{011} mode at B_p = 78 mT and Q-drop in the TM_{010} mode starting at 108 mT. After baking the cavity at 115 °C for shorter time (12 h) the maximum field in the TM_{010} still improved significantly (17%) but with a residual Q-drop starting at about 128 mT and up to 140 mT. The TE_{011} mode quenched at 70 mT, most probably due to a defect.

By baking the cavity at the same temperature but for different durations, it was possible to study the effect of time on the variation of the BCS surface resistance, Q-drop and mean free path. Figure 80 shows the relative variation of the surface resistance before and after baking at 115 °C for different durations. The data are consistent with a previous study done by Kneisel at 145 °C [11] which shows that the reduction of the BCS surface resistance by baking saturates above about 48 h.

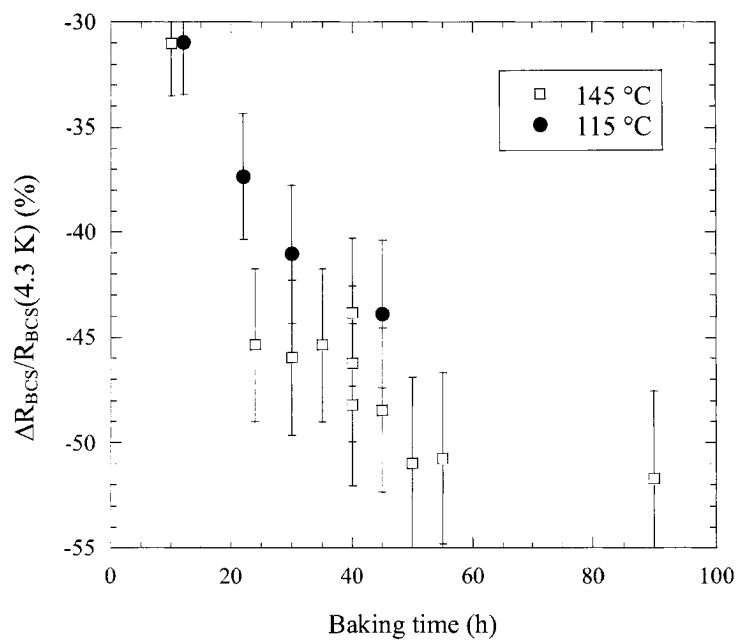

FIG. 80. Variation of the BCS surface resistance at 4.3 K after baking at 115 °C (solid circles) for different amount of time, compared with data from Kneisel [11] at 145 °C (open squares).

The analysis of the temperature dependence of the surface resistance with the BCS theory shows that, at 115 °C, twelve hours of baking are already sufficient to lower the mean free path on the 40 nm deep surface to about 25 nm, which is close to the value corresponding to the theoretical minimum of the BCS surface resistance.

The improvement in the maximum field by baking at 115 °C was about the same (~15%) for all the various durations (with the exception of the 22 h bake where the field improved by about 25%), with some residual Q-drop still present at the highest field. Nevertheless, a study done at Saclay [104] showed that baking at 100 °C for 3 h was not sufficient to achieve the full benefits in terms of Q-drop recovery and maximum field improvement as given by baking for 60 h. Figure 81 shows the Q_0 vs. B_p curves for the TM_{010} mode obtained after baking at 115 °C for different durations, showing that the maximum field was about 140 mT.

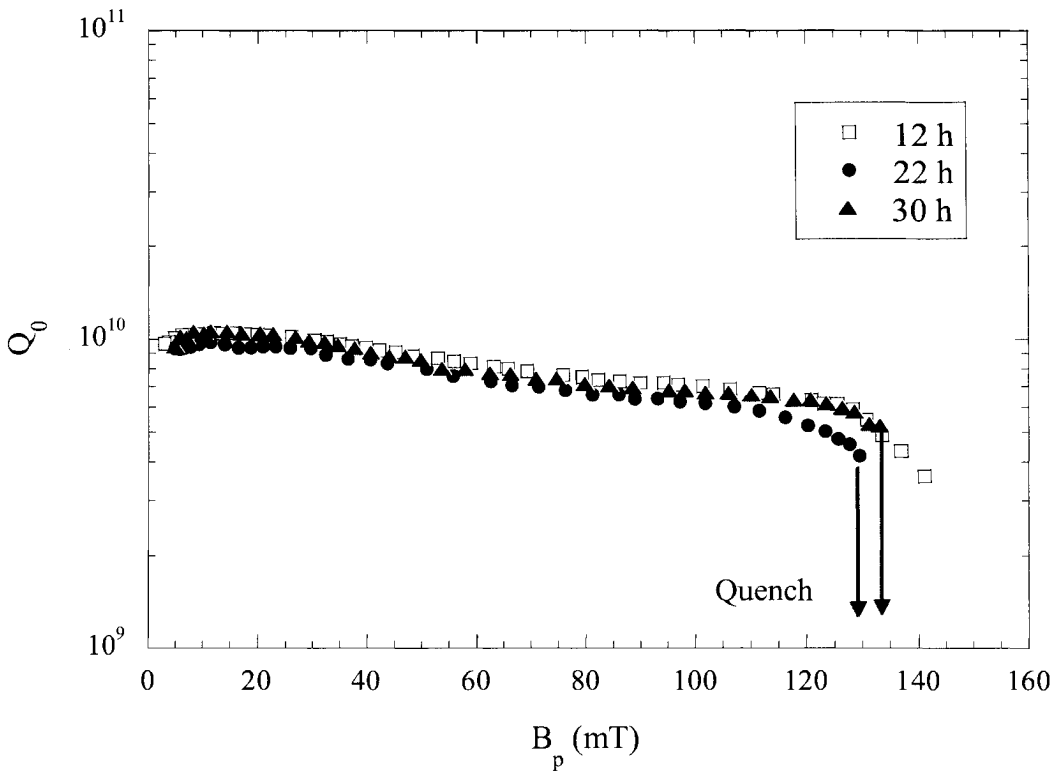

FIG. 81. Q_0 vs. B_p at 2 K for the TM_{010} mode after post-purification and baking at 115 °C for different durations.

7.5 Models comparison

The comparison of the data on the temperature dependence of the surface resistance between 4.3 and 1.9 K with the BCS theory allows to obtain information on the values of $\Delta(0\ \mathrm{K})/kT_c$, $l(40\ \mathrm{nm})$ and the residual resistance. The average values of those parameters before (10 rf tests) and after (6 rf tests) baking at 100-120 °C for the TM_{010} and TE_{011} mode are shown in Table XIV.

TABLE XIV. Average values of material parameters in 40 nm depth for the TM_{010} and TE_{011} before and after baking at 100-120 °C for 12-48 h.

	TM_{010} mode		
	Δ/kT_c (40 nm)	l (40 nm) (nm)	R_{res} (nΩ)
Baselines	1.725 ± 0.007	93 ± 12	6.7 ± 0.1
100-120 °C bake	1.824 ± 0.003	27 ± 37	15.2 ± 0.2
	TE_{011} mode		
	Δ/kT_c (40 nm)	l (40 nm) (nm)	R_{res} (nΩ)
Baselines	1.760 ± 0.006	120 ± 23	10.2 ± 0.3
100-120 °C bake	1.793 ± 0.008	31 ± 11	13.5 ± 0.9

The variations of the material parameters by baking are consistent with the results presented in chapter 6. The normal electrons' mean free path is independent of frequency, within the experimental error, and is reduced by a factor of ~3.5 by baking. The energy gap is slightly lower than measured on the single cell used for the study in chapter 6 and it also increased more (~ 6%) by baking in the TM_{010} mode than in the TE_{011} mode (~ 2%). The cause for the lower value of the energy gap than previously found is not clear, since the chemical treatment and oxidizing conditions were the same, and might be due to a different texture and grain structure of the niobium used to fabricate the two cavities [105].

The residual resistance in the baseline tests is higher in the TE_{011} mode than in the TM_{010} mode by about a factor of 1.5 and could be explained by its higher frequency,

although the dependence is not as strong as ω^2, as proposed in section 4.2.3. The residual losses were doubled by baking in the TM_{010} mode while they increase only about 30% in the TE_{011} mode: this would be consistent with the hypothesis of electric interface losses due to enhanced structural disorder at the oxide/metal interface because of oxygen diffusion and oxide decomposition.

The low-field Q-drop for these cavity tests did not appear as pronounced as for the ones presented in chapter 6 and could not be studied systematically in the TE_{011} mode either since the mode could not be reliably locked with the rf system for fields lower than about 10 mT. The following sections present an analysis of the medium field Q-slope and the high field Q-drop.

7.5.1 Medium field Q-slope

The data relative to the medium field Q-slope have been analyzed in a similar way as in section 6.3.2. Before post-purification, the dependence of the surface resistance with B_p is mainly quadratic for both modes, becoming more linear for the TM_{010} mode after baking. After post-purification, the linear dependence is best for both modes before and after baking.

Table XV shows the average values of the fitting coefficients R_{res}^{1}, γ^* and R_{s0} of Eq. (125) before and after baking for both modes at 2 K, before and after post-purification. The quadratic coefficient (γ^*) becomes undetermined after post-purification. The linear coefficient (R_{res}^{1}) is increased by more than a factor of two by post-purification. Baking increases both R_{res}^{1} and γ^* in the TE_{011} mode, while γ^* appears to be slightly reduced in the TM_{010} mode. The values of R_{res}^{1} and γ^* for the TM_{010} mode after post-purification are consistent with the values at 2 K obtained in section 6.3.2. The higher value of the low-field surface resistance (R_{s0}) after post-purification is mainly due to a higher residual resistance caused by trapped flux due to a non optimal shielding of the Earth's magnetic field.

TABLE XV. Average values of the fitting parameters $R_{res}{}^{1}$, γ^{*} and R_{s0} and fit correlation factor r^2 for both TM_{010} and TE_{011} mode at 2 K before and after baking, before and after post-purification.

	Before post-purification			
	Before baking		After 100-120 °C baking	
	TM_{010}	TE_{011}	TM_{010}	TE_{011}
R_{s0} (nΩ)	26.9 ± 0.2	51.5 ± 0.4	16.7 ± 0.2	36.3 ± 0.2
$R_{res}{}^{1}$ (nΩ)	7.46 ± 1.46	0.003 ± 3.7	27.1 ± 1.3	5.32 ± 2.40
γ^{*}	1.55 ± 0.11	2.76 ± 0.14	0.97 ± 0.13	3.34 ± 0.14
r^2	0.995	0.994	0.998	0.997
	After post-purification			
	Before baking		After 100-120 °C baking	
	TM_{010}	TE_{011}	TM_{010}	TE_{011}
R_{s0} (nΩ)	28.7 ± 0.1	79.3 ± 0.3	23.3 ± 0.3	52.7 ± 0.3
$R_{res}{}^{1}$ (nΩ)	16.4 ± 1.1	24.1 ± 2.8	34.1 ± 2.0	71.9 ± 1.5
γ^{*}	0.01 ± 0.07	0.00 ± 0.06	0.00 ± 0.13	0.25 ± 0.03
r^2	0.987	0.988	0.993	0.989

The data in Table XV indicate that before post-purification, heating of the rf surface is the main component to the medium field Q-slope (quadratic dependence) but baking enforced a linear dependence in the TM_{010} mode probably due to higher hysteresis losses. The larger surface resistance of the TE_{011} mode makes heating prevail even after baking. Post-purification increases the thermal conductivity of the niobium which re-crystallizes in millimeter-size grains: the first effect lowers the heating contribution so that the linear dependence is the best description of the medium field Q-slope for both modes. The data of Table XV also shows that the larger grain size yields increased hysteresis losses. This tendency was also found in niobium thin films [94] and suggests weaker links by wider grain boundaries, possibly due to stronger impurity segregation.

Table XVI gives the theoretical estimate of the linear coefficient $R_{res}{}^{1}$ given by Eq. (124) and of the quadratic coefficients γ and γ^{*}, given by Eqs. (86) and (83), at 2 K before

and after post-purification and before baking. The grain size a_J was set to be 200 μm and 2 mm before and after post-purification, respectively, while the thermal conductivity [99] and Kapitza resistance [106] of *RRR* ~ 300 niobium were calculated at 2 K from the following functions:

$$\kappa(T) = 0.7e^{1.65T-0.1T^2}\ \frac{\mathrm{W}}{\mathrm{m\,K}} \tag{129}$$

$$R_K(T) = 2.7\cdot 10^{-3}T^{-2.85}\ \frac{\mathrm{W}}{\mathrm{m^2\,K}}. \tag{130}$$

After post-purification, the thermal conductivity of *RRR* ~ 700 niobium at 2 K was 30 W/(m K) [99] and the Kapitza resistance was calculated from [100]

$$R_K(T) = 1.61\cdot 10^{-3}T^{-3.93}\ \frac{\mathrm{W}}{\mathrm{m^2\,K}}. \tag{131}$$

TABLE XVI. Theoretical estimate of the linear ($R_{res}{}^1$) and quadratic (γ^* and γ) coefficients at 2 K before baking for both modes before and after post-purification.

	Before post-purification		After post-purification	
	TM_{010}	TE_{011}	TM_{010}	TE_{011}
$R_{res}{}^1$ (nΩ)	6.9	9.9	20.0	28.4
γ^*	0.67	1.47	0.19	0.78
γ	2.33	3.40	1.72	2.59

The estimates of $R_{res}{}^1$ with Eq. (124) are in good agreement with the experimental values, assuming $J_{cJ} = 2\times10^{13}$ A/m^2 before post-purification, being reduced to $J_{cJ} = 7\times10^{11}$ A/m^2 after post-purification. The values of the quadratic fit coefficient before post-purification are between the estimated values of γ^* and γ. After post-purification, the BCS non-linear correction, introduced in the parameter γ, is too strong compared to the data. Figure 82 shows the relative variation of the surface resistance at 2 K as a function of the ratio B_p/B_c before and after post-purification for both modes, showing the change from quadratic to linear dependence.

The two cases where the outer surface of the cavity was in helium atmosphere during bake-out did not show a consistent improvement of the medium field Q-slope compared to air and therefore more tests will be necessary to asses the influence of the "baking gas" on the Kapitza resistance.

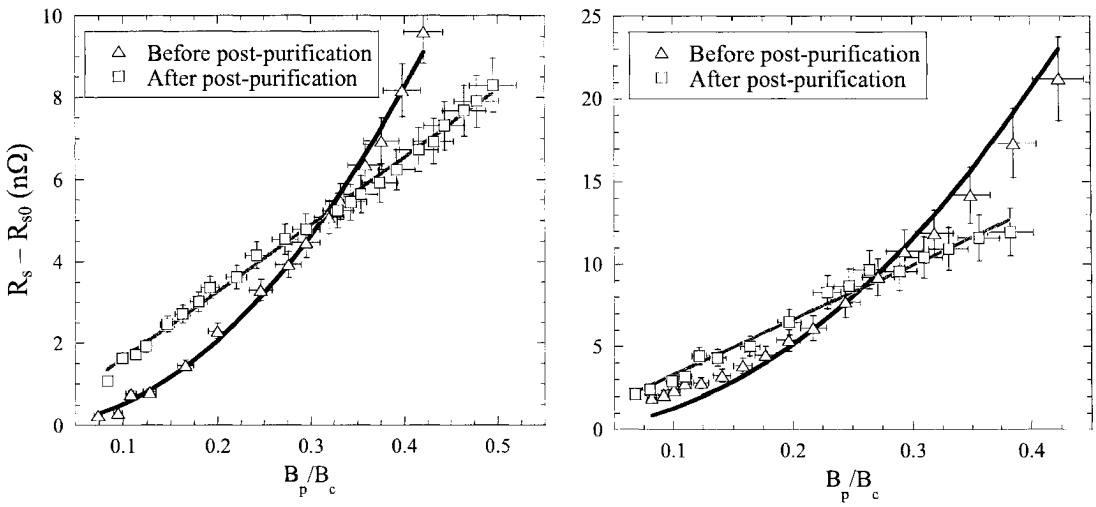

FIG. 82. Increase of the surface resistance at 2 K as a function of B_p/B_c for the TM_{010} (left) and TE_{011} (right) modes before and after post-purification. Solid lines represent fits with Eq. (125).

7.5.2 High field Q-drop

The most important result from the cavity rf tests is the presence of the high field Q-drop and its recovery after baking in the TE_{011} mode. This finding supports the idea of magnetic field induced anomalous losses, contrary to what is predicted by the ITE model.

A comparison of the data with the thermal instability model of section 4.8.4 shows that the Q-drop in the TE_{011} mode before the post-purification process is consistent with the hypothesis of "global heating" of the cavity surface. This is due to the higher frequency and therefore higher heat flux ($q \propto R_s \propto f^2$) for the TE_{011} mode. On the other hand, the thermal instability model cannot explain the high field Q-drop for the TM_{010} mode, using the same thermal conductivity and Kapitza resistance functions which give

good agreement on the TE_{011} data. Figure 83 shows a plot of Q_0 vs. B_p for both TE_{011} and TM_{010} data, compared with the prediction of the TI model with and without the non-linear correction to the BCS surface resistance. The functions (129) and (130) were used for the temperature dependence of thermal conductivity and Kapitza resistance of *RRR* ~ 300 niobium. However, the same comparison on the data after the post-purification shows that the TI model is not adequate anymore to describe the Q-drop for the TE_{011} mode. For this calculation, the thermal conductivity of *RRR* ~ 700 niobium was 30 W/(m K) (approximately temperature independent up to ~ 2.7 K) and the temperature dependence of the Kapitza resistance was given by Eq. (131). Figure 84 shows the comparison between data and TI model with and without the non-linear correction to the BCS surface resistance for both modes. Figures 83 and 84 show that the TI model with the non-linear correction gives a good description of the medium field Q-slope for the TM_{010} mode at 2 K, both before and after post-purification, while it overestimates the slope for the TE_{011} mode.

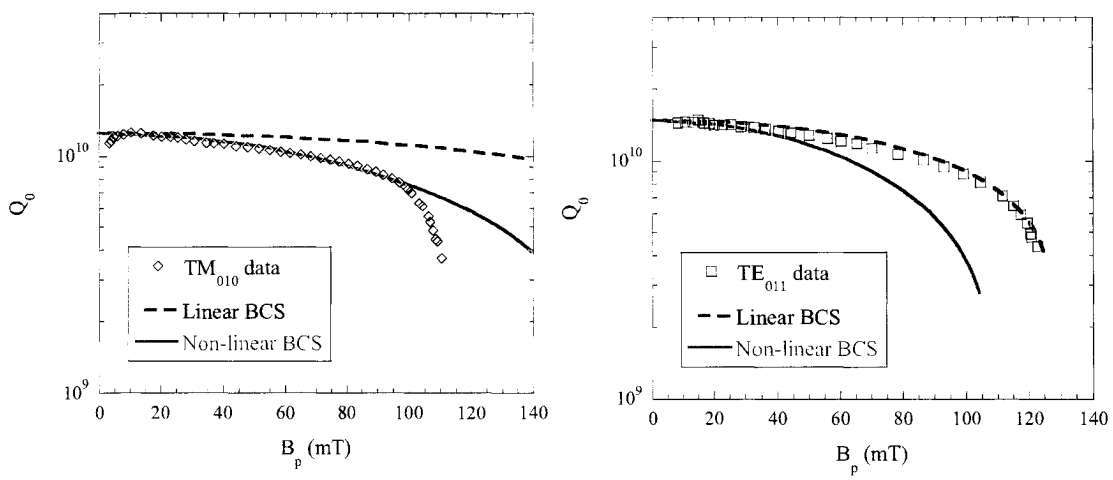

FIG. 83. Q_0 vs. B_p data compared with the TI model with and without non-linear correction to the BCS surface resistance at 2 K for both TM_{010} (left) and TE_{011} modes (right).

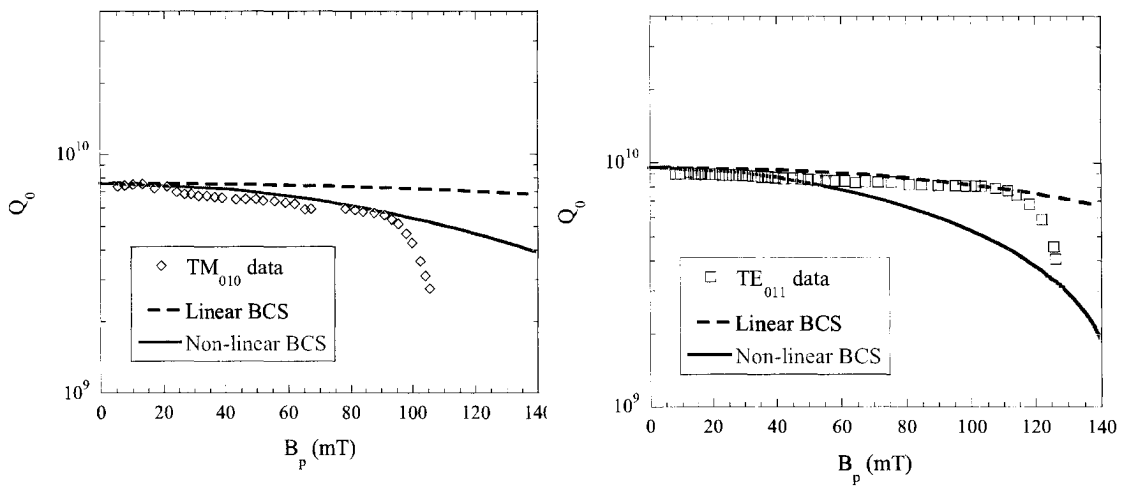

FIG. 84. Q_0 vs. B_p data compared with the TI model with and without non-linear correction to the BCS surface resistance at 2 K after post-purification for both TM_{010} (left) and TE_{011} modes (right).

The average values of the pre-exponential factor b, the Q-drop onset E_0 and the constant c obtained from a fit of the data with the ITE model [Eq. (127)] are shown in Table XVII for the TM_{010} mode before and after baking for different cavity treatments. The exponential dependence of the surface resistance with the peak rf field of the ITE model gives an excellent numerical description of the data, although in few cases the onset E_0 could not be obtained since the fit gave a positive value for the negative term $-e^{-c/E_0}$ of Eq. (127). The pre-exponential factor b is proportional to the niobium oxide thickness and density of localized states and it is reduced by baking. While this parameter changes significantly for new surface preparations, the values of the "sharpness" of the Q-drop, c, are more consistent also with the data presented in Table X in chapter 6. The value of c is reduced by anodization, indicating a stronger Q-drop with thicker oxide layer, but the value of b is also lower, in contrast with the model ($b \propto dn_L$). Again, the major drawback of the ITE model is its inability to predict the high field Q-drop in a mode with no surface electric field (TE_{011}) which is clearly measured after post-purification of the niobium cavity.

TABLE XVII. Average values of the parameters b, E_0, c and correlation factor for the ITE model compared with Q-drop data at 2 K for the TM_{010} mode for different cavity treatments.

	b (Ω)	c (MV/m)	E_0 (MV/m)	r^2
Before baking	105	959	-	0.998
After 100-120 °C bake	18.6	952	41.1	0.997
Anodization	0.40	727	-	0.999
After 115 °C bake	5.80	990	45	0.998
Post-purification	33.3	952	40.8	0.994
After 115-120 °C bake	0.02	867	49.2	0.966

The values of the fitting parameters β_0 and σ for the MFE model for both TE_{011} and TM_{010} mode before and after baking are given in Table XVIII for different cavity treatments. The average grain boundary size was taken to be 50 μm and 1 mm before and after post-purification respectively. This model also gives a very good numerical agreement with the data. The values of the fitting parameters at 2 K before bake-out are consistent with the values obtained for the single cell used for the baking study of chapter 6. The center of the distribution of field enhancement factors, β_0, increases by post-purification and this could be caused by the more pronounced grain structure. β_0 is also smaller for the TE_{011} mode and this could be due to a smoother surface on the cavity wall compared to the equator area where the weld produces large steps. This could also be the reason why the onset field for the Q-drop in the TE_{011} mode is about 17% higher than in the TM_{010} mode. β_0 is reduced by baking in the TM_{010} mode due to a smoother Q-drop, although the model does not provide a physical explanation for this reduction. The Q-drop is absent in the TE_{011} after baking.

TABLE XVIII. Average values of the fitting parameters β_0 and σ of the MFE model for the TM_{010} and TE_{011} mode at 2 K before and after baking for different cavity treatments.

	TM_{010}		TE_{011}	
	β_0	σ	β_0	σ
Before baking	1.49	0.0060	1.21	0.0070
After 100-120 °C bake	1.19	0.0072	-	-
Anodization	1.42	0.0070	1.48	0.0070
After 115 °C bake	1.14	0.0075	-	-
Post-purification	1.64	0.0067	1.4	0.0070
After 115-120 °C bake	1.32	0.0075	-	-

CHAPTER 8

EXPERIMENTS TO ACHIEVE THE CRITICAL FIELD

8.1 "High field" cavity

In order to push the rf field in a superconducting niobium cavity close to the theoretical limit ($B_p \approx 200$ mT) a two-cell cavity was designed by J. Sekutowicz with the purpose of achieving high surface electric and magnetic fields in localized areas of the cavity walls. In order to do that, the cavity was excited in the two pass-band modes of the TM_{010}, with both frequencies close to 1.4 GHz. The following sections describe the cavity design and rf test results.

8.1.1 Cavity design

A two-cell resonant cavity can be described as coupled oscillators such that each cell's resonant mode (the TM_{010} in this case) corresponds to two "pass-band" modes of the whole cavity. This is because the field in one cell can resonate in phase (0-mode) or with opposite phase (π-mode) with respect to the field in the other cell. The resonant frequencies of the pass-band modes are close to each other and the difference depends on the so-called cell-to-cell coupling factor, which is set by the iris opening between the two cells.

Figure 85 shows a drawing of the cavity, which was named "high field" cavity: the main electromagnetic parameters of the 0- and π-mode were calculated with a 2D finite element code [107] and are given in Table XIX. The major difference consists in the peak surface electric field in the 0-mode being almost a factor of four higher than in the π-mode for the same stored energy.

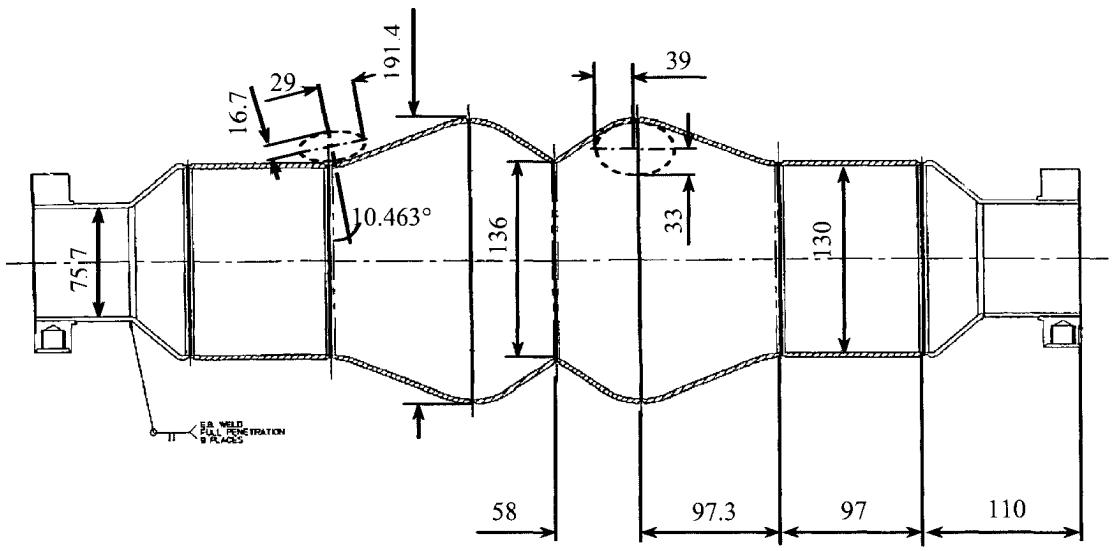

FIG. 85. Drawing of the two-cell "high field" cavity. Dimensions are in millimeters. The vertical lines separate the pieces of the cavity which are joined together by EBW.

TABLE XIX. Main electromagnetic parameters of the TM_{010}-0 and -π modes of the "high field" cavity.

	TM_{010}-0	TM_{010}-π
Frequency (MHz)	1381.8	1494.6
$E_p/\sqrt{U}$ [(MV/m)/√J]	2.9	11.3
$B_p/\sqrt{U}$ (mT/√J)	23	24.5
G (Ω)	406	426

Figure 86 shows the distribution of the surface electric field for both modes: the π-mode has a peak at the iris between the two cells while the 0-mode has a node at that location. The distribution of the magnetic field on the cavity surface for both modes is shown in Fig. 87: the B-field is high anywhere between the equators of the two cells in the 0-mode, while it has a node at the iris between cells in the π-mode. It is important to notice that the fields are maxima in areas where welds are present, which can limit the cavity performance [108].

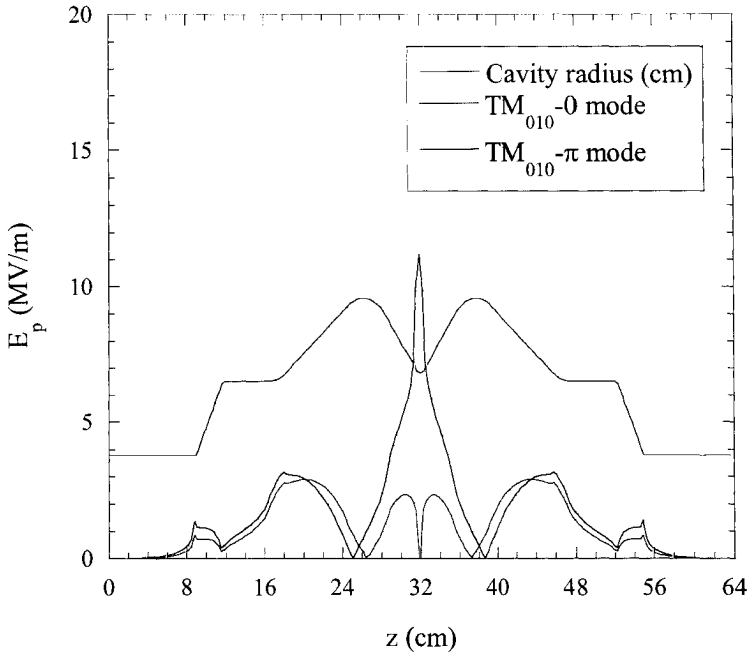

FIG. 86. Electric field distribution on the cavity surface for both TM_{010}-0 and TM_{010}-π modes calculated for a cavity stored energy of 1 J.

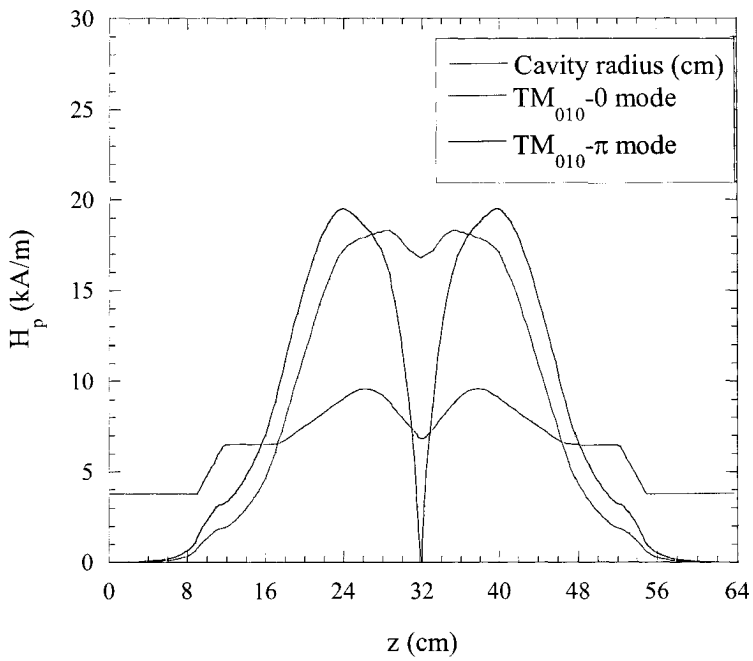

FIG. 87. Magnetic field distribution on the cavity surface for both TM_{010}-0 and TM_{010}-π modes calculated for a cavity stored energy of 1 J.

The cavity was made of *RRR* ~ 300 niobium 3.175 mm thick and it has Nb55Ti flanges at each end. Coupling to both modes is obtained with a coaxial input and pick-up antennas assembled on stainless steel blanks which are sealed to the cavity flanges with $AlMg_3$ gaskets. Figure 88 shows a picture of the cavity after fabrication.

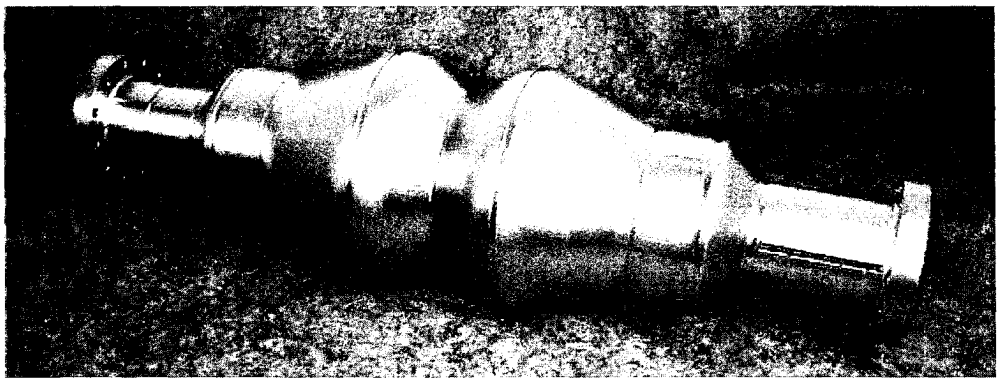

FIG. 88. Two-cell "high field" cavity after fabrication.

8.1.2 Cavity preparation and test results

The cavity had standard preparation procedures, as described in section 5.2. After fabrication, about 150 μm were chemically etched from the inner cavity surface by BCP 1:1:1. The cavity was tested six times and a total of about 50 μm were removed. In some cases, multipacting was observed in both modes at very low field (E_p ~ 5 MV/m) and was typically overcome by about 30 min of rf processing. The best results from the rf test at 2 K are shown in Fig. 89: both modes achieved a peak surface magnetic field of 100 mT with a mild Q-drop in absence of field emission. The Q_0 vs. B_p curves of both modes basically overlap while the E_p in the π-mode is almost a factor of four higher than in the 0-mode (E_{pmax} = 45 MV/m in the π-mode, E_{pmax} = 12.5 MV/m in the 0-mode). This suggests that electric field losses do not contribute significantly to the high field Q-drop, consistent with the measurements of the TM/TE-mode cavity. The cavity performance did not improve by "in-situ" baking.

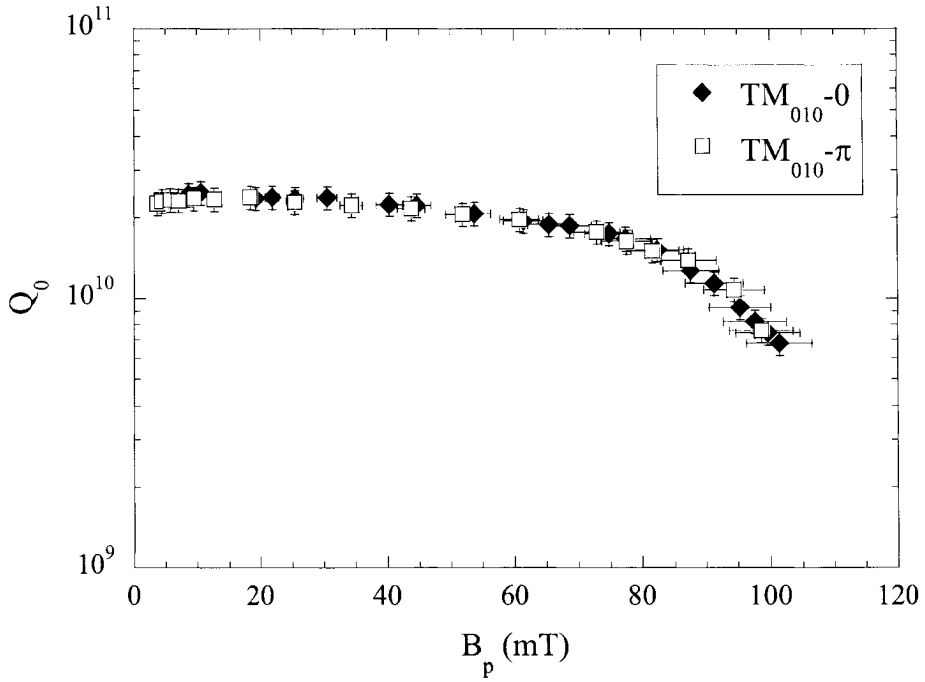

FIG. 89. Q_0 vs. B_p in the TM_{010}-0 and -π modes of the "high field" cavity measured at 2 K.

In order to improve the thermal conductivity of the niobium to try to push the fields to higher values, the cavity was post-purified in a titanium box heated in a vacuum surface up to 1250 °C, with the same procedure used on the single cell used for the TM_{010}/TE_{011} study (see section 7.3.2). The cavity was chemically etched both on the inside and outside surface removing about 70 μm and 20 μm respectively by BCP 1:1:1. The cavity was then high-pressure rinsed for two hours. The rf test at 2 K showed Q-drop in the π-mode starting at about 100 mT and up to 127 mT. The quality factor in the 0-mode was lower than in the π-mode, indicating a higher residual resistance, and the onset field for the Q-drop was also lower by about 25%. The origin of these additional losses is not clear but they might be located at the iris weld between the two cells, where the magnetic field in the 0-mode is close to its maximum.

The cavity was "in-situ" baked with hot nitrogen at 120 °C for 48 h and was tested again at 2 K. The quality factor increased in both modes, by about 48% in the π-mode

and by a factor of ~ 2.3 in the 0-mode. This improvement is consistent with a ~ 50% reduction of the BCS surface resistance and no increase in the residual term. In the case of the 0-mode, the "anomalous" losses causing a lower Q_0 were also eliminated by baking. The Q-drop was still present in both modes but it started at about 135 mT and the maximum (quench) field was ~ 170 mT and ~ 150 mT in the π- and 0-mode, respectively. The magnetic field in the π-mode was among the highest ever achieved in niobium superconducting rf cavities. Figure 90 shows the plot of Q_0 vs. B_p in both modes before and after baking. The maximum peak surface electric field after baking was 77 MV/m in the π-mode while it was only 19 MV/m in the 0-mode. Therefore, losses due to the electric field (as suggested by the ITE model) do not limit the cavity performance, as obtained for the results before the post-purification and consistently with the TM_{010}/TE_{011} study.

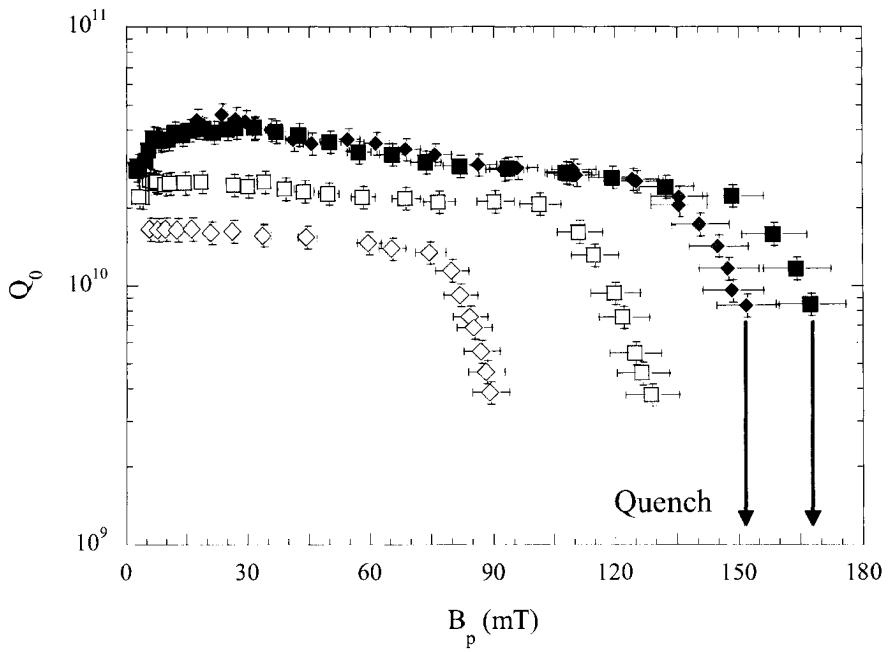

FIG. 90. Q_0 vs. B_p in the TM_{010}-0 (diamonds) and -π (squares) modes at 2 K after post-purification (open symbols) and after baking at 120 °C for 48 h (solid symbols).

8.2 Electropolishing

Over the last few years electropolishing proved to be a chemical treatment which allows one to reach a higher accelerating gradient with better reproducibility than with BCP [109]. The main advantage consists in smoother surfaces, which can also be better cleaned by HPR. Jefferson Lab recently acquired the capability to electropolish niobium cavities and began to develop a program to optimize the parameters for this chemical treatment to achieve the best cavity performances.

A single cell cavity of the CEBAF shape was fabricated ten years ago with the same procedure used to build the cavity used for the baking study described in chapter 6: prior to electron beam welding, the half-cells were post-purified in a titanium box at 1400 °C for 4 h to increase the thermal conductivity. This cavity was electropolished as described in section 5.2.2 with a constant voltage (15 V) and current oscillating between 17.5 A and 22.5 A, corresponding to an average current density of 52 mA/cm^2; about 70 μm were removed. The cavity was rotating at 1 rpm while the acid flow was about 3 l/min. The acid outlet temperature was about 26 °C. The cavity was high-pressure rinsed for 1 h, dried overnight in clean room class 10, assembled with niobium flanges and evacuated to about 10^{-8} mbar. The rf test at 2 K showed the high field Q-drop starting at about B_p = 105 mT without field emission. The residual resistance was 2.3 ± 0.3 nΩ. The cavity was "in-situ" baked at 120 °C for 48 h with hot nitrogen and the subsequent rf test at 2 K showed no trace of the Q-drop and the cavity quenched at B_p = 150 mT. The residual resistance did not increase, within the experimental error (2.8 ± 0.5 nΩ) and the mean free path l(40 nm) decreased from 936 ± 400 nm to 25 ± 150 nm.

Figure 91 shows the Q_0 vs. B_p plots before and after baking. The medium field Q-slope before baking is well described by both linear and quadratic dependence of R_s as a function of B_p. The linear slope coefficient R_{res}^1 is 4.4 nΩ at 2 K and 0.3 nΩ at 1.6 K while the quadratic slope coefficient γ^* is 0.48 at 2 K and 0.72 at 1.6 K. After baking, R_{res}^1 at 2 K increased to 25 nΩ while γ^* decreased to 0.18, consistently with cavities treated by BCP.

The results from this test are consistent with other laboratories [73, 86], showing that the Q-drop is a common feature of BCP and EP treated cavities and that heating occurs in

both cases in areas around the equator. The Q-drop data are well fitted by the ITE and MFE models as shown in Fig. 92. The fitting parameters are reported in Table XX and they are comparable to the parameters obtained on the BCP cavity in Table X.

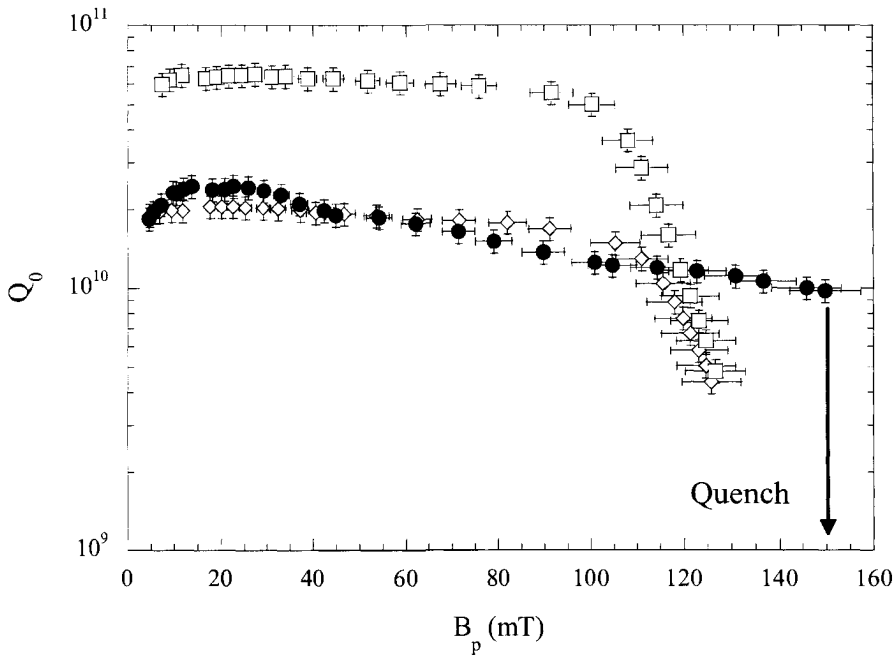

FIG. 91. Q_0 vs. B_p for an electropolished single cell at 2 K (open diamonds), at 1.6 K (open squares) and at 2 K after baking at 120 °C for 48 h (solid circles).

TABLE XX. Fitting parameters of the ITE and MFE models for the Q-drop data for the electropolished single cell.

		ITE model		MFE model	
T (K)	b (Ω)	c (MV/m)	E_0 (MV/m)	β_0	σ
1.6	0.65	847	39	1.49	0.007
2	2.16	914	35	1.49	0.007

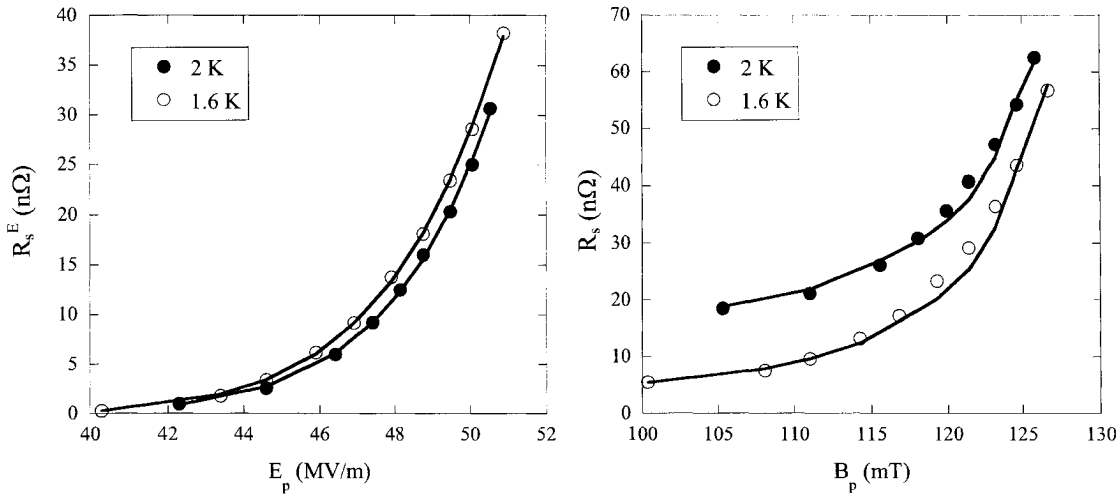

FIG. 92. Electric surface resistance as function of E_p fitted with the ITE model (solid lines) (left), and surface resistance as function of B_p fitted with the MFE model (solid lines) (right) for the electropolished single cell.

8.3 Single grain cavity

Recently, the company CBMM was able to produce two high *RRR* niobium ingots 10" in diameter with a large single grain, of diameter about 7", in the middle and a few centimeter-size grains on the outer edge. A load test on a sample from this material showed an elongation up to 100% before breaking, compared to about 60% achievable with standard polycrystalline material [110]. Due to its high ductility, this material can be used to form niobium cavities by standard fabrication methods (deep drawing). Sheets 3 mm thick were cut from the ingot by wire EDM (electrical discharge machining) and half-cells were formed by deep drawing. The cups were electron beam welded and niobium beam pipes were welded at the iris forming complete cavities. Two single cell cavities of the "High Gradient" (HG) shape [111], proposed for the upgrade of the CEBAF accelerator, were produced. The cavities resonate at 1.495 GHz in the TM_{010} mode and the equatorial diameter was larger than the single grain so that few large grains were present on the equator area close to the weld. The cavities were prepared using standard BCP 1:1:1 and were heat treated at 800 °C for 3 h in a vacuum surface to remove hydrogen absorbed in the niobium during the wire EDM process. The rf test

results at 2 K showed the Q-drop starting at about B_p = 108-120 mT [112]. After "in-situ" baking at 120 °C for 48 h, the cavities recovered from the Q-drop but the maximum field did not improve and they quenched at about B_p = 127-140 mT.

In order to build a cavity made of a single grain, the HG cavity shape was scaled to a resonant frequency of 2.26 GHz in the TM_{010} so that it could be built with discs of smaller diameter. Figure 93 shows a picture of the niobium discs and of the completed single cell and Table XXI lists the main electromagnetic parameters.

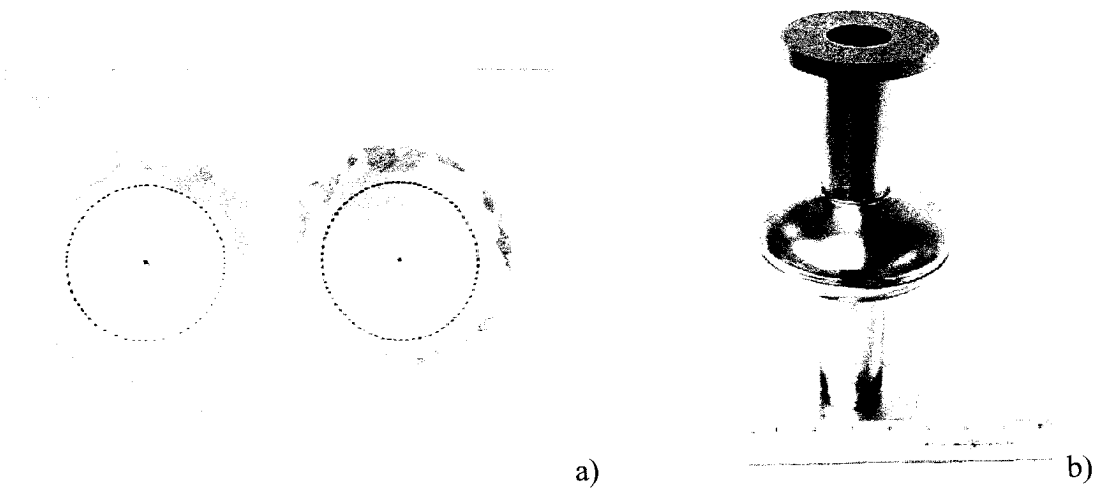

FIG. 93. Niobium sheets sliced from the ingot showing the single crystal from which the half-cell discs were cut (dashed line) (a) and completed cavity (b).

TABLE XXI. Main electromagnetic parameters of the TM_{010} mode of the HG cavity shape scaled to 2.26 GHz calculated with a 2D finite element code [107].

Frequency (MHz)	2256.2
E_p/E_{acc}	1.67
B_p/E_{acc} [mT/(MV/m)]	4.29
G (Ω)	270

The cavity was fabricated as the two previous ones, 120 μm were removed by BCP 1:1:1 and it was heat treated in a vacuum furnace at 800 °C for 3 h to remove the dissolved hydrogen from the wire EDM. About 60 μm were removed with BCP 1:1:1 after heat treatment, followed by 30 min HPR. Niobium flanges with coupling antennas were assembled on the cavity in a class 10 clean room and the single cell was evacuated to about 10^{-8} mbar and cooled down to 2 K. After the chemical treatment the smoothness of the inner surface was remarkable. The roughness of a sample treated in the same way as the cavity was analyzed with a 3D profilometer: the root-mean-square (rms) height on a 200×200 μm area was 27 nm. Samples of polycrystalline material treated with BCP 1:1:1 and EP showed on the same area an rms roughness of 1274 nm and 251 nm respectively [113].

The results of the rf test at 2 K showed Q-drop starting at B_p = 123 mT. The cavity was baked at 120 °C for 48 h and tested again at 2 K. Field emission was detected starting at about B_p = 120 mT (E_p = 46.7 MV/m), degrading the quality factor, and the maximum field achieved was B_p = 162 mT above which the cavity would quench. After a quench the surface temperature rapidly decreases due to the cooling action of the superfluid helium and the cavity would become superconducting again. The rf field in the cavity increased up to B_p = 185 mT but decayed to 162 mT in about 300 ms, most probably due to overheating and to field emission loading. The cavity was high-pressure rinsed again to eliminate field emission and the new rf test at 2 K confirmed the recovery from the Q-drop but the cavity quenched at B_p = 150 mT. Figure 94 shows a plot of Q_0 vs. B_p at 2 K before and after baking and Fig. 95 shows a picture of the transmitted power from the cavity ($P_t \propto B_p^2$) reaching 185 mT for about 40 ms.

The cavity was post-purified at 1250 °C following the same procedure described in section 7.3.2, followed by BCP 1:1:1 removing about 70 μm and 30 min HPR. The *RRR* of a sample from the same ingot as the cavity was measured before and after post-purification and it increased from 275 to 315. The reason for the modest *RRR* improvement might be due to the high tantalum content (~ 800 ppm) of this ingot compared to the usual content of about 100 ppm in polycrystalline niobium sheets.

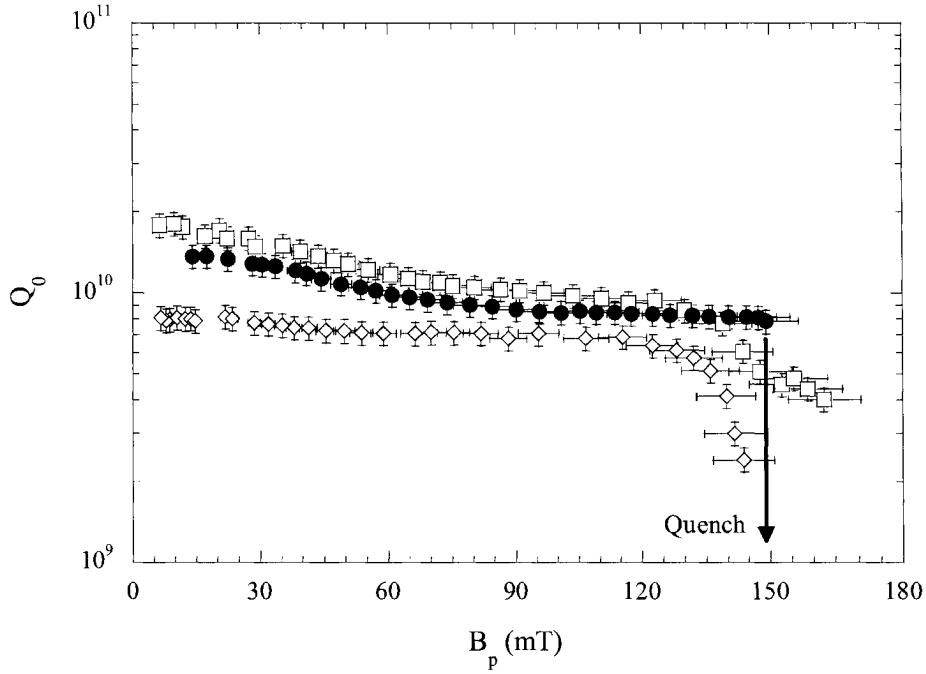

FIG. 94. Q_0 vs. B_p measured at 2 K on a single grain single cell before baking (open diamonds), after baking at 120 °C for 48 h (open squares) and after and additional high-pressure rinsing (solid circles). The degradation of the quality factor at high field after baking was due to field emission.

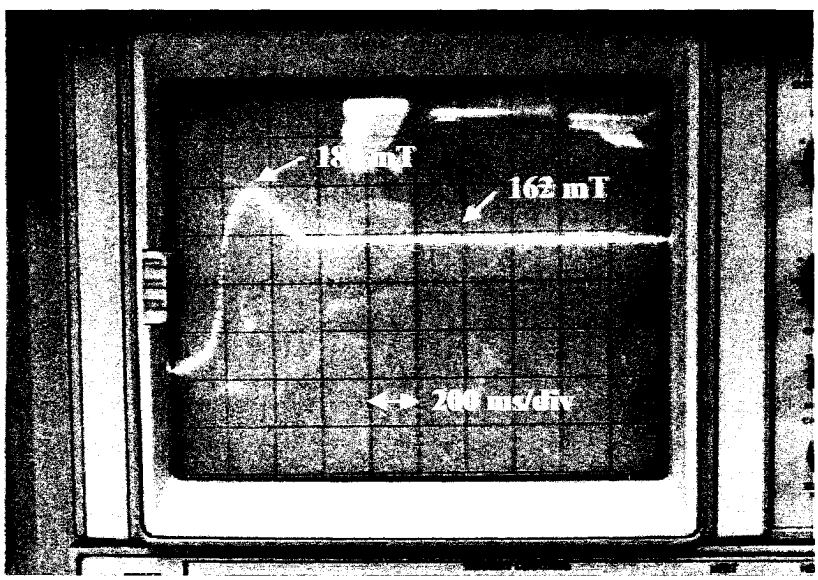

FIG. 95. Oscilloscope trace showing the transmitted power from the cavity reaching a peak field of 185 mT for about 300 ms, before decaying to 162 mT.

The dependence of the surface resistance on the rf field was measured at four different temperatures between 1.55 K and 2 K to gain some insight on the medium field Q-slope. Figure 96 shows a plot of Q_0 vs. B_p after post-purification and after baking.

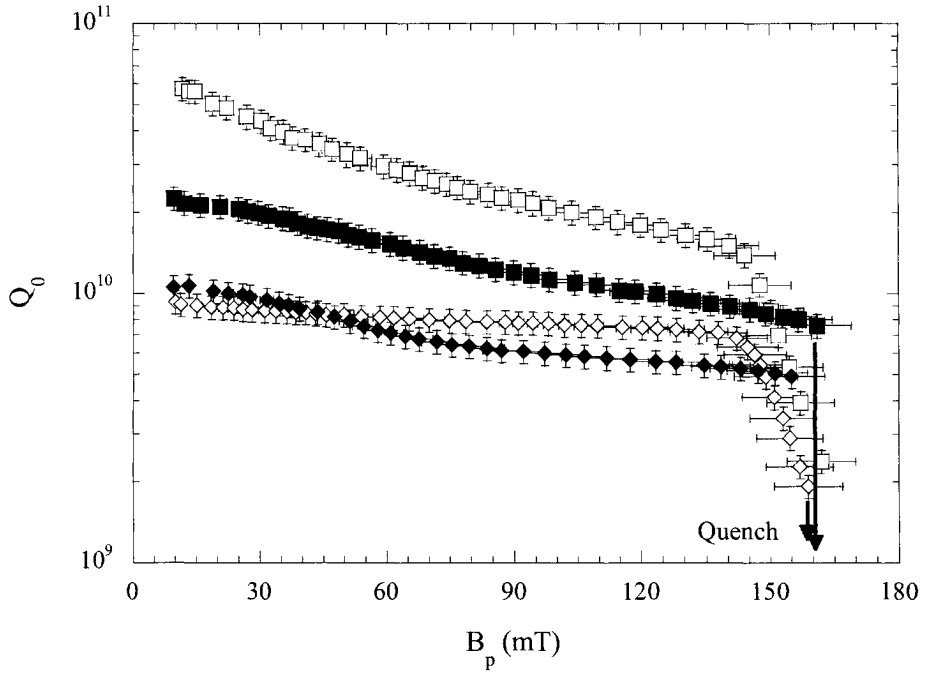

FIG. 96. Q_0 vs. B_p for a single grain cavity at 2 K (diamonds) and 1.55 K (squares) after post-purification (open symbols) and after baking at 120 °C for 48 h (solid symbols).

In order to have a direct comparison of the single grain cavity with standard fine-grain material, a single cell with the same shape as the single grain one was built using standard *RRR* ~ 300, with grain size ASTM 6 niobium. The cavity was treated in the same way as the single grain one; the rf test at 2 K showed a Q-drop starting at B_p = 115 mT and up to the same field as the single grain cavity before post-purification (B_p = 143 mT). After 120 °C, 48 h "in-situ" baking, the cavity was tested again at 2 K: the Q-drop was still present even though the onset was shifted to higher field (135 mT) and reached a maximum value of 163 mT. The dependence of the surface resistance from the

rf field was measured at four different temperatures and Fig. 97 shows a plot of Q_0 vs. B_p at 2 K and 1.55 K before and after baking. Figure 98 is a plot of the Q_0 vs. B_p curves at 2 K for the single crystal and polycrystalline cavity, showing very similar performance.

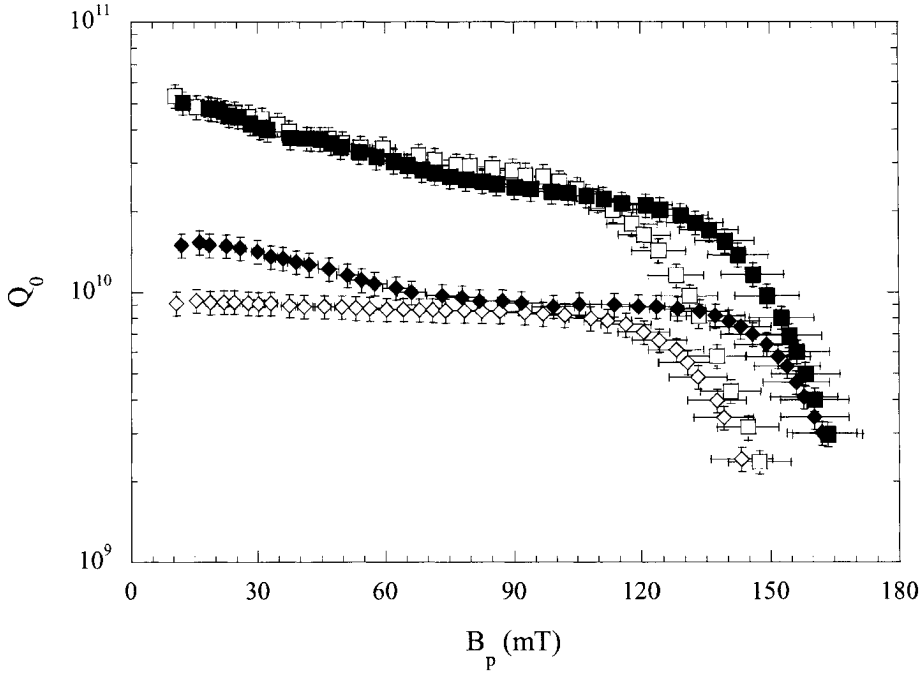

FIG. 97. Q_0 vs. B_p for a HG single cell at 2.26 GHz made of standard niobium measured at 2 K (diamonds) and 1.55 K (squares) before (open symbols) and after baking at 120 °C for 48 h (solid symbols).

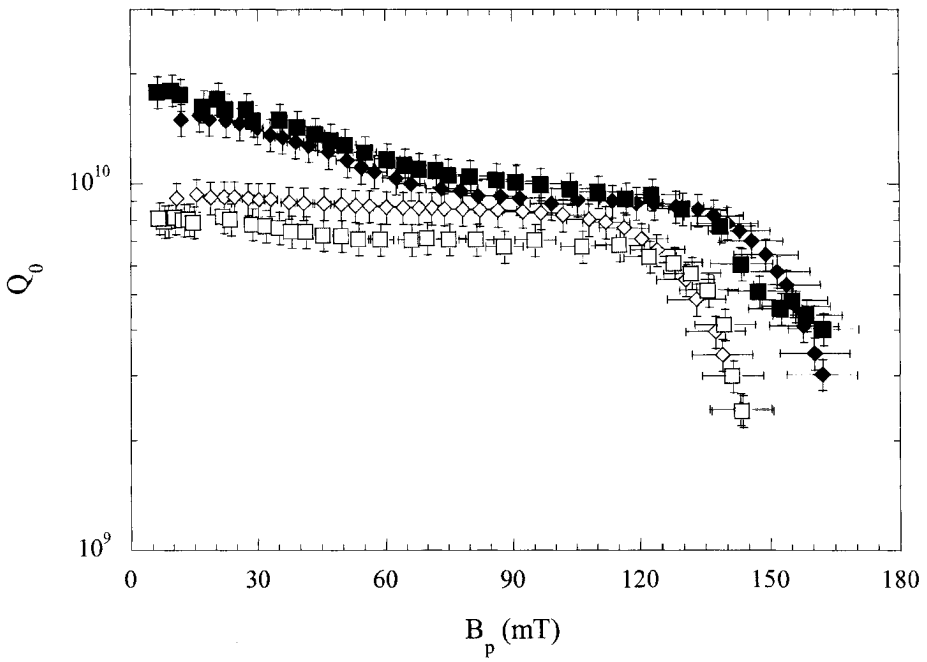

FIG. 98. Q_0 vs. B_p for two single cell cavities of the HG shape at 2.26 GHz, one made of single crystal (squares) and one made of standard polycrystalline niobium (diamonds) tested at 2 K before (open symbols) and after 120 °C, 48 h baking (solid symbols). The Q_0 degradation at high field in the single crystal cavity after baking was due to field emission.

The material parameters of both cavities before and after baking were obtained from a fit of the temperature dependence of the surface resistance at low field (B_p ~ 12 mT) with the BCS theory and they are summarized in Table XXII. In all cases, baking decreased the BCS surface resistance at 4.3 K by about 43% and the mean free path l(40 nm) to about 24 nm while increasing the residual resistance 2-10 nΩ. The energy gap at 0 K also increased by about 5% by baking. It is worthwhile to notice that the residual resistance of the single grain cavity was less than 1 nΩ before baking and this may be due to the absence of grain boundaries.

TABLE XXII. Material parameters of both single and polycrystalline niobium single cell cavities obtained from a fit of R_s vs. T with the BCS theory and surface resistance measured at 4.3 K and 2 K before and after baking at 120 °C for 48 h.

	Single crystal cavity				
	R_{BCS}(4.3 K) (nΩ)	R_{res} (nΩ)	R_s(2 K) (nΩ)	Δ(0 K)/kT_c	l(40 nm) (nm)
Baseline	2011 ± 160	0 ± 0.5	34 ± 3	1.76 ± 0.02	89 ± 30
Baked	1151 ± 92	1.5 ± 0.8	15 ± 1	1.94 ± 0.01	27 ± 130
Post-purified	1974 ± 158	0.8 ± 0.4	29 ± 2	1.83 ± 0.03	291 ± 83
Baked	1109 ± 90	10 ± 0.3	25 ± 2	1.90 ± 0.01	26 ± 140
	Polycrystalline cavity				
	R_{BCS}(4.3 K) (nΩ)	R_{res} (nΩ)	R_s(2 K) (nΩ)	Δ(0 K)/kT_c	l(40 nm) (nm)
Baseline	2013 ± 161	2.1 ± 0.4	30 ± 2	1.87 ± 0.03	659 ± 370
Baked	1156 ± 93	4.8 ± 0.2	18 ± 1	1.92 ± 0.02	15 ± 9

The medium field Q-slope has been fitted with Eq. (125) and the fitting coefficients $R_{res}{}^1$, γ^* and R_{s0} are given in Table XXIII at different temperatures, before and after baking for both single and polycrystalline cavities. Before baking, the dependence of R_s vs. B_p is mainly linear at all temperatures, with no clear temperature dependence of the slope ($R_{res}{}^1$). After baking, the data show a stronger increase of $R_{res}{}^1$ at 2 K up to a field $B_p \cong$ 65-70 mT, followed by a more quadratic increase. This behavior is clearly shown in Fig. 99 for the single crystal cavity. Similar conclusions hold for the polycrystalline cavity. The value of $R_{res}{}^1$ after baking is reduced at lower temperatures while γ^* is increased, as found in the analysis of the data in section 6.3.2, and the reasons for these dependencies are not yet clear. The relative variation of $R_{res}{}^1$ after baking as function of temperature is shown in Fig. 100, and is the same, within the errors, for the polycrystalline and single crystal cavity. The value of $R_{res}{}^1$, which describes hysteresis losses, is higher for the single crystal cavity than for the polycrystalline one. This result was found also in section 7.5.1. For the single crystal cavity, the process of deep-drawing half-cells from the single crystal disks introduces defects in the lattice and impurities could segregate there during the oxidation process.

TABLE XXIII. Fitting coefficients and correlation factor of Eq. (125) describing the medium field Q-slope data at different temperatures for the post-purified 2.2 GHz single crystal cavity and for the polycrystalline cavity before and after baking at 120 °C for 48 h.

	Post-purified single crystal cavity, before bake			
T (K)	R_{s0} (nΩ)	$R_{res}{}^{1}$ (nΩ)	γ^{*}	r^2
2	29.1 ± 0.2	12.3 ± 1.3	0.00 ± 0.06	0.983
1.84	18.3 ± 0.2	14.3 ± 1.1	0.00 ± 0.08	0.994
1.69	8.7 ± 0.2	11.8 ± 1.0	0.95 ± 0.14	0.997
1.55	4.2 ± 0.1	20.0 ± 0.6	0.00 ± 0.2	0.999
	Post-purified single crystal cavity, after bake			
T (K)	R_{s0} (nΩ)	$R_{res}{}^{1}$ (nΩ)	γ^{*}	r^2
2	24.3 ± 1.1	55.4 ± 2.1	1.03 ± 0.05	0.980
1.84	15.0 ± 1.0	43.5 ± 1.5	1.77 ± 0.13	0.978
1.69	11.8 ± 0.2	36.7 ± 0.6	2.52 ± 0.08	0.995
1.55	10.1 ± 0.2	24.5 ± 0.8	2.81 ± 0.07	0.975
	Polycrystalline cavity, before bake			
T (K)	R_{s0} (nΩ)	$R_{res}{}^{1}$ (nΩ)	γ^{*}	r^2
2	28.1 ± 0.3	9.3 ± 2.0	0.00 ± 0.13	0.946
1.84	16.0 ± 0.3	9.3 ± 2.0	0.00 ± 0.21	0.947
1.69	8.7 ± 0.2	9.6 ± 1.2	0.00 ± 0.23	0.987
1.55	4.6 ± 0.2	11.4 ± 1.2	0.00 ± 0.47	0.993
	Polycrystalline cavity, after bake			
T (K)	R_{s0} (nΩ)	$R_{res}{}^{1}$ (nΩ)	γ^{*}	r^2
2	13.8 ± 0.3	37.9 ± 1.6	0.69 ± 0.14	0.979
1.84	8.3 ± 0.3	30.7 ± 1.1	0.87 ± 0.09	0.979
1.69	6.5 ± 0.2	14.8 ± 1.0	1.50 ± 0.23	0.971
1.55	4.3 ± 0.1	14.6 ± 0.4	3.10 ± 0.10	0.987

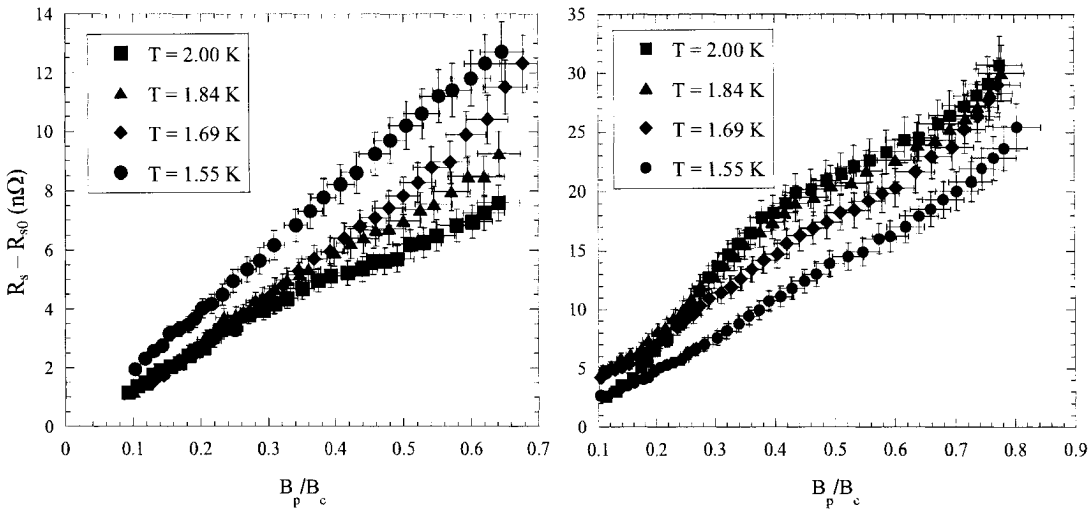

FIG. 99. Increase of surface resistance as function of B_p/B_c for the post-purified single crystal cavity measured at different temperatures before (left) and after 120 °C, 48 h baking (right).

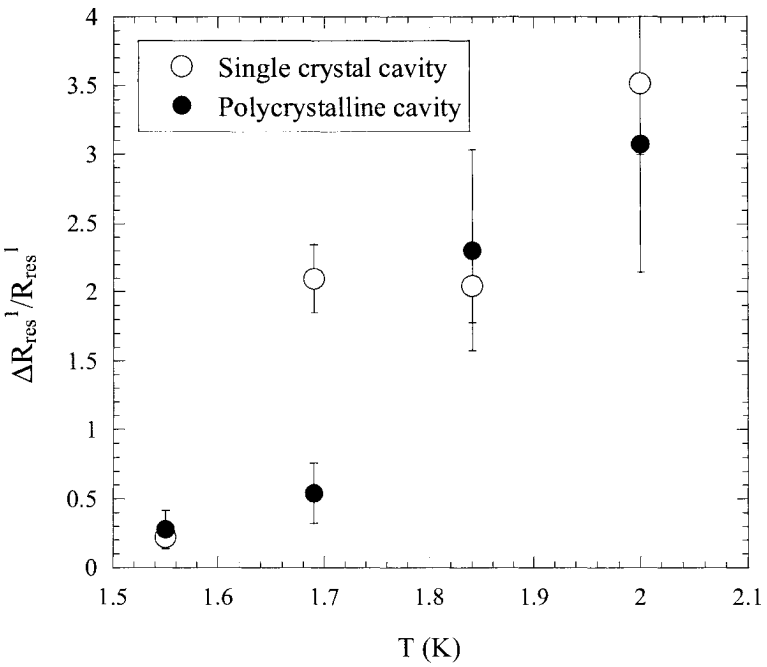

FIG. 100. Relative variation of the linear coefficient R_{res}^{-1} by baking as function of temperature for the single crystal and polycrystalline cavities.

The experimental data for the high field Q-drop have been compared to the ITE and MFE model and the fitting parameters are listed in Table XXIV. The presence of Q-drop in the single crystal cavity excludes quenches at grain boundaries as a cause of the high field losses and the fact that the surface of the cavity is smooth on a nanometer scale excludes roughness as a cause of the magnetic field enhancement, posing serious doubts about the MFE model. The calculations with the MFE model for the polycrystalline single cell were done assuming an average grain size of 50 μm.

TABLE XXIV. Fitting parameters of the ITE and MFE models of the high field Q-drop for the single crystal and polycrystalline single cell at different temperatures.

		Single crystal cavity				
		ITE model				
	T (K)	b (Ω)	c (MV/m)	E_0 (MV/m)		
Baseline	2	$1.8\ 10^7$	1874	-		
Post-purified	1.55	101	1369	54.4		
	1.69	62.8	1368	56.0		
	1.84	2000	1487	54.3		
	2	397	1378	54.9		
		Polycrystalline cavity				
		ITE model			MFE model	
	T (K)	b (Ω)	c (MV/m)	E_0 (MV/m)	β_0	σ
Baseline	1.55	0.099	854	-	1.14	0.0052
	1.69	0.87	955	-	1.14	0.0052
	1.84	12.0	1068	-	1.14	0.0055
	2	4.49	1015	-	1.12	0.0058
Baked at 120 °C, 48 h	1.55	4.99	1223	-	1.12	0.0031
	1.69	8.09	1271	-	1.08	0.0032
	1.84	42.7	1367	-	1.08	0.0032
	2	50.2	1353	-	1.10	0.0032

Figure 101 shows the electric surface resistance of both cavities at 2 K as function of E_p, fitted with the ITE model, and the surface resistance as function of B_p at 2 K for the

polycrystalline cavity before and after baking, fitted with the MFE model. The center of the field enhancement factor distribution (β_0) is approximately temperature independent and does not change significantly after baking, as expected from the model. The increase in the onset field of the Q-drop after baking is obtained with the MFE model by decreasing the width of the distribution of βs, which indicates that the losses disappeared in some locations.

The ITE model indicates a sharper slope for the single crystal cavity and the slope is approximately temperature independent. In most of the cases the value of the onset field E_0 could not be determined with Eq. (127) because the additive constant $-be^{-c/E_0}$ in the model turned out to be positive from the data fit.

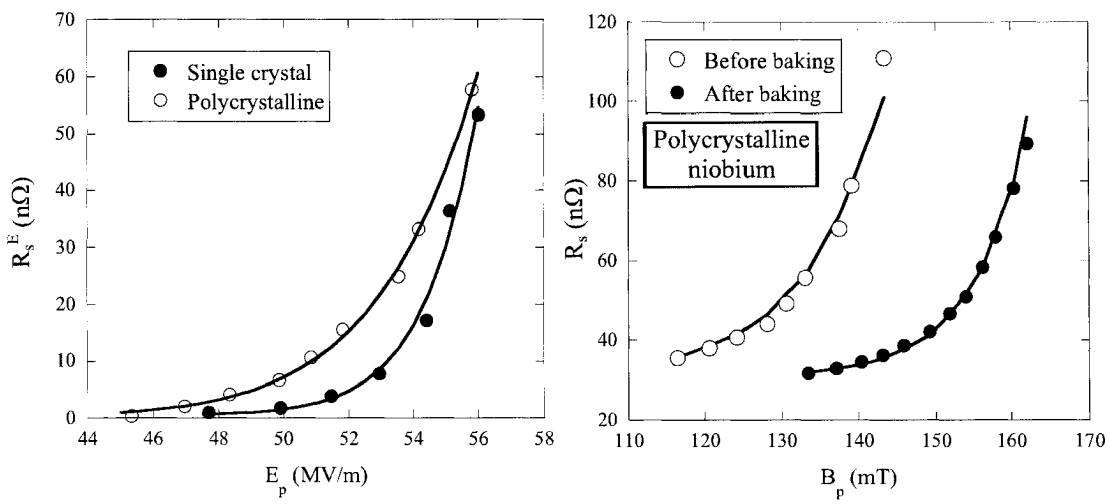

FIG. 101. Electric surface resistance at 2 K as function of E_p fitted with the ITE model (solid lines) for the single crystal and polycrystalline cavity (left), and surface resistance at 2 K as function of B_p fitted with the MFE model (solid lines) for the polycrystalline cavity before and after 120 °C, 48 h baking (right).

CHAPTER 9

DISCUSSION OF THE HIGH FIELD Q-DROP AND THE BAKING EFFECT

The characteristics of the high field Q-drop determined experimentally can be summarized as follows:

- the onset field is temperature independent, within errors
- heating starts to appear in localized areas in the equator region of the cavity, where the magnetic field is highest. The temperature of these hot-spots increases exponentially with higher rf fields
- the Q-drop is present in the TE_{011} mode which has only surface magnetic field, and the onset is ~ 15% higher than in the TM_{010} mode
- an oxide layer ~ 30 times thicker than the natural oxide on the niobium surface does not modify significantly any aspect of the Q-drop
- the Q-drop is present in a cavity made of single crystal niobium, with an exceptionally smoother surface
- the Q-drop is present in cavities treated by electropolishing, which results in smoother surfaces than BCP
- trapped flux due to a residual dc magnetic field does not change the Q-drop

The experimental findings on the effect of the low-temperature "in-situ" baking can be summarized as follows:

- the BCS surface resistance at low field decreases for increasing baking temperature and times and reaches a saturation point at about 120 °C, 48 h where the improvement is approximately 45%. This effect is due to a reduction of the mean free path from a few hundred nanometers to a few tens of nanometers and a slight increase of the energy gap (~ 5%). Deeper in the material (up to 300 nm) there is a steady decrease of the mean free path and a reduction of the surface *RRR* for baking temperatures higher than 120 °C

- the residual resistance increases 1-10 nΩ after baking. No clear correlation with the baking temperature was found, while the increase is smaller for shorter baking times
- higher tantalum content uniformly distributed in the niobium (up to about 1000 ppm) do not seem to affect the Q-drop [114]
- polycrystalline cavities treated by BCP show a shift to a ~ 16% higher onset field for the Q-drop onset but the high field losses are still present. There is no change in the Q-drop by baking at atmospheric pressure
- polycrystalline cavities with larger grains obtained by post-purification of niobium at temperatures greater than 1200 °C and treated by BCP recover from the Q-drop. The quench field becomes lower for baking temperatures higher than 120 °C
- the Q-drop in single crystal or very large crystal cavities treated by BCP is recovered by baking, regardless of post-purification
- the Q-drop of polycrystalline niobium cavities treated by electropolishing is recovered by baking, regardless of post-purification [8]
- the changes in the niobium material parameters and low field surface resistance by baking, outlined in the first bullet, are the same whether the high field Q-drop recovers or not
- the effect of baking is maintained even after several months of exposure of the cavity surface to air and successive HPR [115].

The experimental data summarized above are in contradiction with all the models proposed so far to explain the origin of the Q-drop cause and the baking effect:

- the ITE model explains the Q-drop as caused by enhanced surface resistance due to the electric field acting on localized electrons in the oxide states, but there is enough experimental evidence (temperature maps, TE_{011} test results, high-field cavity test results) showing the Q-drop to be caused by high magnetic fields
- the MFE model assumes the Q-drop to be caused by a geometric magnetic field enhancement due to rough areas on the cavity, but high field losses are also present in cavities with much smoother surfaces (single crystal and

electropolished) and the low-temperature baking does not modify the surface structure on a micrometer scale

- the analysis of the Q-drop data shows that the thermal resistance of niobium is low enough so that the TI model cannot explain the sharp decrease of the quality factor at about $B_p \approx 100$ mT
- the Q-drop is not caused by weakly linked grain boundaries becoming normal conducting at high field, since it has been observed on a cavity made of a single crystal.

The test results on resonant modes at different frequency seem also to show that there might be a frequency dependence of the Q-drop onset. None of the models takes this into account. Figure 102 shows the average onset of the Q-drop measured at different frequencies.

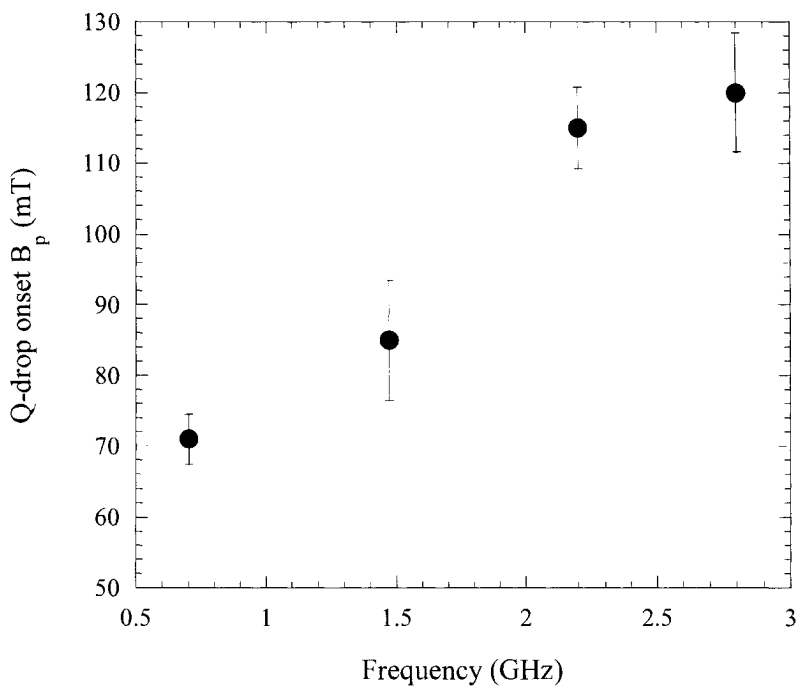

FIG. 102. Onset field of the high-field Q-drop as a function of frequency. The data point at 0.7 GHz is from [104], the one at 2.82 GHz is measured in the TE_{011} mode.

It is also interesting to plot the distribution of the onset of the Q-drop at 1.47 GHz (Fig. 103): before post-purification the average value is 87 ± 11 mT. After post-purification treatment the onset increases up to 104 ± 9 mT but it is distributed on a wider range of values. The Q-drop starts at higher fields in large grain cavities.

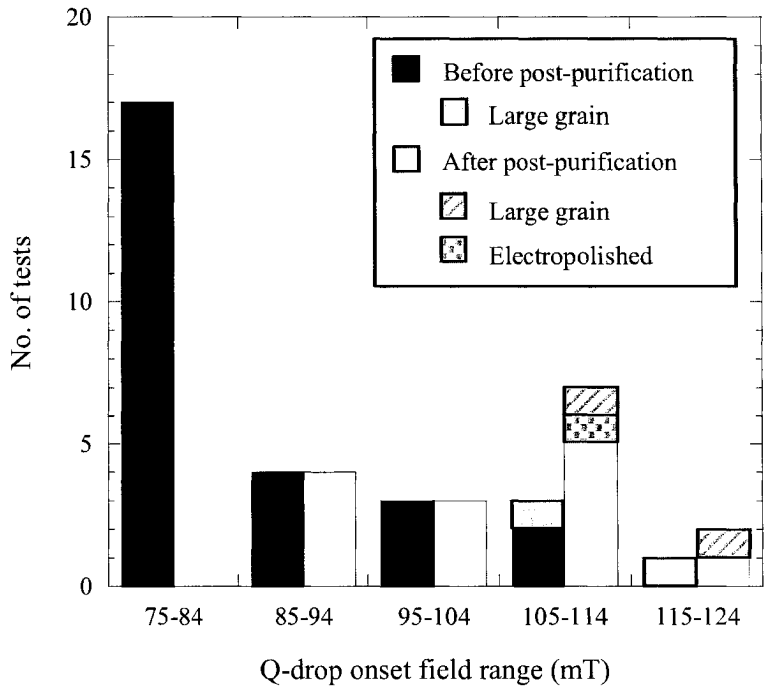

FIG. 103. Distribution of the Q-drop onset field for single cell cavities at 1.47 GHz before and after post-purification.

9.1 Oxygen diffusion model

As discussed in section 6.3, surface analysis of niobium samples indicate that baking at progressively higher temperatures produces a decomposition of the natural Nb_2O_5 layer to metallic suboxides (NbO, NbO_2) and oxygen diffusion in the niobium causing an overall reduction of the oxide layer thickness.

Measurements of the kinetics of the reduction of the niobium pentoxide on anodized niobium samples heated at 325 – 450 °C for 5 min shows the following sequence [116]

$$Nb_2O_5 \xrightarrow{k_1} NbO_2 \xrightarrow{k_2} NbO. \tag{132}$$

Ma and Rosenberg [88] measured the pre-exponential factor (A) and the activation energy (E_a) of the oxide total reduction rate (k) from Nb_2O_5 to NbO at about 200 °C, given by:

$$k(T) = Ae^{-E_a/RT} \tag{133}$$

with parameters $A \cong 3\times10^9$ 1/s and $E_a \cong 135$ kJ/mol.

Furthermore, interstitial oxygen is already present in the niobium before baking and concentration up to 10 at. % was measured in a nanometer thick layer next to the NbO/Nb interface [117]. Oxygen diffuses deeper in the niobium during bake-out and the diffusion coefficient (D) in the range 100-150 °C is given by [118]:

$$D(T) = 0.0138e^{-111530/RT} \ \left(\mathrm{cm^2/s}\right). \tag{134}$$

Up to now the analysis of the oxygen diffusion during bake-out has followed one of two extreme approaches: either the niobium surface is considered as an infinite source of oxygen (coming from the oxide layer) [118] or no additional source is present [119]. Surface analysis measurements show that some oxygen, besides the one already present interstitially, coming from the dissolution of the oxide layer may diffuse during bake-out. The diffusion process is modeled with a one-dimensional diffusion equation. In order to make the model more realistic, a time- and temperature-dependent source, representing the oxygen freed by the oxide dissolution, must be included:

$$\frac{\partial u(x,t)}{\partial t} = D(T)\frac{\partial^2 u(x,t)}{\partial x^2} + q(x,t,T) \tag{135}$$

here $u(x, t)$ represents the oxygen concentration. $q(x, t, T)$ is the source term given by:

$$q(x,t,T) = u_0 k(T) e^{-k(T)t}\delta(x). \tag{136}$$

The exponential time-dependence is given by the first-order reduction kinetic and the source is concentrated at the niobium/oxide interface at $x = 0$. Equation (135) can be solved by Fourier transformation and the solution is given by the following function

$$u(x,t) = \frac{u_0}{\sqrt{\pi D(T)}}\int_0^t \frac{k(T)e^{-k(T)s}}{\sqrt{t-s}} e^{-\frac{x^2}{4D(T)(t-s)}} ds. \tag{137}$$

The solution $v(x, t)$ of the homogeneous equation, representing the diffusion of the interstitial oxygen initially present in the niobium, must be added to Eq. (137)

$$v(x,t)=\frac{v_0}{\sqrt{4\pi D(T)t}}e^{-\frac{x^2}{4D(T)t}}, \tag{138}$$

where the value at $t = 0$, v_0, was chosen to be 10 at. % nm, as found in Ref. [117]. The general solution of the diffusion Equation (135) is then given by

$$c(x,t)=u(x,t)+v(x,t). \tag{139}$$

In this diffusion model, secondary effects such as the possibility of oxygen segregating into oxide clusters and surface anisotropy are not included.

Kneisel was able to measure the BCS surface resistance at 4.3 K after baking at 145 °C for 45 h at different depths by anodizing the surface up to a certain thickness and then removing the oxide layer with HF [11]. From the dependence of the surface resistance with mean free path given by the BCS theory, it is possible to obtain the mean free path at each depth and therefore the normal-state resistivity (ρ) through the material constant ρl (= 3.75×10^{-16} Ω m^2 for niobium [54]). The oxygen concentration can be obtained from its linear dependence with the resistivity, given in Ref. [58]

$$\rho(\mu\Omega\,\mathrm{cm})=4.99\,c_O(\mathrm{at.\ \%}). \tag{140}$$

A comparison (Fig. 104) of the data with the solution of the diffusion equation [Eq. (139)] allows estimating the value of the constant u_0 as of the order of 1000 at. % nm.

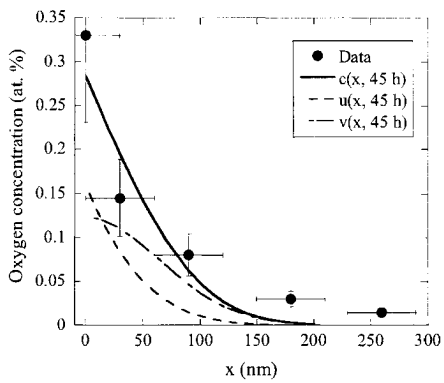

FIG. 104. Oxygen concentration as a function of depth obtained from BCS surface resistance measurements [11] and calculated from the diffusion equation with T = 145 °C, t = 45 h. The functions v and u represent the contribution due to the interstitial oxygen originally present and as a result of the oxide dissolution, respectively.

A calculation of the oxygen concentration at the niobium oxide interface ($x = 0$) with Eq. (139) for baking at different temperatures for 48 h (Fig. 105) shows that there is a minimum in the temperature range 130-145 °C. At lower temperatures the oxide layer does not dissociate significantly and the main contribution comes from the interstitial oxygen originally present, while at higher temperatures the concentration at the interface increases due to stronger oxide dissociation.

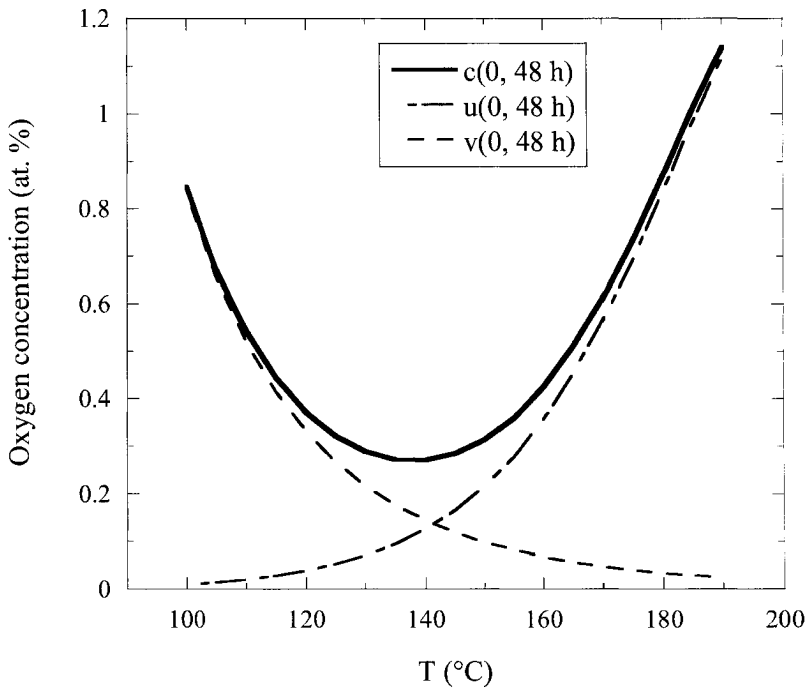

FIG. 105. Oxygen concentration at the niobium/oxide interface as a function of baking temperature. The functions v and u represent the contribution due to the interstitial oxygen originally present and as a result of the oxide dissolution, respectively.

The fact that oxygen is the impurity involved in the baking process and in the change of the material parameters is supported by the agreement between the data and the model, shown in Fig. 104. The most common other impurities in niobium are hydrogen, nitrogen and carbon. Hydrogen is very mobile even at room temperature (the diffusion constant at 300 K is of the order of 4×10^{-6} cm^2/s [120]) while nitrogen and carbon are far less mobile

than oxygen (the diffusion constant of nitrogen at 120 °C is about six orders of magnitude lower than for oxygen at the same temperature [121]). A sketch of the niobium surface before and after baking is given in Fig. 106 which shows the oxide reduction, oxygen diffusion and segregation upon cooling to room temperature.

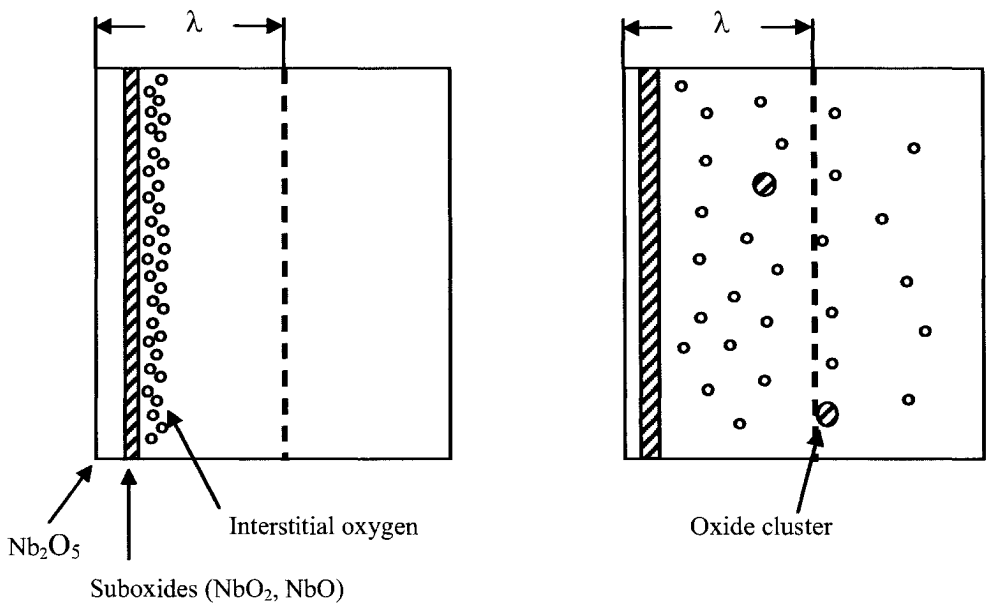

FIG. 106. Schematic representation of the niobium surface before (left) and after (right) low-temperature "in-situ" baking.

This model of oxygen diffusion can be usefully linked to the Q-drop and the baking effect influencing it by considering the role of impurities on the lower critical field of niobium. The analytical formula for H_{c1} given by Eq. (65) is valid only for materials with $\kappa_{GL} >> 1$ while for niobium ($\kappa_{GL} \approx 0.8$) a plot of the ratio B_{c1}/B_c as a function of κ_{GL}, obtained from a numerical solution of the Ginzburg-Landau equations, is shown in Fig. 107, from Ref. [122].

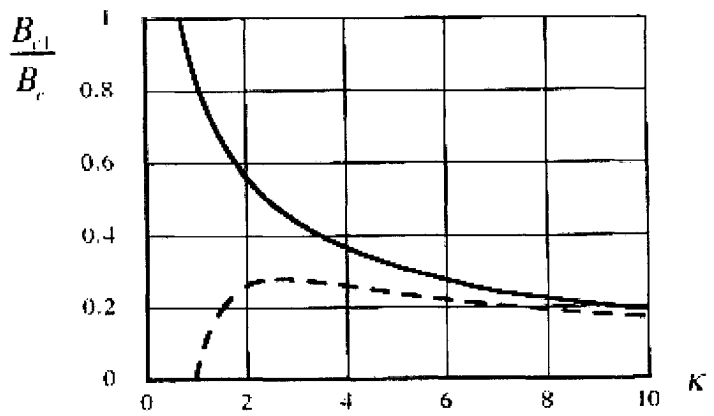

FIG. 107. B_{c1} as a function of the Ginzburg-Landau parameter showing the exact result (solid curve) and the large κ_{GL} approximation (broken curve) from [122].

If we assume that the Q-drop onset of about 90 mT represents B_{c1} of the niobium surface and B_c = 200 mT, the corresponding Ginsburg-Landau parameter from Fig. 107 is $\kappa_{GL} \cong 2.4$. Measurements of κ_{GL} of niobium for different interstitial oxygen concentrations show that $\kappa_{GL} \cong 2.4$ corresponds to about 0.56 at. % of oxygen [58], which is consistent with the quantity measured on the surface of niobium used for rf cavities. This idea suggests that, before baking, the presence of a significant amount of oxygen makes the niobium surface a stronger type II superconductor, with reduced H_{c1} (H_c is not altered significantly) while baking at the right temperatures (100-120 °C) dilutes oxygen deeper in the niobium, reducing κ_{GL} and increasing H_{c1} towards the value for pure niobium.

Baking at too high temperature increases the oxygen concentration near the surface, as shown in Fig. 105, and causes the observed degradation of the Q-drop and premature quench. In the case of baking in air rather than in ultra-high vacuum, there is an additional oxygen source from the ambient, which contributes to the pollution of the niobium surface and therefore preventing an improvement of the Q-drop.

Bean and Livingston [123] proposed in 1964 the existence of a surface barrier which inhibits flux entry at fields higher than H_{c1}. This effect was observed experimentally [124]; however, a reduction of this barrier in the presence of defects and irregularities on the surface was also measured, so that the field of first flux penetration is restored to H_{c1}

[125]. Flux penetration in niobium cavities may occur first in rougher regions of the surface, where the surface barrier is reduced.

Fluxoids penetrating the niobium surface are subjected to several forces [95]:

1. the Lorentz force $\mathbf{f}_L$ due to the transport current **J** flowing on the surface, given by

$$\mathbf{f}_L = \mathbf{J} \times \mathbf{B} \tag{141}$$

2. the image force $\mathbf{f}_I$, due to an "image" fluxoid of opposite orientation in the vacuum space to assure $J_\perp = 0$ on the surface, given in one dimension by

$$f_I = -\frac{\Phi_0^2}{2\pi\mu_0\lambda^3} K_1\left(\frac{2x}{\lambda}\right) \tag{142}$$

valid in the assumption of a perfectly flat surface

3. a viscous force $\mathbf{f}_V$, given by

$$\mathbf{f}_V = -\eta\mathbf{v} = -\left(\frac{B_{c2}}{\rho}\right)(\mathbf{J} \times \mathbf{n}) \tag{143}$$

where **n** is the unit vector along the vortex line

4. a pinning force $\mathbf{f}_P$, which depends on the type of pinning.

Figure 108 shows a schematic of the forces acting on a fluxoid inside the niobium in one dimension in the absence of pinning: in the positive half rf period, the fluxoid moves slowly towards the inside, while in the negative half rf period it moves outwards. The net result is an oscillatory motion of the fluxoid in the niobium. A detailed analysis of this motion would require a detailed knowledge of all the acting forces.

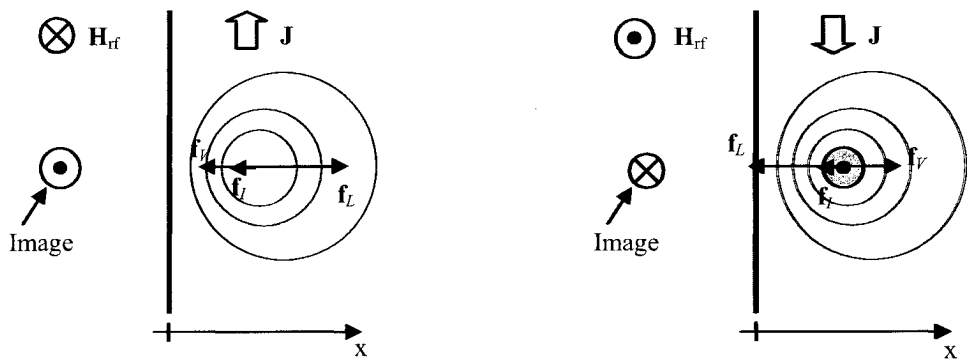

FIG. 108. Schematic representation of the forces acting on a fluxoid inside the niobium during the positive (left) and negative (right) half rf period.

An Abrikosov fluxoid inside the niobium generates losses due to its normal conducting core and to its resistive motion and would cause the quality factor of the cavity to rapidly decrease for increasing rf field. A Q-drop caused by normal-conducting fluxoids might be consistent with the observed frequency dependence of the onset field: at higher frequencies, the rf field at the surface would change faster than the fluxoid nucleation time. The speed of flux penetration in niobium was measured to be about 40 m/s [44], which would correspond to about 13 nm at a 1.5 GHz rf field and decrease at higher frequencies. This is of the order of the magnetic field penetration depth.

Rabinowitz [126] was able to estimate the power loss due to a single isolated fluxoid trapped near the surface of a superconductor in the presence of rf field. He calculated that the dependence of the surface resistance from the peak magnetic field, above the onset of flux penetration, is given by

$$R_s\left(B_p\right) \propto e^{B_p/D}, \tag{144}$$

where D is given by[8]

$$D = \frac{\mu_0 \Delta(0\mathrm{K})}{kF} \sqrt{\frac{\kappa_1}{NRa\ln(b/a)}}. \tag{145}$$

The function F is given by

$$F = e^{-d/\lambda} \sqrt{1.57 \mathrm{I}_1(2a/\lambda)} \tag{146}$$

where d is the distance of the center of the fluxoid from the surface of the superconductor, a is the radius of the fluxoid and I_1 is the first order modified Bessel function of the first kind. The function R is given by

$$R = \frac{\rho}{2\pi\lambda} \tag{147}$$

where ρ is the effective normal state resistivity, which depends on whether the viscous force dominates or not. N is a factor to correct for the departure from cylindrical symmetry, b is the wall thickness and κ_1 is the derivative of the thermal conductivity $d\kappa/dT$ in the range 3 to 9 K. The results from the fit of the Q-drop data from all cavity tests with Eq. (144) are given in Appendix C.

---

[8] In the case of a fluxoid parallel to the surface.

Rabinowitz [127] was also able to show that in the case of negligible viscous damping and negligible pinning, the onset field for flux penetration is linearly proportional to the rf frequency, consistently with the data shown in Fig. 102. However, the results shown in Fig. 68 indicate that fluxoids trapped in the niobium due to a residual dc magnetic field do not create additional high field losses: this could be due to the fact that they are pinned during the cool-down below T_c and the Lorentz force acting on them might not be stronger than the pinning force.

The effect of baking on cavities with different grain size could be related to the particular mechanism of diffusion along grain boundaries and requires further investigation. The fact that the change on the low-field material parameters by baking appears to be virtually independent of the high field behavior could be due to the fact that those parameters are obtained by comparison of the BCS theory with the surface impedance averaged over the whole cavity surface. Temperature maps show that heating occurs at rather localized regions of the cavity and the material parameters in those locations might deviate significantly from the average.

Another model to explain the high field Q-drop proposed by Saito [128] invokes a magnetic field dependence of the energy gap given by:

$$\frac{\Delta(H_p)}{\Delta(0)} = \sqrt{1-\left(\frac{\beta H_p}{\sqrt{2}H_c}\right)^2}, \tag{148}$$

with β being the geometric field enhancement factor. Equation (148) yields approximately an exponential dependence of the surface resistance on the magnetic field allowing a good fit of the data (H_c/β being a fit parameter). Although such $\Delta(H)$ dependence has been measured on thin films, both theory and experiments agree that for $T << T_c$ and in the clean limit (niobium surface before baking) the energy gap is independent of the magnetic field in bulk superconductors with thickness at least ten times larger than the penetration depth [129, 130].

The measurements of the rf surface resistance suggest that the energy gap might vary spatially, being lower on the surface, possibly due to metallic suboxides, and closer to the theoretical value for a pure material in the bulk. The thin (thickness $\approx$ 0.5-1 nm) metallic suboxide layer becomes superconducting by proximity but might quench at high fields,

introducing additional losses. Nevertheless, the Q-drop is recovered by baking which increases the thickness of the suboxide layer. An attempt has been made as shown below to model the experimental data with a thermal analysis.

9.2 Thermal analysis

The thermal behavior of a quarter of a niobium disk 3 mm thick, 1.5 cm radius has been analyzed using ANSYS™ Workbench 9.0 [131] in order to verify whether the additional heat generated in the Q-drop is compatible with an area of the cavity becoming normal-conducting. In the simulation, a circular area of 100 μm radius at the center of the disk is supposed to become normal-conducting, with R_s = 1.8 mΩ, at B_p = 90 mT. The heat flux generated is given by

$$q = \frac{1}{2} R_s H^2. \tag{149}$$

The rest of the surface is superconducting and the heat flux generated by the rf field is given by Eq. (149) with R_s being the temperature dependent BCS surface resistance [Eq. (98)] plus the residual component. The boundary condition on the top surface of the disk is given by convection, simulating the Nb/He bath interface, with a temperature dependent film coefficient given by the Kapitza conductance $H_K(T_b, T_s)$ [132]

$$H_K\left(T_b, T_s\right) = 200 T_b^{4.65}\left[1 + 1.5\left(\frac{T_s}{T_b} - 1\right) + \left(\frac{T_s}{T_b} - 1\right)^2 + 0.25\left(\frac{T_s}{T_b} - 1\right)^3\right]\left(\frac{\mathrm{W}}{\mathrm{m^2K}}\right) \tag{150}$$

valid for T_s-$T_b \leq$ 1.4 K. T_s and T_b are the temperature of the niobium surface and of the helium bath (2 K) respectively. The temperature dependent thermal conductivity of niobium for $RRR \sim 300$ used for the simulation is shown in Fig. 109 [99]. The temperature distribution in the disk for B_p = 90 mT is shown in Fig. 110. The simulation has been repeated for different values of peak surface magnetic field and defect size and Fig. 111 shows the temperature rise at a point on the outer surface in the center of the disk, along with the results from the "defect-free" TI model and the experimental data for the hot-spot shown in Fig. 57.

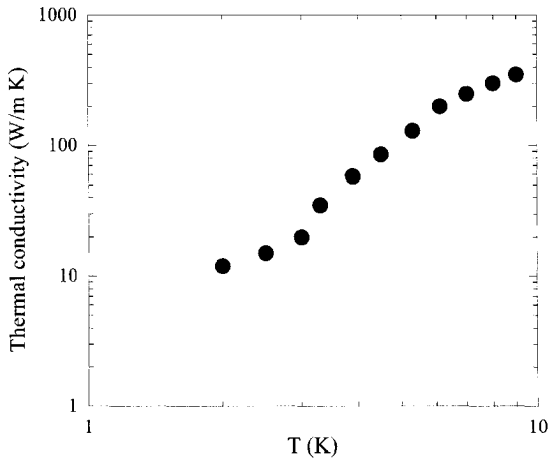

FIG. 109. Thermal conductivity of *RRR* ~ 300 niobium used for the thermal analysis [99].

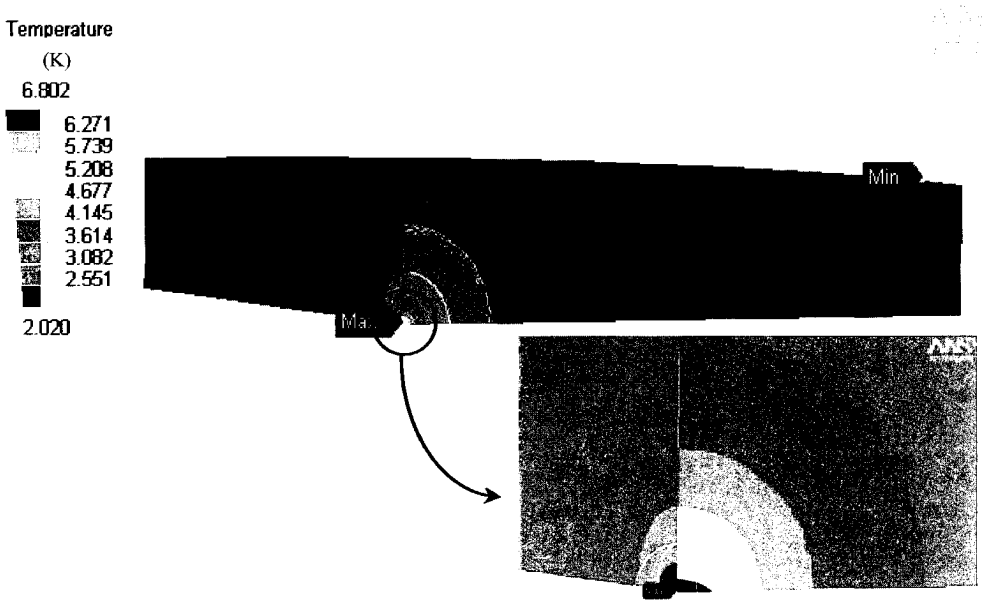

FIG. 110. Temperature distribution in a quarter section of a niobium disk with a normal-conducting area 100 μm radius at the center with a field of B_p = 90 mT applied to the bottom surface. The top surface is cooled by liquid helium at 2 K.

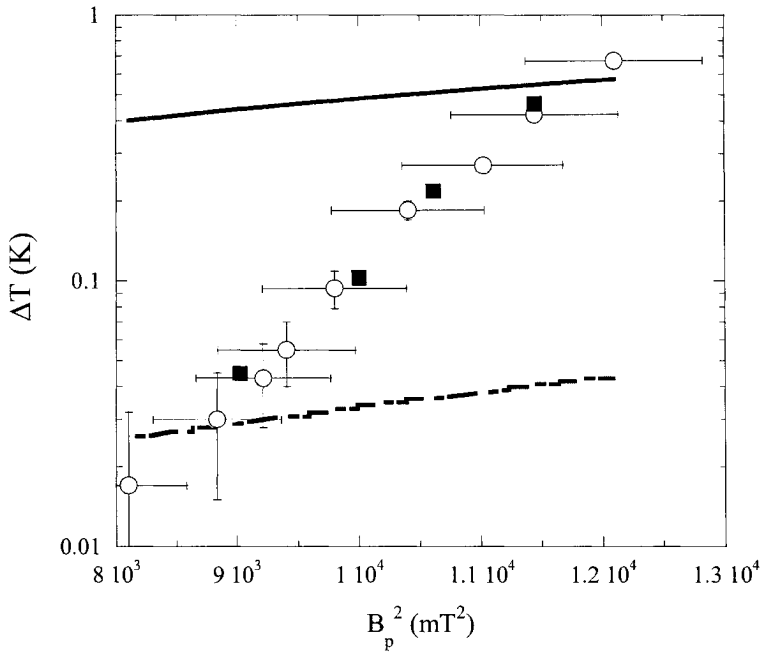

FIG. 111. Temperature rise of a hot spot (open circles) in the Q-drop region measured by a thermometer on the outer cavity surface (Fig. 57) compared with ΔT on the outer surface on top of a normal conducting area (100 μm radius) in a 3 mm thick niobium calculated with ANSYS™ (solid line) and surface heating predicted by the TI model in absence of any defect (dashed line). Also shown are the results from the thermal analysis done with increasing defect size at increasing field (solid squares), as in Fig. 112. The simulation predicts a quench for defect radius > 100 μm at B_p = 110 mT.

The results from the simulation show that the experimental data could be well reproduced[9] by assuming a normal conducting region growing with field only up to B_p = 110 mT, above which a quench is predicted (at 110 mT the transition temperature is 6.2 K), but not observed experimentally. Since the cavity is thermally stable up to 110 mT, the only possible explanation for the growth of the normal conducting area with field is by introducing a field enhancement factor. Figure 112 shows the defect radius as a

[9] We neglect the efficiency of the thermometer, which is about 35%.

function of B_p^2 and the field enhancement factor β (= B_c/B_p) as a function of the defect radius.

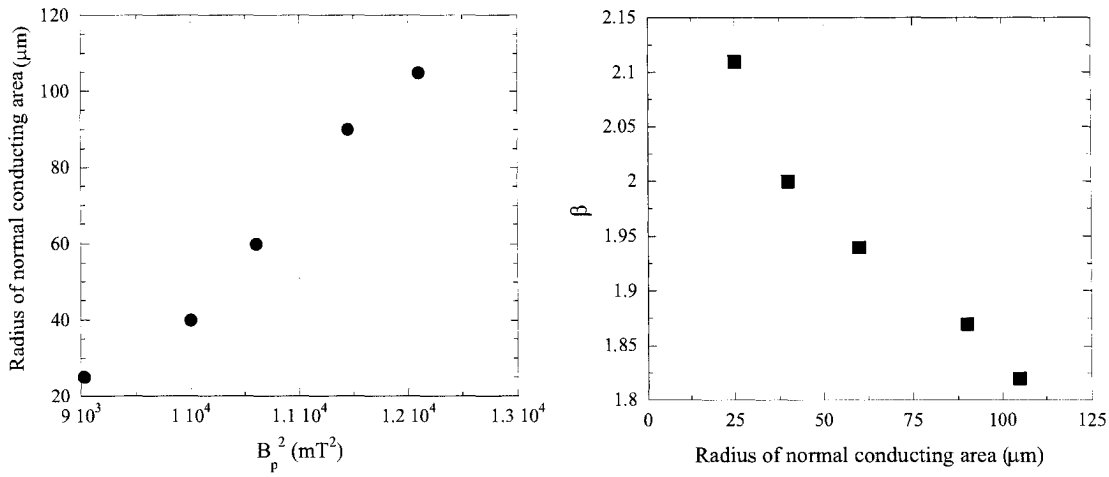

FIG. 112. Radius of the normal conducting area as a function of B_p^2 which gives good agreement between the thermal analysis simulation and the thermometry data (left) and corresponding field enhancement factor as a function of the radius of the normal conducting area (right).

Although a β value of about 2 is possible at a sharp corner [14], it will rapidly decrease a few microns away from the edge, while Fig. 112 shows that it would reduce only by about 15% over a distance of about 100 μm. The roughest region of the cavity surface is at the equator weld [133], where the magnetic field is close to the peak value in the TM_{010} mode, and there exist measurements which indicate a degradation of cavity performance due to defective welds [108]. In the measurement of the TE_{011} mode, where the peak field is away from the weld, the onset of the Q-drop is about 20% higher than in the TM_{010} but this could be due to a frequency dependence of the onset, as shown in Fig. 102, rather than a smoother surface. In order to fully investigate the role of the weld and possible geometric field enhancements on the Q-drop, future tests will be conducted on seamless cavities.

Figure 113 shows the temperature rise along the cavity contour at different field levels for thermometers on the same board, showing an expansion of heat-affected zone. The temperature distribution on the outer surface of the disk used for the thermal simulation is narrower than the one from the data.

In conclusion, Fig. 111 shows that a field-independent surface resistance used in the finite element model and the quadratic field dependence used in the TI model both are not adequate to describe the temperature rise in a hot-spot causing the Q-drop, measured with a thermometer on the outer cavity surface.

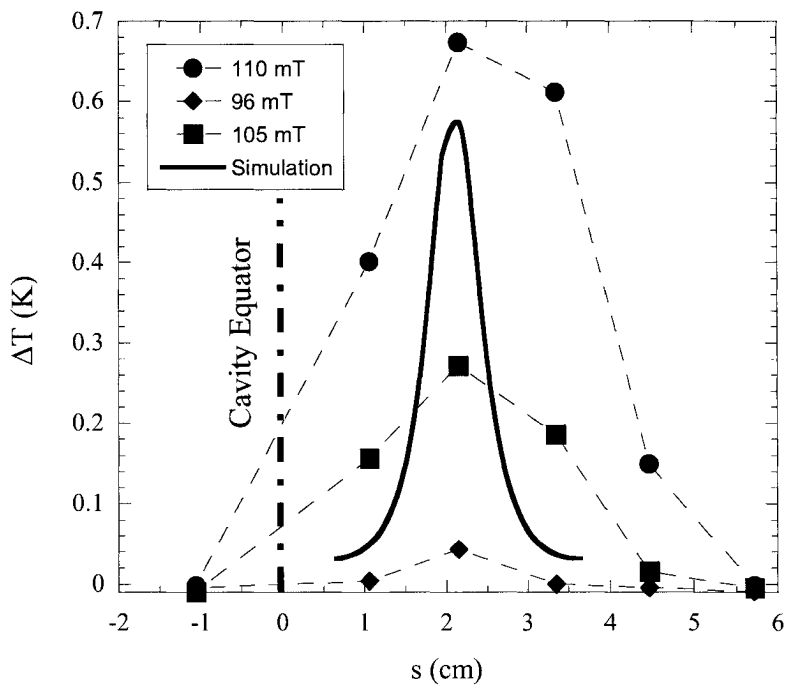

FIG. 113. Temperature rise of a hot spot (No. 1 in Fig. 57) along the cavity contour for thermometers on the same board, at different field levels. Superimposed is the temperature distribution calculated with ANSYS™ for a niobium disk with a normal conducting area (100 μm radius) at a field level of 110 mT.

CHAPTER 10

CONCLUSIONS

The data reported in this thesis present a systematic experimental investigation of the effect of different surface treatments and metallurgical properties of high purity niobium on the rf losses in superconducting cavities at low, medium and high field regimes and on the niobium material parameters at different depths. In particular, the effects produced by a low-temperature "in-situ" baking were examined in details because of its importance to achieve high accelerating fields with reduced losses.

The niobium material parameters up to a depth of about 40 nm and 300 nm were obtained from a comparison of the low-field surface resistance with the BCS theory in the range 1.37–4.3 K and 7–9.25 K respectively. The results show that the energy gap at the surface is about 6% lower than it is deeper in the bulk, due to the presence of an oxide layer. The normal electrons' mean free path at the surface is about 200 nm and increases by about one order of magnitude in the bulk. The residual resistance ranges between 2-10 nΩ.

Low-temperature "in-situ" baking reduces the mean free path on the surface to about 25 nm while increasing the energy gap by 5% at the most. These changes cause a reduction of the BCS surface resistance up to 45% at the optimum baking parameters of 120 °C for 48 h. The description of the BCS surface resistance changes from the "clean" to the "dirty" limit behavior by baking. The residual resistance increases by about 4–5 nΩ. Higher baking temperatures cause a significant reduction of the mean free path and of the *RRR* in a depth up to 300 nm. These observations can be explained by oxygen, already interstitially present near the surface and coming from the oxide layer, diffusing in the niobium, consistently with the results from surface analysis techniques. Although measurements on hydrogen are not yet conclusive, it appears that it is not involved in the changes of the material parameters produced by baking.

The surface resistance of niobium in the gigahertz range is sometimes observed to decrease for peak surface magnetic fields up to about 20 mT. The data shown in

Chapter 6 can be successfully described by a model based on non-equilibrium superconductivity at the niobium surface caused by oxide precipitates. This effect is enhanced by the low-temperature baking due to oxygen diffusion. However, it is difficult to predict the presence of this effect before testing a cavity with a freshly prepared surface due to its dependence on the detailed history, preparation and cleaning conditions and impurity content of the material.

The surface resistance is observed to increase at higher field, up to $B_p \cong 80$ mT, with a dependence which includes linear and quadratic terms in B_p. A linear dependence of R_s vs. B_p is explained by hysteresis losses due to "strong-links" formed on the niobium surface during oxidation. A quadratic dependence is related to an overheating of the surface due to the poor heat transfer to the helium bath. Theoretically, it has been calculated that the BCS surface resistance has an intrinsic quadratic dependence on the rf field, but a comparison of this model with data taken at 2 K shows that this contribution is overestimated. The effect of the low-temperature baking is to increase the slope of R_s vs. B_p and the dependence becomes more markedly linear and this could be linked to an increased number of "strong-links" with reduced critical current density due to oxygen diffusion. A post-purification of the niobium reduces the quadratic term due to lowered thermal resistance. Although there is good agreement between the values of the linear and quadratic terms at 2 K and for various frequencies with the predictions of the models, there is no clear explanation for their temperature dependence. The measurements also show that the linear term is higher for cavities with wider grain boundaries, similarly to cavities made by sputtered niobium thin films, and this could be due to stronger impurity segregation. The influence of the gas species on the outside of a cavity during "in-situ" baking is not clear and needs additional investigation. It should also be remarked that there exists a significant scatter in the values of the slope on cavities treated in the same way [134] and this indicates that all the parameters which influence it are not yet clear and under control. It is also possible that losses contributing to the medium field slope are localized rather than uniformly distributed on the surface.

Although field emission is still the major technological limitation towards reliably achieving high accelerating fields in multi-cell cavities, a new source of additional losses appears at $B_p \cong 90$ mT with a sharp, exponential increase of the surface resistance. These

losses have been found on all niobium cavities, independent of the surface preparation (EP, BCP, anodization) roughness or crystallographic properties (fine grain, single grain) of the material, although the onset field seems to depend on those parameters.

Measurements of the TE_{011} mode and of two modes of a "high field" cavity with different B_p/E_p showed that the cause of the Q-drop is a high magnetic field. Temperature maps showed that losses occur at several localized areas near the equator, where the magnetic field is maximum in the TM_{010} mode. The temperature rises exponentially with field which is incompatible with ohmic-type losses. The effect of "in-situ" baking on BCP-treated cavities is to increase the onset field for fine grain niobium while it allows an overall reduction of the Q-drop in cavities with reduced number of grain boundaries.

These observations provide substantial arguments against any of the Q-drop models proposed so far, although they can fit the data very well. We propose a model based on reduced B_{cl} due to oxygen contamination, allowing fluxoids to oscillate in the cavity surface due to the rf field and generating additional losses. Baking at the optimum temperature allows a reduction of the near-surface oxygen concentration, therefore restoring the proper B_{cl} of pure niobium. The oxygen diffusion mechanism depends critically on the surface morphology and seems to be more effective on smooth surfaces with reduced number of grain boundaries. A baked single crystal cavity achieved a B_p close to the critical field of niobium for a few hundred milliseconds.

A complete understanding of the origin of the high field Q-drop will require further experimental investigation. In particular, it seems necessary to reproduce these high field losses on niobium samples, which could be analyzed by surface analysis methods in order to identify differences between lossy and loss-free areas. Further progress from the theoretical point of view is also necessary, to try to give a coherent explanation to the significant amount of data already collected over the last few years. These challenges are important for a deeper understanding of rf superconductivity and for applications such as the International Linear Collider project, which requires performance levels close to the fundamental limit of the material.

REFERENCES

[1] http://www.sns.gov

[2] http://xfel.desy.de/content/e169/index_eng.html

[3] J. A. Nolen, in *Proceedings of the 2002 Linear Accelerator Conference, Gyeongju, 2002,* edited by Inn Soo Ko (POSTECH, Pohang, South Korea, 2002), p. 29.

[4] Report of the European Technical Working Group on ADS, 2001.

[5] http://jkj.tokai.jaeri.go.jp

[6] http://www.interactions.org/linearcollider

[7] http://www.jlab.org

[8] L. Lilje, in *Proceedings of the 2004 European Particle Accelerator Conference, Lucerne, 2004,* edited by J. Poole *et al.* (PSI, Villigen, Switzerland, 2004), p. 129.

[9] P. Kneisel, K. Saito, and R. Parodi, in *Proceedings of the 8th Workshop on RF Superconductivity, Abano Terme, 1997*, edited by V. Palmieri and A. Lombardi (LNL-INFN, Legnaro, Italy, 1998), p. 463.

[10] E. Kako *et al.*, in *Proceedings of the 8th Workshop on RF Superconductivity, Abano Terme, 1997* (Ref. [9]), p. 491.

[11] P. Kneisel, in *Proceedings of the 9th Workshop on RF Superconductivity, Santa Fe, NM, 1999*, edited by Krawczyk (Los Alamos National Laboratory, Santa Fe, NM, 2000), p. 328.

[12] B. Visentin, J. P. Charrier, and B. Coadou, in *Proceedings of the 1998 European Particle Accelerator Conference, Stockholm, 1998,* edited by S. Myers *et al.* (Institute of Physics Publishing, Bristol, UK, 1998), p. 1885.

[13] J. Halbritter, Z. Physik B **31**, 19 (1978).

[14] J. Knobloch, R. L. Geng, M. Liepe, and H. Padamsee, in *Proceedings of the 9th Workshop on RF Superconductivity, Santa Fe, NM, 1999* (Ref. [11]), p. 77.

[15] B. Bonin and H. Safa, Supercond. Sci. Technol. **4**, 257 (1991).

[16] S. Ramo, J. R. Whinnery, and T. Van Duzer, *Fields and Waves in Communication Electronics* (Wiley & Sons, New York, 3rd edition, 1993).

[17] J. H. Billen and L. M. Young, Los Alamos National Laboratory Report No. LA-UR-96-1834, 2004.

[18] http://www.ansoft.com

[19] http://www.cst.com

[20] J. Knobloch, Ph. D. Thesis, Cornell University, 1997.

[21] H. Kammerlingh Onnes, Electrician **67**, 657 (1911).

[22] W. Meissner and R. Ochsenfeld, Naturwissenshaften **21**, 787 (1983).

[23] E. Maxwell, Phys. Rev. **78**, 477 (1950).

[24] R. E. Glover and M. Tinkham, Phys. Rev. **104**, 844 (1956).

[25] W. S. Corak, B. B. Goodman, C. B. Satterthwaite, and A. Wexler, Phys. Rev. **102**, 656 (1956).

[26] C. J. Gorter and H. B. G. Casimir, Physica **1**, 306 (1934).

[27] F. and H. London, Proc. R. Soc. London, Ser. A **149**, 71 (1935).

[28] F. London, *Superfluids* (Wiley & Sons, New York, 1950), Vol. 1.

[29] A. B. Pippard, Proc. R. Soc. London, Ser. A **216**, 547 (1953).

[30] J. Bardeen, L. N. Cooper, and J. R. Schrieffer, Phys. Rev. **108**, 1175 (1957).

[31] T. P. Sheenhan, Phys. Rev. **149**, 368 (1966).

[32] V. L. Ginzburg and L. D. Landau, Zh. Eksp. Teor. Fiz. [Sov. Phy.-JETP] **20**, 1064 (1950).

[33] L. P. Gor'kov, Zh. Eksp. Teor. Fiz. [Sov. Phy.-JETP] **36**, 1918 (1959).

[34] M. Tinkham, *Introduction to Superconductivity* (McGraw-Hill, New York, 1996).

[35] J. Halbritter, Z. Phy. **243**, 201 (1971).

[36] G. E. H. Reuter and E. H. Sondheimer, Proc. R. Soc. London, Ser. A **195**, 336 (1948).

[37] J. Halbritter, Z. Phy. **266**, 209 (1974).

[38] J. Halbritter, Forschungszentrum Karlsruhe Report No. FZK 3/70-6, (1970).

[39] A. A. Abrikosov, Zh. Eksp. Teor. Fiz. [Sov. Phy.-JETP] **32**, 1442 (1957).

[40] A. C. Rose-Innes and E. H. Rhoderick, *Introduction to Superconductivity* (Pergamon Press, New York, 1978).

[41] D. Saint-James, G. Sarma, and E. J. Thomas, *Type II Superconductivity* (Pergamon Press, Oxford, 1969).

[42] D. Saint-James and P. G. de Gennes, Phys. Lett. **7**, 306 (1963).

[43] J. Matricon and D. Saint-James, Phys. Lett. A **24**, 241 (1967).

[44] R. B. Flippen, Phys. Lett. A **17**, 193 (1965).

[45] T. Yogi *et al*, Phys. Rev. Lett. **39**, 826 (1977).

[46] K. Saito, in *Proceedings of the 11th Workshop on RF Superconductivity, Travemünde, 2003*, edited by D. Proch (DESY, Hamburg, Germany, 2004), MoO02.

[47] T. Hays and H. Padamsee, *Proc. of the 8th Workshop on RF Superconductivity*, (Ref. [9]) p. 789.

[48] J. P. Turneaure, J. Halbritter, and H. A. Schwettman, J. of Supercond. **4**, 341 (1991).

[49] J. P. Turneaure and I. Weissman, J. Appl. Phys. **39**, 4417 (1968).

[50] P. Kneisel, O. Stoltz, and J. Halbritter, J. Appl. Phys. **45**, 2296 (1974).

[51] S. Casalbuoni, L. von Sawilski, and J. Kotzler, in *Proceedings of the 11th Workshop on RF Superconductivity, Travemünde, 2003* (Ref. [44]), WeO13.

[52] D. K. Finnemore, T. F. Stromberg, and C. A. Swenson, Phys. Rev. **149**, 231 (1966).

[53] C. P. Poole, Jr., *Handbook of Superconductivity* (Academic Press, San Diego, 2000).

[54] R. A. French, Cryogenics **8**, 301 (1968).

[55] A. T. Fromhold and E. L. Cook, Phys. Rev. **158**, 158 (1967).

[56] J. Halbritter, Appl. Phys. A **43**, 1 (1987).

[57] J. Halbritter, IEEE Trans. Appl. Supercond. **11**, 1864 (2001).

[58] C. C. Koch, J. O. Scarbrough, and D. M. Kroeger, Phys. Rev. B **9**, 888 (1974).

[59] B. Piosczyk, P. Kneisel, O. Stoltz, and J. Halbritter, IEEE Trans. Nucl. Sci. **20**, 108 (1973).

[60] B. Bonin and R. W. Röth, in *Proceedings of the 5th Workshop on RF Superconductivity*, edited by D. Proch (DESY, Hamburg, Germany, 1991), p. 210.

[61] J. Halbritter, in *Proceedings of the 2nd Workshop on RF Superconductivity*, edited by H. Lengeler (CERN, Geneva, Switzerland, 1984), p. 427.

[62] J. Halbritter, in *Proceedings of the 38th Eloisatron Workshop, Erice, 1999*, edited by L. Cifarelli and L. Maritato (University of Salerno, Salerno, Italy, 2001), p. 9.

[63] H. Safa *et al.*, in *Proceedings of the 9th Workshop on RF Superconductivity, Santa Fe, NM, 1999* (Ref. [11]), p. 267.

[64] A. Dacca, Ph. D. Thesis, INFN and University of Genoa, 2000.

[65] K. Saito, in *Proceedings of the 10th Workshop on RF Superconductivity, Tsukuba, 2001*, edited by S. Noguchi *et al.* (KEK, Tsukuba, Japan, 2003), p. 419.

[66] R. H. Fowler and L. Nordheim, Proc. R. Soc. London, Ser. A **119**, 173 (1928).

[67] P. Kneisel, in *Proceedings of the 6th Workshop on RF Superconductivity, Newport News, 1993*, edited by R. M. Sundelin (TJNAF, Newport News, VA, 1994), p. 628.

[68] H. Padamsee, J. Knobloch, and T. Hays, *RF Superconductivity for Accelerators* (Wiley & Sons, New York, 1998).

[69] W. Singer, D. Proch, and A. Brinkmann, in *Proceedings of the 8th Workshop on RF Superconductivity, Abano Terme, 1997* (Ref. [9]), p. 850.

[70] P. Kneisel, J. Less Common Met. **139**, 179 (1988).

[71] J. Halbritter, in *Proceedings of the 10th Workshop on RF Superconductivity, Tsukuba, 2001* (Ref. [62]), p. 292.

[72] J. Halbritter, in *Proceedings of the 1st Workshop on RF Superconductivity, Karlsruhe, 1980*, edited by M. Kuntze (Institut für Kerphysik, Karlsruhe, Germany, 1980), p. 190.

[73] B. Visentin, J. P. Charrier, B. Coadou, and D. Roudier, in *Proceedings of the 9th Workshop on RF Superconductivity, Santa Fe, NM, 1999* (Ref. [11]), p. 198.

[74] A. Gurevich, in *Proceedings of the Pushing the Limits of RF Superconductivity Workshop, Argonne, 2004*, edited by K.-J. Kim and C. Eyberger (ANL, Argonne, IL, 2005) p. 17.

[72] K. Saito *et al.*, in *Proceedings of the 4th Workshop on RF Superconductivity, Tsukuba, 1989*, edited by Y. Kojima (KEK, Tsukuba, Japan, 1990), p. 635.

[76] C. Z. Antoine *et al.*, in *Proceedings of the 9th Workshop on RF Superconductivity, Santa Fe, NM, 1999* (Ref. [11]), p. 295.

[77] K. Zapfe-Duren, F. Herrmann, D. Hubert, and P. Schumser, in *Proceedings of the 8th Workshop on RF Superconductivity, Abano Terme, 1997* (Ref. [9]), p. 457.

[78] J. Halbritter, J. Appl. Phys. **41**, 4581 (1971).

[79] G. Müller and P. Kneisel, Cornell University Report No. SRF 851291 EX, 1985.

[80] W. A. Lanford, Nucl. Instrum. Methods Phys. Res. B **66**, 65 (1992).

[81] A. Phillipp and J. Halbritter, IEEE Trans. Magn. **19**, 999 (1983).

[82] R. Schwab, Forschungszentrum Karlsruhe Report No. 6023, 1997.

[83] E. L. Wolf, J. Zasadzinski, J. W. Osmun, and G. B. Arnold, J. Low Temp. Phys. **40**, 19 (1980).

[84] B. W. Maxfield and W. L. MacLean, Phys. Rev. **139**, 1515 (1965).

[85] M. Hakovirta, in *Proceedings of the 10th Workshop on RF Superconductivity, Tsukuba, 2001* (Ref. [62]), p. 433.

[86] L.Lilje *et al.*, in *Proceedings of the 9th Workshop on RF Superconductivity, Santa Fe, NM, 1999* (Ref. [11]), p. 74.

[87] G. Eremeev, H. Padamsee, M. Liepe, and R. Roy, in *Proceedings of the 11th Workshop on RF Superconductivity, Travemünde, 2003* (Ref. [44]), MoP18.

[88] Q. Ma and R. A. Rosenberg, in *Proceedings of the 10th Workshop on RF Superconductivity, Tsukuba, 2001* (Ref. [62]), p. 368.

[89] A. Dacca', G. Gemme, L. Mattera, and R. Parodi, Appl. Surf. Sci. **126**, 219 (1998).

[90] K. Kowalski *et al.*, in *Proceedings of the 11th Workshop on RF Superconductivity, Travemünde, 2003* (Ref. [44]), ThP09.

[91] W. DeSorbo, Phys. Rev. **132**, 107 (1963).

[92] S. W. Van Sciver, *Helium Cryogenics* (Plenum Press, New York, 1986).

[93] J. Halbritter, J. of Supercond. **8**, 691 (1995).

[94] J. Halbritter, J. of Appl. Phys. **97**, 083904 (2005).

[95] K. Fossheim and A. Sudboe, *Superconductivity: Physics and Applications* (Wiley & Sons, Chichester, 2004).

[96] J. Halbritter, P. Kneisel, and K. Saito, in *Proceedings of the 6th Workshop on RF Superconductivity, Newport News, 1993* (Ref. [63]), p. 617.

[97] M. A. Peck, Ph. D. Thesis, Technical University Wien, 1999.

[98] J. Halbritter, in *Proceedings of the 11th Workshop on RF Superconductivity, Travemünde, 2003* (Ref. [44]), MoP44.

[99] P. Bauer *et al*, Fermi National Accelerator Laboratory Report No. TD-05-020, 2005.

[100] J. Amrit, C. Z. Antoine, M. X. Francois, and H. Safa, Cryogenics **47**, 499 (2002).

[101] J. Knobloch and H. Padamsee, in *Proceedings of the 8th Workshop on RF Superconductivity, Abano Terme, 1997* (Ref. [9]), p. 337.

[102] L. Young, *Anodic Oxide Films* (Academic Press, New York, 1961).

[103] H. Safa *et al.*, in *Proceedings of the 7th Workshop on RF Superconductivity, Gif sur Yvette, 1995*, edited by B. Bonin (IN2P3, Orsay, France, 1995), p. 649.

[104] B. Visentin, in *Proceedings of the Pushing the Limits of RF Superconductivity Workshop, Argonne, 2004*, (Ref. [70]), p. 94.

[105] S. R. Agnew, F. Zeng, and G. R. Myneni, *Materiaux & Techniques*, **7-8-9**, 38 (2003).

[106] S. Bousson *et al.*, in *Proceedings of the 9th Workshop on RF Superconductivity, Santa Fe, NM, 1999* (Ref. [11]), p. 263.

[107] J. Sekutowicz, in *Proceedings of the 1994 Linear Accelerator Conference, Tsukuba, Japan,* edited by Takata (KEK, Tsukuba, Japan, 1995), p. 284.

[108] A. Brinkmann *et al.*, in *Proceedings of the 8th Workshop on RF Superconductivity, Abano Terme, 1997* (Ref. [9]), p. 452.

[109] L. Lilje, in *Proceedings of the 10th Workshop on RF Superconductivity, Tsukuba, 2001* (Ref. [62]), p. 287.

[110] G. R. Myneni (private communication).

[111] G. Ciovati, D. Barni, P. Kneisel, and J. Sekutowicz, Jefferson Lab Report No. TN-01-015, 2001.

[112] P. Kneisel, G. Ciovati, G. R. Myneni, and T. Carneiro, in *Proceedings of the 2005 Particle Accelerator Conference, Knoxville, 2005*, edited by N. Holtkamp (unpublished).

[113] A. Wu (private communication).

[114] P. Kneisel *et al.*, in *Proceedings of the 2005 Particle Accelerator Conference, Knoxville, 2005*, edited by N. Holtkamp (unpublished).

[115] B. Visentin *et al.*, in *Proceedings of the 11th Workshop on RF Superconductivity, Travemünde, 2003* (Ref. [44]), MoP19.

[116] B. R. King, H. C. Patel, D. A. Gulino, and B. J. Tatarchuk, Thin Solid Films **192**, 351 (1990).

[117] I. Arfaoui, C. Guillot, J. Cousty, and C. Antoine, J. of. Appl. Phys. **91**, 9319 (2002).

[118] C. Benvenuti, S. Calatroni, and V. Ruzinov, in *Proceedings of the 10th Workshop on RF Superconductivity, Tsukuba, 2001* (Ref. [62]), p. 441.

[119] H. Safa, in *Proceedings of the 10th Workshop on RF Superconductivity, Tsukuba, 2001* (Ref. [62]), p. 279.

[120] D. Richter, and T. Springer, Phys. Rev. B **18**, 126 (1978).

[121] C. Y. Ang, Acta Metall. **1**, 123 (1953).

[122] J. R. Waldram, *Superconductivity of Metals and Cuprates* (Institute of Physics Publishing, Bristol, 1996).

[123] C. Bean and J. D. Livingston, Phys. Rev. Lett. **12**, 14 (1964).

[124] A. Joseph and W. J. Tomasch, Phys. Rev. Lett. **12**, 219 (1964).

[125] R. D. Blois and W. de Sorbo, Phys. Rev. Lett. **12**, 499 (1964).

[126] M. Rabinowitz, J. of. Appl. Phys. **42**, 88 (1971).

[127] M. Rabinowitz, Appl. Phys. Lett. **19**, 73 (1971).

[128] K. Saito, in *Proceedings of the 11th Workshop on RF Superconductivity, Travemünde, 2003* (Ref. [44]), ThP17.

[129] J. Bardeen, Rev. Mod. Phys. **34**, 667 (1962).

[130] D. H. Douglass, Phys. Rev. Lett. **7**, 14 (1961).

[131] http://www.ansys.com

[132] K. Mittag, Cryogenics **13**, 94 (1973).

[133] R. L. Geng, J. Knobloch, and H. Padamsee, in *Proceedings of the 9th Workshop on RF Superconductivity, Santa Fe, NM, 1999* (Ref. [11]), p. 238.

[134] G. Ciovati, in *Proceedings of the Pushing the Limits of RF Superconductivity Workshop, Argonne, 2004*, (Ref. [70]), p. 52.

[135] W. H. Press, S. A. Teukolsky, W. T. Vetterling, and Brian P. Flannery, *Numerical Recipes in C++: The Art of Scientific Computing* (Cambridge University Press, Cambridge, 2002).

[136] G. Buzzi Ferraris, *Microsoft Visual C++ Applicazioni Scientifiche*, (Mondadori Informatica, Milan, 2000).

[137] J. C. Slater, *Microwave Electronics* (Van Nostrand, New York, 1950).

[138] J. Auer and H. Ullmaier, Phys. Rev. B **7**, 136 (1973).

APPENDIX A

COMPUTER CODE TO FIT SURFACE RESISTANCE AND PENETRATION DEPTH OF A SUPERCONDUCTOR

In order to calculate the material parameters of a superconductor such as the critical temperature T_c, the energy gap at 0 K divided by the Boltzmann constant and the critical temperature Δ/kT_c, the London penetration depth λ_L, the coherence length ξ and the electronic mean free path l using the BCS theory, a computer code has been developed which allow to fit the experimental data of the temperature dependence of the surface resistance and penetration depth with the theoretical data.

The code has been written in Microsoft Visual C++ 6.0©, which allows the realization of applications in Windows© environment, with an easy user interface. The BCS theory involves non-analytical relations between the material parameters and the surface impedance and the original algorithms written in Fortran by Halbritter [38] have been used.

Besides using the BCS theory, it is possible to fit the data with the following simplified expressions for surface resistance R_s and penetration depth λ:

$$R_s(T) = \frac{a_0}{T} \ln\left(\frac{4kT}{hf}\right) e^{-a_1 \frac{T_c}{T}} + a_2 \tag{A1}$$

$$\lambda(T) = \frac{\lambda_L \sqrt{1+\frac{\xi}{l}}}{\sqrt{1-\left(\frac{T}{T_c}\right)^4}} - \lambda(T_0). \tag{A2}$$

(A1) is valid for temperatures lower than $T_c/2$, a_1 is the ratio Δ/kT_c and a_2 is the residual resistance. (A2) is the expression of the penetration depth according to the two-fluid model and $\lambda(T_0)$ is an additional constant.

The algorithm that performs the mean square fit of the data is the Levenberg-Malquardt algorithm [135], which can be applied to any non-linear fit. It requires the

derivative of the function to be fitted with respect to each parameter and, in case of (A1) and (A2) these derivatives can be calculated analytically, but when the data have to be fitted with the BCS theory they have to be computed numerically:

$$\frac{dy}{da_i}\left(a_0, a_1, \ldots a_N, T_j\right) = \frac{y(a_0, a_1, \ldots, a_i + h_i, \ldots a_N) - y(a_0, a_1, \ldots, a_i, \ldots a_N)}{h_i} \qquad (A3)$$

$$i = 0, \ldots, N \quad j = 0, \ldots, NP$$

where a_i are the N parameters and T_j are the NP temperature values. The increment h has been chosen to be 5% of the parameter's value for each parameter. As for any non-linear fit, the initial guess value for the parameters is very important to improve the goodness of fit, since initial values too far from the solution may result in an higher chi-squared or a non-convergent calculation. Fig. A1 shows the main window of the program.

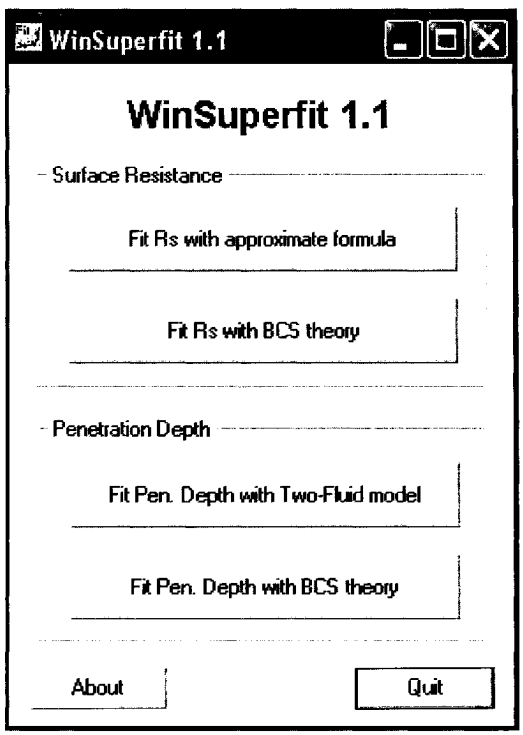

FIG. A1. Main window of the WinSuperfit program.

Selecting for example "Fit Rs with BCS theory", a window with all the available parameters appears, as shown in Fig. A2. Although all six material parameters could be

fitted at once, more meaningful results are obtained when the number of fit parameters does not exceed three.

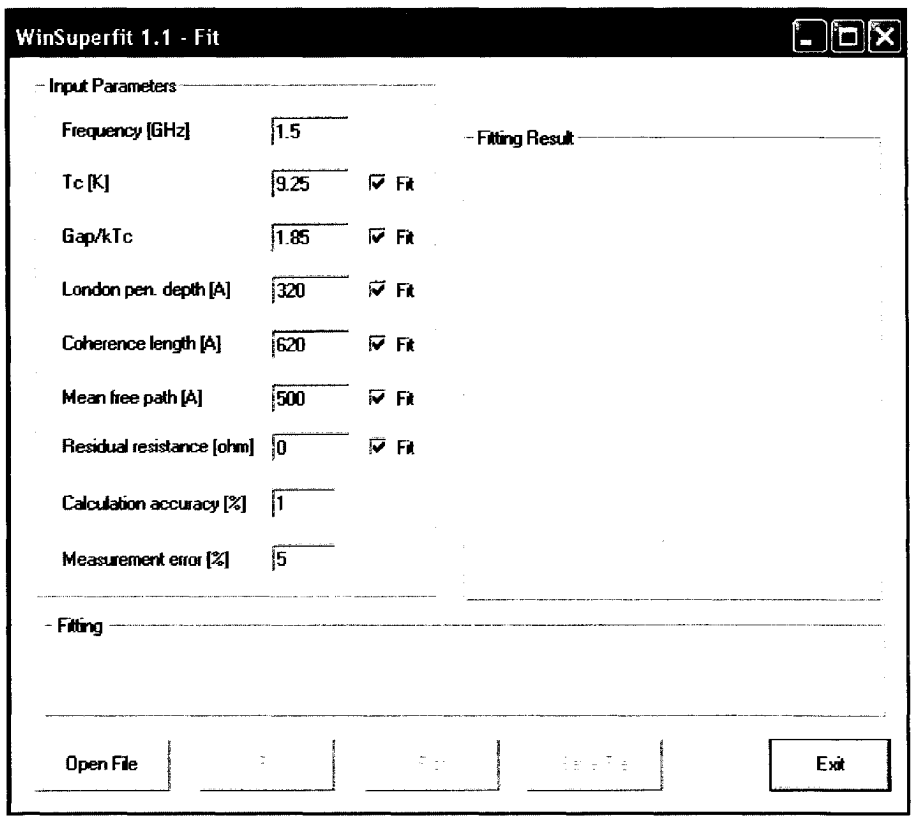

FIG. A2. Window for analyzing surface resistance vs. temperature data with BCS theory.

The input file is an ASCII text file starting with the number of data points followed by two columns indicating the temperature and surface resistance values in kelvin and ohm respectively. An optional third column could be included for the standard deviation of the surface resistance values. Alternatively, it is possible to specify a fixed percentage error for the data in the "Measurement error" box. The accuracy of the BCS theory numerical calculations can be modified with the "Calculation accuracy" box.

An example of the input file is shown in Fig. A3. The second column would indicate penetration depth values in angstrom for fitting penetration depth vs. temperature data.

```
28
4.313     1.049E-06
4.085     8.855E-07
3.950     7.561E-07
3.806     6.592E-07
3.690     5.722E-07
3.558     5.051E-07
3.431     4.380E-07
3.223     3.272E-07
3.082     2.768E-07
2.961     2.208E-07
2.871     1.958E-07
2.785     1.706E-07
2.700     1.404E-07
2.645     1.294E-07
2.569     1.088E-07
2.490     9.319E-08
2.418     7.848E-08
2.345     6.742E-08
2.264     5.529E-08
2.193     4.617E-08
2.136     3.368E-08
2.112     3.141E-08
2.087     2.929E-08
2.046     2.673E-08
1.972     2.197E-08
1.921     1.986E-08
1.864     1.761E-08
1.843     1.712E-08
```

FIG. A3. Example of input file for surface resistance analysis.

Once the data are loaded, a "guess" value for the parameters has been assigned and it has been decided which parameters to fit for, the "Fit" button becomes enabled. By pressing it the mean-square fit algorithm starts. The final results are shown on the right side of the window.

The results after each iteration step are shown at the bottom of the window. These include the iteration number, the chi-square, the variable "alamda", which is an indication of the variation applied to the fitting parameters, and finally the fitting parameters a_i (i =

0,1...5) corresponding to the material parameters listed from top to bottom. The calculations can be stopped at any time by pressing the "Exit" button and then the "Quit" button in the main window. Fig. A4 shows the fitting parameters result appearing at the end of the fitting process.

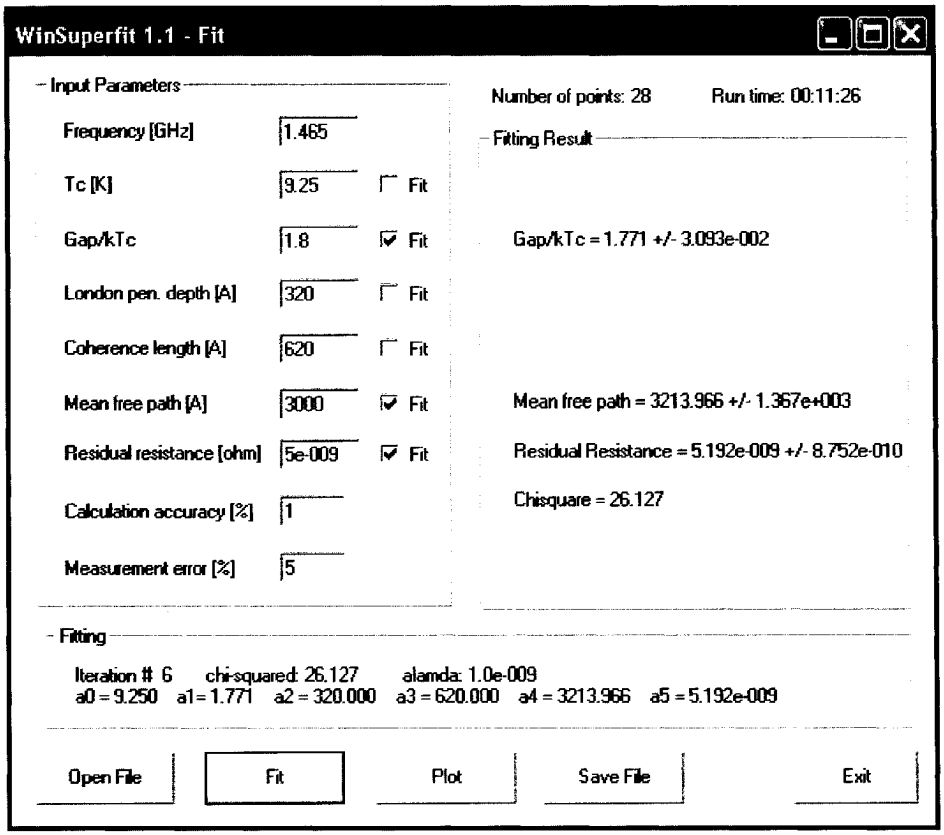

FIG. A4. Material parameters result at the end of the fitting process.

Once the fitting process is completed, the "Plot" button is enabled and allows creating a plot of the input data and the fitting curve, shown for example in Fig. A5. The plot function has been done using a graphic library included in Ref. [136].

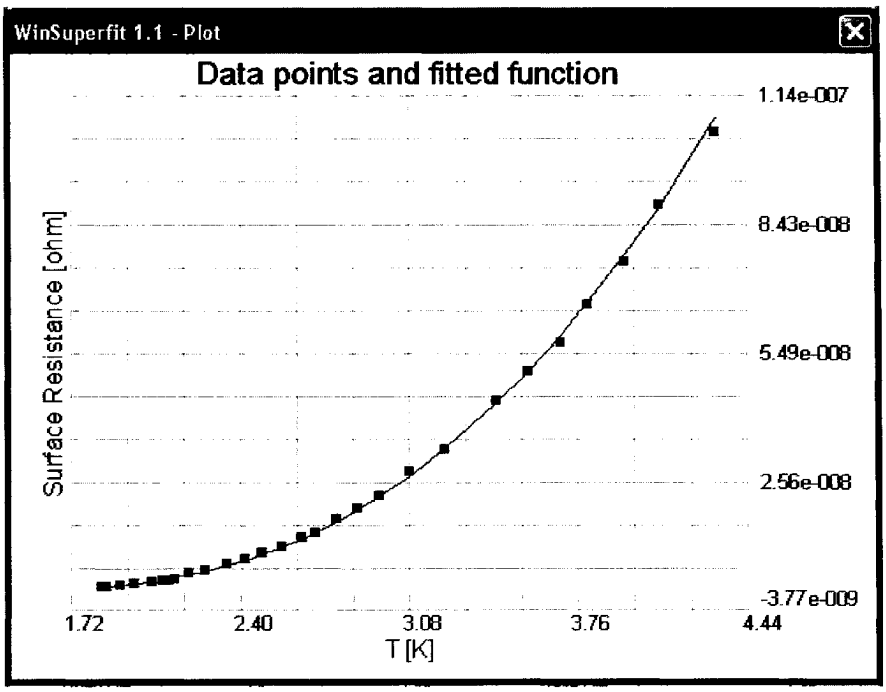

FIG. A5. Surface resistance data (squares) fitted with the BCS theory (solid line).

With the "Save file" button is possible to save an output file containing the initial parameters, the fit results and four columns containing the input data, fitted data and the standard deviation, shown for example in Fig. A6.

Result from fitting Surface Resistance vs. T with BCS theory

Initial parameters:
Gap/kTc (a0) = 1.75
Critical temperature (a1) [K] = 9.25
London penetration depth (a2) [A] = 320
Coherence length (a3) [A] = 620
Mean free path (a4) [A] = 3000
Residual Resistance (a5) [ohm] = 9e-009

chi-squared = 26.1273
a0 = 1.77096 +/- 0.0309282
a4 = 3214.11 +/- 1366.8
a5 = 5.1919e-009 +/- 8.75187e-010

T [K]	Rs [ohm]	Rs fit [ohm]	stdev [ohm]
4.313	1.049e-006	1.08272e-006	5.245e-008
4.085	8.855e-007	8.80539e-007	4.4275e-008
3.95	7.561e-007	7.72795e-007	3.7805e-008
3.806	6.592e-007	6.67101e-007	3.296e-008
3.69	5.722e-007	5.88621e-007	2.861e-008
3.558	5.051e-007	5.06301e-007	2.5255e-008
3.431	4.38e-007	4.33919e-007	2.19e-008
3.223	3.272e-007	3.2937e-007	1.636e-008
3.082	2.768e-007	2.68091e-007	1.384e-008
2.961	2.208e-007	2.21501e-007	1.104e-008
2.871	1.958e-007	1.90352e-007	9.79e-009
2.785	1.706e-007	1.63314e-007	8.53e-009
2.700	1.404e-007	1.39147e-007	7.02e-009
2.645	1.294e-007	1.2483e-007	6.47e-009
2.569	1.088e-007	1.06709e-007	5.44e-009
2.49	9.319e-008	8.98562e-008	4.6595e-009
2.418	7.848e-008	7.61924e-008	3.924e-009
2.345	6.742e-008	6.39194e-008	3.371e-009
2.264	5.529e-008	5.20706e-008	2.7645e-009
2.193	4.617e-008	4.31273e-008	2.3085e-009
2.136	3.368e-008	3.68625e-008	1.684e-009
2.112	3.141e-008	3.44561e-008	1.5705e-009
2.087	2.929e-008	3.20898e-008	1.4645e-009
2.046	2.673e-008	2.85076e-008	1.3365e-009
1.972	2.197e-008	2.29266e-008	1.0985e-009
1.921	1.986e-008	1.96924e-008	9.93e-010
1.864	1.761e-008	1.66143e-008	8.805e-010
1.843	1.712e-008	1.56126e-008	8.56e-010

FIG. A6. Output file generated with the WinSuperfit program.

APPENDIX B

FREQUENCY SENSITIVITY DUE TO PRESSURE VARIATIONS

A differential pressure applied to a resonant cavity causes a shift of the modes' resonant frequency by deforming the walls. The frequency change due to a variation of the cavity volume is given by the so-called Slater's theorem [137]:

$$\frac{\Delta f}{f_0} = \frac{1}{4U} \int_{\delta V} \left(\varepsilon_0 E^2 - \mu_0 H^2 \right) dV, \tag{B1}$$

where the integral is calculated over the volume change.

During the helium pump-down to lower the temperature from 4.3 to 2 K, the pressure on the cavity walls decreases from 830 torr to 2 torr. The frequency of TM_{010} mode was measured to increase at a rate 110 Hz/torr while the frequency in the TE_{011} mode decreases at a rate 350 Hz/torr, due to the absence of the electric field on the cavity surface and the different surface magnetic field distribution.

Besides the pressure due to the helium bath, the cavity walls are subjected to the radiation pressure exerted by the electric and magnetic field. Both effects slightly modify the contour of the cavity and, consequently, a shift of the modes resonant frequencies. The amplitude of the shift depends critically on the mechanical constraints the cavity might be subjected to.

The coefficient of proportionality between Δf and the square of the rf field is called Lorentz force coefficient (K_L) and it is an important parameter for pulsed rf accelerators. During the rf tests at 2 K, the single cell cavity has essentially no constraints and K_L was measured to be -0.162 Hz/(mT^2) for the TM_{010} mode and -0.349 Hz/(mT^2) for the TE_{011} mode.

APPENDIX C

EXPONENTIAL FIT OF THE Q-DROP DATA

The temperature map data and the overall surface resistance of the cavity as a function of the rf field concur in showing an exponential increase characterizing the Q-drop. Although we don't have a clear physical explanation for such dependence yet, the Q-drop data from all the experiments presented in this theses have been fitted with the following equation

$$R_s\left(B_p\right) = R_{s0} + be^{B_p/D}, \tag{C1}$$

with R_{s0}, b and D being fitting parameters. The correlation factor is greater than 0.971 in all cases and the value of fitting parameters are given in Table XXV. The parameter b is lowest in the TE_{011} mode and in the single crystal cavity and the average value of D is 6.85 ± 1.09 mT.

An estimate of the function D given by Eq. (145) for an isolated fluxoid near the surface of a niobium cavity is about 2 T, significantly higher than the results from the data fit. A possible cause for this discrepancy might be the fact that for a type II superconductor with Ginzburg-Landau parameter close to 1 such as niobium, there is a discontinuous increase of flux density from zero to a certain value B_0 when B_{c1} is exceeded [138]. The value of D could therefore be reduced by a larger number of fluxoids penetrating the surface.

TABLE XXV. Fitting parameters of Eq. (C1) compared with the Q-drop data from all cavity tests at 2 K.

	R_{s0} (nΩ)	b (nΩ)	B_l (mT)
Fig. 51	23.4	8.15×10^{-7}	6.54
Fig. 52	22.3	6.87×10^{-7}	5.83
Fig. 53	17.3	2.46×10^{-6}	8.05
Fig. 55	32.4	5.44×10^{-6}	6.56
Fig. 75, TM mode before baking	30.6	2.64×10^{-7}	5.85
Fig. 75, TM mode after baking	46.1	2.53×10^{-7}	6.69
Fig. 77, TM mode before baking	33.8	8.64×10^{-8}	5.26
Fig. 77, TM mode after baking	37.0	3.17×10^{-5}	8.55
Fig. 78, TM mode before baking	40.1	3.17×10^{-4}	8.62
Fig. 78, TM mode after baking	39.1	3.17×10^{-6}	7.37
Fig. 79, TM mode	29.7	5.82×10^{-7}	6.58
Fig. 79, TE mode	67.3	2.55×10^{-11}	4.97
Fig. 91	15.9	5.62×10^{-7}	6.90
Fig. 94	36.9	1.85×10^{-9}	5.90
Fig. 96	28.4	1.99×10^{-8}	7.07
Fig. 97, before baking	33.7	7.59×10^{-7}	7.78
Fig. 97, after baking	30.5	7.54×10^{-8}	7.92

APPENDIX D

COPYRIGHT FORM

Reprinted with permission from

G. Ciovati, Journal of Applied Physics Vol. 96 No. 3, pp.1591-1600 (2004), Copyright 2004, American Institute of Physics.

Dear Gianluigi Ciovati:

Copyright permission forms are usually supplied by the requestor.

We can, however, grant permission in the form of this e-mail.

Permission is granted for the following:

Journal of Applied Physics Vol. 96 No. 3, pp.1591-1600 (2004), to be reproduced as part of your Ph.D. thesis for Jefferson Lab/Old Dominion University. Please be sure to include an appropriate credit line referencing the original publication. Our preferred credit line is (please fill in the information indicated by CAPITAL LETTERS): Reprinted with permission from FULL CITATION. Copyright YEAR, American Institute of Physics.

If you have any further questions, please feel free to contact us.

Sincerely,

Susann Brailey

Office of the Publisher, Journals and Technical Publications

Rights & Permissions

American Institute of Physics

Suite 1NO1

2 Huntington Quadrangle

Melville, NY 11747-4502

516-576-2268 TEL

516-576-2450 FAX

rights@aip.org

VITA

Gianluigi Ciovati was born on September 8, 1976 in Legnano, Italy. He obtained his Bachelor degree in Physics from University of Milan in 2000.

Gianluigi moved to Jefferson Lab, in Newport News VA, USA, in June 2000 and he was hired as an accelerator engineer in 2001. He was admitted to graduate studies in Physics at Old Dominion University, in Norfolk, VA in 2002 and he obtained a Master of Science degree in 2003.